

A Search for Emerging Jets at $\sqrt{s} = 13$ TeV at ATLAS Run 2

by

Colleen J. Treado

A DISSERTATION SUBMITTED IN PARTIAL FULFILLMENT
OF THE REQUIREMENTS FOR THE DEGREE OF
DOCTOR OF PHILOSOPHY
DEPARTMENT OF PHYSICS
NEW YORK UNIVERSITY

JANUARY, 2021

Andy Haas

© COLLEEN J. TREADO

ALL RIGHTS RESERVED, 2021



Dedication

TO MY PARENTS.

Acknowledgments

I WOULD LIKE TO ACKNOWLEDGE everyone who has supported me and contributed to my success with this Ph.D. This is a feat I am deeply proud of, and none of it would have been possible without the help of many along the way.

First and foremost, thank you to my advisor, Andy Haas, who helped guide my work over the many years of my studies. You were an excellent mentor, providing insight and knowledge into all things particle physics, helping integrate me into the ATLAS collaboration, and pushing me when I really needed it. You always steered me in the right direction, but you also allowed me a great deal of freedom to explore and learn on my own, which has truly been an invaluable experience that I am deeply grateful for.

Thank you also to my committee members, Allen Mincer, Josh Ruderman, David Grier, and Maryam Modjaz, for your time and feedback throughout this process. You all made my defense an enjoyable, although nerve-wracking, experience, and your comments and questions only helped to improve my thesis. And thank you to all the NYU ATLAS faculty, Andy, Allen, Kyle Cranmer and Peter Nemethy. It was a pleasure to be a part of a group doing such unique and diverse work.

Thank you especially to my colleague and teammate, James Beacham, without whom the Emerging Jets analysis would not exist. You are incredibly brilliant, kind, and helpful, and

I learned more from you than from anyone. I admire you greatly, and it was an honor to work with you. I could not have asked for a better collaborator. We took on a behemoth of a task with this analysis, and while it pains me not to be able to see it all the way to fruition, I am proud of the work we did together, and I know it remains in good hands with you and the rest of the analysis team.

Thank you, as well, to the UEH Exotics and RPV/LL SUSY groups, whose joint dedication and collaboration made this technically challenging analysis more manageable. Thank you to everyone involved for pushing forward and making possible LLP physics at the LHC. And thank you to the entire ATLAS collaboration.

Finally, I owe a debt of gratitude to my family, who has always been loving and supportive. Thank you to my siblings, Bridgette, Lisa, Paul, Jeff, and Jason, and to my nieces, Evelyn and Fiona, for helping to put a smile on my face in what often felt like the darkest of times. Thank you to my parents, who always believed in me, even when I did not quite believe in myself. Dad, thank you for inspiring and encouraging me to be a physicist and for never letting me give up. Mom, thank you for being a shoulder to cry on, a friend to laugh with, and a never-ending well of support. Thank you both for always being proud of me, for affording me all the opportunities in my life, and for helping me get to where I am today. And thank you immensely to my partner, Jared, for your constant patience, understanding, and optimism in the most stressful and uncertain year of our lives, and always. I could not have made it through this last year without you.

Thank you, everyone.

Abstract

An ongoing search is presented for emerging jets, new exotic objects arising in models with QCD-like hidden sectors where dark quarks undergo dark showering, yielding long-lived dark hadrons that subsequently decay to visible jets with multiple small and varyingly-displaced vertices within the jet cone. Pair production of a new scalar mediator that connects the two sectors and decays to a SM quark and a dark quark thus results in a four-jet final state of two QCD jets and two emerging jets. The search uses 139 fb^{-1} of $\sqrt{s} = 13 \text{ TeV}$ proton-proton collision data collected by the ATLAS experiment at the LHC during Run 2 in 2015-2018 and relies heavily on dedicated large-radius tracking and displaced-vertexing techniques, special reconstruction algorithms developed specifically for identifying long-lived particle signatures. The search probes emerging jets produced in the inner detector from dark scalar mediators with masses between $m_{X_d} = 600 \text{ GeV}$ and $m_{X_d} = 1400 \text{ GeV}$ and dark pions with lifetimes between $c\tau_{\pi_d} = 0.5 \text{ mm}$ and $c\tau_{\pi_d} = 300 \text{ mm}$.

Contents

DEDICATION	iv
ACKNOWLEDGMENTS	v
ABSTRACT	vii
LIST OF FIGURES	xii
LIST OF TABLES	xviii
LIST OF APPENDICES	xix
o INTRODUCTION	I
I THE STANDARD MODEL	6
I.1 Overview	6
I.2 Particle content	9
I.3 Quantum chromodynamics (QCD)	13
I.3.1 Asymptotic freedom	15
I.3.2 Color confinement, hadronization, and jets	16
I.4 Electroweak theory	18
I.4.1 Electroweak symmetry breaking and the Higgs mechanism	21
I.5 Limitations of the Standard Model	25
I.5.1 Baryon asymmetry	29
I.5.2 Dark matter	35
I.5.3 BSM theories	43

2	EMERGING JET THEORY	47
2.1	Dark QCD	47
2.2	Emerging Jet phenomenology	53
3	THE ATLAS EXPERIMENT	59
3.1	The Large Hadron Collider	59
3.2	The ATLAS Detector	71
3.2.1	The inner detector	73
3.2.1.1	Pixel detector	76
3.2.1.2	Semiconductor tracker (SCT)	77
3.2.1.3	Transition radiation tracker (TRT)	79
3.2.2	The calorimeters	81
3.2.2.1	LAr electromagnetic calorimeter	83
3.2.2.2	Hadronic calorimeters	84
3.2.3	The muon spectrometer	87
3.2.4	The trigger system	88
3.2.4.1	Level-I (L1) Trigger	89
3.2.4.2	High-Level (HLT) Trigger	91
3.3	Simulation of collision events	93
3.3.1	Event generation	95
3.3.1.1	Hard scatter	97
3.3.1.2	Parton showering	98
3.3.1.3	Hadronization	98
3.3.1.4	Underlying event	100
3.3.1.5	Unstable decay	100
3.3.2	Detector simulation	101

3.3.3	Digitization	102
3.3.4	Fast chain	103
3.3.4.1	Fast simulation	103
3.3.4.2	Fast digitization	107
3.3.4.3	Fast reconstruction	108
3.4	Reconstruction of collision events	109
3.4.1	Inner detector track reconstruction	112
3.4.1.1	Standard tracking	118
3.4.1.2	Large Radius Tracking	123
3.4.2	Vertex reconstruction	132
3.4.2.1	Primary vertexing	133
3.4.2.2	Secondary vertexing: VrtSecInclusive	136
3.4.3	Jet reconstruction	152
3.4.3.1	Topological cell clustering	154
3.4.3.2	Reconstructed jets at ATLAS	158
3.4.3.3	Jet calibration	159
3.4.3.4	Jet quality selection	168
4	EMERGING JETS SEARCH	172
4.1	Signal model	173
4.2	Data and MC samples	180
4.2.1	Data samples	180
4.2.1.1	Data-flow	181
4.2.2	Monte Carlo samples	194
4.2.2.1	MC signal samples	194
4.2.2.2	MC background samples	227

4.3	Signal selections	229
4.3.1	Selection overview	229
4.3.2	Event preselection	233
4.3.3	Baseline physics object selection	235
4.3.3.1	Baseline jets	236
4.3.3.2	Baseline tracks	236
4.3.4	Analysis region selection	237
4.3.4.1	Search region	237
4.3.4.2	Validation region	240
4.3.5	Displaced vertex selection	241
4.3.5.1	Displaced vertex selection working points	242
4.3.5.2	Displaced vertex reconstruction efficiency	261
4.3.6	Emerging jet selection	285
4.3.6.1	Emerging jet selection working points	285
4.3.7	Leading N-jet selection	295
4.3.8	Overall event cutflow and signal efficiency	304
4.4	Background estimation	314
4.4.1	Overview of ABCD method	315
4.4.2	Proposed ABCD planes and method	319
4.4.3	Shifted validation region method	325
4.4.4	Validation of background estimation method	329
4.4.5	Initial background estimate results	334
5	CONCLUSION	337
APPENDICES		342
REFERENCES		412

List of figures

1.1	SM particle content	10
1.2	QCD color confinement	17
1.3	QCD hadronization	18
1.4	CMB measure of baryon density	32
1.5	SUSY exclusion limits	46
2.1	Dark QCD schematic	51
2.2	EJ schematic	54
2.3	EJ Feynman diagrams and cross section	56
2.4	EJ Feynman diagram (hard process)	56
2.5	EJ signature schematic	58
3.1	CERN accelerator complex	67
3.2	Integrated luminosity	70
3.3	Luminosity-weighted pileup	70
3.4	ATLAS detector	71
3.5	ATLAS inner detector	74
3.6	ATLAS inner detector quadrant	75
3.7	ATLAS inner detector sensors	76
3.8	TRT HT fraction	80
3.9	ATLAS calorimeters	82
3.10	Electromagnetic calorimeter X_e vs $ \eta $	85

3.11	Calorimeter X_0 vs $ \eta $	86
3.12	ATLAS muon spectrometer	88
3.13	ATLAS TDAQ	90
3.14	ATLAS simulation chain flow	94
3.15	String hadronization model	99
3.16	Fast simulation schemes	106
3.17	Fast digitization	108
3.18	Particle paths in ATLAS detector	110
3.19	Charged particle trajectory in ATLAS detector	115
3.20	ATLAS track parametrization in perigee representation	117
3.21	Track reconstruction efficiency	123
3.22	Feynman diagrams for LRT BSM models	127
3.23	LRT reconstruction efficiency	129
3.24	LRT technical reconstruction efficiency	131
3.25	Hit pattern consistency check	140
3.26	Incompatibility graph	142
3.27	DV track phi asymmetry and cleaning	146
3.28	Feynman diagrams for VSI BSM models	147
3.29	VSI truth handling	148
3.30	VSI reconstruction efficiency	151
3.31	JES calibration scheme	161
3.32	Jet- p_T pileup dependence before and after pileup correction	164
3.33	JVT	169
3.34	Jet cleaning efficiency	171
4.1	DRAW_RPVLL rates for 2018 run 358333	184

4.2	DRAW_RPVLL rates for 2017	185
4.3	Average 2017 DRAW_RPVLL rate versus average $\langle \mu \rangle$	186
4.4	DAOD operations	190
4.5	Signal grid	199
4.6	Fixed vs running coupling: orphan p_T	204
4.7	Fixed vs running coupling: jet girth	205
4.8	Truth signal distributions: n dark pions	207
4.9	Truth signal distributions: dark pion $\beta\gamma$ and p_T	208
4.10	Truth signal distributions: dark pion η and ϕ	209
4.11	Truth signal distributions: n dark pion decay vertices	211
4.12	Truth signal distributions: dark pion decay vertex r and z	213
4.13	Truth signal distributions: dark pion decay vertex opening angle	214
4.14	Truth signal distributions: dark pion decay vertex n-descendants and invariant mass	215
4.15	Truth signal distributions: dark pion decay vertex descendant p_T	217
4.16	Truth signal distributions: dark pion decay vertex descendant η and ϕ	218
4.17	Truth signal distributions: dark pion decay vertex descendant d_o and z_o	220
4.18	Truth signal distributions: n jets and constituents	222
4.19	Truth signal distributions: n emerging jets and constituents	223
4.20	Truth signal distributions: jet p_T	224
4.21	Truth signal distributions: jet η and ϕ	224
4.22	Truth signal distributions: jet girth	225
4.23	Truth signal distributions: n jet-matched dark pion decay vertices	226
4.24	Truth signal distributions: n jet-matched dark pion descendants	227
4.25	Multijet trigger efficiency (2015 + 2016)	240
4.26	Material Map veto	244

4.27	DV selections: track cleaning	246
4.28	DV selections: fiducial volume	248
4.29	DV selections: χ^2/N_{DoF} and mass	250
4.30	DV selections: p_T	252
4.31	DV selections: minimum impact parameters and errors	254
4.32	DV selections: cutflow	256
4.33	DV selections: N_{DV} cutflow	258
4.34	DV selections: N_{DV} cutflows (by-jet vs by-N-lead-jet)	260
4.35	Tracking efficiency: inclusive vs r, d_o	263
4.36	Tracking efficiency: inclusive, standard, large-radius vs r	265
4.37	Tracking efficiency: inclusive, standard, large-radius vs d_o	267
4.38	Tracking efficiency: inclusive vs average $\langle \mu \rangle$	269
4.39	Vertexing efficiency: match score	271
4.40	Vertexing efficiency: average n-track, mass vs r	273
4.41	Vertexing efficiency: factorized efficiencies vs r	275
4.42	Vertexing efficiency: acceptance vs r	277
4.43	Vertexing efficiency: core efficiency vs r	278
4.44	Vertexing efficiency: algorithmic efficiency vs mass, n selected tracks	280
4.45	Vertexing efficiency: factorized efficiencies vs $\langle \mu \rangle$	282
4.46	Vertexing efficiency: factorized signal efficiencies vs r	283
4.47	Vertexing efficiency: total inclusive and signal efficiencies vs r	284
4.48	EJ selections: hard p_T, η , and m	288
4.49	EJ selections: $p_T^{N_{\text{sv}}}$ and $N_{\text{jet-trk}}^{N_{\text{sv}}}$	290
4.50	EJ selections: cutflow	292
4.51	EJ selections: N_{EJ} cutflow	294
4.52	NJetX selections: $H_T^{\text{NJet}}, m_{\text{sum}}^{\text{NJet}}$, and p_T^{NJet}	299

4.53	NJetX selections: $H_T^{\text{NJetJJ,max-}p_T}$, $m_{\text{sum}}^{\text{NJetJJ,max-}p_T}$, and $p_T^{\text{NJetJJ,max-}p_T}$	300
4.54	NJetX selections: H_T^{NJet} cutflow	302
4.55	NJetX selections: $H_T^{\text{NJetJJ,max-}p_T}$ cutflow	303
4.56	Signal cutflow: Loose DVs	308
4.57	Signal cutflow: Medium DVs	309
4.58	Signal cutflow: Tight DVs	310
4.59	Signal cutflow: Loose vs Tight EJs	311
4.60	Signal cutflow: $N_{\text{EJ}} = 2$	312
4.61	Full signal cutflow	313
4.62	ABCD method: average N_{DV} vs X^{NJet}	320
4.63	ABCD plane: Model A	323
4.64	ABCD plane: Model B	324
4.65	Shifted VR ABCD method	329
A.1	<code>BCM_RDOAnalysis</code>	348
A.2	<code>PixelRDOAnalysis</code>	349
A.3	<code>SCT_RDOAnalysis</code>	350
A.4	<code>TRT_RDOAnalysis</code>	351
A.5	<code>TileRDOAnalysis</code>	353
A.6	<code>LArRDOAnalysis</code>	354
A.7	<code>MDT_RDOAnalysis</code>	356
A.8	<code>CSC_RDOAnalysis</code>	357
A.9	<code>RPC_RDOAnalysis</code>	358
B.1	<code>DiLep DRAW_RPVLL</code> filter rates in 2017 and 2018	367
B.2	<code>DiLep_SiPhotonX DRAW_RPVLL</code> filter rate versus luminosity	368
B.3	<code>DV DRAW_RPVLL</code> filter rates in 2017 and 2018	370

B.4	DV_MultiJet DRAW_RPVLL filter rate versus luminosity	371
B.5	KinkedTrack DRAW_RPVLL filter rates in 2017 and 2018	374
B.6	KinkedTrack DRAW_RPVLL filter rates versus luminosity	376
B.7	HnL DRAW_RPVLL filter rates in 2017 and 2018	378
B.8	HV DRAW_RPVLL filter rates in 2017 and 2018	383
B.9	Emerging DRAW_RPVLL filter rates in 2017 and 2018	386
B.10	Emerging filter trigger issue	387
B.11	DRAW_RPVLL rates for representative 2017 and 2018 runs	389
B.12	Overall DRAW_RPVLL rate versus average physics_Main , $\langle\mu\rangle$	390
B.13	DRAW_RPVLL filter fractions and rates	391
D.1	Pythia validation: n dark quark decay products and off-diagonal mesons . .	404
D.2	Number of diagonal dark pions and dark rhos	405
D.3	Pythia validation: number and decay position of inclusive dark pions . . .	406
D.4	Pythia validation: orphan p_T	408
D.5	Pythia validation: number of dark and truth jets	409
D.6	Pythia validation: dark and truth jet p_T	410
D.7	Pythia validation: dark and truth jet width	411

List of tables

2.1	Dark QCD particle content	50
3.1	LHC Run2 parameters	68
3.2	Inner detector pixel layer parameters	78
3.3	Standard track selection working points	122
3.4	Standard tracking vs LRT selections	124
3.5	LRT truth particle fiducial selections	128
3.6	DV selected track criteria	137
3.7	DV two-track seed criteria	139
3.8	DV associated track criteria	144
4.1	Benchmark models	178
4.2	Signal m_{X_d} - $c\tau_{\pi_d}$ parameter space	178
4.3	Signal sub-grid	200
4.4	Background MC samples	229
4.5	Analysis event selection	231
4.6	Analysis DV selection working points	242
4.7	Analysis EJ selection working points	286
4.8	ABCD validation: MC	332
4.9	ABCD validation: data	333
4.10	ABCD initial results	335
B.1	DRAW_RPVLL filters	363

List of appendices

APPENDIX A	RDOAnalysis DIGITIZATION VALIDATION PACKAGE	343
APPENDIX B	DRAW_RPVLL MONITORING	359
B.1	DRAW_RPVLL filter stream	362
B.1.1	RPVLL SUSY filters	362
B.1.1.1	Dilepton displaced vertices (DiLep) filters	363
B.1.1.2	Mult-track displaced vertices (DV) filters	368
B.1.1.3	Disappearing tracks (KinkedTrack) filters	372
B.1.2	UEH Exotics filters	377
B.1.2.1	Heavy neutral leptons (HnL) filters	377
B.1.2.2	Displaced jets (HV) filters	379
B.1.2.3	Emerging jets (Emerging) filters	384
B.1.3	Overall rates in Run 2	388
B.2	TriggerAPI implementation	391
APPENDIX C	TRUTH DARK JETS	395
APPENDIX D	PYTHIA HV RUNNING COUPLING VALIDATION	400

0

Introduction

PARTICLE PHYSICS is the study of elementary matter, the fundamental building blocks of the universe, as well as forces that describe how they interact with one another. Scientists' understanding of these particles and forces has developed over time, from the discovery of subatomic particles in the late 19th and early 20th centuries, to the search for a strong

nuclear force and the “particle zoo” of hadron discoveries in the 1950s and 1960s, which led to the development of the quark model and eventually to the development of the current theory of particle physics, the Standard Model of particle physics [1], which describes the known elementary particles and their interactions, except gravity. The Standard Model has been repeatedly confirmed through experiment, most notably and recently with the discovery of the Higgs boson [2, 3] at the Large Hadron Collider [4] by both the ATLAS [5] and CMS [6] experiments in 2012, nearly 50 years after it was first theorized.

The Standard Model is a combined theory of the Glashow, Weinberg, and Salam theory of the electroweak interaction [7–9] with quantum chromodynamics (QCD) [10, 11], the theory of the strong interaction. In the electroweak theory, electromagnetic and weak forces are unified above the unification scale on order of a few hundred GeV but appear as two separate forces on everyday energy scales due to spontaneous electroweak symmetry breaking caused by the Higgs mechanism [12]. While the Standard Model, sometimes referred to as the “theory of *almost* everything”, is generally a very successful and self-consistent theory, it falls short of being a complete theory of the fundamental interactions of the universe and leaves a few very important questions unanswered, like how to describe gravity or explain the large discrepancy between the weak scale and the Planck scale, known as the hierarchy problem. The Standard Model also provides no viable dark matter candidate or reasonable explanation for the observed dark matter and baryonic asymmetries in

the universe.

Dark matter is invisible, non-baryonic matter making up about twenty-five percent of the critical density and about eighty percent of the matter density of the universe [13]. Evidence of dark matter comes from astrophysical observations of galaxies and gravitational lensing suggesting they contain more mass than is visible and from measurements of the thermal relic density of matter in the universe left over from the Big Bang, which indicates baryonic matter only accounts for about five percent of the critical density, while total matter comprises around thirty percent. The evidence suggests dark matter must be stable, to account for its large relic density, as well as gravitationally interacting, neutral, and non-colored; however, no reasonable dark matter particle candidate exists within the Standard Model, implying there must be a new, beyond the Standard Model (BSM) realm of physics where the dark matter candidate lives.

Many dark matter candidates have been theorized and searched for at the LHC in recent years, including the most popular candidate, weakly interacting massive particles (WIMPs) [14], but to no avail. This fact, along with observed astrophysical anomalies that point away from standard cold dark matter and the need to resolve the coincidence between the energy density of dark matter and baryons, allow for the possibility of dark matter theories with more complicated dark sectors, like asymmetric dark matter [15] with dark QCD [16], where a QCD-like dark sector exists at the GeV scale [17]. Such models postulate the ob-

served similarity between dark and baryonic mass and number densities is due to a shared asymmetry between QCD and dark QCD, where a TeV-scale mediator, charged under both the visible and dark sectors, acts as a portal between the two. The GeV-scale dark sector arises naturally from the requirement that the dark matter mass be approximately five times that of the proton to reproduce the observed dark matter density. Such a dark QCD model contains a light stable dark baryon, analogous to the proton, that acts as the dark matter candidate, as well as a zoo of unstable dark mesons, the lightest of which, the dark pion, can decay back to the Standard Model. Because of the GeV-to-TeV hierarchy, this decay can be very slow, resulting in dark pions with macroscopic decay lengths of order centimeters to meters. At the collider, this phenomenon could manifest in the form of *emerging jets*, where dark jets are comprised primarily of dark pions that decay to the visible sector at different displacements within the respective dark jet, thus resulting in visible jets that *emerge* into the detector over a macroscopic length scale with multiple displaced and distinct vertices.

In this thesis, an ongoing search is presented for emerging jets in four-jet final states from the pair production of dark scalar mediators and their subsequent decays to SM-dark quark pairs. The search is based on 139 fb^{-1} integrated luminosity of 13-TeV center-of-mass energy proton-proton collision data collected by the ATLAS experiment at the LHC during Run 2 between the years 2015 and 2018. An introduction to the Standard Model of particle physics

is presented in Section 1, followed by an overview of the theory of emerging jets, including dark QCD, in Section 2. The Large Hadron Collider and the ATLAS experiment are discussed in Section 3, with special attention paid to the dedicated reconstruction of displaced tracks and vertices required for long-lived particle analyses. Finally, the search for emerging jets in its current state is detailed in Section 4, and conclusions and outlooks for the future are presented in Section 5.

1

The Standard Model

1.1 OVERVIEW

THE STANDARD MODEL (SM) OF PARTICLES PHYSICS is a well-established gauge-invariant quantum field theory (QFT) describing the known fundamental particles in the universe and the interactions between them [18–21]. As a theoretical framework construct-

ed from experimental data, the Standard Model has proven highly successful in predicting elementary particle physics phenomena and has been repeatedly substantiated over the years by observations and new discoveries.

Modern particle physics and the Standard Model were developed throughout the mid-twentieth century in an attempt to describe the strong, weak, and electromagnetic forces through a coherent set of renormalizable QFTs, based on the success of quantum electrodynamics (QED). Prior to this development, the universe was understood as containing four distinct and very different forces: the strong nuclear force, the weak force, the electromagnetic force, and gravity. The strong force is responsible for binding the atomic nucleus together due to interactions between color-charged quarks and gluons, described in Section 1.2. With a strength of order $\alpha_s \approx 1$ at a range of 10^{-15} m (roughly the radius of the proton), it is the strongest of the fundamental forces, hence the name. The weak force, on the other hand, responsible most notably for its role in nuclear decay and fusion, is far weaker, with a strength of order $10^{-6} - 10^{-7}$ and a range of about 10^{-17} m. The *intrinsic* strength of the weak interaction, however, is much larger, and in fact even larger than the electromagnetic strength, at $\alpha_w \approx 1/30$, but the large masses of the weak mediators yield effectively weak interactions at relatively low energies. The electromagnetic force, governing much of the macroscopic physics in the universe, has a strength of $\alpha \approx 1/137$, where α is the fine-structure constant, and an infinite range. Gravity is the weakest force, with an infinite range

and a very low strength of order 10^{-38} .

The development of the Standard Model [I] allowed all of these fundamental forces but gravity to be commonly described in the language of quantum gauge field theories, even elegantly combining the electromagnetic and weak forces into a single electroweak gauge theory, in the same vein as Maxwell's unification of electricity and magnetism. This established theory of strong and electroweak interactions was followed by a long era of experimental verification over a wide range of energies and phenomena, culminating in the discovery of the Higgs boson at the LHC in 2012, effectively “completing” the Standard Model.

The Standard Model is a renormalizable non-Abelian quantum field theory with underlying local gauge symmetry

$$SU(3) \times SU(2) \times U(1), \quad (\text{I.I})$$

where $SU(3)$ describes quantum chromodynamics (QCD) [IO, II], the gauge theory for the strong interaction between color-charged particles (see Section I.3), and $SU(2) \times U(1)$ describes the unified electroweak gauge theory [7–9] with spontaneously broken symmetry via the Higgs mechanism [12] (see Section I.4). The particles in the Standard Model, as in all quantum field theories, are described by fields. A scalar field $\varphi(x)$ represents a spin-0 particle, or the Higgs boson, which breaks electroweak symmetry and gives particles mass. Vector fields $A_\mu(x)$ represent spin-1 particles, or gauge bosons, which mediate interactions through their exchange. Spinor fields $\psi(x)$ represent spin-1/2 particles, or fermions, classi-

fied as either quarks or leptons, which make up matter. For a detailed description of the full SM particle content, see Section [1.2](#).

That the SM is renormalizable allows for precise predictions of measurable quantities to higher orders in perturbation theory. The local gauge invariance of the theory refers to the symmetry of the Lagrangian under local phase transformations of the fermion fields. Requiring local gauge invariance introduces gauge fields, corresponding to gauge bosons, to the free Lagrangian that induce interaction terms. Additional gauge-invariant kinetic terms describing the propagation of free gauge fields and their self-interactions are also required. The Standard Model Lagrangian describing the elementary particles and their interactions can be written in terms of its two independent components:

$$L_{\text{SM}} = L_{\text{QCD}} + L_{\text{EW}}, \quad (1.2)$$

corresponding to the $SU(3)$ color and $SU(2) \times U(1)$ electroweak sectors, which are detailed in Sections [1.3](#) and [1.4](#), respectively [[22](#), [23](#)].

1.2 PARTICLE CONTENT

The particle content of the Standard Model consists of two types of fundamental particles: half-integer-spin fermions and integer-spin bosons. A summary of these particles and their quantum numbers can be found in Figure [1.1](#). A brief description is provided below.

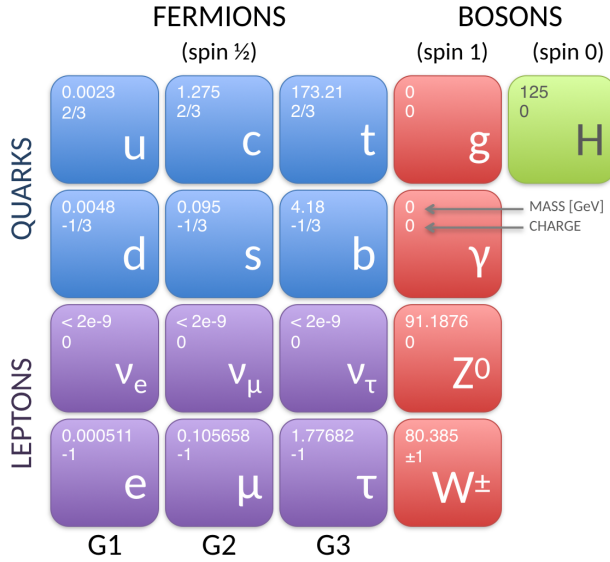


Figure 1.1: The elementary particles organized by type. The spin-1/2 fermions are listed by generation from left to right, with the quarks in blue and the leptons in purple. The spin-1 gauge bosons are in red and the spin-0 Higgs boson is in green. The top left corner of each box lists the particle mass in GeV and the particle charge in units of the proton charge.

Spin-1/2 fermions, represented by spinor fields, are elementary particles of matter. There are twelve (12) fundamental fermions, each with a corresponding antiparticle with opposite sign quantum numbers. Fermions are categorized into two groups of six quarks and six leptons, which are each further paired into three generations of increasing mass and decreasing stability that are otherwise identical. All higher generation particles decay to first generation particles, which make up all stable, everyday matter in the universe, like the protons, neutrons, and electrons in atoms.

Quarks come in six (6) flavors: up (u), down (d), charm (c), strange (s), top (t), and bottom (b), arranged into three generations of (up-type, down-type): (u, d), (c, s), and (t, b).

Up-type and down-type quarks carry electric charge $+2/3$ and $-1/3$, respectively, and, in the case of left-handed particles, weak-isospin $+1/2$ and $-1/2$, respectively (right-handed particles do not carry weak isospin); thus, quarks undergo electroweak interactions. Handedness refers to the particle's helicity, or the projection of the particle's spin onto the direction of its momentum, where a right-handed, or $+1$ -helicity, particle is one with spin parallel to its momentum, and a left-handed, or -1 -helicity, particle is one with spin antiparallel to its momentum. Quarks also come in three experimentally indistinguishable “colors”: red (r), green (g), and blue (b), referring to the quark being charged under $SU(3)$ color symmetry; thus, the quarks undergo strong interactions. Quarks also carry a baryon number of $+1/3$. The baryon number $B = \frac{1}{3}(n_q - n_{\bar{q}})$ is a conserved additive quantum number of any particle interaction. The up, down, and strange quarks are the lightest quarks, while the charm, top, and bottom are much heavier, with the top quark being extremely massive and therefore too short-lived to form hadrons before decaying.

The six leptons consist of three (3) charged, massive particles: electron (e), muon (μ), and tau (τ), and three (3) corresponding neutrinos: electron-neutrino (ν_e), muon-neutrino (ν_μ), and tau-neutrino (ν_τ), which are neutral and nearly massless (note: the Standard Model treats neutrinos as though they are massless, but they are known to have some very small mass from experiment). Electron-type leptons carry electric charge -1 and weak-isospin $-1/2$ (again, only left-handed leptons carry weak-isospin) and thus undergo elec-

Electroweak interactions. Neutrinos, being neutral and carrying weak-isospin $+1/2$, only undergo weak interactions and only exist as left-handed particles. Leptons do not carry color charge and thus do not interact with the strong force. Like baryon number for quarks, leptons carry a lepton number $L = (n_l - n_{\bar{l}})$ of $+1$.

Gauge bosons, represented by vector fields, are spin-1 mediator particles, or fundamental force carriers. They are exchanged between particles to mediate interactions between fields in the corresponding QFTs. Gluons (g) are the gauge bosons associated with the strong force, mediating interactions between color-charged particles. They are massless, neutral, and bi-colored, carrying one unit of color and one unit of anticolor, and exist in eight independent states. Being color-charged themselves, they not only couple to quarks, but also to one another, resulting in the unique features of asymptotic freedom (Section 1.3.1) and color confinement (Section 1.3.2) in QCD. The massless, neutral photon (γ) is the mediator of the electromagnetic force, and the massive W/Z bosons (W^\pm, Z) are the mediators of the weak force. The photon and W/Z bosons arise as linear combinations of the electroweak gauge fields after electroweak symmetry breaking (see Section 1.4.1), which generates masses for the W/Z bosons on order of the electroweak scale ($m_{EW} = \mathcal{O}(100 \text{ GeV})$). The W and Z boson have weak-isospin ± 1 and 0 and masses determined experimentally to be 80.2 GeV and 91.2 GeV, respectively. The W bosons mediate the weak charged-current (CC) interactions, such as decays. These interactions are the only ones to change particle

flavor and violate parity. Meanwhile, the Z boson mediates the weak neutral-current (NC) interactions. Like gluons, the W/Z bosons also couple with one another, although at least a pair of charged W bosons must be involved in the interaction. The two W-boson charge states are each other's antiparticles, while the gluons, photon, and Z boson are their own antiparticles.

The final SM particle is the spin-0 Higgs boson, represented by a scalar field. It arises as an excitation of the Higgs field, which has a non-zero vacuum expectation value, thereby providing the mechanism by which electroweak symmetry is broken and the W/Z bosons acquire mass. Fermionic couplings to this nonzero Higgs field also generate masses for the quarks and leptons. The Higgs boson (H) is neutral and colorless, has a weak-isospin of $-1/2$, and is its own antiparticle. It was famously discovered at the LHC by both ATLAS and CMS in 2012 with a mass of about 125 GeV [2,3].

1.3 QUANTUM CHROMODYNAMICS (QCD)

QCD is the gauge invariant theory of the strong interaction, defined by the $SU(3)$ color symmetry group, and corresponding to the L_{QCD} sector of the SM Lagrangian. The $SU(3)$ group is the set of all “special”, or determinant-one, unitary 3×3 matrices, and $SU(3)$ color symmetry refers to invariance under rotations in color space. The fundamental representation of the group is described by color triplets of the fermion fields, $\Psi_q = (\psi_{q_1}, \psi_{q_2}, \psi_{q_3})^T$,

for each quark flavor q . The group has eight (8) generators, or basis vectors, T_a , given by

$$T_a = \frac{1}{2} \lambda_a, \quad a = 1, \dots, 8 \quad (I.3)$$

in the triplet representation, where λ_a are the 3×3 Gell-Mann matrices. As a non-Abelian group, the generators of $SU(3)$ do not commute, resulting in non-zero real structure constants f_{abc} :

$$[T_a, T_b] = if_{abc}. \quad (I.4)$$

The generators are associated with the eight gauge fields, representing the gluons, introduced by local gauge invariance. The QCD Lagrangian is given by

$$L_{\text{QCD}} = -\frac{1}{4} G_{\mu\nu}^a G^{a,\mu\nu} + \sum_{q=1}^6 \bar{\Psi}_q (i\gamma^\mu D_\mu - m_q) \Psi_q, \quad (I.5)$$

where $D_\mu = \partial_\mu + ig_s \frac{\lambda_a}{2} G_\mu^a$ is the covariant derivative acting on the quark triplets, and $G_{\mu\nu}^a = \partial_\mu G_\nu^a - \partial_\nu G_\mu^a - g_s f_{abc} G_\mu^b G_\nu^c$ is the QCD analog of the QED field strength tensor $F_{\mu\nu}$, describing the interactions between the gauge (gluon) and fermion (quark) fields, with strong coupling constant g_s related to the strong fine-structure constant by $\alpha_s = \frac{g_s^2}{4\pi}$. The kinetic term in the QCD Lagrangian contains not only quadratic terms, describing the free propagation of the gluon fields, but also cubic and quartic terms, corresponding to gluon self-couplings, since gluons are also charged under $SU(3)$ color symmetry. As a consequence

of these self-interactions, QCD exhibits two identifying behaviors: asymptotic freedom [24, 25] and color confinement [26], detailed in the next two sections, respectively.

1.3.1 ASYMPTOTIC FREEDOM

Renormalizable quantum field theories contain running couplings that change with the energy scale. The process of renormalization removes infinities from higher-order loop corrections by “regularizing” them, or making them temporarily finite through some additional parameters, and letting observables, like mass and the coupling constant, absorb these regularized divergences through the introduction of some unphysical “renormalization scale” μ_R on which the renormalized physical quantities explicitly depend. In QCD, with both quark and gluon loops involved and contributing with opposite sign, this effect is significant, resulting in a strong running coupling that is large at low energy scales and sufficiently small at high energy to recover perturbation theory calculation techniques.

The renormalized strong coupling $\alpha_s(\mu_R^2)$ is described as a function of momentum transfer by the following renormalization group equation (RGE):

$$\mu_R^2 \frac{d\alpha_s}{d\mu_R^2} = \beta(\alpha_s) = -(b_0\alpha_s^2 + b_1\alpha_s^3 + \dots), \quad (1.6)$$

where b_o is the one-loop β -function coefficient:

$$b_o = \frac{11n_c - 2n_f}{12\pi}. \quad (1.7)$$

To first order, the running coupling evolves with momentum transfer q^2 as follows:

$$\alpha_s(q^2) = \frac{\alpha_s(\mu_R^2)}{1 + b_o \alpha_s(\mu_R^2) \ln(q^2/\mu_R^2)} = \frac{1}{b_o \ln(q^2/\Lambda^2)}. \quad (1.8)$$

Since $n_c = 3$ (the number of colors) and $n_f = 6$ (the number of quark flavors), $b_o > 0$ and $\beta(\alpha_s) < 0$, resulting in a running coupling that decreases with increasing momentum transfer and becomes sufficiently small for hard processes. The parameter Λ in the above equation represents the QCD confinement scale, below which the coupling constant becomes large and strong physics becomes nonperturbative, and satisfies $1 = g^2(b_o/8\pi^2) \ln(\mu_R^2/\Lambda)$.

1.3.2 COLOR CONFINEMENT, HADRONIZATION, AND JETS

It has become clear through experimental observations that quarks and gluons cannot exist as free particles; rather, the hypothesis of color confinement postulates that colored particles are always confined to color-singlet states, as a consequence of gluon self-interactions, due to gluons being color-charged themselves. While not analytically proven, color confinement has not been experimentally refuted, either, with colored objects always being

observed in color-singlet (or colorless, with total color charge of zero) combinations, or hadrons. The simplest $SU(3)$ color singlet configurations are quark-antiquark and three-quark or three-antiquark combinations. Fortunately, these are exactly the hadronic states observed in nature: mesons, bound states of $q\bar{q}$, and baryons, bound states of qqq or $\bar{q}\bar{q}\bar{q}$.

Color confinement can be understood qualitatively as follows: if a quark-antiquark pair is attempted to be separated, the attractive interactions between the virtual color-charged gluons being exchanged serve to effectively squeeze the color field between the quarks into a flux tube (see Figure 1.2), increasing the potential energy linearly with distance, and requiring an infinite amount of energy to separate the quarks completely. At some point, enough energy exists to form new quark-antiquark pairs, which naturally arrange themselves into hadrons, since it is more energetically favorable to exist in color-singlet states, rather than as free colored particles with enormously vast gluon fields between them.

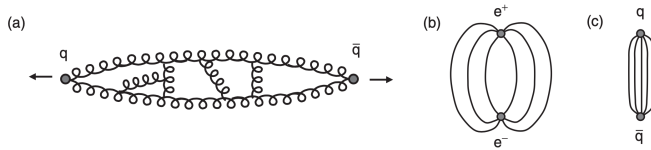


Figure 1.2: A qualitative picture of color confinement in QCD, with (a) showing the attractive interactions of virtual gluons exchanged between quarks, (b) showing the behavior of field lines in QED, and (c) showing the color field tube characteristic of QCD [19, p. 249].

In the case of high energy collisions, this phenomenon leads to the formation of jets, or collimated bunches of final state hadrons and partons, in a process known as hadronization, shown schematically in Figure 1.3. Quark pair production yields two initially free quarks

back-to-back in the center-of-mass (CM) frame, rapidly separating and stretching the color field between them into a tube with very large energy density. At a certain energy, a new quark-antiquark pair is created, breaking the color field tube and generating a new one between the new pair. This process continues until the energy of the quarks and antiquarks is low enough to arrange themselves into hadrons. What results is two jets of hadrons traveling in the directions of the initial quark and antiquark.

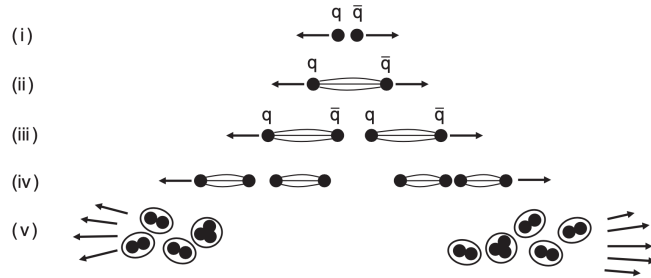


Figure 1.3: A qualitative picture of the hadronization process in QCD where a quark-antiquark pair produced in a high energy collision produces two jets as a consequence of color confinement [19, p. 253].

1.4 ELECTROWEAK THEORY

The gauge invariant theory of the unified electromagnetic and weak, or electroweak, interaction is defined by the $SU(2) \times U(1)$ symmetry group and corresponds to the L_{EW} sector of the SM Lagrangian. Here, $SU(2)$ is the weak-isospin (\vec{I}) symmetry group, which acts only on left-handed fermion fields, and $U(1)$ is the weak-hypercharge (Y) symmetry group, which acts on both left-handed and right-handed fermion fields. The electric charge can be

retained from the $SU(2) \times U(1)$ associated charges using the Gell-Mann-Nishijima relation:

$$\mathcal{Q} = I_3 + \frac{1}{2}Y, \quad (1.9)$$

where I_3 is the third component of weak isospin.

The fundamental representation of the group is described by left-handed doublets, with

$I_3 = \pm \frac{1}{2}$, and right-handed singlets, with $I_3 = 0$, of the lepton and quark families:

$$\begin{aligned} & \left(\begin{array}{c} \nu_e \\ e \end{array} \right)_L, \left(\begin{array}{c} \nu_\mu \\ \mu \end{array} \right)_L, \left(\begin{array}{c} \nu_\tau \\ \tau \end{array} \right)_L, e_R, \mu_R, \tau_R \\ & \left(\begin{array}{c} u \\ d \end{array} \right)_L, \left(\begin{array}{c} c \\ s \end{array} \right)_L, \left(\begin{array}{c} t \\ b \end{array} \right)_L, u_R, d_R, c_R, s_R, t_R, b_R \end{aligned} \quad (1.10)$$

There are four generators:

$$T_a = I_a, (a = 1, 2, 3) \quad \text{and} \quad T_4 = Y, \quad (1.11)$$

where I_a are the isospin operators, and Y is the hypercharge, with commutators

$$[T_a, T_b] = i\epsilon_{abc}I_c \quad \text{and} \quad [T_a, T_4] = 0. \quad (1.12)$$

The $SU(2) \times U(1)$ generators are associated with four massless gauge fields: an isotriplet W_μ^a for $SU(2)$ and an isosinglet B_μ for $U(1)$. The initial gauge-invariant Lagrangian for the group with unbroken symmetry is given by

$$L_{EW_0} = L_{\text{gauge}} + L_{\text{fermions}} = -\frac{1}{4} W_{\mu\nu}^a W^{\mu\nu,a} - \frac{1}{4} B_{\mu\nu} B^{\mu\nu} + \sum_{f=1}^{12} \bar{\psi}_f i\gamma^\mu D_\mu \psi_f, \quad (I.13)$$

where $\psi_f = \psi_L + \psi_R$ for an individual fermion field. The field strength tensors are defined as

$$\begin{aligned} W_{\mu\nu}^a &= \partial_\mu W_\nu^a - \partial_\nu W_\mu^a - g_W f_{abc} W_\mu^a W_\nu^b \\ B_{\mu\nu} &= \partial_\mu B_\nu - \partial_\nu B_\mu, \end{aligned} \quad (I.14)$$

and the covariant derivative is

$$D_\mu = \partial_\mu + ig_W I_a W_\mu^a + ig_Y \frac{Y}{2} B_\mu, \quad (I.15)$$

where g_W and g_Y are the coupling constants associated with weak-isospin and weak-hypercharge, respectively. This Lagrangian describes the kinetics of the electroweak gauge fields, including self-interactions, and the interactions between fermions and gauge bosons; however, this model contains one major shortcoming: local gauge invariance induces *massless* gauge bosons, but W/Z bosons are known to have significant mass. Moreover, the

fermions are also introduced into the Lagrangian as massless particles, since their corresponding mass terms are not $SU(2)$ invariant. Therefore, $SU(2) \times U(1)$ symmetry must be *spontaneously broken* via the Higgs mechanism (see Section 1.4.1) to generate masses in a gauge-invariant way. After symmetry breaking, the full electroweak Lagrangian can be written as

$$L_{\text{EW}} = L_{\text{gauge}} + L_{\text{fermion}} + L_{\text{Higgs}} + L_{\text{Yukawa}}, \quad (1.16)$$

where $L_{\text{gauge}} + L_{\text{fermions}} = L_{\text{EW}_0}$, defined above, and L_{Higgs} and L_{Yukawa} are described below.

1.4.1 ELECTROWEAK SYMMETRY BREAKING AND THE HIGGS MECHANISM

The Higgs mechanism introduces a single isospin doublet of complex scalar fields, $\Phi = (\varphi^+ \varphi^0)^T$, to induce electroweak spontaneous symmetry breaking and generate masses for gauge and fermion fields. The Higgs field couples to the existing gauge fields as follows:

$$L_{\text{Higgs}} = (D_\mu \Phi)^\dagger (D^\mu \Phi) - V(\Phi), \quad (1.17)$$

where $V(\Phi) = -\mu^2 \Phi^\dagger \Phi + \frac{\lambda}{4} (\Phi^\dagger \Phi)^2$ is the Higgs potential with constants μ^2 and λ , describing the self-interaction of the Higgs field. The above Lagrangian is gauge-invariant under $SU(2) \times U(1)$ transformations, but the ground state of the Higgs field, where the potential

is minimized, is not, since it has a nonzero expectation value:

$$\langle \Phi \rangle = \frac{1}{\sqrt{2}} \begin{pmatrix} 0 \\ v \end{pmatrix}, \quad v = \frac{2\mu}{\sqrt{\lambda}}. \quad (1.18)$$

The vacuum thus selects a preferred direction in weak isospin plus hypercharge space, thereby spontaneously breaking the larger gauge symmetry of the group down to $U(1)_{EM}$, under which the electrically neutral ground state is invariant. The overall gauge symmetry of the Lagrangian remains but is essentially hidden by this preferred direction in the vacuum state.

In the unitary gauge, the Higgs field can be written as

$$\Phi(x) = \frac{1}{\sqrt{2}} \begin{pmatrix} 0 \\ v + H(x) \end{pmatrix}, \quad (1.19)$$

and the potential becomes

$$V = \mu^2 H^2 + \frac{\mu^2}{v} H^3 + \frac{\mu^2}{4v^2} H^4 = \frac{M_H^2}{2} H^1 + \frac{M_H^2}{2v} H^3 + \frac{M_H^2}{8v^2} H^4, \quad (1.20)$$

representing a real field H , describing a scalar neutral particle, the Higgs boson, with mass $m_H = \mu\sqrt{2}$, and its self-interactions. Here, three of the four degrees of freedom of the Higgs field have been transformed away, reappearing as the longitudinal components of the

now massive W/Z bosons, which appear as linear combinations of the electroweak gauge fields:

$$W_\mu^\pm = \frac{1}{\sqrt{2}}(W_\mu^1 \mp iW_\mu^2)$$

$$\begin{pmatrix} Z_\mu \\ A_\mu \end{pmatrix} = \begin{pmatrix} \cos \vartheta_W & \sin \vartheta_W \\ -\sin \vartheta_W & \cos \vartheta_W \end{pmatrix} \begin{pmatrix} W_\mu^3 \\ B_\mu \end{pmatrix} \quad (I.21)$$

where W_μ^\pm , Z_μ , and A_μ represent the W/Z boson and photon fields, respectively, and ϑ_W is known as the weak mixing, or Weinberg, angle. The mass terms for the physical electroweak gauge bosons come from the couplings of the gauge fields to the nonzero Higgs field:

$$m_W = \frac{1}{2}g_W v, \quad m_Z = \frac{1}{2}\sqrt{(g_Y^2 + g_W^2)}v. \quad (I.22)$$

The weak mixing angle can be expressed in terms of the vector boson masses and electro-weak coupling constants:

$$\cos \vartheta_W = \frac{g_W}{\sqrt{g_Y^2 + g_W^2}} = \frac{M_W}{M_Z}, \quad g_W = \frac{e}{\sin \vartheta_W}, \quad g_Y = \frac{e}{\sin \vartheta_W} \quad (I.23)$$

Similarly, fermion mass terms appear by introducing Yukawa couplings between the Higgs field and the fermion fields. In the unitary gauge, the Yukawa term of the Lagrangian

appears simply as

$$L_{\text{Yukawa}} = - \sum_{f=1}^{12} m_f \bar{\psi}_f \psi_f - \sum_{f=1}^{12} \frac{m_f}{v} \bar{\psi}_f \psi_f H, \quad (1.24)$$

where $m_f = G_f \frac{v}{\sqrt{2}}$ is the mass of the charged fermion and G_f is the corresponding individual Yukawa coupling constant, meaning the fermion masses are proportional to their couplings to the Higgs field as well as to the Higgs vacuum expectation value.

Realistically, in the case of three generations of fermions, one must account for flavor mixing in the quark sector by requiring the Yukawa couplings to be 3×3 matrices $G_f = (G_{ij}^f)$. These coupling matrices are in general non-diagonal but can be diagonalized through four unitary matrices, $V_{L,R}^{u,d}$, to obtain the mass eigenstates. The resulting physical quark states couple to the charged vector current through the Cabibbo-Kobayashi-Maskawa (CKM) matrix [27] V_{CKM} :

$$V_{\text{CKM}} \equiv V_L^u V_L^{d\dagger} \equiv \begin{pmatrix} V_{ud} & V_{us} & V_{ub} \\ V_{cd} & V_{cs} & V_{cb} \\ V_{td} & V_{ts} & V_{tb} \end{pmatrix} \quad (1.25)$$

which is a 3×3 unitary matrix, parameterized by three mixing angles and one CP-violating phase angle and representing the allowed mixing of quark flavors.

1.5 LIMITATIONS OF THE STANDARD MODEL

While the Standard Model is a well-established and experimentally sound theory of particle physics, it is known to be an incomplete description of the universe.

A number of fundamental phenomena have been observed that the SM cannot adequately explain, such as the gravitational force, the neutrino masses, the asymmetry between the relic abundances of matter and antimatter, and the existence of dark matter and dark energy. Additionally, the SM exhibits several ad hoc features that present theoretical problems motivating the need for a more fundamental theory, including the number of free parameters, the strong CP problem, the hierarchy and naturalness problem, and the theory of grand unification. The Standard Model is thus potentially an approximation of a larger gauge symmetry that is broken at lower energy scales. Beyond the Standard Model (BSM) theories propose new physics to reasonably modify the SM such that it is consistent with existing data and explains one or more of its current theoretical shortcomings.

The most obvious limitation of the Standard Model is that it does not include gravity, as there is thus far no complete, consistent renormalizable quantum field theory formalized to describe the gravitational force. The graviton is the theoretical force carrier mediating the gravitational force analogously to the other gauge bosons mediating the other three forces, but this particle with a quantum description at high energies, i.e. the Planck scale of order 10^{19} GeV, has yet to be successfully incorporated into the SM framework.

The SM is also inconsistent with massive neutrinos. The theory predicts massless neutrinos, but observations of neutrino oscillations, where neutrinos change flavor mid-flight, require neutrinos to have small but nonzero mass. These mass terms can be added to the SM by hand, but the mechanism that generates the neutrino masses remains unclear.

The theory also contains a large number of free parameters, including the gauge couplings, the nonzero particle masses, the CKM mixing angles, and the Higgs vacuum expectation value, which are not predicted by theory but rather determined by experiment. The origins of the experimental values are unknown. While not inherently wrong or problematic, a theory with such a large number of seemingly arbitrary and unrelated parameters is considered by many to be inelegant and somewhat disconcerting.

The strong CP problem manifests because, theoretically, CP violation should occur in the strong sector, as terms naturally exist in the QCD Lagrangian that could break CP symmetry, but there is no evidence to suggest that it ever does. Coefficients for these terms are thus fine-tuned to be sufficiently small to make these CP-violating terms negligible and explain them away. Such fine-tuning of parameters is considered unnatural.

One of the broader theoretical mysteries of the SM is the vast discrepancy between the electroweak scale, of order 100 GeV, and the Planck scale, of order 10^{19} GeV, where the Planck scale represents the highest energy of the universe, associated with the physics of gravity. This puzzle, known as the hierarchy problem, manifests most clearly in the ob-

served Higgs boson mass, which receives very large quantum loop corrections in renormalization from couplings of SM particles, which must be exactly canceled through manual fine-tuning of the parameters in order to resolve the mass at the electroweak scale. The physical, observable Higgs boson mass is equal to the bare mass plus the radiative loop corrections, which are contributed by all of the particles that couple to the Higgs field, including any potential BSM massive particles yet to be discovered. The leading order corrections are proportional to the cutoff scale, or the energy scale up to which the SM theory is valid and above which new physics appears, meaning the quantum corrections can become enormously large if the SM extends to very high energies. Assuming the Planck scale as the cutoff, one should expect the Higgs boson mass in the range of the Planck mass, $m_{\text{Pl}} \approx 10^{19}$ GeV, but the observed mass is in fact 17 orders of magnitude smaller. Without new BSM physics to naturally resolve the huge difference between the corrections and the physical mass, the Higgs boson mass needs to be fine-tuned to cancel the large corrections by manually assigning an equally large bare mass. Again, such large fine-tuning is somewhat unsettling, as one would expect the theory to arise more naturally than having to directly manipulate the parameters in such a way. This fine-tuning can theoretically be avoided with the introduction of additional corrections that naturally cancel the existing SM corrections, but there is no way to do so with the physics of the SM alone.

Related to the hierarchy problem is the idea of grand unification, where the running cou-

pling constants of the three SM symmetries of color, weak-isospin, and weak-hypercharge, which evolve with energy, are observed to nearly converge around the “grand unification scale”, around 10^{16} GeV. This motivates the notion of a “Grand Unified Theory” (GUT), where the electroweak and strong forces are combined into a larger gauge group with a universal coupling and a single gauge symmetry that is spontaneously broken to the SM gauge group at the GUT scale ($\Lambda_{\text{GUT}} \approx 10^{16}$ GeV). It is quite natural to assume the strong and EW forces should unify into a single interaction above some high energy scale, analogously to the unification of the electromagnetic and weak forces into the electroweak interaction. In the GUT, all three forces are thus different manifestations at different energies of a single underlying interaction, and the SM is a subgroup of some larger gauge symmetry broken at the GUT scale. The energy evolution of the coupling constants, however, is determined by the particle content of the low-energy theory, i.e. the SM, and exact unification requires additional particles in the theory. Such absolute convergence is not possible in the SM but can be realized in BSM theories.

Finally, the origin of baryon asymmetry and the existence of dark matter in the universe are two outstanding fundamental problems of particle physics, as the SM framework provides no reasonable explanation for either, which are particularly relevant to the model used for the search presented in this thesis and are thus described in more detail below.

1.5.1 BARYON ASYMMETRY

The outstanding problem of baryon asymmetry, or matter - antimatter asymmetry, in modern physics is the observed abundance of baryonic matter over antimatter in the universe of unknown origin [28]. It is challenging to explain this nonzero positive baryon number density based solely on fundamental principles. The universe as observed today is mostly matter, not antimatter, but it is assumed by the Standard Model that the overall baryon number in the universe should be zero, as matter and antimatter should have been created and destroyed in equal amounts in the Big Bang (BB) and in the subsequent early universe. This is a consequence of the *CPT* theorem, where particles and their corresponding antiparticles have opposite charges but the same masses and lifetimes, so they are produced at the same rates and exist in the same amounts. Matter and antimatter are always pair-produced and, upon contact, annihilate one another, resulting in pure radiation. During the hot and dense early universe immediately following the BB, assuming an initial symmetric universe, matter and antimatter should have been continuously created and destroyed at the same rate, leaving equal amounts of each or nothing behind. However, some small amount of matter must have survived this period in order to produce the relic abundance observed today.

This is known not to be a local phenomenon, where the known matter-dominated corner of the universe is balanced by some other antimatter-dominated corner, as there is no

experimental evidence of significant concentrations of antimatter anywhere in the observable universe; otherwise, this boundary between the two matter-dominated and antimatter-dominated regions would be violent and rife with annihilation, and no such evidence exists in the Cosmic Microwave Background (CMB), or the relic radiation from the early universe.

Instead, the observed abundance requires some early mechanism, i.e. symmetry breaking, that favors the creation of matter over antimatter under certain conditions, i.e. those of the early universe, to generate it. This hypothetical mechanism is known as baryogenesis, or a baryon-generating interaction, [29], and there is no such mechanism in the SM alone that sufficiently explains the asymmetry.

The set of three criteria for a baryogenesis process to produce matter and antimatter at different rates such that an observed abundance results are:

1. baryon number B violation;
2. C - and CP -symmetry violation;
3. departure from thermal equilibrium;

as proposed by Andrei Sakharov in 1967 [30] and known as the “Sakharov conditions”.

Such requirements imply the process responsible for the baryon asymmetry must have violated the conservation of lepton and baryon numbers and of CP -symmetry during a period where the universe was substantially out of equilibrium.

The net baryon number of the universe must not be conserved, but rather must change over time, in order to produce an excess of baryons over antibaryons.

C -symmetry is the symmetry under charge conjugation or under particle - antiparticle transformation, and CP symmetry is the combined symmetry of charge and parity reversal, where parity inversion is the flip in chirality or spatial coordinate. C and CP violation are required for the rate of interactions to differ between matter and antimatter counterparts; otherwise, no asymmetry could evolve from an initially symmetric state. Specifically, C violation is needed so interactions producing more baryons are not counterbalanced by interactions producing more anti-baryons, and CP violation is required to produce different amounts of left-handed baryons and right-handed anti-baryons, and vice versa.

Interactions must occur out of thermal equilibrium or compensating processes increasing and decreasing baryon number would occur, as governed by CPT symmetry, effectively removing the generated asymmetry.

The total baryon content of the universe is calculated today from thermal measurements of the CMB. The average density of baryons $\Omega_b h^2$, as measured by the Planck satellite [31], is

$$\Omega_b h^2 = 0.02237 \pm 0.00015, \quad (1.26)$$

where $\Omega_X = \rho_X / \rho_{\text{crit}}$, with ρ_{crit} being the critical density of the universe, and $h \equiv H_0 / 100 \text{ km s}^{-1} \text{ Mpc}^{-1}$ is the present Hubble parameter, with H_0 the Hubble constant. The total energy density of the universe in units of the critical density today is measured to be $\Omega_{\text{total}} = \Omega_\Lambda + \Omega_m = 1.00 \pm 0.01$, and the Hubble constant is measured as $H_0 =$

67.36 ± 0.54 , implying baryonic matter comprises approximately 5% of the total density of the universe. This measurement is consistent with the baryonic abundance required by observation of the lightest element abundances and predicted by Big Bang Nucleosynthesis (BBN): $\Omega_b = (0.021 - 0.024)h^{-2}$ [23], as illustrated in Figure 1.4.

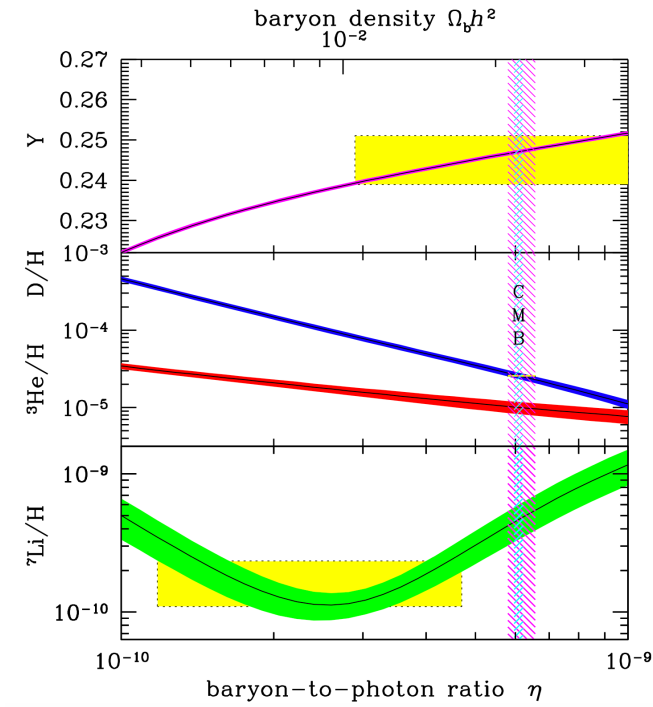


Figure 1.4: The CMB measurement of the cosmic baryon density indicated by the narrow vertical band (at 95% CL) [23]

On the other hand, the amount of antimatter measured by the AMS-02 experiment, among others, is consistent only with secondary production from matter collisions with

the interstellar medium, and not with a relic abundance leftover from the Big Bang, as for baryons [32]. The measured asymmetry between baryons and antibaryons is defined in terms of the total entropy density just before the total annihilation of antimatter in the early universe, or, equivalently, the average photon number density remaining today:

$$\eta = \frac{n_b - n_{\bar{b}}}{n_\gamma} \approx \frac{n_b}{n_\gamma} \quad (1.27)$$

Measured abundances of the lightest elements and constraints from BBN are all consistent with a baryon asymmetry of approximately $\eta \approx 5 \times 10^{-10}$, indicating this level of discrepancy between baryons and antibaryons in the early universe. So the question remains: if matter and antimatter were presumably produced in pairs during the radiation dominated period of the early universe directly after the Big Bang, why are there so many more baryons than antibaryons detected today?

Baryogenesis is theoretically possible in the SM, since it meets all of the Sakharov conditions and is thus able to generate a baryon asymmetry starting from a symmetric universe. Baryon number can be violated through a non-perturbative anomalous electroweak baryon-number non-conserving process [33], where B-L is conserved, but B+L changes under $SU(2)_L$ gauge transformations at first order phase transitions. The SM is a chiral theory, meaning left-handed and right-handed fermions behave differently, with only left-handed fermions undergoing electroweak interactions. Therefore, parity is maximally violated, so

C must also be violated, since CP is conserved in the SM without quark mixing. However, a small amount of explicit CP violation can be introduced in the SM through the CKM quark mixing matrix. Finally, the departure from thermal equilibrium arises quite naturally, as both the universe expansion of the standard cosmology model Λ CDM (Lambda cold dark matter) and the first order electroweak phase transition contribute to creating out-of-equilibrium conditions, with the EW phase transition contribution being much larger. While the SM meets the Sakharov conditions and can therefore theoretically generate a baryon asymmetry during the EW phase transition, the amount of CP violation and the strength of the first order phase transition are not large enough to sufficiently create enough asymmetry to reproduce the observed baryon abundance. Instead, one must look to BSM theories for an effective baryogenesis mechanism.

Various BSM models provide extensions to the SM that both meet the Sakharov conditions and generate a sufficient baryon asymmetry: GUTs could provide larger phase transitions associated with the breaking of larger unified gauge groups than the EW transition of the SM; new light particles introduced could increase the strength of the EW phase transition itself; and the decay of a new massive exotics particle could act as an entirely different mechanism to generate the asymmetry.

1.5.2 DARK MATTER

Dark matter (DM) is non-luminous matter that only interacts gravitationally and very weakly with standard baryonic matter and comprises approximately 25% of the total energy density of the universe and approximately 80% of the total matter density of the universe, existing with nearly five times the abundance of baryonic, luminous matter [13, 23, 34].

Evidence for dark matter comes from astrophysical and cosmological observations and measurements. The first evidence resulted from astrophysical observations of motions of galaxies, which suggested the galaxies contained more mass than was visible. Velocity distributions of luminous objects around their orbital centers were observed to be higher than expected given the gravitational force of the visible mass, and galaxy and cluster masses were measured to be hundreds of times larger than their visible masses, suggesting the existence of more non-luminous matter within them. Additionally, studies of gravitational lensing calculated masses much larger than those inferred from the object luminosities, confirming the extra mass measured by the galactic velocity studies. Further evidence then emerged from the concordance between BBN predictions and observations of thermal relic densities and from measurements of the CMB temperature anisotropies. The BBN light element abundances provide a measure of the baryon abundance, which is seen to only account for a fraction of the total matter density, and measurements of fluctuations in the CMB indicate a non-baryonic matter-dominated universe required for the early formation of large

scale structures.

All of the evidence points to a new type of invisible, non-baryonic matter that only interacts with the weak force and with gravity and was non-relativistic at the onset of structure formation, known as cold dark matter. Such dark matter is favored in the Λ CDM parametrization of the Big Bang cosmology, or the standard model of cosmology, in which the universe expanded adiabatically from an initial hot, dense state and is now isotropic and homogenous on large scales. The most well-motivated candidate for dark matter is the WIMP (weakly interacting massive particle), which is an electrically neutral, non-colored, stable particle with mass of order a few GeV to a few TeV. Electric and color charge neutrality are required for the DM particle to be non-interacting with the EM and strong forces; stability is required for the DM to remain and be observable in such large quantities today; and a weak-scale particle is preferred to yield the correct relic density, based on its self-annihilation cross section.

There is no way to account for the observed dark matter in the universe or any candidate DM particle with the Standard Model alone, as no SM particles exist matching the criteria required of a DM candidate. Instead, various BSM models with WIMP-like particles are proposed to explain dark matter. Recent searches for WIMPs, however, have proven unsuccessful, with no discoveries of WIMP-like particles or the models that support them, resulting in a need to consider alternative theories and candidates of dark matter.

The first evidence for dark matter came from velocity studies of astrophysical objects in the twentieth century. In studies of doppler shifts of stars moving near the galactic plane in the early 1930s, J. H. Oort observed the velocities of the stars in the galaxy to be too high given the luminous mass of the galaxy [35]. Stars moving with the observed velocities at such large radii should have escaped the gravitational pull of the luminous mass, indicating more non-luminous mass must have been present within the galaxy. Meanwhile, from calculations of the velocity dispersions of individual galaxies in the Coma cluster using the observed doppler shifts in the galactic spectra, F. Zwicky calculated the cluster mass with the virial theorem to be fifty times that measured from standard mass-to-luminosity (M/L) ratios of the nebulae in the cluster [36], indicating the galactic luminous matter only accounts for a small fraction of the total cluster mass. Finally, in studying the rotation curves of 60 isolated galaxies through spectral line analysis to determine the rotational velocity and distance of the region of interest from the galactic center in the 1970s, Vera Rubin discovered “flat” galactic rotation curves, rather than “Keplerian” ones, as expected [37]. The rotation curve of a galaxy is the variation in the orbital circular velocities of objects at various distances from the galactic center, and Keplerian behavior is one that mimics the orbital rotations of the planets within the solar system. The rotational velocity of an object on a stable Keplerian orbit of radius r around the galaxy is given by $v(r) = \sqrt{GM(r)/r}$, where G is Newton’s gravitational constant and $M(r)$ is the total mass contained within orbit. As-

suming r is outside the visible part of the galaxy and that mass tracks light, $v(r) \propto 1/\sqrt{r}$, implying the velocity of the rotating body should decrease with the distance from the center of the orbit. A flat rotation curve, on the other hand, is one where the velocity is slowly increasing or constant far from the galactic center, implying the mass in the galaxy is increasing linearly with the radius and not concentrated in the galactic center, as expected, given the distribution of the luminosity. Instead of velocity decreasing with distance from the galactic center, v is seen to become approximately constant out to the largest values of r , where the rotation curves are measured, indicating the existence of a dark halo with mass density $\rho(r) \propto 1/r^2$, which falls off at some unknown radius.

The extra galactic mass measured in studies of galactic velocities has also been confirmed through gravitational lensing, in which a distant bright object, the source, behind a close massive object, the lens, appears as an “arclet”, or a partial Einstein ring, with the radius of the arclet defined by the Einstein radius: $\theta_E = \sqrt{(4GM/c^2)(d_{LS}/d_L d_S)}$, where M is the mass of the lens and d_{LS} , d_L , and d_S are the angular-diameter distances between the lens and the source, to the lens, and to the source, respectively. The radius of the arclet is used to measure the mass within the lensing object, and the calculated mass from this method is found to be much larger than that inferred from the object luminosity. The most prominent and recent evidence of such a phenomenon comes from the Bullet cluster, which recently passed through another larger galaxy cluster [38]. The location of the majority of

the baryonic mass in the two clusters, identified by the x-ray radiation emitted from the collision of the hot gas forming most of the clusters' baryonic mass, and the location of the majority of the clusters' total mass, measured through weak gravitational lensing, differed significantly, as the baryonic mass was decelerated from the collision, but most of the mass within the clusters continued unaffected on ballistic trajectories, indicating the majority of the mass within the clusters was weakly interacting and non-baryonic.

Abundant cosmological evidence from BBN and the CMB also establishes the existence of dark matter. Big Bang Nucleosynthesis (BBN) refers to the period very shortly after the Big Bang in the early, hot universe when neutrons and protons fused together to form light elements. One can calculate theoretical BBN elemental abundances in the standard cosmological model [39], and predictions from standard BBN with a baryon-to-photon ratio $\eta \approx 5 \times 10^{-10}$ are found to be in precise agreement with observations of light element abundances today. The nuclear reactions during the BBN period of $t \simeq 0.01 - 100$ s ($T \simeq 10 - 0.1$ MeV) produced substantial amounts of light elements, particularly deuterium, for which no contemporary astrophysical processes can account. As the deuterium abundance is inversely related to the value of η , the observed deuterium-to-hydrogen (D/H) ratio provides a lower limit on the deuterium abundance and an upper limit on η and thus characterizes the overall baryonic matter density. Based on the concordance between BBN prediction and observation, the baryon abundance is measured to be $0.021 \leq \Omega_b h^2 \leq 0.024$

[23], which only accounts for approximately 20% of the total matter density.

The Cosmic Microwave Background (CMB) is an excess background temperature of 2.73 K produced from the surface of last scattering of photons in the early universe [40].

Right after the Big Bang, the universe was a dense plasma of relativistic charged particles and photons that initially rapidly expanded then cooled until reaching the epoch of recombination, when neutral atoms formed and the universe became transparent to EM radiation, marking the end of thermal equilibrium, with the photons released from this last scattering appearing as the CMB radiation today. The CMB, and thus the early universe, is highly uniform and a near perfect blackbody but contains fundamental anisotropies, or fluctuations in temperature, corresponding to primeval density inhomogeneities of the early universe. These inhomogeneities, which depend on the amount of baryons in the universe at the time of recombination, initiate large-scale structure formation and grow into the large inhomogeneities, like galaxies, of the universe today. These perturbations, as measured via the CMB anisotropies [41], are too small ($\partial\varrho/\varrho < 10^{-4}$) to produce the observed large-scale structure given a universe dominated by baryonic matter, requiring the existence of non-baryonic dark matter, as density perturbation growth can only begin during the matter-dominated epoch. If the universe is dominated by baryonic matter, the matter-dominated epoch does not begin until recombination and photon decoupling, when baryons are no longer tightly coupled to photons and neutral atoms form, and not

enough time has passed since this period for the observed structure of the universe to form, given the size of the measured anisotropies. If the universe is instead dominated by non-baryonic dark matter, the matter-dominated epoch jump starts well before recombination, allowing for earlier initial growth of the density perturbations and thus earlier formation of the first large-scale structures, consistent with observations of the large-scale structure of the present universe.

Finally, fitting of cosmological parameters to precise measurements of the CMB anisotropies with the Wilkinson Microwave Anisotropy Probe (WMAP) [42] and the Planck satellite [31] and to spatial distributions of galaxies yield precise constraints on the total, baryonic, and dark matter densities:

$$\Omega_m b^2 = 0.1430 \pm 0.0011, \quad \Omega_b b^2 = 0.02237 \pm 0.00015, \quad \Omega_{DM} b^2 = 0.1200 \pm 0.0012,$$
(1.28)

providing explicit evidence that baryonic matter is not the only or main form of matter in the universe and that dark matter, the nature of which is not totally understood, is a real component of the universe.

While the existence of dark matter is well-established, the exact nature and particle make-up of dark matter is not yet understood. Structure formation observations together with CMB measurements imply the need for dark matter that is cold, or non-relativistic at the

onset of galaxy formation. Additionally, a number of conditions are set that particle dark matter candidates must meet: DM candidates must be stable on cosmological time scales, or they would have already decayed by now and would no longer be observable as relic abundances; they must be weakly interacting with EM radiation, or they would not be dark and would be immediately visible; and they must yield the correct relic density to be consistent with cosmological and astrophysical measurements. The prime candidate is the WIMP, or the weakly interacting massive particle, with a mass between a few GeV and a few TeV and with a weak-scale pair annihilation cross section. Assuming the WIMPs are initially in thermal equilibrium with SM particles in the early universe, the present relic abundance can be measured from the WIMP density at “freeze out”, when the rate of reactions interchanging WIMPs and SM particles becomes smaller than the Hubble expansion rate of the universe and the WIMPs drop out of thermal equilibrium. This WIMP production rate is proportional to the WIMP number density times the WIMP pair annihilation cross section and the relative velocity of the annihilating WIMPs, and freeze out occurs at $T_F \simeq m_X/20$, resulting in a non-relativistic WIMP at the time of decoupling from the thermal plasma.

This results in the following WIMP relic density:

$$\Omega_X h^2 \simeq \text{const} \cdot \frac{T_0^3}{M_{\text{Pl}}^3 \langle \sigma_A v \rangle} \simeq \frac{\text{o.ipb} \cdot c}{\langle \sigma_A v \rangle}, \quad (1.29)$$

where Ω_X is the WIMP relic density relative to the critical density, T_0 is the current CMB

temperature, \mathcal{M}_{Pl} is the Planck mass, σ_A is the annihilation cross section of a WIMP pair into SM particles, v is the relative velocity between two WIMPs in the center-of-mass system, and $\langle \dots \rangle$ denotes thermal averaging. The above equation naturally indicates a weak-scale pair annihilation cross section: $\langle \sigma_A v \rangle \simeq 3 \cdot 10^{-26} \text{ cm}^3 \text{s}^{-1}$. WIMPs, or other DM candidates, could also be subject to an asymmetry, much like the baryon asymmetry, if the WIMP is not its own antiparticle, and this asymmetry could potentially be generated by the same mechanism for both dark and baryonic matter, as is the case in “asymmetric DM” models. WIMPs exist in various simple extensions to the Standard Model and have been searched for through both production at the LHC and through direct and indirect detection at dedicated WIMP detectors. As of yet, no evidence of WIMPs has been found, and many WIMP models have recently been significantly constrained by the lack of discovery at the LHC and in dedicated WIMP searches, which has resulted in a plethora of new and more complicated dark matter models to be explored instead.

1.5.3 BSM THEORIES

Many of the problems addressed above can be solved through a number of beyond the Standard Model theories. The most popular BSM theory is supersymmetry (SUSY), which is an extension to the Standard Model that introduces an additional symmetry between fermions and bosons, interchanging the two by modifying the spin of each particle by $1/2$, and effectively doubling the particle content of the SM. In the theory of SUSY, every boson

is associated with a fermionic superpartner, denoted by an “ino” suffix (i.e. the gluino is the superpartner of the gluon), and every fermion is associated with a bosonic superpartner, denoted by an “s” prefix (i.e. the stop is the superpartner of the top quark). SUSY and SM partners differ in spin by $1/2$ but are otherwise identical, with the same internal quantum numbers and mass. Current mass limits from collider searches, however, indicate that SUSY must be a broken symmetry with particles heavier than their SM counterparts. Otherwise, the SUSY particles would have the same masses as the SM particles and would have been readily discovered by now.

The simplest and most general SUSY extension to the SM is the Minimal Supersymmetric Standard Model (MSSM) with conserved R -parity = $(-1)^{2s}(-1)^{3B+L}$, where s is the particle spin, B is the baryon number, and L is the lepton number, and R -parity = ± 1 for SM and SUSY particles, respectively. In the MSSM, R -parity, or the difference between the number of SUSY and anti-SUSY particles, is conserved instead of B or L , which are inherently violated in SUSY. This conservation of R -parity results in the stability of the lightest supersymmetric particle (LSP), since it is forbidden from decaying to lighter SM particles.

SUSY is an attractive theory in part because it provides potential solutions to several problems arising in the SM, including the hierarchy problem, grand unification, and dark matter. SUSY naturally solves the hierarchy problem with the addition of the superpartners, as contributions from SUSY particles to loop corrections to the Higgs boson mass

enter with opposite sign to the existing loop corrections from SM particles, making the cancellation of the corrections exact and automatic. With broken SUSY at the TeV scale, the observed Higgs mass can naturally be recovered. SUSY also makes possible the proper convergence of the running coupling constants into a unified gauge coupling at the GUT scale with the introduction of the MSSM particle content. Finally, many SUSY models with R -parity conservation provide a natural dark matter candidate in the form of the LSP, which is naturally colorless, neutral, and stable. In the MSSM, the LSP is most likely the neutralino, which also yields the correct dark matter relic density if its mass is of order 100 GeV. For a detailed review of supersymmetry, see Reference [43].

Despite being a well-motived and enticing theory, SUSY has suffered from a lack of observation at the LHC over its first two runs, yielding significant constraints to its parameter space, as illustrated in Figure 1.5. Additionally, while SUSY provides solutions to many of the existing problems of the SM, it may leave some unanswered, particularly if more non-standard dark matter theories with more complicated dark sectors prevail over standard cold dark matter and WIMPs. As such, non-supersymmetric “exotics” BSM theories have recently gained more traction. One such theory is presented in the next chapter and is the basis of the work presented in this thesis.

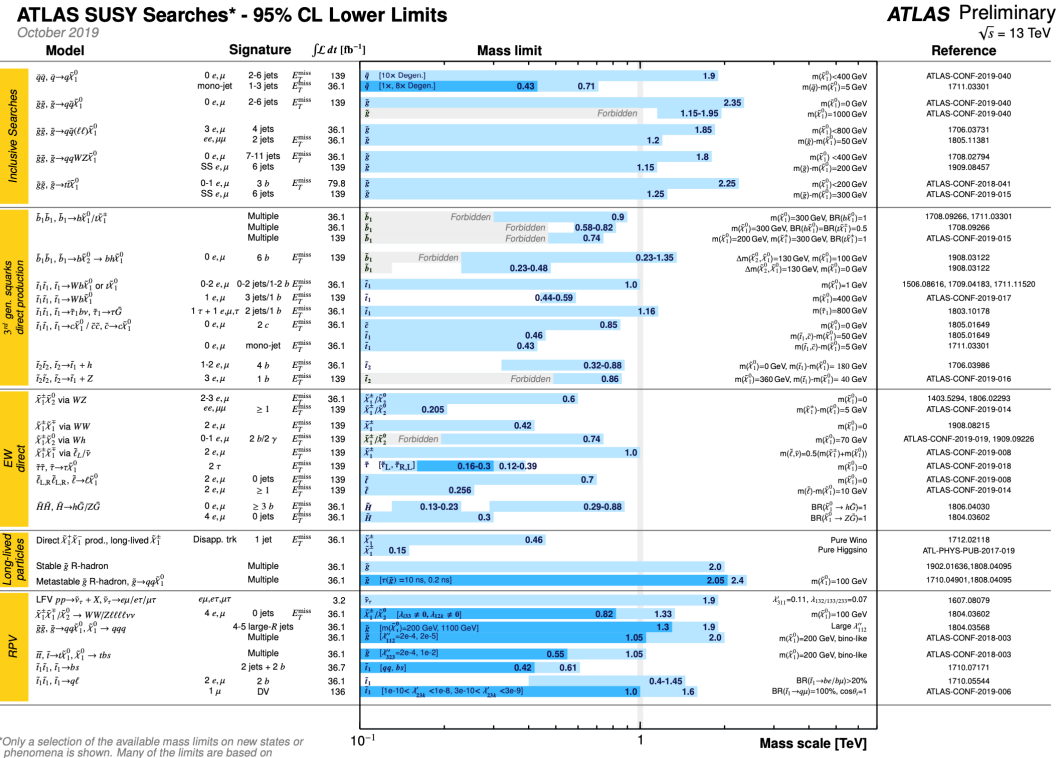


Figure 1.5: SUSY mass exclusion limits as set by various ATLAS SUSY searches [23].

2

Emerging Jet Theory

2.1 DARK QCD

Although dark matter is a known manifestation of BSM physics, its origin and particle makeup has yet to be discovered. Searches for the leading dark matter candidate, the weakly interacting massive particle, or WIMP, have thus far proved unsuccessful. Moreover, standard cold dark matter theories may be inadequate to explain recent astrophysical anomalies.

lies that instead favor dark matter with large self-interactions, which naturally arise in theories with confining hidden sectors. Finally, the puzzle of the coincidence between the energy density of dark and baryonic matter can be explained in terms of asymmetric dark matter (ADM), which proposes that the dark matter relic density is due to a dark particle-antiparticle asymmetry just like the asymmetry responsible for baryon abundance and that these asymmetries share a common origin, suggesting a connection between the physics and cosmological evolution of dark and baryonic matter and a portal between the dark and visible sectors [15].

The problems above can all be solved by combining the ideas of an asymptotically-free and confining hidden sector with that of asymmetric dark matter into a single model of *dark QCD* [16, 17]. Many asymmetric dark matter models explain the similar number densities between dark and baryonic matter quite readily, but the coincidence between mass scales is much more challenging to come by and is often manually put in by hand. With a confining hidden sector, however, the GeV scale for the dark sector arises quite naturally. In dark QCD models, a dark gauge group much like the $SU(3)$ color group of QCD is introduced, along with a new TeV-scale mediator that generates the shared asymmetry and is therefore charged under both dark QCD and QCD and acts as a portal between the two sectors. The dark sector contains a dark matter candidate in the form of the lightest stable dark baryon, analogous to the proton, as well as a plethora of unstable dark mesons that

can decay with long lifetimes to SM particles.

Dark QCD extends the Standard Model symmetry group as such:

$$G_{SM} \times SU(N_d), \quad (2.1)$$

where $G_{SM} = SU(3) \times SU(2) \times U(1)$ is the gauge symmetry of the Standard Model, $SU(N_d)$ is the gauge symmetry of the dark QCD sector, and $N_d \geq 2$ is the number of dark colors. The n_f dark fermions, or dark quarks Q_d form the fundamental representation of $SU(N_d)$, and the heavy complex scalar mediator X_d is a bifundamental under both $SU(3)$ and $SU(N_d)$. As such, it is charged under both QCD and dark QCD and thus connects the two sectors. The dark confinement scale and the mass of the dark pions, the lightest mesons, are set to be of order $1 - 10$ GeV, per motivations from asymmetric dark matter. The dark matter energy density has been measured to be $\Omega_{DM} h^2 = 0.1200 \pm 0.0012$ [31], or a factor $\Omega_{DM}/\Omega_B = 5.36 \pm 0.06$ times the baryon energy density. Theories of asymmetric dark matter suggest the coincidence of dark and baryonic matter number densities, $n_{DM} \sim n_B$, due to a common asymmetry mechanism; therefore, the dark matter mass should be approximately five times mass of the proton:

$$\frac{\Omega_{DM}}{\Omega_B} = \frac{m_{DM} \times n_{DM}}{m_p \times n_B} \approx 5 \implies m_{DM} \sim 5 \times m_p \quad (2.2)$$

In the dark QCD model, the dark matter candidate is the dark proton, with mass on order of the dark confinement scale, $m_{p_d} \sim \Lambda_d$, analogous to the similarity between the proton mass and the QCD confinement scale. The dark pion lifetime upper limit of approximately one second, motivated by Big Bang nucleosynthesis (BBN), sets a loose upper bound on the scalar mediator of about 100 TeV (see equation 2.6); however, lower mediator masses, on the order of 1 TeV, are preferred, as they are more likely to lead to a dark QCD confinement scale close to that of QCD. Dark baryon number is conserved, leading to a stable dark proton, the lightest dark baryon, analogous to the proton, that acts as the dark matter candidate. No such meson number exists, so dark mesons are unstable and can decay back to the Standard Model. A schematic of the dark QCD model just described is shown in Figure 2.1, and the particle content, assuming a model with $N_d = 3$ and a scalar mediator with hypercharge 1/3, is displayed in Table 2.1.

Field	$SU(3) \times SU(2) \times U(1)$	$SU(3)_d$	Mass	Spin
Q_d	(1,1,0)	(3)	$\mathcal{O}(\text{GeV})$	1/2
X_d	(3,1, $\frac{1}{3}$)	(3)	$\mathcal{O}(\text{TeV})$	0

Table 2.1: Particle content, relevant to phenomenology, of dark QCD model, where the number of dark colors $N_d = 3$.

The dark scalar mediator X_d can be pair-produced, with each X_d decaying to a right-handed down-type SM quark and a dark quark. The Lagrangian for the Yukawa coupling

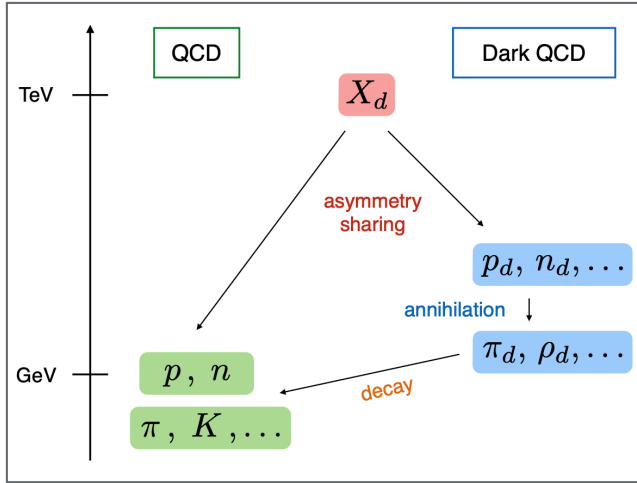


Figure 2.1: A schematic of the dark QCD model presented here. The mediator X_d generates a shared asymmetry for baryonic and dark matter, yielding an abundance of both the QCD and dark baryons. The lightest dark baryon, the dark proton, is stable and acts as the dark matter candidate for the model. The symmetric part of the dark sector annihilates to dark pions, which decay to the SM. Since the number of densities of dark and baryonic matter are naturally of the same order, the mass of the dark baryons must be of order $1 - 10$ GeV to recover the expected dark matter relic density [17].

between the mediator and the SM and dark quarks is

$$L_K = \kappa_{ij} \bar{Q}_{d_i} q_j X_d + h.c., \quad (2.3)$$

where κ_{ij} is an $n_f \times 3$ matrix of Yukawa couplings. The full fundamental Lagrangian for the dark QCD model is

$$L \supset \bar{Q}_{d_i} (\gamma^\mu D_\mu - m_{d_i}) Q_{d_i} + (D_\mu X_d) (D^\mu X_d)^\dagger - M_{X_d}^2 X_d X_d^\dagger - \frac{1}{4} G_d^{\mu\nu} G_{\mu\nu,d} + L_K + L_{SM}, \quad (2.4)$$

where $G_d^{\mu\nu}$ is the dark gluon field strength tensor, D_μ is the covariant derivative containing

the couplings to the gauge fields, L_K is the Yukawa coupling Lagrangian above, and L_{SM} is the full Lagrangian for the Standard Model [17].

Analogous to QCD pions, the dark pions in this model are the lightest composite states and act as pseudo-Goldstone bosons of the $SU(n_f)_L \times SU(n_f)_R$ chiral symmetry, which is spontaneously broken by the Yukawa couplings of L_K , generating small masses for the dark pions and allowing for dark pion decays to down-type SM quarks with decay width

$$\Gamma(\pi_d \rightarrow \bar{d}d) = \frac{\kappa^4 N_c f_{\pi_d}^2 m_{\text{down}}^2}{32\pi M_{X_d}^4} m_{\pi_d}, \quad (2.5)$$

where κ represents the Yukawa couplings, N_c is a Standard Model color factor, f_{π_d} is the dark pion decay constant, and m_{down} is the mass of a SM down-type quark. The dark pion proper lifetime is thus given by

$$c\tau_0 = c\hbar/\Gamma \approx (80 \text{ mm}) \times \left(\frac{1}{\kappa^4}\right) \left(\frac{2 \text{ GeV}}{f_{\pi_d}}\right)^2 \left(\frac{100 \text{ MeV}}{m_{\text{down}}}\right)^2 \left(\frac{2 \text{ GeV}}{m_{\pi_d}}\right)^2 \left(\frac{M_{X_d}}{1 \text{ TeV}}\right)^4, \quad (2.6)$$

where the centimeter-to-meter decay length for GeV-scale dark pions and a TeV-scale mediator becomes obvious.

2.2 EMERGING JET PHENOMENOLOGY

The dark QCD model described above yields events with the unique collider signature of *emerging jets* (EJ), postulated by Schwaller, Stolarski, and Weiler in [17] and shown schematically in Figure 2.2.

An emerging jet event begins with the production of a TeV-scale field that decays to dark quarks with energies much larger than the dark confinement scale; thus, the dark quarks shower and hadronize, producing a multitude of dark mesons. Given a QCD-like dark sector, this process looks very much like standard QCD hadronization, and the dark hadrons form dark jets. Since the dark mesons decay into SM quarks with lifetimes of order centimeters, and the exponential decay law dictates these decays all happen at different points in the detector, the dark jets gradually “emerge” into the visible sector over a macroscopic length scale. The details of this process are described below.

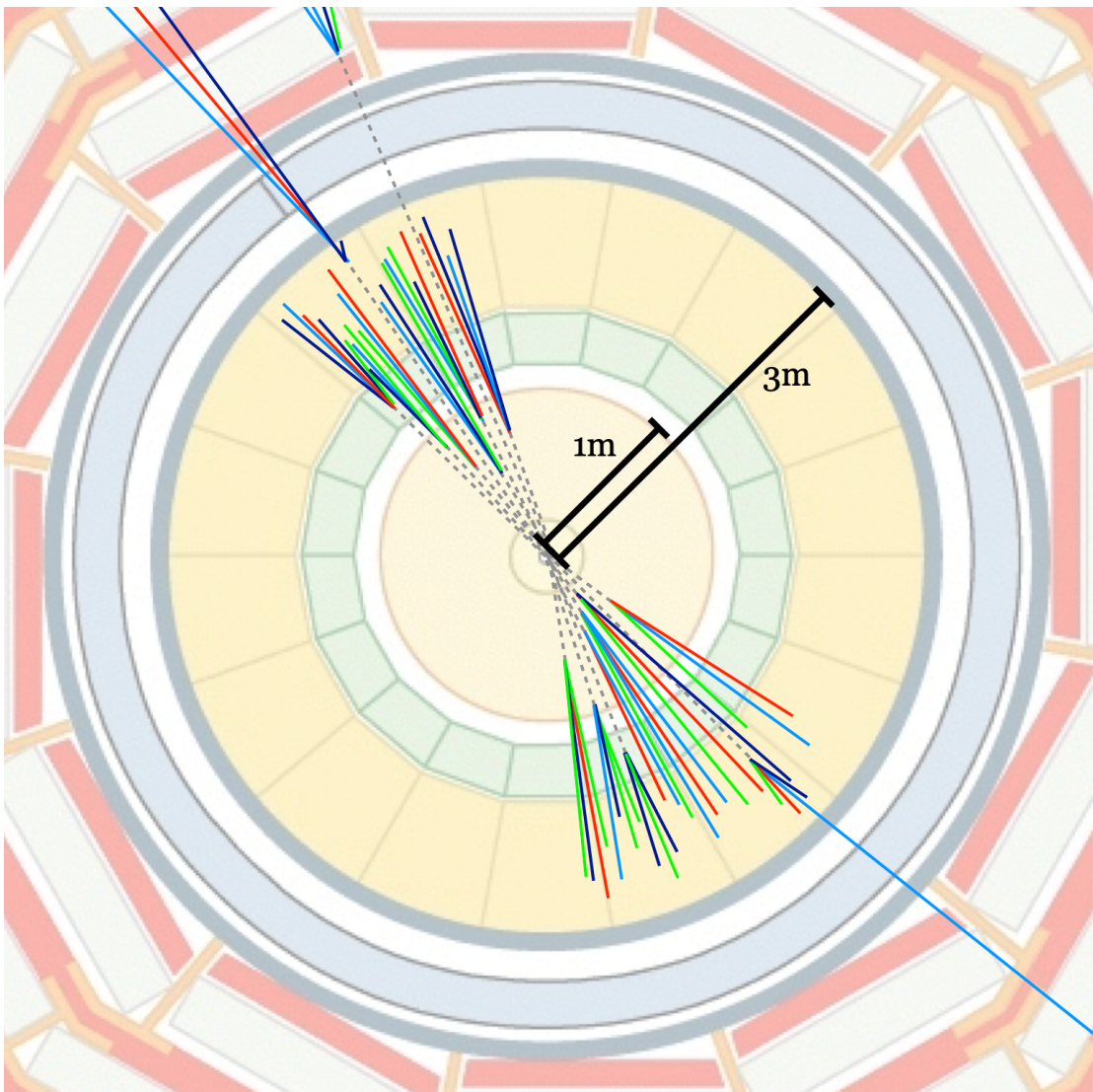


Figure 2.2: A schematic of two emerging jets, formed from dark quark pair production, shown in the transverse plane of a generic detector, with the beam pipe going into the page. The dashed lines represent the dark mesons, which are invisible to the detector, while the solid lines represent the SM hadrons resulting from the dark pion decays to SM quarks [17].

At the collider, dark scalar mediators are pair-produced through a virtual gluon from either initial quark or gluon states ($pp \rightarrow X_d X_d^\dagger$), as shown in Figure 2.3. The scalar mediators each immediately decay to a quark and a dark quark before the onset of hadronization, so the X_d pair production and subsequent decay ($pp \rightarrow X_d X_d^\dagger \rightarrow q \bar{Q}_d \bar{q} Q_d$) can be treated as a single hard-process, as shown in Figure 2.4. The SM quarks naturally appear as standard QCD jets, while the dark quarks undergo dark showering and hadronization on a time scale Λ_d^{-1} much shorter than dark meson decays. Dark showering occurs much in the same way as regular parton showering, which is well-understood for any non-Abelian gauge theory and can be described by the DGLAP evolution equations, and therefore results in dark jet-like objects very similar in nature to QCD jets. Baryon production in the dark sector is suppressed relative to mesons in the large N_d limit, as in QCD, [44], and all heavier dark mesons decay to dark pions, again on very short time scales Λ_d^{-1} , resulting in dark jets comprised mostly of dark pions, which originate from the interaction point (IP) but are completely invisible to detector.

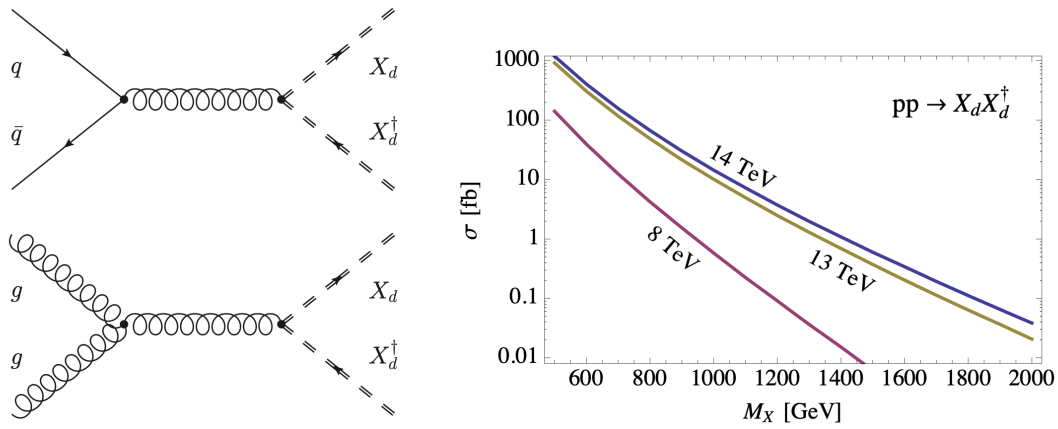


Figure 2.3: Left: Feynman diagrams for dark scalar mediator X_d pair production. Right: Tree-level cross section for X_d pair production at various center-of-mass energies at the LHC. The cross section is similar to stop-quark pair production multiplied by the number of dark colors N_d [17].

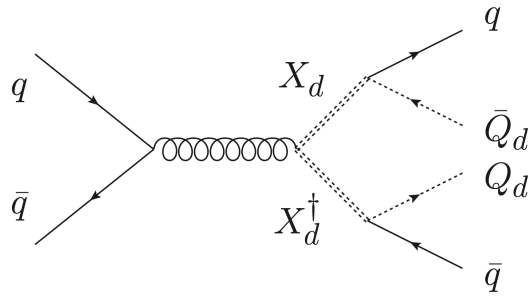


Figure 2.4: Feynman diagram for EJs hard process: dark scalar mediator X_d pair production and subsequent decay to quark - dark quark pairs.

The dark pions within the dark jets eventually decay to SM particles after traveling some appreciable distance. With characteristic decay length $\beta\gamma c\tau_{\pi_d}$, where $\beta\gamma$ is the momentum-dependent boost factor of each individual dark pion, and exponential distributions of the actual lifetime, each dark pion decays at a different displacement within the original dark jet. The average transverse decay distance $\beta_T\gamma_T c\tau_{\pi_d} = (p_T/m_{\pi_d})c\tau_{\pi_d}$, around which most of the decays occur, scales proportionally to the dark pion proper lifetime and inversely to its mass, assuming a fixed dark mediator mass, and places most of the decays within the tracker. As the dark pions decay back to the Standard Model, multiple small sub-jets appear within the cone of the original dark jet. Each sub-jet consists of a few SM hadrons originating from a common displaced vertex, and each vertex for each sub-jet is distinct and differently displaced. From afar, the jet appears much like a standard (albeit somewhat displaced) jet, with a number of hadrons all stemming from approximately the same place and headed in the same direction, but the radial profile shows very little visible energy at the IP and more and more further and further into the tracker. Thus, the jets *emerge* into the detector with the distinct signature of multiple varyingly displaced vertices within the overall jet cone. The pair production of dark scalar mediator leads to two standard QCD jets and two emerging jets in the event, as illustrated in Figure 2.5

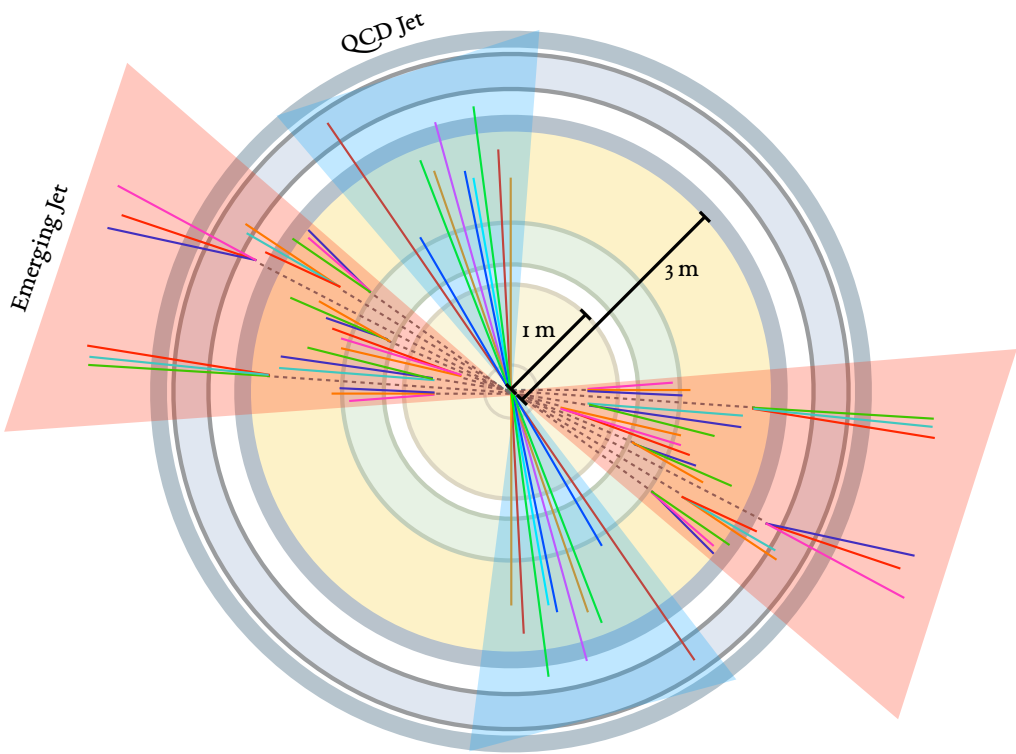


Figure 2.5: Schematic of EJs search final-state signature: 2 QCD jets + 2 emerging jets, shown in the transverse plane of a generic detector, with the beam pipe going into the page. The blue cones represent the QCD jets, comprised of SM hadrons, represented by solid colored lines, and the red cones represent the emerging jets, comprised of SM hadrons resulting from the displaced decays of dark mesons, depicted by the dashed colored lines, to SM quarks.

3

The ATLAS Experiment

3.1 THE LARGE HADRON COLLIDER

The Large Hadron Collider (LHC) is a high-energy circular proton-proton collider located at the European Organization for Nuclear Research (CERN) in Geneva, Switzerland, designed to test the Standard Model and search for new physics [4, 45]. To date, it is the largest, highest-energy, and highest-luminosity particle accelerator in the world, with a cir-

cumference of 26.7 km, design center-of-mass collision energy of 14 TeV, and a design peak instantaneous luminosity of $1.0 \times 10^{34} \text{ cm}^{-2} \text{ s}^{-1}$. Housed in the former Large Electron-Positron (LEP) collider tunnel, approximately 100 m underground, the LHC consists of two superconducting rings carrying high-energy proton or heavy-ion beams that collide at four interaction sites within detectors along the ring. The LHC is currently home to seven experiments: ATLAS, ALICE, CMS, and LHCb, larger experiments with detectors built around each of the collision sites at Point 1 (P₁), Point 2 (P₂), Point 5 (P₅), and Point 8 (P₈), respectively, and the much smaller and more specialized TOTEM, LHCf, and MoEDAL.

ATLAS [5, 46, 47], or A Toroidal LHC ApparatuS, and CMS [6], or Compact Muon Solenoid, are the largest experiments and the two general purpose detectors, designed to study any and all possible physics produced from proton-proton collisions at the LHC. These high-luminosity detectors perform similar experiments with statistically independent datasets for the purpose of cross-checking each other's results. The ATLAS detector, used for the Emerging Jets search, is explained in detail in Section 3.2.

ALICE [48] and LHCb [49] are more specialized low-luminosity detectors designed to study specific phenomena. ALICE, or A Large Ion Colliding Experiment, is a heavy-ion detector designed to recreate conditions immediately after the Big Bang and to study quark-gluon plasma. Heavy ions at the LHC are not relevant to the search presented in this thesis and will therefore not be discussed further. LHCb, or LHC beauty/bottom, is a b-physics

experiment studying CP-violation in b-hadron interactions in order to better understand matter-antimatter asymmetry.

TOTEM, LHCf, and MoEDAL are the smallest and most specialized experiments, using detectors positioned outside the main interaction points. TOTEM, or TOTal, Elastic, and diffractive cross section Measurement, consists of detectors spread around the CMS interaction point and performs precision measurements of forward protons coming from collisions within the CMS detector. LHCf, or LHC forward, uses detectors placed along the beam line on either side of the ATLAS collision point to simulate cosmic rays from forward particles. MoEDAL, or MOnopole and Exotics Detector At the LHC, is a magnetic monopole and stable massive particle search that uses detectors near LHCb.

The LHC first turned on in September 2008 and began Run 1 in March 2010 with a center-of-mass energy of $\sqrt{s} = 7 \text{ TeV}$, an energy 3.5 times higher than ever before at any particle accelerator. Run 1 lasted from 2010 to the end of 2012, with 7 TeV runs in 2010 and 2011 for beam commissioning and performance limit exploration and an 8 TeV run in 2012 for physics production, during which over 20 fb^{-1} of integrated luminosity was delivered and the Higgs boson was discovered, but no new physics was found. After the first long shutdown (LS1) for initial upgrades and maintenance, Run 2 began at $\sqrt{s} = 13 \text{ TeV}$ in April 2015 and concluded at the end of 2018, delivering over 150 fb^{-1} of data over the course of the run and frequently reaching peak instantaneous luminosities of twice the design

value. Run 3, scheduled to begin in 2021, is expected to run at nominal center-of-mass energy, $\sqrt{s} = 14$ TeV.

Particle colliders accelerate particles to ultra-relativistic speeds and collide them at high energies to probe their inner structure and produce new states. The available energy in a collision is the most important parameter in collider experiments, since the higher the incoming interaction energy, the larger the possibilities of new particles to produce. New heavy particles can theoretically be produced if the interaction energy is greater than the outgoing particle's rest energy, based on $E = mc^2$, providing the main motivation for the historical push to larger and higher-energy colliders. The outgoing particles produced in high-energy collisions are then measured and studied in detectors. Circular colliders, like the Large Hadron Collider, circulate counter-rotating beams and collide them at fixed points along a circle. The benefits of such an experiment include larger center-of-mass energies than fixed-target experiments from the head-on collisions and higher integrated luminosities from the reusability of the circular beams.

Particles are accelerated to high energies through a series of alternating electric fields in radiofrequency (RF) cavities [50]. An RF cavity is a metallic chamber containing an electromagnet field that accelerates charged particles. The field inside the cavity is made to oscillate, or switch direction, at a given frequency such that ideally-timed particles with the exact right energy will not be accelerated, while particles with slightly different energies that

arrive earlier or later than expected will be accelerated or decelerated to stay close to the ideal energy. At the LHC, the RF cavities oscillate at 400 MHz. Such an oscillating behavior results in the beam being sorted into discrete packets, or bunches.

The beams are circulated around the circular collider at a constant radius with the use of magnets, with dipole magnets used to bend the beam around the ring and quadrupoles used to focus the beam. The force \vec{f} on a particle with charge q and velocity \vec{v} moving through a magnetic field \vec{B} is given by

$$\vec{f} = q\vec{v} \times \vec{B}, \quad (3.1)$$

and the radius R of the circle of the particle's trajectory is then given by

$$R = \frac{p}{qB}, \quad (3.2)$$

where p is the momentum of the particle traveling perpendicular to the dipole magnetic field of strength B . For protons, with charge $q = e$, the energy of the beam is then given by

$$E_{\text{beam}} = 0.3BR, \quad (3.3)$$

where B is in units of Tesla. For the 7 TeV design beam energy at the LHC, with a 27 km

ring, a magnetic field of 8.33 T is thus required. Such large field strengths necessitate superconducting magnets operating at low temperatures.

The other essential parameter in collider experiments is the number of events, or useful interactions, available to study, especially when searching for rare events with small cross sections [51]. The number of expected events N_{exp} for a given process is the product of the cross section σ_{exp} of interest times the integral of the instantaneous luminosity \mathcal{L} over time:

$$N_{\text{exp}} = \sigma_{\text{exp}} \times \int \mathcal{L} dt = \sigma_{\text{exp}} \times \mathcal{L}_{\text{int}}, \quad (3.4)$$

where the cross section describes the probability of a given process occurring and has dimensions of area, and the luminosity is a measure of the accelerator's ability to produce the required number of interactions. The integrated luminosity, the integral of the instantaneous luminosity over time, is a measure of the total amount of data taken over a period of time, while the instantaneous luminosity is a measure of the amount of data produced in the detector per unit area per unit time, or the collision rate. The instantaneous luminosity is defined in terms of the colliding beams:

$$\mathcal{L} = f_{\text{coll}} \frac{n_1 n_2}{4\pi \sigma_x^* \sigma_y^*} \mathcal{F} = f_{\text{coll}} \frac{n_1 n_2}{4\pi \sqrt{\epsilon_x \beta_x^* \epsilon_y \beta_y^*}} \mathcal{F}, \quad (3.5)$$

where n_1 and n_2 are the number of particles per colliding bunch N_b for each of the two

beams, σ_x^* and σ_y^* represent the root-mean-square (rms) transverse beam sizes in the x and y directions, ε_x and ε_y represent the emittance of the beam, and β_x^* and β_y^* describe the transverse displacement of the particles in the beam. The sigma and beta functions vary with position along the beam, with the asterisks representing the values of the functions at the interaction point. \mathcal{F} is a reduction factor of order one that accounts for geometric and dynamic effects like crossing angle and beam focusing, and f_{coll} equals the number of bunches per beam n_b times the revolution frequency f_{rev} for a circular collider [23]. The luminosity can thus be increased by increasing the number of protons per bunch or the number of bunches per beam or by reducing the spread of particles in x and y at the interaction point, known as “squeezing” the beam. Throughout an individual physics run, the instantaneous luminosity falls from its initial peak as the beams circulate and the number of protons per bunch decreases.

While colliders often aim to maximize the collision rate to produce as much data as possible, such high instantaneous luminosities lead to the complicated effect of high pileup, or multiple simultaneous collisions taking place in the same event. In-time pileup refers to multiple collisions occurring in a single bunch crossing (BC), while out-of-time pileup refers to additional collisions from bunch crossings outside of the collision of interest, due to the detector read-out being longer than the time between bunch cross crossings, or the bunch spacing. Both types of pileup typically result in a number of soft particles that con-

taminate the final-state signal of the hard scatter, or the single large momentum-transfer collision of interest, and complicates its reconstruction. It is thus important to understand the pileup distribution in an event and to discriminate between hard-scatter and pileup processes. The pileup is primarily described by the number of primary vertices per event N_{PV} and the average number of inelastic interactions per bunch crossing $\langle\mu\rangle$. The average $\langle\mu\rangle$ at ATLAS Run 2 was approximately 33 interactions per BC, and the peak was approximately 70.

The beams at the LHC are produced and accelerated in the CERN accelerator complex, shown in Figure 3.1, before being injected into the LHC ring, where they are boosted to their final target energy. The injection chain begins with the production of protons from hydrogen atoms ionized in an electric field. The protons are then injected into Linear Accelerator 2 (Linac 2), which accelerates them to 50 MeV using a series of RF cavities. The protons then enter the Proton Synchrotron Booster, consisting of four superimposed synchrotron rings that accelerate the protons to 1.4 GeV, before injecting them into the Proton Synchrotron (PS), with a circumference of 628 m and a final energy of 25 GeV. Then, the protons are passed to the Super Proton Synchrotron (SPS), the second-largest machine after the LHC with a circumference of 7 km, where they are accelerated with conventional magnets to 450 GeV, sufficient energy for stable beams, which are finally injected into the LHC, which accelerates the proton beams to their final target energy of 6.5 TeV.

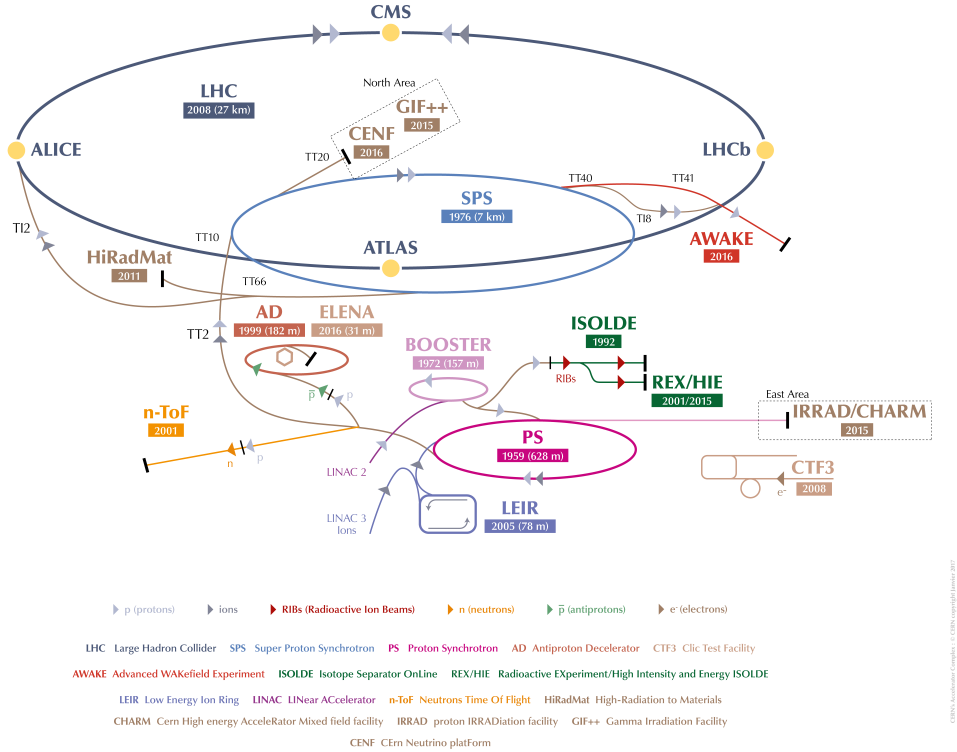


Figure 3.1: The CERN accelerator complex: a sequence of machines that accelerate particles to increasingly higher energies, with each machine boosting the the beam and injecting it into the next machine in the chain. The LHC (the dark blue ring) is the final element in the series [52].

Inside the LHC, 16 superconducting single-cell RF cavities, eight per beam, deliver a maximum voltage of 2 MV per cavity, totaling 16 MV per beam, and oscillate at 400 MHz. This provides each proton beam with an energy boost of 16 MeV per revolution around the LHC, with the maximum energy being reached in approximately 20 minutes. With a tunnel diameter of only 3.7 m, the accelerator circulates both beams in opposite directions within separate magnetic fields and vacuum beam-pipes but inside a single cryostat. Thousands of superconducting electromagnets, cooled to 1.9 K, are installed throughout the ac-

celerator to guide the beams around the ring, including 1232 main bending dipole magnets, which generate a peak magnetic field of 8.33 T, and 392 quadrupole magnets that focus the beams and squeeze them before collisions inside the detectors.

The beam parameters, and the resulting luminosities and pileups, for each data-taking year in Run 2 are shown in Table 3.1. Run 2 began in 2015 with a beam energy of 6.5 TeV and a bunch spacing of 25 ns, versus the 4 TeV beam energy and 50 ns bunch spacing at the end of Run 1. Data-taking conditions evolved throughout Run 2, improving year to year, with peak instantaneous luminosities reaching double the design value due to an increase in the number of colliding bunch pairs n_b and the average bunch currents, as well as stronger focusing at the interaction point, parameterized by β^* , resulting in smaller transverse beam sizes.

Parameter	Design	2015	2016	2017	2018
Energy [TeV]	7.0	6.5	6.5	6.5	6.5
Number of bunches (n_b)	2808	2232	2208	2554/1909	2544
Bunch spacing [ns]	25	25	25	25/8b4e	25
Bunch population (N_b) [10^{11} protons]	1.15	1.1	1.1	1.1/1.2	1.1
β^* [m]	0.55	0.8	0.4	0.3	0.3-0.25
Peak luminosity [$10^{34} \text{ cm}^{-2} \text{ s}^{-1}$]	1.0	0.5	1.3	1.6	1.9
Peak pileup ($\langle\mu\rangle$)	..	16	41	45/60	55
Lumi-weighted pileup	..	13	25	38	36
Total integrated luminosity [fb^{-1}]	..	4.0	38.5	50.2	63.4

Table 3.1: Typical LHC Run 2 parameters for $p\bar{p}$ collisions at $\sqrt{s} = 13$ TeV during data-taking years 2015-2018, as well as their design values, where relevant. Values are shown for runs representing the best accelerator performance during normal physics operation. The 2017 columns shows values for both run configurations that year: standard 25 ns bunch train operation and '8b4e', a bunch train pattern of eight 25 ns-separated bunches followed by a four bunch-slot gap [53].

Luminosity is measured at ATLAS with multiple luminosity detectors, primarily the LUCID2 Cherenkov detector and the beam conditions monitor (BCM) diamond detectors, which perform bunch-by-bunch measurements, as well as offline measurements of the multiplicity of reconstructed charged particles [53]. The luminosity counts are integrated over some well-defined time interval where the detector and luminosity conditions are expected to be relatively constant. These time intervals are referred to as luminosity blocks, or lumi-blocks, and are typically around 60 seconds in length. Total integrated luminosity is then determined by integrating over all lumi-blocks in a given time period. Over the course of Run 2, a total of 156 fb^{-1} of data was delivered to ATLAS by the LHC, 147 fb^{-1} was recorded by ATLAS, and 139 fb^{-1} was certified to be good quality for physics use by ATLAS. Figures 3.2 and 3.3 show the cumulative integrated luminosity over time and the luminosity-weighted pileup, respectively, throughout Run 2 as recorded by the ATLAS detector.

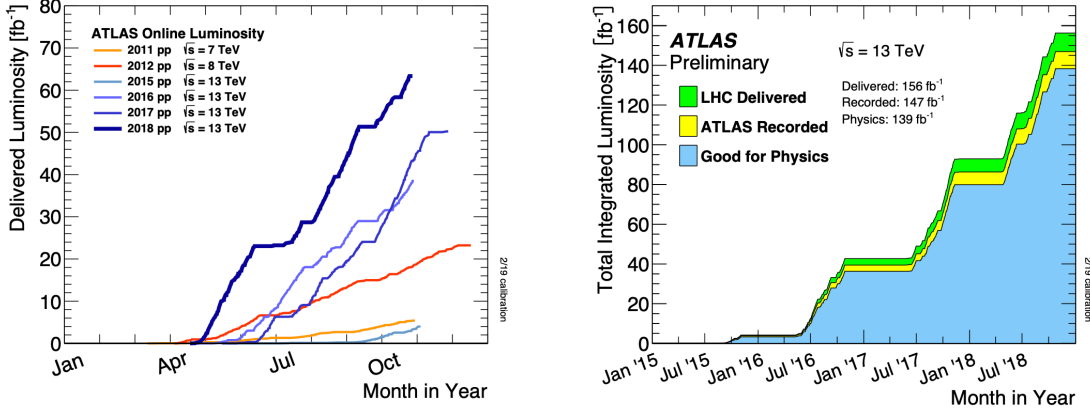


Figure 3.2: Integrated luminosity delivered to ATLAS by the Large Hadron Collider per year (left) and for all of Run 2 (right) [54]. Left: The integrated luminosity delivered to ATLAS per year during stable beams for $p\bar{p}$ collisions at 7-13 TeV center-of-mass energy in 2011-2018. Right: Cumulative integrated luminosity versus time delivered to ATLAS by LHC (green), recorded by ATLAS (yellow), and certified good quality by ATLAS and used for physics (blue) during stable beams for $p\bar{p}$ collisions at 13 TeV center-of-mass energy in 2015-2018.

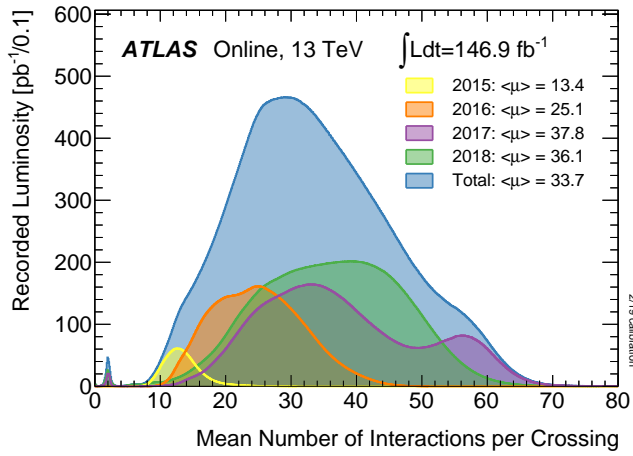


Figure 3.3: Luminosity-weighted distribution of the mean number of interactions per crossing ($\langle \mu \rangle$) for 13 TeV center-of-mass energy $p\bar{p}$ collision data collected between 2015-2018 and recorded by ATLAS [54].

3.2 THE ATLAS DETECTOR

The ATLAS detector is a large general purpose detector, 44 m in length, 25 m in diameter, and weighing nearly 7000 t, with forward-backward symmetric cylindrical geometry and nearly full solid angle coverage around the interaction point [5, 46, 47], as illustrated in Figure 3.4.

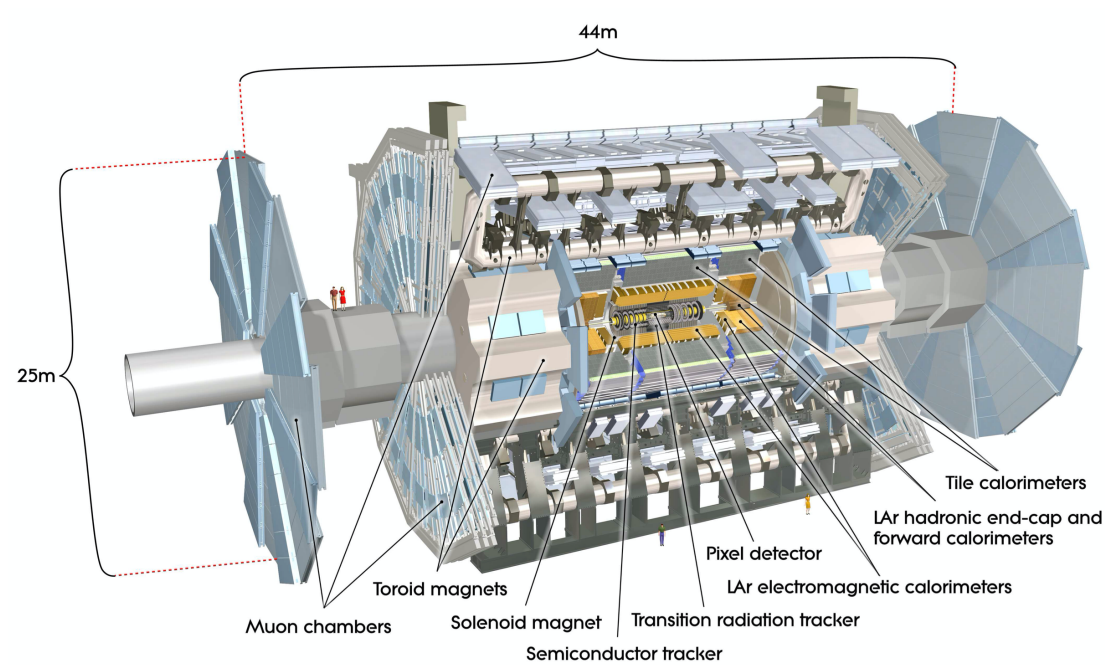


Figure 3.4: A cutaway diagram of the ATLAS detector [5].

ATLAS uses a right-handed Cartesian coordinate system with the origin at the nominal interaction point (IP) at the detector center. The z -axis points along the direction of the beam, and the xy plane is transverse to the beam direction, with the x -axis pointing inwards

to the center of the LHC ring and the y -axis pointing upwards. Cylindrical coordinates (r , φ) are often used for measurements in the transverse plane, where $r = \sqrt{x^2 + y^2}$ is the transverse distance from the IP, and φ is the azimuthal angle measured around the beam axis. The polar angle ϑ is the angle from the beam axis, but it is preferable to describe the particle angle relative to the beam axis in terms of the pseudorapidity $\eta = -\ln \tan(\vartheta/2)$, since differences in η are Lorentz invariant under longitudinal boosts and particle production is roughly constant in η in the central region at hadron colliders. Pseudorapidity is an approximation of the rapidity $Y = 1/2 \ln[(E + p_z)/(E - p_z)]$ in the ultra-relativistic limit, or where the mass of the particle is negligible. The pseudorapidity goes to zero for a particle perpendicular to the beam and to positive or negative infinity along the beam line. The distance between two objects is often defined in terms of the angular separation ΔR in pseudorapidity-azimuthal space, where $\Delta R = \sqrt{\Delta\eta^2 + \Delta\varphi^2}$.

With the goal of studying a wide range of particles, including precise measurements of the Standard Model and searches for new Beyond the Standard Model (BSM) physics, the ATLAS detector is designed with the following criteria in mind:

- fast, radiation-hard electronics and sensors;
- high detector granularity to handle large particle fluxes and reduce the effects of pileup;
- large acceptance in η with almost full coverage in φ ;
- inner tracking with precise charged-particle momentum measurement and high reconstruction efficiency;

- calorimetry with large coverage for identifying and precisely measuring electrons, photons, jets, and missing energy;
- dedicated muon identification and momentum resolution over a wide range of momenta;
- highly efficient triggering with large background rejection.

The detector consists of concentric layers of specialized sub-detectors surrounding the beam-pipe, with the cylindrical shells making up the central barrel region and the disk layers sandwiching the barrel on either end making up the forward end-caps. The bulk of the detector is comprised of three main sub-detectors: the inner detector, the calorimeters, and the muon spectrometer, each designed to identify and measure different particle types and properties. To aid in these measurements, two superconducting magnet systems are configured to bend the charged particle trajectories, with the direction and radius of curvature allowing for charge and momentum measurements, respectively. Additionally, a tiered trigger and data acquisition system provides a means of filtering the extraordinarily large data output to a more manageable rate. The individual components of the detector are described in detail below.

3.2.1 THE INNER DETECTOR

The inner detector (ID), or tracker, shown schematically in Figure 3.5, is the innermost component of the ATLAS detector, immediately surrounding the interaction point, and is designed to reconstruct charged particle tracks and vertices and to precisely measure their

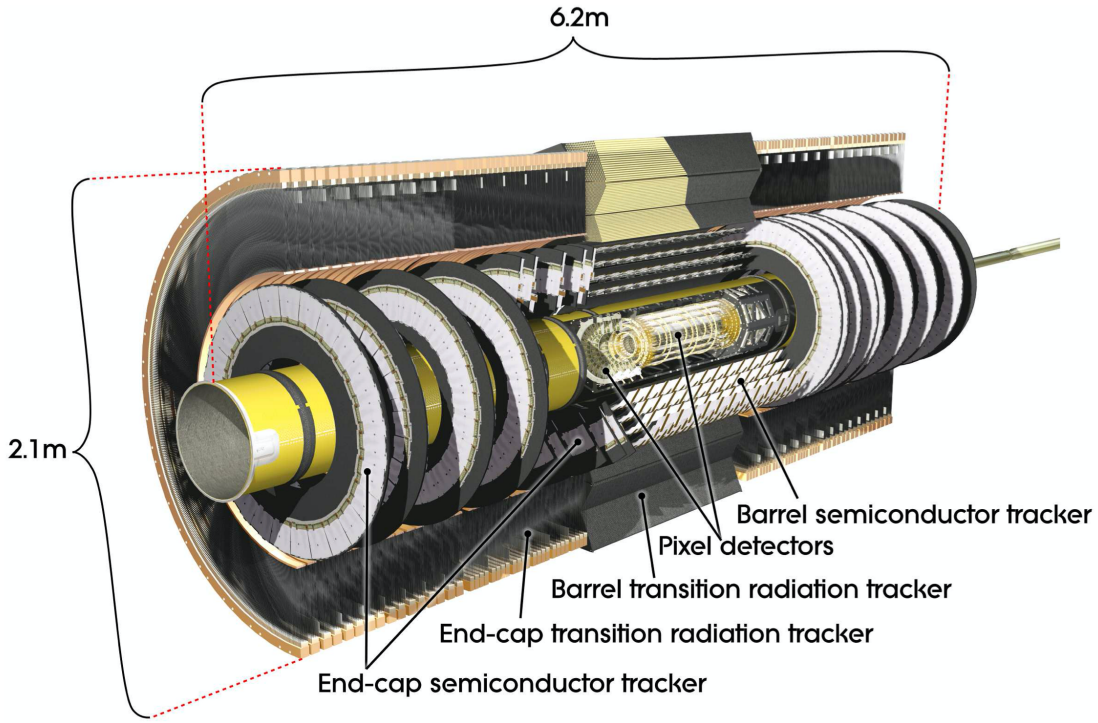


Figure 3.5: A cutaway diagram of the ATLAS inner detector (ID) [5].

momenta. It is made up of three subsystems from inside out: the silicon pixel layer (Pixel), the semiconductor tracker (SCT), and the transition radiation tracker (TRT). The Pixel consists of four layers of high-granularity silicon pixel detectors, including the newest and innermost layer, the insertable B-layer (IBL), while the SCT consists of four double layers of silicon microstrips. Together, the Pixel and SCT silicon detectors are responsible for precision tracking and vertex finding and provide coverage up to $|\eta| < 2.5$. The TRT is a straw tracker and transition radiation detector designed for further tracking and electron identification covering the range $|\eta| < 2.0$. The entire inner detector is surrounded by the

central solenoid, a thin superconducting solenoid of length 5.3 m and diameter 50 mm that generates a 2 T axial magnetic field. The magnetic field deflects the charged particles in the tracker, allowing for charge and momentum measurements from the curvature and direction of the particle trajectories. The inner detector is contained in a cylindrical envelope of $z = \pm 3512$ mm and $r = 1150$ mm, covers the pseudorapidity range $|\eta| < 2.5$, and tracks particles with $p_T > 0.5$ GeV, where p_T is the transverse component of the particle momentum. The layout of the inner detector is shown in Figure 3.6, and the sensors and structural elements of the inner detector are shown in Figure 3.7.

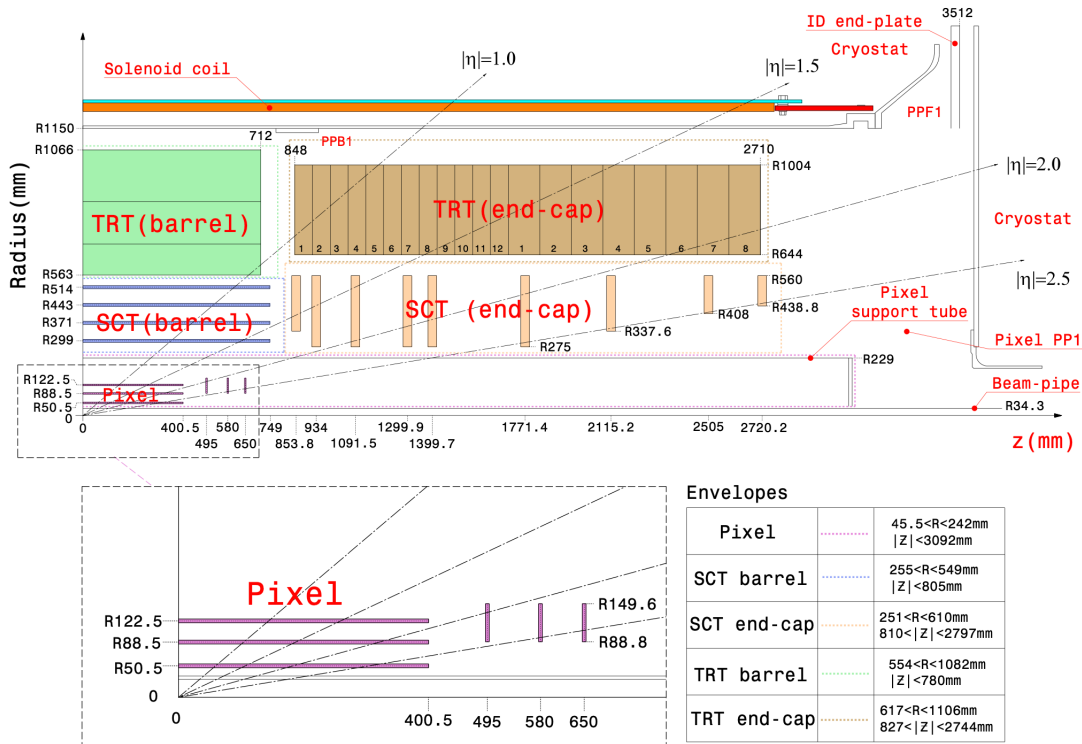


Figure 3.6: A diagram of a quadrant of the ATLAS inner detector [5].

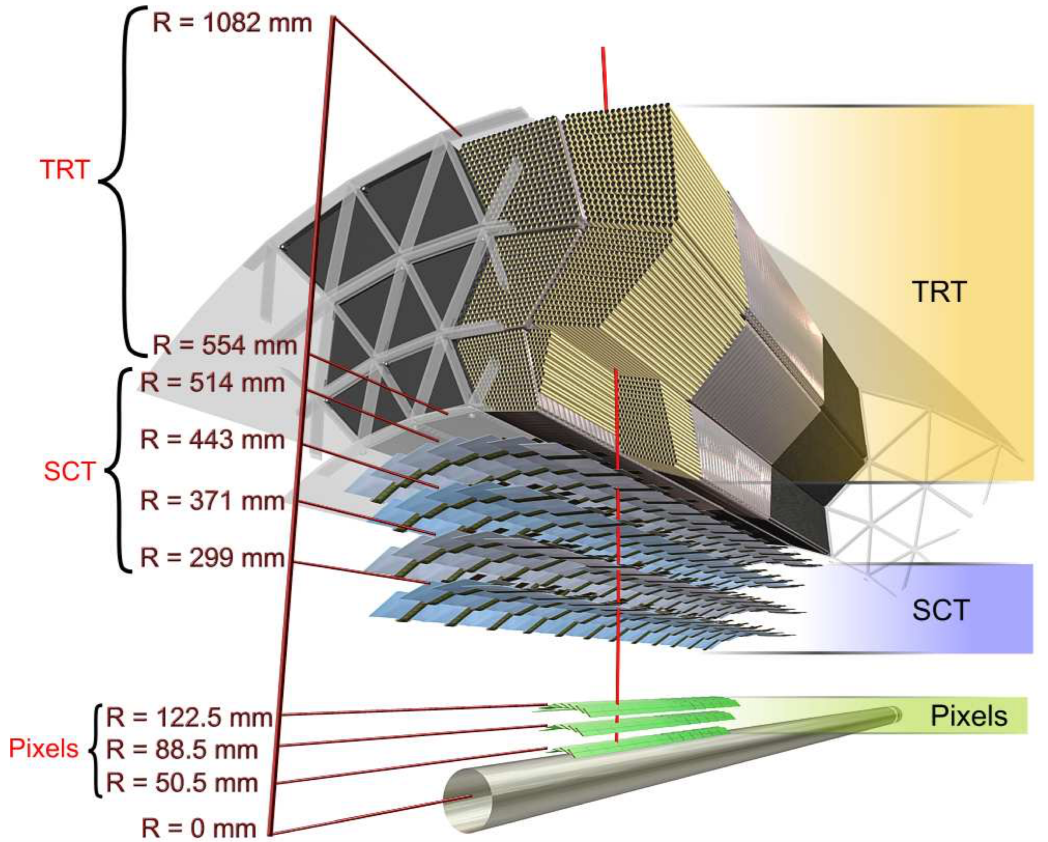


Figure 3.7: A diagram showing the sensors and structural elements of the ATLAS inner detector barrel [5].

3.2.1.1 PIXEL DETECTOR

The Pixel is the innermost tracker and the sub-detector closest to the beam. It consists of a central cylindrical barrel and two disk-shaped end-caps. The barrel is made up of four concentric cylindrical layers parallel to the beam: the insertable B-layer (IBL), the B-layer, Layer 1, and Layer 2 at $r = 33$ mm, 50.2 mm, 88.5 mm, and 122.5 mm, respectively. The IBL, the innermost layer, was newly integrated into the detector before Run 2 to improve ver-

tex reconstruction and b-jet identification. The end-caps are comprised of three disk layers each, perpendicular to the beam at $|z| = 495$ mm, 580 mm, and 650 mm. The Pixel provides the finest granularity and highest number of readout channels of the detector and is designed to precisely measure track positions and impact parameters and to reconstruct the pp interaction point with very high spatial resolution in three dimensions. The two inner B-layers are also responsible for b-tagging, or identifying signatures from b-hadron decays. The Pixel is a semiconductor detector with silicon pixel sensors, where a high-energy charged particle passing through a sensor ionizes the silicon, producing electron-hole pairs and resulting in measurable signal currents. Signal hits are recorded in pixel sensors where the charge deposited by a traversing particle is greater than some threshold, and thus the detector can measure the particle's position and trajectory, based on which pixels sensors record a hit, and the amount of energy deposited by the particle, by calculating the time-over-threshold (ToT), or the amount of time the charge exceeded the threshold. The Pixel contains over 92 million pixel readout channels, divided between modules mounted on staves/sectors arranged among the barrel/end-cap layers [55]. Table 3.2 lists the Pixel parameters for each layer and for the total pixel detector as a whole.

3.2.1.2 SEMICONDUCTOR TRACKER (SCT)

The SCT is a silicon microstrip detector and another semiconductor precision tracker, located immediately outside the Pixel. It consists of silicon-strip modules arranged in four

Barrel	Radius [mm]	Staves	Modules	Pixels
IBL	33	14	280	12.0×10^6
Layer-0	50.5	22	286	13.2×10^6
Layer-1	88.5	38	494	22.8×10^6
Layer-2	122.5	52	676	31.2×10^6
Total barrel		126	1736	79.2×10^6
End-cap (per side)	z [mm]	Sectors	Modules	Pixels
Disk 1	495	8	48	2.2×10^6
Disk 2	580	8	48	2.2×10^6
Disk 3	650	8	48	2.2×10^6
Total per end-cap		24	144	6.6×10^6
Total both end-caps		48	288	13.2×10^6
Total		174	2024	92.4×10^6

Table 3.2: Parameters of the pixel detector. The number of pixels, modules, staves/sectors, as well as average radial and longitudinal positions, are shown for each layer and for the the detector as a whole [56, 57]. Modules are mounted on mechanical/cooling supports, called staves (barrel) or disk sectors (end-caps). Pixel modules are $250 \mu\text{m}$ thick. Each pixel in all layers is $50 \times 400 \mu\text{m}^2$ in size, except in the IBL, where the pixel size is $50 \times 250 \mu\text{m}^2$.

concentric radial barrel layers at $r = 299 \text{ mm}$, 371 mm , 443 mm , and 514 mm and nine disk layers per end-cap, positioned in $|z|$ between 934 mm and 2720 mm [58]. The modules are positioned parallel to the beam line in the barrel and arranged radially in the end-caps. An SCT module is built of two pairs of silicon-strip sensors, with two sensors per side wire-bonded together to create a 12-cm long strip, glued back-to-back with a 40-mrad stereo angle between them. This way, each barrel or disk layer provides two strip measurements at the stereo angle, which are combined to build three-dimensional space points. The channels in the SCT are larger than in the Pixel, since less stringent requirements on resolution and radiation sensitivity are placed farther away from the beam-pipe. The SCT contains 768 readout strips per sensor pair and 4088 silicon strip modules, with 2112 in the barrel and

988 per end-cap, containing 16,000 sensors, yielding a total of 6.3 million readout channels.

Each silicon-strip sensor pair is 126 mm \times 80 μm in size and 285 μm thick. Unlike the pixel detector, the SCT records only binary hit information, that is the presence of a hit-over-threshold, but not the time-over-threshold of the hit.

3.2.1.3 TRANSITION RADIATION TRACKER (TRT)

The TRT is a straw tracker and the outermost layer of the inner detector, providing two-dimensional position measurements in $r\text{-}\phi$ and particle identification [59]. It works as a drift chamber with approximately 300,000 straw drift tubes interleaved with radiator material. The barrel, which spans the region $560 < r < 1080$ mm and $|z| < 720$ mm, contains 73 layers of 144-cm long straws arranged parallel to the beam, thus yielding no spatial resolution in z . The end-caps, covering $827 < |z| < 2774$ mm and $617 < r < 1106$ mm, each consist of 160 layers of 37-cm long straws arranged radially in wheels and aligned perpendicular to the beam, thus providing no spatial resolution in r . The straws are 4 mm in diameter and are filled with a xenon-based gas mixture, chosen for its high absorption efficiency of transition radiation photons. Each straw contains a 31- μm diameter gold-plated tungsten anode wire set to ground potential at the straw center. The straw wall is meanwhile set to negative potential. When a charged particles traverses the straw, it ionizes the gas inside, resulting in ionized electrons drifting toward the anode wire and cascading in the strong electric field close to the anode, producing an amplified detectable signal. The signal

is compared against two thresholds, low threshold (LT) and high threshold (HT), allowing for simultaneous tracking measurements and identification of large energy deposits characteristic of electrons. Tracking measurements are performed by calculating the distance of closest approach of a charged particle to the anode wire from the drift time of the ionization signal over the LT. Electron identification takes place when transition radiation photons, or soft x-rays emitted in the radiator material due to the passage of highly-relativistic charged particles through the inhomogeneous media of the detector, are absorbed by the active gas inside the straw tubes, yielding large signals exceeding the HT. Particle identification can be further discriminated between electrons and charged pions by analyzing the fraction of HT hits per track, with a lower fraction of HT hits being representative of pions, as shown in

Figure 3.8. The TRT provides up to 36 hits per tracks.

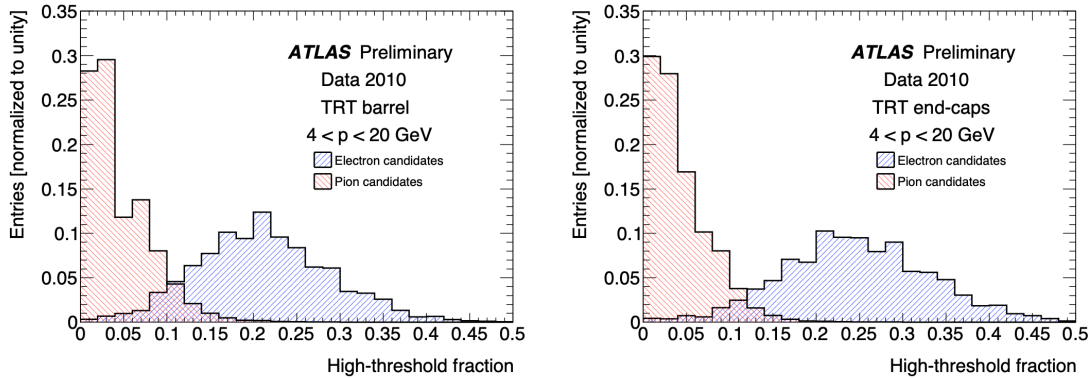


Figure 3.8: The HT fraction for electron and pion candidates in the TRT barrel (left) and end-caps (right) [59].

3.2.2 THE CALORIMETERS

Surrounding the inner detector, outside of the central solenoid, is the system of electro-magnetic and hadronic calorimeters, designed to measure the energies of electromagnetic and strongly interacting particles, respectively. Together, the calorimeters cover the pseudorapidity range $|\eta| < 4.9$ and provide full φ symmetry and coverage around the beam-axis. The calorimetry system consists of liquid argon (LAr) and tile sampling calorimeters that interleave layers of absorbing and sampling material. The absorbers are made of high-density materials designed to stop traversing particles by inducing showers such that all of the particle energies are deposited in the calorimeter, while the samplers contain active material that measure the energy deposited by the particle showers. The LAr EM calorimeter identifies and precisely measures electrons and photons with fine granularity using lead/liquid-argon (LAr) barrel and end-cap sampling calorimeters in $|\eta| < 3.2$, while the hadronic calorimeters measure hadrons with coarser granularity sufficient to reconstruct jets and measure missing energy using a steel/scintillator tile barrel calorimeter in $|\eta| < 1.7$ and copper/LAr end-cap calorimeters in $1.5 < |\eta| < 3.2$. The forward copper-tungsten/LAr calorimeter (FCal) provides coverage close to the beam in $3.1 < |\eta| < 4.9$, with copper and tungsten absorbers optimized for electromagnetic and hadronic measurements, respectively. A schematic of the calorimetry system and its components is illustrated in Figure 3.9.

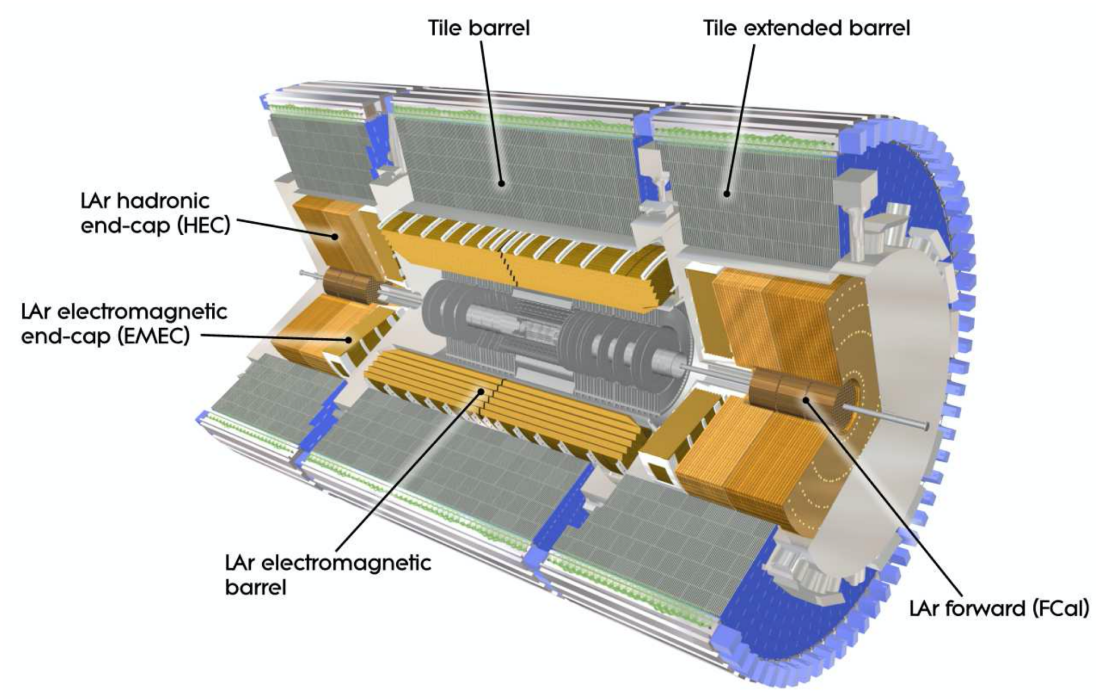


Figure 3.9: A cutaway diagram of the ATLAS sampling calorimeters [5].

Important criteria for the calorimeter are to provide good containment for electromagnetic and hadronic showers and to limit punch-through of particles to the muon spectrometer, so the calorimeter depth must be carefully designed. The geometric size of the calorimeters is determined primarily by the space required to fully stop the particles passing through given the materials used in the calorimeters. The electromagnetic calorimeter material is characterized by the radiation length X_0 , defined as the mean distance a high-energy electron travels through the material before losing all but $1/e$ of its initial energy through bremsstrahlung [23]. The hadronic calorimeter material is analogously characterized by

the interaction length λ , defined as the mean free path of a hadron between inelastic collisions. The total thickness of the EM calorimeter is at least 22 (24) X_0 in the barrel (end-cap) region. The thickness of the active hadronic calorimeter is approximately 9.7 (10) λ in the barrel (end-caps) and approximately 11λ in total, including the additional 1.3λ from the outer support at $\eta = 0$.

3.2.2.1 LAr ELECTROMAGNETIC CALORIMETER

The electromagnetic calorimeter (ECal) is the innermost calorimeter, responsible for precise measurements of electromagnetically interacting particles, particularly electrons and photons. A lead-LAr detector, the ECal uses lead absorber plates with accordion geometry and liquid argon active material. Liquid argon is chosen for its stability of response over time and intrinsic radiation-hardness, and the accordion geometry naturally provides full φ symmetry and coverage, with no azimuthal cracks. The ECal is comprised of a central barrel, covering the pseudorapidity region $|\eta| < 1.475$, and two end-caps, covering the region $1.375 < |\eta| < 3.2$. The barrel is divided into two identical half-barrels, separated by a 4-mm gap at $z = 0$. Each half-barrel measures 3.2 m in length and 2.8 m and 4 m in inner and outer diameter, respectively, and weighs 57 t. The thickness of the barrel increases from $22X_0$ to $30X_0$ between $|\eta| = 0$ and $|\eta| = 0.8$ and from $24X_0$ to $33X_0$ between $|\eta| = 0.8$ and $|\eta| = 1.3$. The end-caps, each 63 cm thick and 27 t in weight, are divided into two coaxial wheels, with the outer wheel covering $1.375 < |\eta| < 2.5$ and the inner wheel covering

$2.5 < |\eta| < 3.2$. The thickness of the end-caps increases from $24X_0$ to $38X_0$ between

$1.475 < |\eta| < 2.5$, corresponding to the outer wheel, and from $26X_0$ to $36X_0$ between

$2.5 < |\eta| < 3.2$, corresponding to the inner wheel.

The precision region ($|\eta| < 2.5$) of the EM calorimeter is segmented in three layers in depth and complemented by a presampler in $|\eta| < 1.8$, a thin active LAr layer of 1.1 (0.5) cm thickness in the barrel (end-caps), used to correct for energy losses by electrons and photons upstream of the electromagnetic calorimeter. The first layer, with a thickness of approximately $4X_0$, has the finest granularity in $\Delta\eta$ to provide good separation between photons and neutral pions. The second layer is the thickest layer, with a thickness of approximately $16X_0$, where most of the electromagnetic shower energy is deposited, and provides good $\eta\varphi$ resolution. The third and final layer is designed to capture high energy particles and separate electromagnetic showers from hadronic ones. The end-cap inner wheel is segmented in two sections in depth, with a coarser granularity than the rest of the calorimeter. Figure 3.10 shows the cumulative radiation lengths for each layer in the electromagnetic calorimeter barrel and end-caps.

3.2.2.2 HADRONIC CALORIMETERS

The hadronic calorimeters consist of the central tile calorimeter with scintillator tiles and steel absorbers over the range $|\eta| < 1.7$, the liquid argon hadronic end-cap calorimeter (HEC) over $1.5 < |\eta| < 3.2$, and the liquid argon forward calorimeter (FCal) with copper or

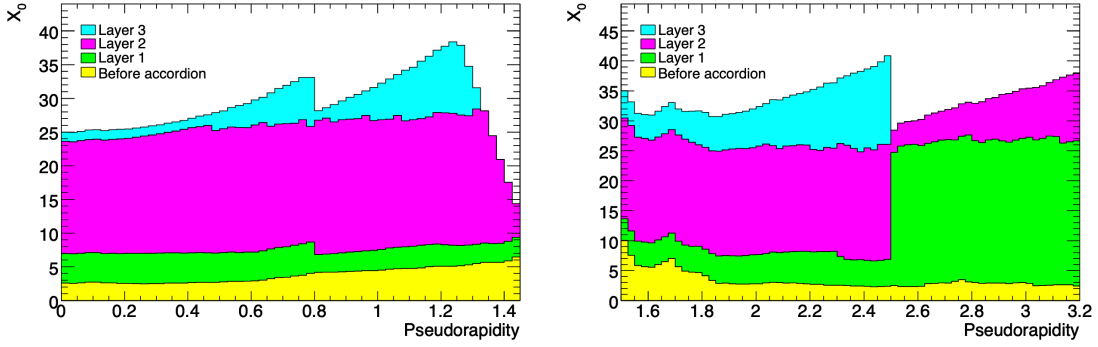


Figure 3.10: Cumulative electromagnetic calorimeter thickness (in radiation length X_0) as a function of $|\eta|$ for each accordion layer and for the material before the accordion in the barrel (left) and end-caps (right) [5].

tungsten absorbers in the region closest to the beam-axis, $3.1 < |\eta| < 4.9$.

The tile calorimeter is a sampling calorimeter using steel as the absorber and scintillating plate tiles as the active material. It is the central hadronic calorimeter, located directly behind the LAr electromagnetic calorimeter, and is comprised of a central barrel, 5.8 m long and covering $|\eta| < 1.0$, and two extended barrels, one on either side of the central barrel, 2.6 m long each, and covering $0.8 < |\eta| < 1.7$. Each barrel region has an inner radius of 2.28 m and an outer radius of 4.25 m and is divided azimuthally into 64 wedge-shaped modules. The tile calorimeter is also then segmented in three layers in depth, with 1.5, 4.1, and 1.8λ thick layers in the barrel and 1.5, 2.5, and 3.3λ thick layers in the extended barrels. The total detector thickness at the outer edge of the tile calorimeter is 9.7λ at $|\eta| = 0$. The detector thicknesses for all hadronic calorimeter layers are shown in Figure 3.II.

The LAr hadronic end-cap calorimeter consists of two independent wheels per end-cap,

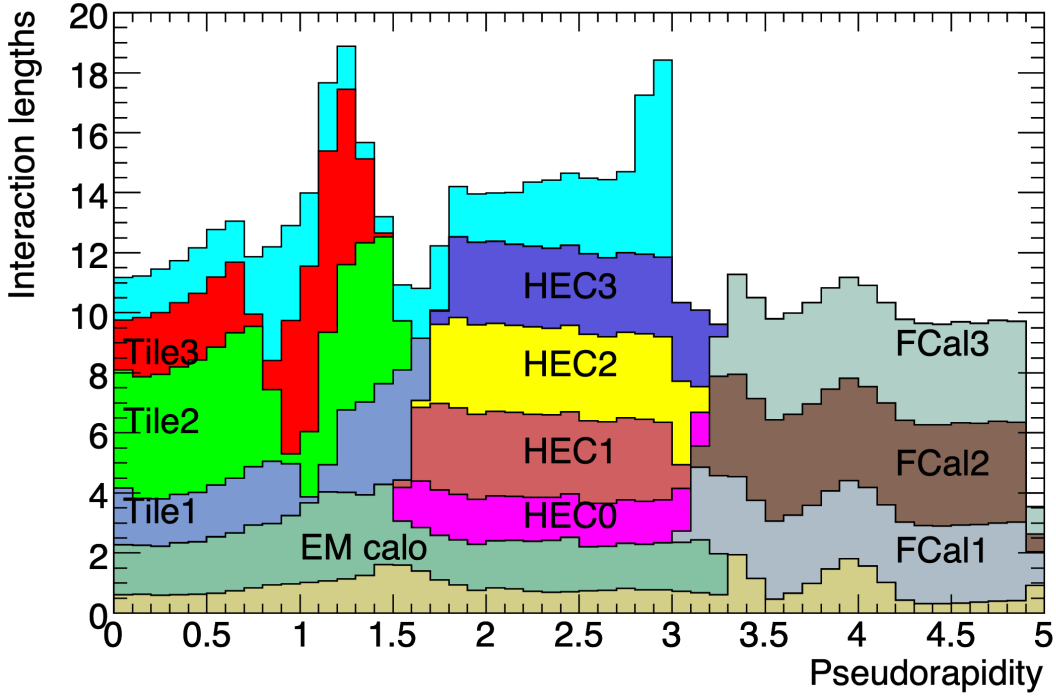


Figure 3.11: Cumulative calorimeter thickness (in interaction length λ) as a function of $|\eta|$ for the region in front of the EM calorimeter, the EM calorimeter itself, each hadronic layer, and the total amount at the end of active calorimetry [5].

which are located directly behind the electromagnetic end-caps. Covering the pseudorapidity $1.5 < |\eta| < 3.2$, the hadronic end-caps overlap slightly with the tile and forward calorimeters, which end at $|\eta| = 1.7$ and begin at $|\eta| = 3.1$, respectively. Each wheel is divided into 32 identical wedge-shaped modules and segmented in two layers in depth, for a total of four layers per end-cap. The inner and outer wheels are made of 25 mm and 50 mm parallel copper absorber plates, respectively, interleaved with 8.5 mm LAr gaps, which serve as the active material. The inner and outer radii of the end-cap wheels are 0.475 m and

2.03 m, respectively.

The LAr forward calorimeter consists of two forward end-caps situated in the end-cap cryostats between the beam-pipe and the HEC wheels. The FCal is located approximately 4.7 m from the interaction point in the z -direction on either side of the detector barrel, and in the range $3.1 < |\eta| < 4.9$, providing coverage in the region closest to the beam-axis. Each end-cap is divided into three modules, with the first layer using copper absorbers optimized for electromagnetic measurements and the second two layers using tungsten absorbers optimized for hadronic measurements. The forward calorimeter is very dense, with a thickness of approximately 10λ over a length of only 1.35 m.

3.2.3 THE MUON SPECTROMETER

The muon spectrometer (MS) surrounds the calorimeter and is the outermost component of the detector, dictating the overall dimensions of the ATLAS detector. Consisting of high-precision tracking chambers, made up of monitored drift tubes (MDT) and cathode strip chambers (CSC), and a dedicated trigger system, provided by resistive plate chambers (RPC) and thin gap chambers (TGC), and sitting within the magnetic field of the surrounding barrel and end-cap superconducting air-core toroid magnets, the MS is designed to capture and measure the muons exiting the calorimeter in the central region. Analogous to the inner detector, the muon spectrometer uses the magnetic fields to bend muon trajectories, from which charge and momentum can be measured based on the curvature of the tracks.

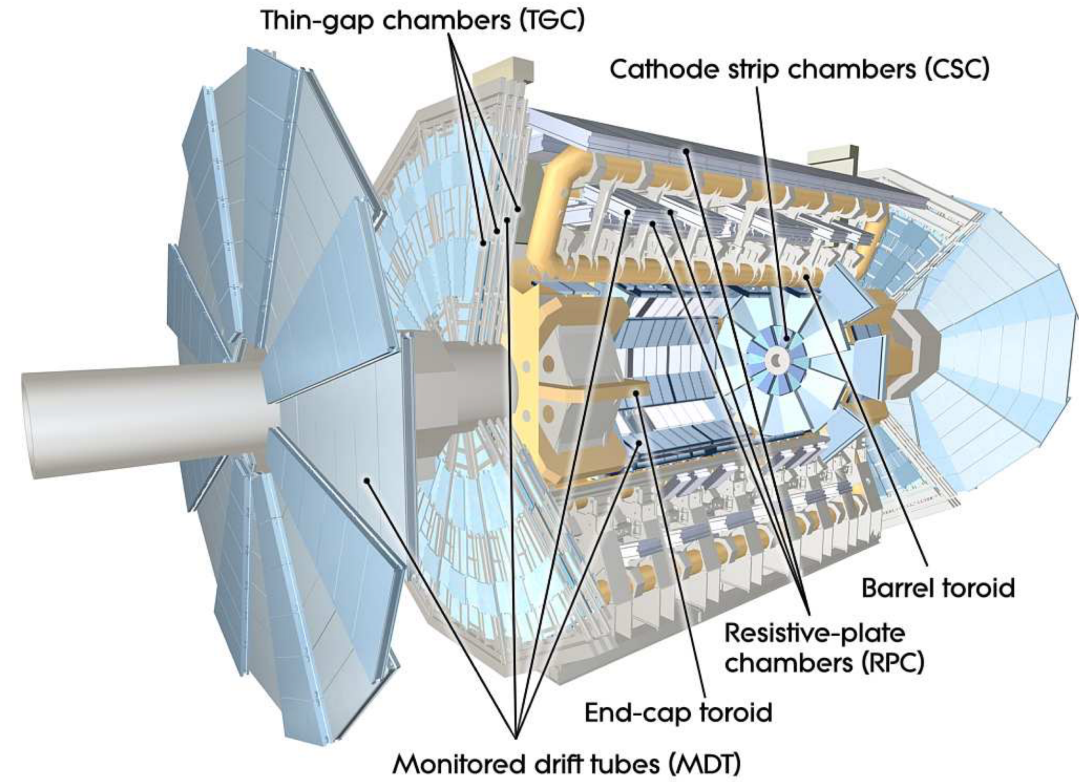


Figure 3.12: A cutaway diagram of the ATLAS muon spectrometer (MS) [5].

Muons are not relevant to the search presented in this thesis, and, therefore, the muon spectrometer is not discussed in more detail here.

3.2.4 THE TRIGGER SYSTEM

Finally, the data is collected with the ATLAS trigger system, designed to select only certain events and reduce the output rate dramatically. With over 100 million detector readout channels, a collision frequency at the LHC of 40 MHz, and a raw event size of over 1.5 MB,

the data recording rate of the ATLAS detector is approximately 60 TB s^{-1} , a rate far too large to process, record, or store. Moreover, only a small fraction of collisions produce events of any interest to analyses, and many signal events being searched for are incredibly rare; therefore, it is essential to carefully and efficiently select a subset of events online that contains the majority of the wide range of interesting physics events while keeping the detector readout at a manageable level. This is achieved with a two-level trigger system [60]. The first-level trigger (Level-1, or L1) is a hardware-based trigger that uses coarse granularity muon detector and calorimeter information to quickly make trigger decisions and reduce the rate from 40 MHz to around 100 kHz. These events are then passed to the High-Level Trigger (HLT), a software-based trigger that uses more sophisticated selection algorithms and the full detector information to determine which events to ultimately store and further reduces the acceptance rate to about 1 kHz. The two-level trigger together with the data acquisition system (TDAQ) is shown schematically in Figure 3.13.

3.2.4.1 LEVEL-1 (L1) TRIGGER

The L1 trigger performs the initial event selection online using limited information from a subset of the total detector, namely the muon spectrometer and the calorimeter, to make a decision in less 2.5 ms, reducing the event rate to 100 kHz. Using coarse granularity readout from the RPC and TGC trigger chambers in the muon spectrometer and from all of the calorimeters, the L1 trigger applies a fast, simplified reconstruction algorithm to define

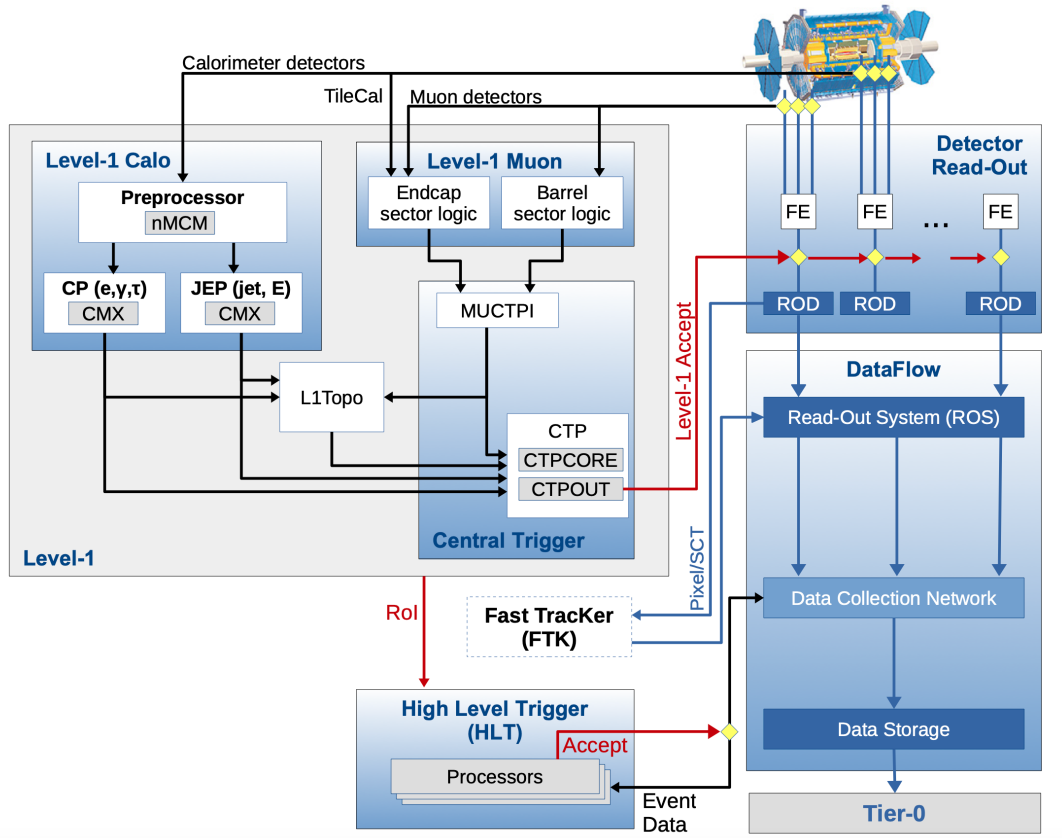


Figure 3.13: ATLAS Trigger and Data Acquisition (TDAQ) System [61].

Regions-of-Interest (RoIs) in the detector where high transverse energy (E_T) objects are identified. Regions of Interest are geographical coordinates in η and ϕ within the detector where relevant signatures exceed certain energy thresholds. The ROI data, including the type of feature identified and the criteria passed, i.e. the particle multiplicity or the energy or momentum threshold, is subsequently used by the HLT.

The Level-1 Calorimeter (L1Calo) trigger uses data from approximately 7200 trigger towers of granularity 0.1×0.1 in $\eta \times \phi$ from the electromagnetic and hadronic calorimeters

to identify and trigger on objects other than muons, including jets [62]. For jet finding, jet trigger elements are defined using 2×2 trigger towers, and a jet sliding window algorithm is applied to sum transverse energies from electromagnetic and hadronic trigger towers and identify local E_T maxima within overlapping windows of 2×2 , 3×3 , or 4×4 jet elements, depending on the desired jet multiplicity. If the window contains an E_T sum exceeding some predefined threshold and surrounds a 2×2 trigger core that is a local maximum, the window is considered an L1 jet RoI, with the location of the local maximum defining the RoI coordinates and the sum- E_T of the window defining the L1 jet energy, and is passed to the HLT. The jet multiplicities and energy thresholds the jet windows are compared against are defined in the Trigger Menu, which specifies the combination of trigger selections to apply during data-taking in order to save processes of interest for various analyses. For jet signatures, these selections include single high- E_T jets or multijets with lower energy thresholds.

3.2.4.2 HIGH-LEVEL (HLT) TRIGGER

The events accepted by the L1 trigger are then processed by the HLT, which runs offline-like reconstruction algorithms using full granularity information from the calorimeters and muon spectrometer, as well tracking information from the inner detector, on a dedicated computer farm outside the detector, reducing the final rate to approximately 1 kHz. Seeded by the RoI information from the L1 trigger, the HLT first makes a rough pass at re-

constructing objects inside the RoI to further refine the trigger selection and then applies more complex reconstruction techniques, similar to those used in offline analysis, to all regions of the detector at full granularity and precision.

Jets are reconstructed in the HLT using data from the full calorimeter and the same topological cell clustering algorithm used for offline jet reconstruction, which is detailed in Section 3.4.3. Jet energies calculated from the sum of the constituent momenta are then calibrated in a manner analogous to offline jet calibration, but without track and vertex information, resulting in HLT jet energies in very good agreement with offline jets and thus very efficient HLT jet triggers.

HLT decisions are made within about 200 ms, and accepted events are written to disk and fully reconstructed offline. Raw data from selected events are then divided into data streams, with `physics_Main` containing events used for physics analysis, and saved in `RAW` format to Tier-0, where they are fully reconstructed. Tier-0, or the CERN Data Center, is the first level of the Worldwide LHC Computing Grid (WLCG), a four-tier global collaboration of computer centers that stores, distributes, and analyzes the LHC data. The ATLAS Distributed Computing (ADC) system manages the data recorded by the ATLAS detector [63]. Data reconstruction and post-processing for offline analysis is performed with the ATLAS common software framework, `Athena`.

3.3 SIMULATION OF COLLISION EVENTS

Analyses performed at ATLAS rely on the use of simulated data samples to model the detector response to the signal and background processes of interest in order to optimize signal region definitions and estimate analysis sensitivities, to predict SM backgrounds, to estimate reconstruction efficiencies and systematic uncertainties, and to compare experimental results to theoretical predictions. Before a search can be performed on ATLAS data, Monte Carlo (MC) samples must be produced through a detailed ATLAS software simulation chain [64] to carry out the necessary studies. The simulation chain is integrated into the ATLAS software framework, Athena [65]. It begins with Monte Carlo event generation, performed by any number of external generators; then, detector simulation is performed with the GEANT4 simulation toolkit [66, 67]. The simulation chain generates and saves truth information, simulates hard scatter and pileup events and models the detector response to a wide range of signal and background physics processes, and produces output in the same format as the actual detector data.

The simulation chain proceeds through the following series of independent steps, each of which is summarized in the corresponding subsection below:

1. event generation of pp collision events and their immediate decays for the process of interest (see Section 3.3.1);
2. core simulation of the detector geometry and its response to the produced particles (see Section 3.3.2);

3. digitization of the energy deposited in the detector's sensitive regions to be comparable to the ATLAS detector readout (see Section 3.3.3).

These simulation steps are then followed by the reconstruction of the simulated events using the same algorithms as those applied for real collision data. Reconstruction at ATLAS is described in Section 3.4.

The full simulation chain and the flow of data throughout is illustrated in Figure 3.14.

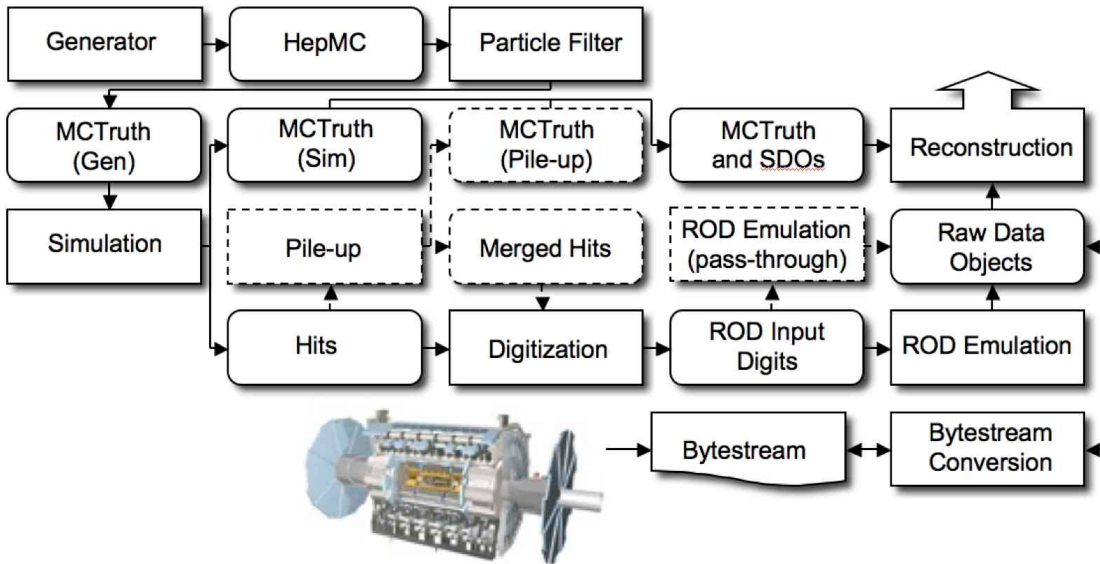


Figure 3.14: The flow of the simulation software chain at ATLAS, beginning with event generation and ending with reconstruction [64]. Rectangular boxes indicate simulation algorithms, and rounded boxes indicate the persistent data objects output by the various algorithms throughout the chain.

A fast simulation chain is also available to be used in place of the standard full simulation, which is slow and CPU-intensive due to the complex detector geometry and detailed physics descriptions that require large computing resources. In some cases, these comput-

ing resources can even be too large to simulate the necessary statistics, necessitating a faster, more efficient simulation chain. This fast simulation chain is summarized in Section [3.3.4](#).

It is also important to validate each step of the simulation chain over the course of continuous software developments and detector upgrades. For this purpose, the `HitAnalysis` and `RDOAnalysis` packages have been developed as validation tools to test the output of the core simulation and digitization jobs, respectively, and to validate the fast chain against the standard simulation and digitization algorithms. A detailed description of the `RDOAnalysis` package and its development can be found in Appendix [A](#).

3.3.1 EVENT GENERATION

Event generation is the simulation of a large number of high-energy collision events with particular final states, consisting of a list of particles and their momenta. The events are generated with a probability approximately proportional to the probability of producing the corresponding events in the real world. Event generation uses the Monte Carlo method of numerical integration with pseudorandom numbers [68] to predict scattering cross sections and simulate events for a given hard scatter process. The overall event generation step is typically partitioned into simulations of the following subprocesses [69–71]:

- the hard scatter (HS) process → constituents of colliding protons, or partons, interact at high momentum to produce outgoing fundamental particles, like SM quarks and leptons or BSM particles, according to matrix element calculations;

- parton showering → color-charged particles involved in the collision radiate virtual gluons and quark-antiquark pairs, which can emit colored particles themselves, resulting in a cascade, or shower, of partons;
- hadronization → as partons lose energy during showering and eventually fall below a certain momentum scale, they become bound into colorless final-state hadrons;
- the underlying event (UE) → some component of the final state exists that is not associated with the primary hard scatter process but rather with the secondary interactions between the other constituent partons of the incoming protons;
- unstable particle decays → many of the produced hadrons are unstable heavy resonances that decay.

The event generation step produces events in the HepMC format [72] that can be used as input to the detector simulation step. Such events contain generator, or MC truth, information, which is essentially a history of generator-level interactions, with each event containing the incoming and outgoing particles from a single interaction with the vertex at the geometric origin. At ATLAS, the event generation is run within Athena using external generators and ATLAS-specific MC generator tunes [73], which define sets of tuned parameters for optimally modeling parton showers, hadronization, and multiple interactions at ATLAS. Generator-level filtering can also be applied to only generate events passing certain selection criteria in order to increase statistics in a particular region of phase space for the given process.

3.3.1.1 HARD SCATTER

Event generation begins with the simulation of the hard scatter process from the high-energy collision of the constituents of the incoming protons via a Monte Carlo generator, using Parton Distribution Functions (PDFs) to describe the incoming partons, and leading order (LO) perturbation theory to describe the probability distribution of the final state partons.

A Parton Distribution Function represents the probability density for finding a given type of parton of a certain momentum fraction within the proton at a particular energy scale. PDFs are used as external inputs to event generators in order to describe the proton substructure and to determine the properties of the colliding partons, including the estimated proton momentum fraction they carry. PDF sets are determined from experimental measurements, where they are measured at low energies in some generic processes and then evolved to higher scales using the QCD evolution equations for parton densities [74, 75]. ATLAS provides a large repository of potential PDFs produced by several different groups to be used in event generation through the Les Houches Accord PDF Interface (LHAPDF) library [76, 77]. Depending on the particular PDF set used, the specifics of the event generation will vary.

Matrix elements calculated from perturbation theory are used to compute the cross sections of the hard scatter processes and to describe the probabilities of producing particular

final states with certain kinematics from given initial states. The generator produces the the specified final state for each collision according to the matrix element of the given hard scatter process.

3.3.1.2 PARTON SHOWERING

The next step in event generation is the parton shower simulation, which represents higher-order QCD corrections to the hard scatter process due to gluon radiation. Accelerating partons in the hard process emit QCD radiation in the form of gluons, which carry color-charge themselves and therefore emit further radiation, resulting in a cascade of partons produced by both initial-state radiation (ISR) from the incoming color-charged particles and final-state radiation (FSR) from the outgoing color-charged particles in the collision. The parton shower is simulated probabilistically as a sequential evolution to lower and lower momentum scales, starting from the high momentum scale of the hard process and ending with the low momentum scale associated with confinement, where perturbation theory breaks down and the hadronization model takes over.

3.3.1.3 HADRONIZATION

The particles produced in the parton shower then undergo hadronization, where the description of the way the partons are confined into final-state colorless hadrons is modeled. Hadronization is indescribable by perturbative QCD since the energy scale where it occurs

is too low. The running QCD coupling increases at low momentum, so at some point in the parton showering, perturbation theory becomes invalid and parton dynamics enter a non-perturbative regime, where the formation of the observed final-state hadrons takes place. Hadronization thus must be modeled by event generators using approximations based on the general features of QCD.

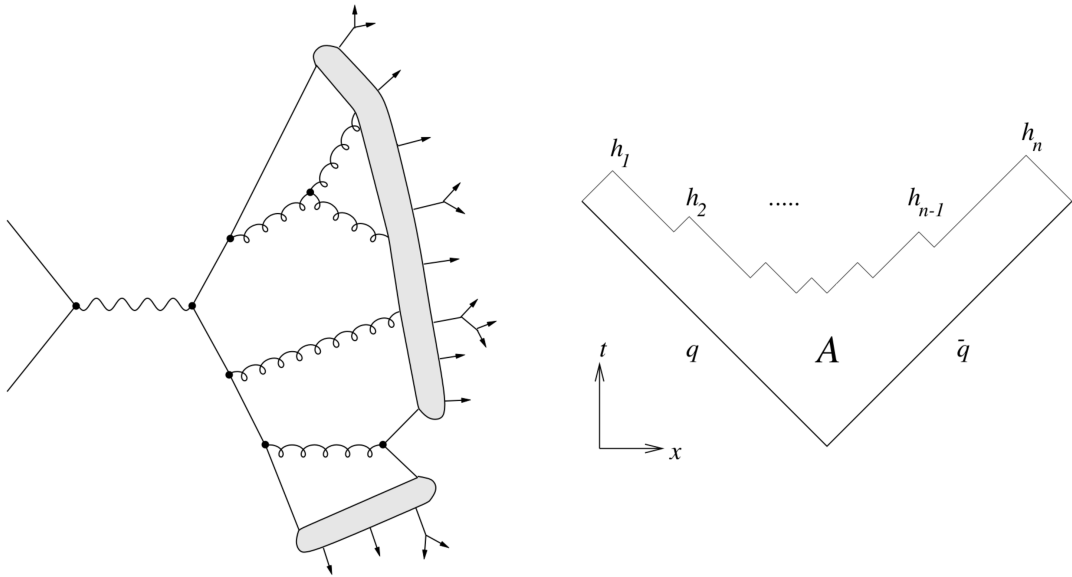


Figure 3.15: Schematics illustrating the string model of hadronization [71] for a generic case (left) and for the simplest case of quark-antiquark pair production in space-time coordinates (right).

There are two main hadronization model classes currently used by event generators: string and cluster. The Lund string model [78, 79] is the hadronization model implemented in Pythia [80, 81], the event generator used in this analysis and described in more detail in Section 4.2.2. Such a string model is based on the observation from lattice sim-

ulations of QCD that at large distances the potential energy between color charges increases linearly with their separation. Gluon field lines then collapse into tubelike regions, or strings, as color charges move apart. These strings stretch and eventually break, or fragment, into new color-charged particles, forming hadrons, as illustrated in Figure 3.15.

3.3.1.4 UNDERLYING EVENT

At this point, the event contains final state particles from the hard process and the subsequent parton showering and hadronization only, and the underlying event and pileup still need to be simulated. The underlying event contains any extra hadronic production due to interactions from partons not participating in the hard scatter process, particularly from multiple parton interactions, the effects of which are simulated by the event generator. In-time and out-of-time pileup effects are included by overlaying additional simulated minimum-bias collision events onto the already generated hard scatter events. These events are generated at the event generation step and overlaid during the digitization step.

3.3.1.5 UNSTABLE DECAY

The final step in event generation is the sequential decay of any unstable particles produced in hadronization. The generator handles prompt decays for particles with proper lifetime $c\tau$ shorter than some default value and stores “generator stable” particles with proper life-time $c\tau$ longer than the default value to be used as inputs to the detector simulation step.

In ATLAS, the default $c\tau$ limit is 10 mm, as particles with larger proper lifetimes are expected to propagate far enough through the detector to interact with the material before decaying. These particles' decays are handled by the detector simulation, while the generator unstable particles, with $c\tau < 10$ mm, are decayed by the event generator, and their detector interactions are ignored.

3.3.2 DETECTOR SIMULATION

Detector simulation, also known as core or **GEANT4** (**G4**) simulation, is the simulation of the response of the detector to the particles produced in the event generation step. Final-state particles output from event generation are propagated through a simulated version of the full ATLAS detector by the **GEANT4** program, which simulates a detailed detector geometry to model the particle interactions with the detector components, materials, and magnetic fields using MC techniques. Energies deposited in sensitive regions of the detector are recorded as “hits”, where a hit provides a record of the total energy deposition, position, and time of the particle interacting with the detector. This information is then written to the simulation output file, or **HITS** file, which contains metadata describing the run configuration, truth information, and the collection of hits for each subdetector. The truth information includes a copy of the MC truth record produced by the event generator, as well as truth tracks and decays from secondary interactions of interest that occur in the detector simulation step. Particle trajectories in the detector and through the magnetic field are mod-

eled using small steps, with possible interactions with the material, like energy loss or new particle production, being considered at each step. These steps continue until particles lose all energy, convert to other particles, or exit the detector.

3.3.3 DIGITIZATION

The digitization step converts hits from the detector simulation into detector responses, or “digits”, which represent digital signals like voltages, currents, and times that act as inputs to the read out drivers (RODs) of the detector electronics. A digit is typically produced when the signal on a particular ROD surpasses a particular threshold within a certain time-window. The digitization job then simulates the ROD electronics and outputs a Raw Data Object (RDO) file in a format comparable, and easily convertible, to the “bytestream” format of the actual detector readout. Digitization also produces Simulated Data Objects (SDOs), which contain simulation truth information about the particles and noise responsible for the digital signals found in a given detector region. Since the detector responses depend on electronics and readout channels that vary between sub-detectors, a separate digitization algorithm exists for each sub-detector. The output from the digitization step is then used in reconstruction.

The digitization step is also where the pileup interactions are included. Pre-simulated hits from inelastic scattering events, including minimum bias, cavern background, beam gas, and beam halo events, are overlaid on top of the hits from the hard scatter process be-

fore the energy deposits are converted into detector readout signals in order to simulate pileup [82].

3.3.4 FAST CHAIN

In order to estimate systematics, model backgrounds, and study rare signal processes with small cross sections, simulated MC datasets are required to be large, detailed, and precise, which is quite CPU-intensive, particularly with the increased luminosity and corresponding increased MC statistics needs at ATLAS Run 2. The largest fraction of the computing time required for simulation is spent on the exhaustive **GEANT4** detector simulation, but with detailed digitization and track reconstruction algorithms also eating up a lot of resources, reduction of the CPU consumption is actually required at every step in the simulation chain. Therefore, fast algorithms for the detector simulation, digitization, and reconstruction steps have been developed, which can be combined together in various ways to define multiple fast simulation chain configurations [83–85].

3.3.4.1 FAST SIMULATION

Multiple fast simulation algorithms are designed to speed up different parts of the detector simulation and are combined into different fast simulation strategies of varying speed and accuracy. Fast simulation is performed with one or more of the following fast simulation tools:

- Frozen showers: pre-simulated particle showers in the calorimeter;
- FastCaloSim: parameterized calorimeter simulation;
- Fatras: fast track simulation;

which are combined into the following fast simulation strategies, listed in order of increasing speed and decreasing accuracy:

1. Fast G₄ Simulation: GEANT₄ with frozen showers;
2. Atlfast-II: FastCaloSim;
3. Atlfast-IIF: FastCaloSim + Fatras.

Frozen showers are designed to speed up the slowest part of full GEANT₄ simulation, the simulation of electromagnetic particle showers in the calorimeters, by replacing low-energy electromagnetic particles with pre-simulated frozen showers from a stored library produced at an earlier time with full simulation. This tool is used in the Fast G₄ setup, which implements full GEANT₄ simulation in the inner detector and muon spectrometer and frozen showers in the calorimeter, resulting in a factor of three CPU-time reduction over full simulation. The frozen showers method is also used as the default in the forward electromagnetic calorimeters.

The Fast calorimeter Simulation (FastCaloSim) [86, 87] tool approximates the calorimeter simulation with a parametrization of the calorimeter cell response and energy distribution based on fully simulated single particle showers in a fine grid of particle energies and

directions in order to reproduce the longitudinal and lateral shower profiles. Charged pions are used to parametrize the hadronic showers, and e/γ 's are used to parametrize the electromagnetic showers. The parameterizations of these single particle shower energy profiles are then used to directly deposit energy onto the calorimeter cells rather than generating particle showers from simulating the particle interactions with the detector material. This method simulates the total particle energy response and models the full longitudinal properties of the shower, including the fluctuations and corrections, but only models the average lateral shape. A simplified detector description, the same as that used in reconstruction, is also implemented with FastCaloSim. This tool is used in the Atlfast-II setup, which implements full GEANT4 simulation in the inner detector and muon spectrometer and FastCaloSim in the calorimeter, as illustrated in Figure 3.16, resulting in a factor of ten CPU-time reduction over full simulation, from several minutes to a few seconds per event. The output of the FastCaloSim algorithm is the energies deposited in the calorimeter cells, which can be input directly to standard reconstruction.

The Fast ATLAS Tracking Simulation (Fatras) [88, 89] is based on the software and simplified geometry of standard track reconstruction, describing the detector with thin layers, instead of volumes, on which the detector volume material properties are projected. The tool also uses the same extrapolation tools as in reconstruction and simulates the interactions of the particles with the detector material using a parametric model pulled from

GEANT4. Fatras is used in the Atlfast-II setup, which implements Fatras in the inner detector and muon spectrometer and FastCaloSim in the calorimeter, resulting in a factor of nearly 100 CPU-time reduction over full simulation. The tool outputs hits in the inner detector and muon spectrometer, which standard reconstruction can readily run over.

The above fast simulation techniques can be combined, with each other or with full simulation, within a single event into various simulation strategies through the use of the Integrated Simulation Framework (ISF) [84]. For many analyses, high-precision, and thus time-consuming, simulation is only required for certain particles or detector regions. Therefore, the ISF is designed to enable flexible combinations of different simulation strategies in the same job in order to accommodate all possible needs and uses. The relative CPU timing of a few different simulation strategies are illustrated in Figure 3.16.

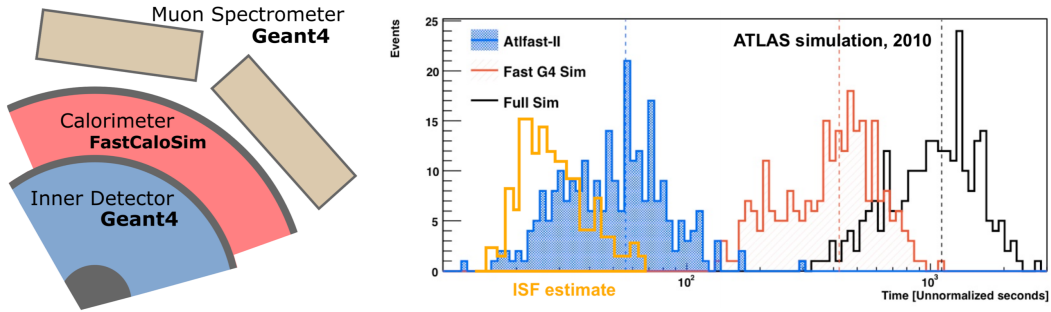


Figure 3.16: Left: schematic of the Atlfast-II fast simulation setup, with FastCaloSim used for the calorimeter simulation and Geant4 simulation used for the rest of the detector components [83]. Right: comparison of the CPU time between simulating $t\bar{t}$ events with full simulation (black), Fast G4 simulation (red), and Atlfast-II (blue) [84]. The estimated ISF timing is overlaid in yellow.

3.3.4.2 FAST DIGITIZATION

Most, about fifty percent, of the time spent on the digitization is spent on digitizing information within the inner detector because of its very high hit density. Therefore, dedicated fast Pixel, SCT, and TRT algorithms have been developed as alternatives to the corresponding standard digitization algorithms. These fast digitization algorithms are parametrized in such a way as to skip the detailed emulation of the detector readout effects performed in standard digitization. The output format of the fast digitization step is a Prep Raw Data (PRD) file, rather than an RDO.

The fast silicon Pixel and SCT algorithms project the simulated particle path length onto the readout surface, correcting for Lorentz angle drifts and smearing to account for multiple scatterings, in order to estimate the charge deposition in each readout channel. Clusters are formed directly from track information, skipping the time-consuming cluster-finding algorithms of standard digitization.

The fast TRT algorithm evaluates the radius of closest approach of the simulated hits and smears the hit position to account for the measurement uncertainty in order to estimate the drift radius, which is used in reconstruction. Additionally, the transition radiation is parametrized to allow for particle identification.

The fast digitization methods for both the silicon detectors and the TRT are illustrated schematically in Figure 3.17.

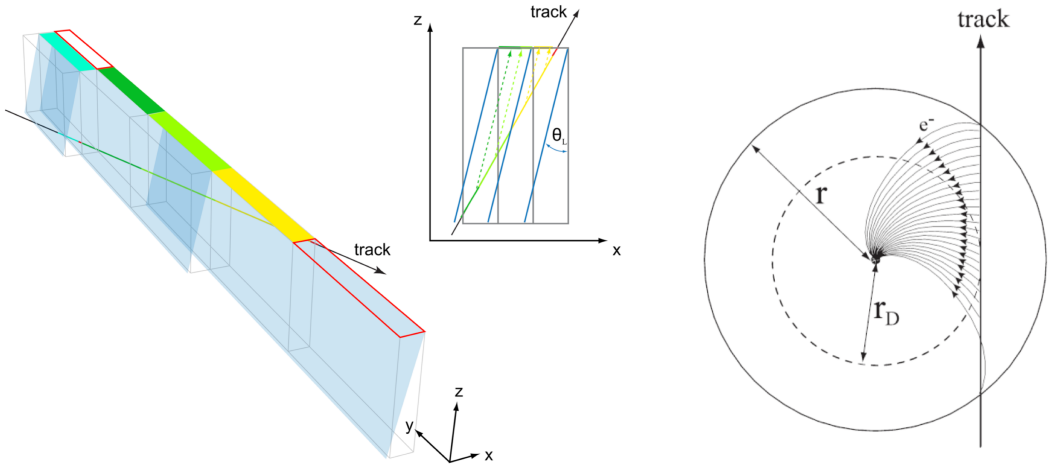


Figure 3.17: Schematics illustrating the fast digitization methods for the silicon detectors (left) and for the TRT (right) [83].

3.3.4.3 FAST RECONSTRUCTION

Like standard digitization, the inner detector is the main consumer of resources during standard reconstruction, as the combinatorial nature of track reconstruction grows in complexity with high pileup, leading to an exponential increase in the reconstruction time. To mitigate this effect, a fast reconstruction algorithm, known as truth-assisted reconstruction, can be implemented in the inner detector. Truth-assisted reconstruction uses MC generator information to emulate the effects of the default reconstruction algorithm. Instead of performing the usual standard tracking steps of pattern recognition, track seeding, and ambiguity solving, the fast track reconstruction uses truth information on simulated hits to directly assign these hits to each track and to fit the particle trajectories. Similar selection cri-

teria as in standard reconstruction are applied to the tracks in order to mimic the effects of the skipped steps. This fast track reconstruction is only applied to pileup tracks to maintain efficiency for signal events.

3.4 RECONSTRUCTION OF COLLISION EVENTS

Event reconstruction is the combination and conversion of digitized detector readout signals from various detector elements into identifiable physics objects produced in the $p\bar{p}$ collision. Reconstructed physics objects include tracks, vertices, calorimeter clusters, missing transverse energy, and particle objects, i.e. electrons, photons, muons, taus, and jets.

Standard reconstruction at ATLAS proceeds through the following independent steps:

1. hit identification and intermediate object formation;
2. physical particle property measurements;
3. particle identification.

Reconstruction begins with the identification of hits and the formation of intermediate objects, such as tracks, vertices, and clusters, from digital signals. The next step is the measurement of physical properties, like charge, momentum, and energy, of the incident particles using particle-like signatures formed from the intermediate objects, i.e. particle trajectories from multiple tracks. Tracking, or track reconstruction, involves the identification of charged particle tracks and the measurement of their momenta through pattern recognition and track fitting algorithms. Vertexing is the reconstruction of the vertices where

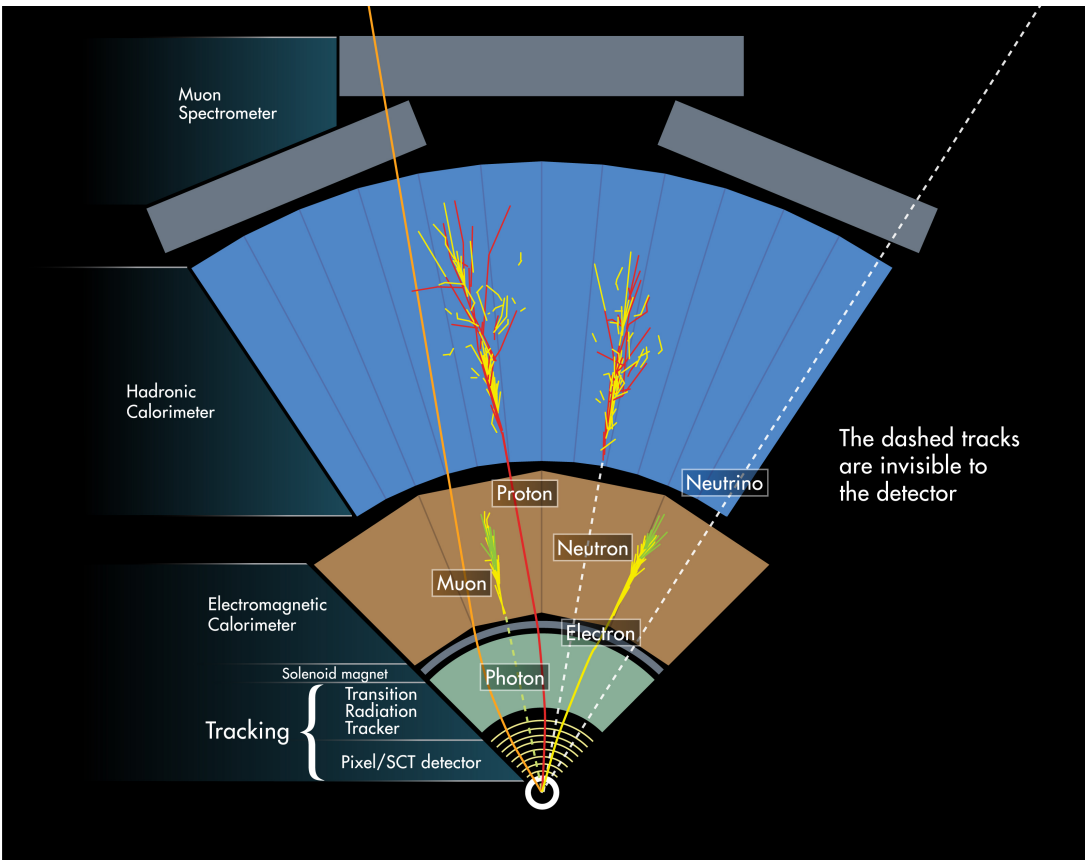


Figure 3.18: Schematic showing the various Standard Model particle signatures throughout the ATLAS detector components [90]

tracks originate. Calorimeter clustering, or calo-clustering, is used in jet and missing energy reconstruction and entails combining the energy deposits in the calorimeter cells into clusters using a topological clustering algorithm. These reconstruction algorithms are discussed in more detail in the following sections. Finally, particle identification is achieved through dedicated algorithms that combine signatures from different parts of the detector in order to classify specific particle objects, as illustrated in Figure 3.18. Electrons and photons are

identified by requiring energy deposited in the electromagnetic calorimeter in conjunction with either a track or the absence of a track, for electrons and photons, respectively. Muon identification is achieved by finding complementary tracks in the inner detector and muon spectrometer. Jets are identified by large energy deposits in the hadronic calorimeter, resulting from strong particles inducing hadronic showers in the HCal. Missing transverse energy (MET) is the result of invisible particles escaping the detector and can therefore be determined as the difference from zero of the total measured momentum in the transverse plane.

Additional nonstandard reconstruction algorithms developed specifically for long-lived particle searches are also available at ATLAS. Standard tracking is designed to reconstruct primary particles, or prompt tracks originating from the interaction point, and is thus optimized for tracks with small impact parameters ($|d_0| < 10$ mm). In turn, standard reconstruction provides very low efficiency for tracks with large impact parameters and for secondary vertices with large displacements from the IP, characteristic of long-lived particle signatures. Special algorithms optimized for reconstructing long-lived particles can then be used in addition to standard reconstruction to recover these displaced tracks and vertices. The dedicated RPVLL reconstruction setup, developed for R-parity violating and long-lived particle analyses, consists of a large- d_0 tracking algorithm and a secondary vertex reconstruction algorithm run on top of standard reconstruction.

The large- d_{o} or large-radius tracking algorithm is an additional tracking pass that targets tracks with large displacements that have been overlooked by standard tracking. This specialized tracking pass is run after standard tracking in order to recover efficiency for tracks produced in LLP decays and not pointing back to the IP. The secondary or displaced vertexing algorithm runs after the additional specialized tracking algorithm and uses the combined collection of standard and large-radius tracks to reconstruct vertices produced far from the IP.

Such a setup is quite computationally expensive, so these additional algorithms are only applied to a filtered subset of the data using a dedicated RPVLL stream. Events are filtered based on a set of RPVLL-analysis-specific triggers and loose object selections. The RPVLL filtering stream is discussed in more detail in Section [4.2.1.1.1](#) and in Appendix [B](#). As these algorithms are run over the filtered events after the standard reconstruction is applied, they are often referred to as “re-tracking” and “re-vertexing” and collectively as “re-reconstruction”.

Only jets, inner detector tracks and vertices, and nonstandard reconstruction objects, i.e. displaced tracks and vertices, are relevant to the this analysis and discussed further.

3.4.1 INNER DETECTOR TRACK RECONSTRUCTION

Inner detector tracking, the identification of charged particle tracks and the determination of charged particle momenta, is the first step in reconstruction, since ID tracks are used as

inputs in many other particle object reconstruction algorithms. Track reconstruction in the inner detector uses pattern recognition and track fitting algorithms to combine individual hits into reconstructed tracks, where pattern recognition algorithms identify common measurements among hits stemming from the same charged particle, and fitting algorithms use identified measurements to estimate the particle tracks. Since MS tracks are not relevant to the Emerging Jets search, MS tracking is not discussed in this thesis, and any further references to tracks, tracking, or track reconstruction indicate those of the inner detector, unless otherwise specified.

Reconstructed tracks parametrize the trajectories of charged particles moving through a magnetic field. A track is formed by a charged particle depositing energy in the tracking detector in the form of ionization. Multiple tracks can then be clustered together to find a common vertex or to identify particle objects through association with energy deposits in the calorimeter.

A charged particle moving through a constant homogeneous magnetic field follows a helical trajectory, as is the case in the ATLAS inner detector, where a solenoidal magnetic field constant in z is applied [23]. In the transverse plane, this trajectory appears as a circle, with the transverse momentum of the particle determinable from the radius R of the circle as follows:

$$R = \frac{p_T}{qB} = \frac{p_T}{0.3B}, \quad (3.6)$$

where R is the radius of curvature of the particle path in the transverse plane, p_T is the component of the particle momentum transverse to the magnetic field, B is the magnetic field strength, and q is the particle charge. The equivalency expressed above is valid when using natural units and when considering R in meters, p_T in GeV, and B in Tesla.

For high- p_T particles, the radius of curvature of its trajectory is too large to be measured directly, as the particle leaves the inner detector before completing a full circle in the transverse plane. Instead, the radius of curvature is measured from the arc of the particle trajectory, which can be constructed from a few points along the track in the transverse plane. The radius of the full circle is thus redefined in terms of the base length L and sagitta s of the arc in order to recover the particle momentum, as illustrated in Figure 3.19:

$$R \approx \frac{L^2}{8s} \quad \rightarrow \quad p_T = 0.3B \frac{L^2}{8s}, \quad (3.7)$$

where L is the length of the base of the arc, or the straight path length between the outermost track points, and s is the sagitta, or the distance from the center of the arc to the center of the base, both measured in meters.

The momentum resolution degrades linearly with the transverse momentum, as particles with higher momenta bend less in magnetic fields:

$$\frac{\sigma p_T}{p_T} = \frac{8p_T}{0.3BL^2} \sigma(s) \quad (3.8)$$

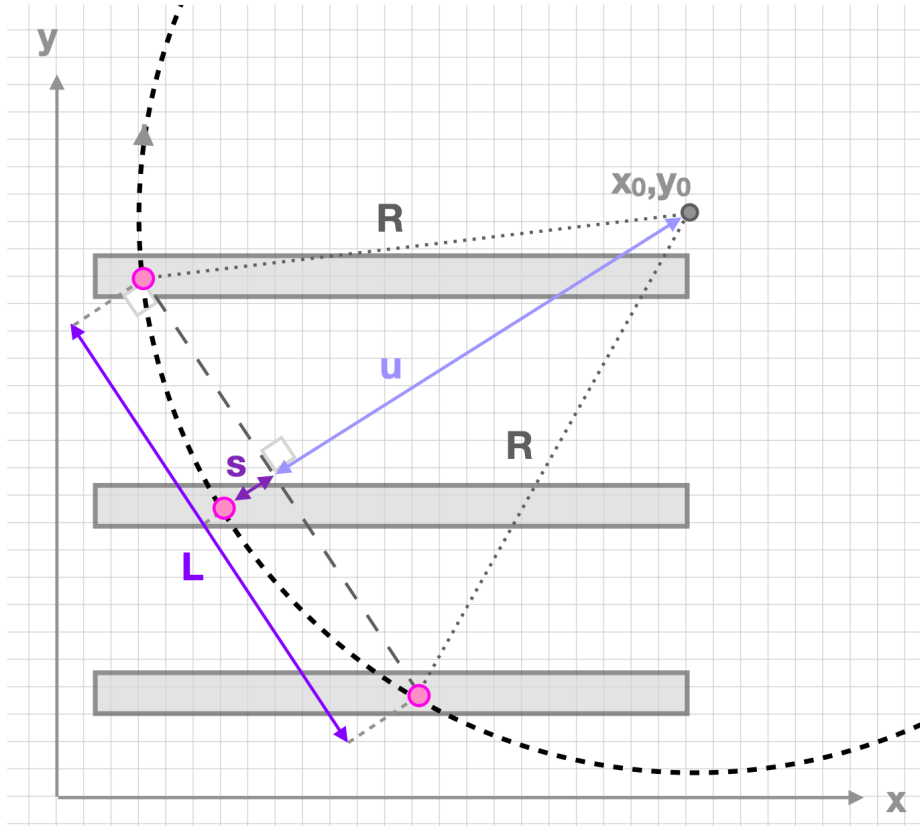


Figure 3.19: Cartoon illustrating a track in the transverse plane interacting with three detector layers to form an arc with sagitta s and base length L . The arc belongs to the circle of radius R formed in the transverse plane by the charged particle's helical trajectory, with its center at (x_o, y_o) [91].

A longer base length thus improves the momentum resolution, which partially motivates

the design of the tracker, particularly the large volume of the TRT.

A reconstructed track is parametrized by five variables describing the charge, momentum, and position of the particle at any given point along the trajectory. These five track parameters are expressed with respect to the perigee, or the point of the track's closest approach to

the beam line in the transverse plane:

$$\text{track} = (q/p, \vartheta, \varphi, d_o, z_o), \quad (3.9)$$

where q/p is the ratio of the track charge to the track momentum magnitude; ϑ is the polar angle of the track momentum, or the angle between the track momentum and the beam axis; φ is the azimuthal angle of the track momentum, or the angle between the track momentum projected in the transverse plane and the x -axis; d_o is the transverse impact parameter, or the radial distance from the perigee to the beam line, representing the point of closest approach in the transverse plane; and z_o is the longitudinal impact parameter, or the longitudinal distance from the perigee to the beam spot, representing the distance along the beam line to the point of closest approach defined by d_o . The track parameterization in the perigee representation just described is illustrated in Figure 3.20.

Standard track reconstruction is optimized for particles originating from the interaction point and thus for tracks with small impact parameters. Strict transverse and longitudinal impact parameter cuts of $|d_o| < 10$ mm and $|z_o| < 250$ mm are therefore imposed on standard tracks to reconstruct primary particles with high efficiency and reasonably low computational resources. These cuts are inefficient for LLP searches, which require reconstruction of tracks that stem from particles with lifetimes of order millimeters to centimeters and are thus largely displaced from the primary vertex. For LLPs, then, standard tracking

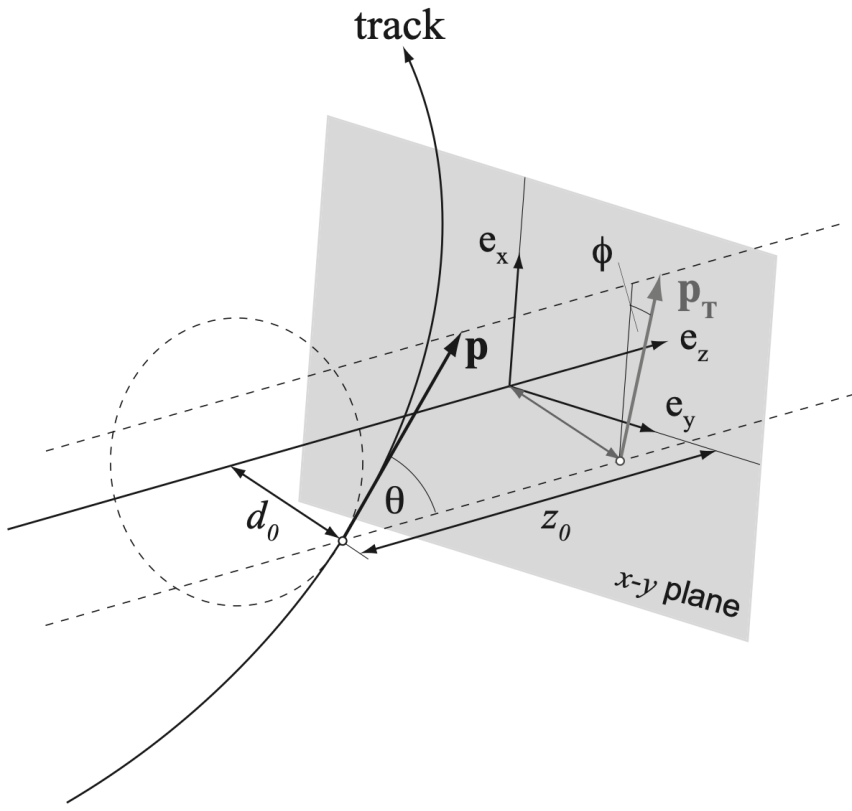


Figure 3.20: Illustration of the perigee representation of the ATLAS track parametrization. The track's point of closest approach to the beam line is given by the signed transverse impact parameter, d_0 , and longitudinal impact parameter, z_0 , and the direction of its momentum is expressed in terms of the azimuthal angle, ϕ , projected in the $x - y$ plane, and the polar angle, ϑ , measured with respect to the z -axis [92]

is followed by an additional tracking pass with loosened impact parameter cuts of $|d_0| < 300$ mm and $|z_0| < 1500$ mm dedicated to reconstructing large-radius tracks, known as Large Radius Tracking (LRT) [93], to recover sensitivity to such highly displaced tracks with large impact parameters.

3.4.1.1 STANDARD TRACKING

Standard tracking reconstructs prompt tracks with $p_T > 500$ MeV using pattern recognition and track fitting algorithms in two consecutive steps, or passes: inside-out and outside-in [94].

3.4.1.1.1 INSIDE-OUT TRACKING The inside-out approach, also known as first pass or forward tracking, seeds tracks using hits in the silicon detector and extends these outwards into the TRT. This method proceeds through the following steps [95], which are summarized below:

1. space point creation and initial track seed finding;
2. candidate track building;
3. ambiguity solving;
4. TRT extension.

First, space points are created by clustering together pixels and SCT strips with significant energy deposits in each layer. Silicon detector hit information is converted into three-dimensional spatial measurements, or space points, regarding where the charged particles crossed the active material of the detector. A pixel space point is formed by combining the two-dimensional pixel cluster centroid with the radial position of the associated Pixel layer, and an SCT space point is formed by combining pairs of SCT clusters with the layers they

appear in and the angle between them. Seed finding is then performed by combining space points in adjacent layers into sets of three, where a seed is a collection of three space points from three separate silicone layers representing an initial direction of a potential track. This step looks for track seeds in the Pixel and SCT by combining space point triplets consistent with a given momentum and impact parameter range. Seeds failing various other cuts are discarded.

Next, track candidates are built by estimating the track parameters from the initial seed and propagating them through the detector [92], incorporating additional space points compatible with the preliminary track, with a window search and combinatorial Kalman filter [96]. The window search creates a wide road along the seed trajectory, where the road defines the range in η and ϕ where the algorithm should look to add hits when extending the track. Hits within this road window are then collected and used in the Kalman filter, which extends the track candidate to all layers in the silicon detector, alternating between fitting the track and identifying hits to add to the track. The Kalman filter roughly estimates the track parameters from the hits associated to the current track seed or candidate assuming a perfect helical track model in a constant magnetic field, as described above and in [95]. These estimates are then used to predict the location of the next hit along the track. A hit consistent with the prediction that lies within the defined road is added to the track, and then the track parameters are updated and a new hit prediction is made. This process is

repeated until the track reaches the end of the silicon detector, at which point a final and detailed refit of the track parameters is executed. and the track candidate is formed. The track candidate quality is finally assessed based on various requirements, including the number of hits, the fit quality, and duplicate associated clusters. If the track candidate fails any of the quality cuts, it is discarded.

Ambiguity solving is then performed to eliminate multiple track candidates that share nearly identical information and to maximally associate hits to a single candidate [97, 98]. This step implements a scoring scheme to compare and rate tracks according to some relative track score based on the numbers of associated hits and holes and the track quality of fit, among other things. The scoring system favors high- p_T and fully formed tracks, with positive scores assigned for unshared hits and good fit qualities and negative scores assigned for holes, missing hits, and shared hits. Track candidates with scores below a certain threshold correspond to random hit combinations and track duplicates and are therefore discarded.

Finally, the silicon-seeded track candidates are extended into the TRT through classical extrapolation. This is done to improve the momentum resolution for the inner detector track, given the longer path length of the TRT. Hits in the TRT that are compatible with the extrapolation and are found within the road defined by the silicon track candidate are assigned to the candidate as a “TRT extension”. A full refit is then performed for the final

track parameters, with the TRT extension included in the final track if the combined track score is greater than the initial silicon track candidate score.

3.4.1.1.2 OUTSIDE-IN TRACKING The outside-in approach, also known as second pass or back tracking, seeds tracks using hits in the TRT and propagates these inwards to the silicon detector. This algorithm runs after inside-out tracking as a means of recovering tracks not initially reconstructed in the first pass. Standalone TRT track segments are reconstructed using pattern recognition in projected planes, as TRT tubes contain only two-dimensional information and can therefore not form three-dimensional space points. Hit patterns are found with the Hough transform [99], where intersecting lines in Hough space represent space points in real space belonging to the same track. Track segments are then traced backwards into the silicon detector, where unassociated compatible hits not already associated to existing tracks from the inside-out pass are added to the track candidate.

3.4.1.1.3 TRACK SELECTIONS Two common sets of track selection criteria, or working points, are defined for analysis at ATLAS: `Loose` and `Tight` [100]. `Loose` selections are designed to select tracks with high efficiency at the cost of a higher rate of reconstructing fake tracks, which arise mostly due to accidental combinations of hits. This is the default selection applied during reconstruction. Alternatively, `Tight` selections are designed to reject fakes at the cost of a reduced efficiency. The selection criteria for the `Loose` and `Tight`

working points are listed in Table 3.3.

Loose
$p_T > 500 \text{ MeV}$
$ \eta < 2.5$
$N_{\text{Si}} \geq 7$
$N_{\text{Si}}^{\text{sh}} \leq 1$
$N_{\text{Si}}^{\text{hole}} \leq 2$
$N_{\text{Pixel}}^{\text{hole}} \leq 1$
Tight
Loose selections
$N_{\text{Si}} \geq 9 \text{ if } \eta < 1.65$
$N_{\text{Si}} \geq 11 \text{ if } \eta > 1.65$
$N_{\text{Pixel}} \geq 1 \text{ for two innermost Pixel layers}$
$N_{\text{Pixel}}^{\text{hole}} = 0$

Table 3.3: Loose and Tight working points for standard track selection, where N_{Si} and N_{Pixel} are the numbers of hits in the combined silicon detector and in the Pixel, respectively, and N_{X}^{sh} and $N_{\text{X}}^{\text{hole}}$ are the numbers of shared hits and holes in the given silicon detector, respectively. Tight selections are applied on top of Loose selections.

The reconstruction efficiency of the Loose and Tight working points are 73 – 91% and 63 – 86%, respectively, and are shown as a function of track η and p_T in Figure 3.21. The track reconstruction efficiency is defined as the fraction of truth particles with $p_T > 500 \text{ MeV}$ and $|\eta| < 2.5$ that are matched to reconstructed tracks. The efficiency decreases with decreasing momentum, due to the increased probability of multiple scattering at low momentum, and with increasing pseudorapidity, due to the higher density of material being traversed. The slight increase in efficiency around $|\eta| = 2$ is related to the increased number of sensitive layers in that region. The efficiency plateaus above $p_T = 5 \text{ GeV}$.

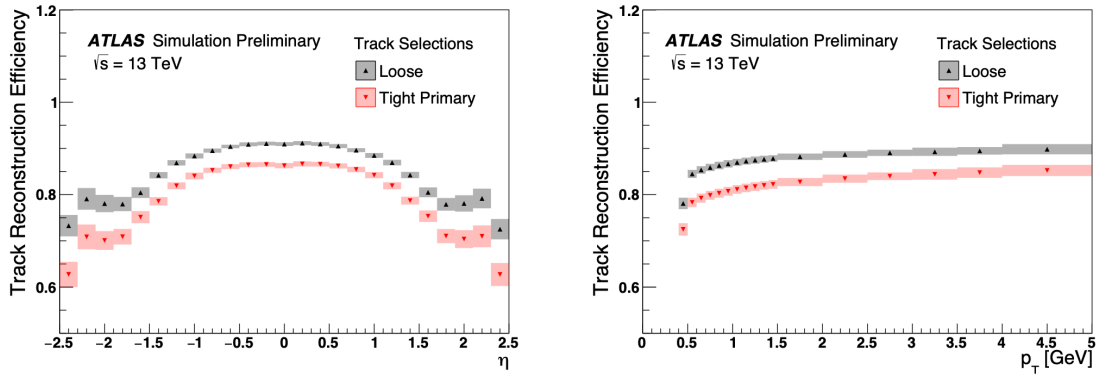


Figure 3.21: Standard track reconstruction efficiency as a function of η (left) and p_T (right) for loose and tight selections, using simulated minimum bias events [101]

3.4.1.2 LARGE RADIUS TRACKING

Many BSM models predict new particles with long lifetimes that travel significant distances before decaying within the inner detector. The decay products of these long-lived particles tend to have large impact parameters with respect to the interaction point. Standard tracking algorithms are not optimized for such displaced decays, as stringent limits are placed on the maximum impact parameter values, which significantly reduces the reconstruction efficiency for secondary particles, or displaced tracks originating from LLPs and not pointing back to the primary vertex. As such, a dedicated track reconstruction algorithm specialized for long-lived particle signals, Large Radius Tracking (LRT) [93], is implemented. This additional “third pass” tracking algorithm uses the leftover hits from standard tracking and applies relaxed selection criteria with loosened requirements on the track impact parameters and hit multiplicities to recover reconstruction efficiency for displaced tracks originating far

from the interaction point within the inner detector. To save computing resources, Large Radius Tracking is only applied to a subset of data potentially containing LLP events.

Large Radius Tracking is a third pass tracking step analogous to the standard first pass inside-out tracking algorithm, but performed with unused hits as inputs and relaxed selection criteria, specifically regarding the impact parameters and hit multiplicities of the candidate tracks, in order to enable reconstruction of largely displaced tracks. The most important cuts applied in both large-radius and standard inside-out tracking are listed in Table 3.4, which illustrates the major differences between the two algorithms.

Tracking algorithm	Standard inside-out	Large radius
Maximum d_o [mm]	10	300
Maximum z_o [mm]	250	1500
Maximum $ \eta $	2.7	5
Minimum p_T [MeV]	500	900
Maximum shared silicon modules	1	2
Minimum unshared silicon hits	6	5
Minimum silicon hits	7	7
Seed extension	Combinatorial	Sequential

Table 3.4: Selections applied in standard ATLAS inside-out and large-radius tracking algorithms.

The LRT algorithm runs after standard tracking and uses the leftover hits not already associated to the existing standard tracks reconstructed from the first two passes. Additionally, the selection criteria are relaxed in the following ways: the seed region is extended, the impact parameter cuts are loosened, the minimum transverse momentum is raised, and the quality cuts are tuned for displaced tracks. Specifically, the large-radius tracking algorithm

reconstructs tracks with impact parameters up to $|d_o| < 300$ mm and $|z_o| < 1500$ mm as opposed to $|d_o| < 10$ mm and $|z_o| < 250$ mm, raises the p_T threshold from 500 MeV to 900 MeV, and allows two shared hits instead of one, necessitating only five unshared hits instead of six, of the required seven silicon detector hits. Along with the loosened requirements optimized to select large-radius tracks, the LRT algorithm differs from the standard inside-out tracking algorithm by using a sequential Kalman filter, rather than the combinatorial one used in the standard reconstruction, to build track candidates. The sequential filter avoids the creation of multiple track candidates, simplifying the algorithm.

The LRT algorithm begins with track seeding and candidate creation, building space points from unused silicon hits leftover after first and second pass standard tracking. The pattern recognition algorithm creates seeds from space points and applies a window search in the direction of the seed trajectory in the same way as standard inside-out tracking to build track candidates with the relaxed track parameter cuts described above (and summarized in Table 3.4). Track candidates are then built with the extrapolation and fitting performed using a sequential Kalman filter, which picks the most likely road for the track instead of creating multiple candidates from the same points. Other than the sequential Kalman filter and the relaxed cuts, the LRT algorithm is essentially the same as the standard inside-out track reconstruction algorithm. Ambiguity solving is performed with the same relaxed parameters used in the track seeding and candidate creation steps in order to retain

high reconstruction efficiency. Tracks are then extended into the TRT in the same way as in standard inside-out tracking but with the same set of loosened selections as applied in the rest of the LRT steps to maintain consistency. The resulting collection of large-radius tracks are merged into the standard track collection, so the final track collection includes tracks from standard track reconstruction and LRT algorithms. The LRT algorithm provides a significant improvement in the reconstruction efficiency of long-lived particles compared to standard tracking, as discussed below.

3.4.1.2.1 LARGE RADIUS TRACKING RECONSTRUCTION PERFORMANCE The performance of the LRT algorithm is studied using two simplified BSM models containing SUSY LLPs with significantly displaced decays occurring with high probability within the geometric acceptance of the inner detector. The Feynman diagrams for these models are shown schematically in Figure 3.22, and the basics of the models are summarized below:

- displaced leptons: an RPV SUSY model with squark pair production, where each squark decays to a squark and the lightest neutralino, which is long-lived and decays through an R-parity violating coupling to a displaced lepton pair and a neutrino; the squark mass is set to 700 GeV, the neutralino mass is set to 500 GeV, and the neutralino lifetime is set to 30 mm, yielding hard final-state leptons with p_T of order 100 GeV;
- displaced hadrons: a split SUSY model where long-lived gluinos are pair-produced and form R-hadrons, bound states of colored SUSY and SM particles, which ultimately produce quarks and neutralinos, resulting in a final state of displaced hadronic jets; the gluino mass is set to 1.4 TeV, and the neutralino mass is set to 1.3 TeV;

this mass scale yields a soft p_T spectrum for the hadronic decay products of a few GeV.

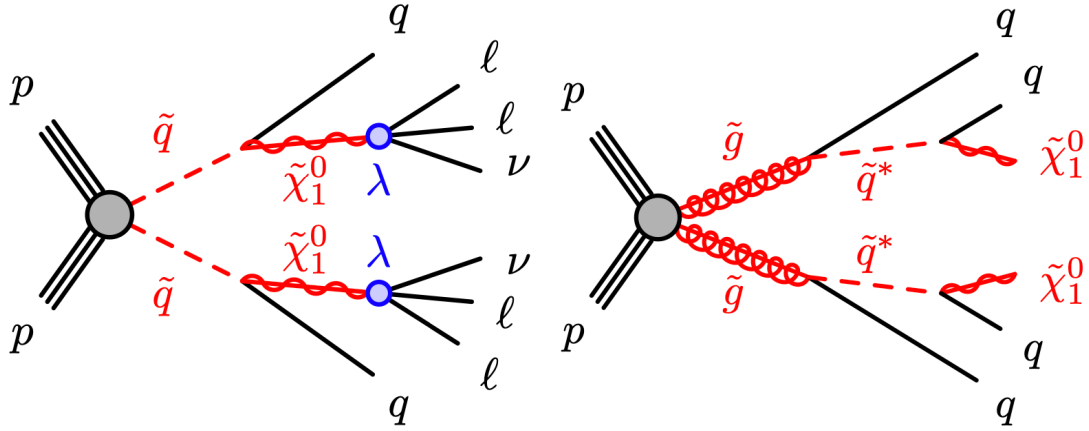


Figure 3.22: Feynman diagrams for the simplified BSM models used in the LRT performance studies: pair-produced squarks decaying via long-lived neutralinos to displaced leptons in R-parity violating SUSY (left) and long-lived gluino pair production resulting in displaced hadrons in split SUSY (right) [93].

The performance studies are conducted with a hit-based truth matching scheme. Tracks are matched to truth particles by associating each hit within the track to the truth particle that produced that hit in GEANT4. Each track is assigned a match score, calculated with respect to the particle most hit-associated to the track, and defined as the ratio of the weighted number of hits originating from the truth particle to the weighted number of hits used in reconstructing the track. This match score represents the probability of the reconstructed track originating from the truth particle and thus corresponding to a real charged particle trajectory. Tracks matched to truth particles with a match score above some threshold are considered “well-reconstructed” tracks. For the LRT performance studies discussed here,

the match score threshold applied is 0.5.

Additionally, a set of fiducial selections are applied to the truth particles under consideration in order to ensure the long-lived particle decays occur within the geometric acceptance of the detector and of the tracking algorithm and can therefore potentially be reconstructed. Truth particles are required to be electrically charged and to have a transverse momentum of at least $p_T = 1 \text{ GeV}$ and a pseudorapidity within $|\eta| < 2.5$. They must also be produced in the decay chain of the signal LLP of interest with a radial displacement below $r_{\text{prod}} = 440 \text{ mm}$. This requirement ensures the truth particle corresponds to an LLP decay and that the LLP decay occurs early enough in the inner detector for the resulting tracks to traverse the multiple layers of the SCT required by the LRT algorithm. The fiducial selections described here are summarized in Table 3.5 below.

$p_T > 1 \text{ GeV}$
$ \eta < 2.5$
$r_{\text{prod}} < 440 \text{ mm}$
charge = ± 1
in LLP decay chain

Table 3.5: Fiducial selections applied to the truth particles used in the LRT performance studies.

The overall track reconstruction efficiency is defined as the fraction of signal truth particles passing the fiducial selections that are matched to reconstructed tracks:

$$\text{reconstruction efficiency} = \frac{\text{N signal truth particles matched to reconstructed tracks}}{\text{N signal truth particles}}. \quad (3.10)$$

The combined efficiency takes into account all tracks, both standard and large-radius, in the final container, while the standard and LRT efficiencies account only for tracks reconstructed from the corresponding algorithms. The combined, standard, and large-radius tracking efficiencies for displaced leptons and displaced hadrons produced in the simplified BSM models are shown in Figure 3.23.

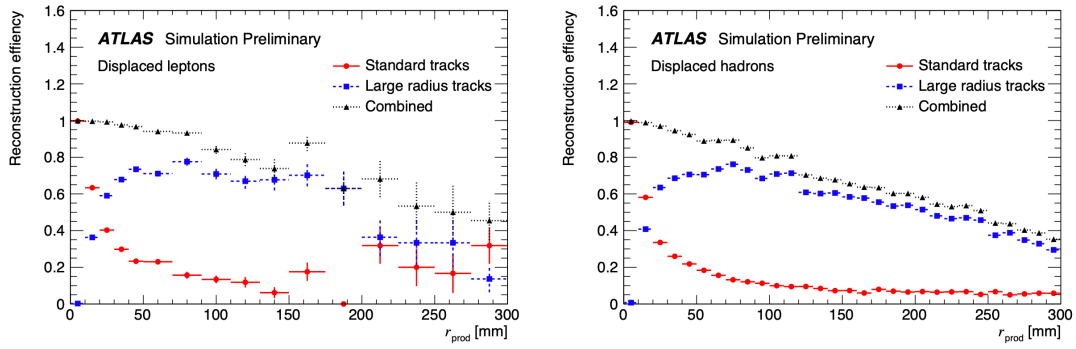


Figure 3.23: Inclusive reconstruction efficiency for displaced leptons (left) and displaced charged hadrons (right) produced by long-lived signal particle decays [93]. The efficiencies are shown for standard (red), large radius (blue), and combined (black) tracks as a function of the production radius r_{prod} of the displaced particles. Truth particles and tracks considered are subject to nominal fiducial selections defining the inclusive reconstruction efficiency. This use of the fiducial selections accounts for the increased standard tracking efficiency over that presented in Figure 3.21, where the tracks and truth particles used in the reconstruction efficiency are only required to pass a $p_T > 500 \text{ GeV}$ and $|\eta| < 2.5$ cut.

The standard efficiency is less than 20% for production radii r_{prod} greater than 50 mm and even lower for larger r_{prod} . The LRT algorithm significantly increases the reconstruction efficiency for tracks with $r_{\text{prod}} > 50 \text{ mm}$, but the efficiency still remains well below 100%. This is partly due to the ID geometry, as tracks with very large impact parameters do not leave enough hits in the inner detector to be adequately reconstructed. The efficiency

dependence on r_{prod} is also a direct result of the sequential tracking algorithm: at small r_{prod} , standard tracking is very efficient and few hits are leftover for use as input to the LRT algorithm, and at large r_{prod} , tracks are unlikely to be reconstructed with standard tracking and are therefore available for LRT reconstruction.

The technical efficiency is defined as the fraction of signal truth particles passing the fiducial selections and capable of producing at least seven silicon hits that are matched to reconstructed tracks:

$$\text{technical efficiency} = \frac{N \text{ reconstructible signal truth particles matched to reconstructed tracks}}{N \text{ reconstructible signal truth particles}}. \quad (3.\text{II})$$

On top of the fiducial criteria described above, further selections are applied to the truth particles in order to mimic the requirements of track reconstruction. Truth particles considered in the calculation of the technical efficiency are additionally required to have at least seven hits in the silicon detector and to be produced with a radial displacement of less than 300 mm. The technical efficiency is designed to isolate the algorithmic efficiency of the track reconstruction from the effect of the detector geometry by only considering truth particles that leave behind enough hits in the silicon detector to be reconstructible via silicon-seeded tracking methods. This efficiency calculation thus provides a more accurate measure of the LRT performance itself. The combined and large-radius tracking technical efficiencies for displaced leptons and displaced hadrons produced in the simplified BSM models are

shown in Figure 3.24.

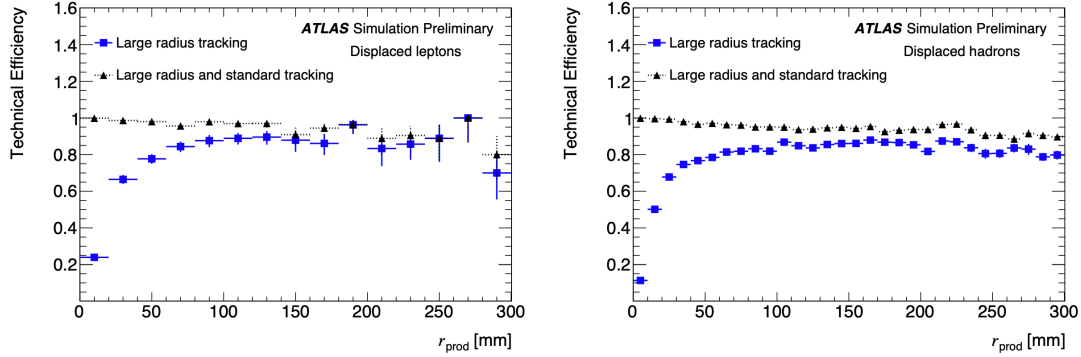


Figure 3.24: Technical reconstruction efficiency for displaced leptons (left) and displaced charged hadrons (right) produced by long-lived signal particle decays [93]. The efficiencies are shown for large radius (blue) and combined (black) tracks as a function of the production radius r_{prod} of the displaced particles. Truth particles and tracks considered are subject to “reconstructible” fiducial selections defining the technical reconstruction efficiency.

The combined technical efficiency is between 80% and 100% for both leptons and hadrons with r_{prod} below 300 mm and begins to decrease above this threshold.

A poor quality, or fake track, is one that is either poorly matched, with a match score of less than 0.5, or not matched at all to a truth particle. Fake tracks often correspond to tracks reconstructed from accidental combinations of hits from different particles, and they tend to have fewer associated hits than true, properly reconstructed tracks. The fake rate is defined as the fraction of reconstructed tracks that are of poor quality:

$$\text{fake rate} = \frac{N \text{ poor quality reconstructed tracks}}{N \text{ reconstructed tracks}}. \quad (3.12)$$

Large-radius tracks have a higher fake rate than standard tracks, since the LRT algorithm

requires fewer hits and applies looser selections, making the large-radius tracks more susceptible to random hit combinations. This fake rate is nearly 80%, meaning almost four out of five reconstructed large-radius tracks are of poor quality, which presents a significant challenge for secondary vertexing, since these fake tracks can randomly cross to produce fake displaced vertices. However, it is more important at this point to maximize the large-radius tracking efficiency rather than to minimize the fake rate so that the maximal amount of information may be reserved, as bad tracks and vertices can be removed later offline.

3.4.2 VERTEX RECONSTRUCTION

Vertex reconstruction, or “vertexing”, involves the grouping together of collections of tracks with common origins into primary and secondary vertices, where a vertex is a point in space where multiple tracks meet. Vertexing is especially useful for identifying specific particle decays and particular physics processes.

Primary vertices (PVs) are those produced at the interaction point and refer to vertices originating from both hard scatter and pileup pp collisions. Reconstruction of the primary vertices is performed through a two-step iterative vertex finding and fitting process, where the seeding and association of tracks is first implemented, followed by a recursive fitting of the vertex and track positions until the vertex position, final collection of associated tracks, and corresponding errors all converge.

Secondary or displaced vertices (DVs) are those located at a measurable distance from the

interaction point and originating from interactions and decays of particles produced in the hard scatter, particularly from decays of long-lived particles. A dedicated secondary vertex reconstruction algorithm is designed for LLP searches in order to reconstruct displaced decay vertices in the inner detector. These reconstructed displaced vertices suffer from large background rates due to random track crossings and material interactions in the detector, as well as to the significant fake rates of the large-radius tracks used as partial inputs to the secondary vertexing algorithm.

3.4.2.1 PRIMARY VERTEXING

All pp collisions in the event, including hard scatter and pileup interactions, are reconstructed as primary vertices. Efficient and precise PV reconstruction is an essential part of all LHC analyses, as it is crucial to distinguish the hard scatter PV of interest, for use in analysis, from the rest of the pileup PVs and to identify the objects produced at each primary vertex. Primary vertex reconstruction is necessary for determining the locations of the hard scatter and pileup interactions and for correctly assigning tracks to the corresponding PVs in order to properly reconstruct the full kinematics of the event. Additionally, PV reconstruction is used in calculating the luminous region, or beam spot, where collisions occur, which is affected by the focusing of the LHC beams in the transverse plane and by the bunch length and the angle of the beam crossing in the longitudinal plane. A general overview of primary vertex reconstruction at ATLAS is presented; for a more detailed de-

scription of the reconstruction and its performance, see Reference [102].

Primary vertex reconstruction is applied through an iterative vertex finding and fitting procedure consisting of the following steps:

1. seed track selection;
2. initial vertex seed position estimation;
3. vertex position determination with adaptive fitting;
4. removal of incompatible tracks and new vertex seeding.

First, seed tracks are selected, where the collection of inner detector tracks passing certain kinematic constraints and seemingly pointing back to the origin are compiled to be used as inputs to the vertex seed finding algorithm. The seed tracks must pass the `Tight` criteria defined in Table 3.3 [103].

Next, the initial PV seed position of the vertex fit is estimated. The initial longitudinal location of the vertex seed is found from the global maximum in the z -position distribution of the input seed tracks, computed at the point of closest approach to the beam spot center.

Then, the vertex position is determined with an “adaptive vertex fitting” algorithm [104] using the tracks associated to the seed vertex as inputs. The best vertex position is estimated with an iterative fit procedure that minimizes the χ^2 of the fit and progressively down-weights poorly matched tracks in each step. Input tracks are iteratively fit with respect to the seed vertex and weighted according to their compatibility with the primary vertex seed. The vertex position is recalculated using these weighted tracks, and then the

tracks are re-weighted with respect to the new vertex position. Tracks with poor fits to the vertex are gradually down-weighted, causing less compatible tracks to contribute less to the overall position calculation. This iterative procedure is repeated until the vertex position no longer changes.

Finally, incompatible tracks are removed from the vertex and a new vertex seed is identified. Incompatible tracks by more than seven standard deviations, corresponding roughly to tracks below a certain weight threshold, are removed from the vertex and used to seed a new vertex. This procedure repeats, beginning with the initial vertex position estimation from the remaining tracks, until all of the tracks are associated to a PV or until no new vertex can be constructed from the remaining set of tracks.

The primary vertex reconstruction algorithm outputs the set of three-dimensional vertex positions and corresponding covariance matrices for all vertices with at least two associated tracks. After the full set of vertices is created, the positions of the vertices are refit using the reconstructed position width of the beam spot. The beam spot itself is reconstructed from a distribution of primary vertices before the aforementioned beam spot refit is applied, with the PV positions used to determine the size, position, and shape of the beam spot. The primary vertex with the largest sum- p_T of associated tracks is selected as the singular primary vertex of the hard scatter process, often referred to simply as “the primary vertex”. The rest of the PVs are then taken as pileup, with the amount of pileup in the event roughly charac-

terized by the number of PVs in the event.

3.4.2.2 SECONDARY VERTEXING: VRTSECINCLUSIVE

Long-lived particles produced in $p\bar{p}$ collisions in the detector and decaying to charged SM particles within the tracker are characterized by macroscopic decay lengths and can be distinguished by significantly displaced vertices and their associated outgoing reconstructed tracks. Displaced, or secondary, vertices (DVs) consist primarily of displaced tracks with large impact parameters from LLP decays, but they can also contain tracks with small impact parameters, so secondary vertex reconstruction is seeded by tracks from both the standard and large-radius tracking algorithms. The secondary vertex algorithm used to reconstruct secondary vertices required by LLP analyses is contained in the `VrtSecInclusive` (VSI) package. The technical details of the package can be found in the corresponding internal note [105], and the package code can be found on gitlab [106].

Secondary vertex reconstruction [107] consists of five main stages, performed sequentially, and summarized below:

1. seed track selection: DV reconstruction is seeded by track pairs approximately compatible with an LLP decay, so seed tracks are first preselected based on a set of quality criteria; such tracks passing preselections are dubbed “selected” tracks;
2. two-track seed finding: the set of all combinations of pairs of selected tracks are formed and those passing loose compatibility criteria are used to form the set of two-track seed vertices;

3. multi-track vertex forming (and track rearrangement): n-track vertices are formed by combining two-track seeds using the incompatibility graph method, and tracks are rearranged to resolve ambiguities;
4. vertex merging: split and nearby vertices are merged using one of a set of merging algorithms;
5. track attachment: tracks initially unselected for vertex seeding but compatible with reconstructed vertices are attached; such tracks are dubbed “associated” tracks.

The first stage in secondary vertex reconstruction is seed track selection, where inner detector tracks are selected for vertex seed formation based on a set of quality criteria, as listed in Table 3.6. Tracks passing the quality criteria and selected to be used for vertex seeding are known as “selected” tracks. The selected track requirements are designed to be loose

All track criteria
$p_T > 1 \text{ GeV}$
$\chi^2/N_{\text{DoF}} < 50$
if $N_{\text{Pixel}} = 0, N_{\text{SCT}} \geq 6$
if $N_{\text{Pixel}} < 2, N_{\text{TRT}} \geq 1$
$2 \text{ mm} < d_0 < 300 \text{ mm}$
$ z_0 < 1500 \text{ mm}$
not already associated to any HS or PU PV
Low- p_T track criteria
if $p_T < 25 \text{ GeV}, N_{\text{SCT}} \geq 7$
if $p_T < 25 \text{ GeV}$ and $ \eta < 1.7, N_{\text{TRT}} \geq 20$

Table 3.6: Preselection requirements for selected tracks used in vertex seed formation. Here, N_{Pixel} , N_{SCT} , and N_{TRT} refer to the number of hits in the Pixel, SCT, and TRT, respectively.

enough to efficiently reconstruct secondary vertices for various physics models, yet tight enough to reduce the inclusion of fake and SM tracks in the secondary vertex seeds. Tracks

are required to have transverse momentum p_T of at least 1 GeV and a reduced goodness of fit χ^2/N_{DoF} of less than 50. A number of hit requirements are applied in order to reject low-quality tracks, and the track is required to not already be associated to any hard scatter or pileup primary vertex, as well as to have a transverse impact parameter $|d_o|$ of at least 2 mm in order to deter the formation of vertex seeds from prompt SM particles. The upper limits on the transverse and longitudinal impact parameters, $|d_o|$ and $|z_o| < 300$ mm and 1500 mm, respectively, are set by the maximum impact parameter cuts applied in the LRT algorithm.

The next step after seed track selection is two-track seed finding. The set of all two-track vertices compatible with an LLP decay are formed from the collection of selected tracks. The criteria defining the compatibility of the two-track seed vertex with an LLP decay are listed in Table 3.7. First, all possible pairs of selected tracks are formed into initial vertex seeds, and the vertex seed positions are approximated from a fast algorithm using the track pair parameters measured at the perigee. Initial seeds are discarded if the estimated radial position is outside of the silicon detector or if either of the tracks are too largely displaced from the initial estimated seed position. Precision fitting using full track extrapolation is then performed to more accurately estimate the vertex seed position for the remaining track pairs. This vertex fitting algorithm minimizes the χ^2 of the vertex seed with a Kalman-filter-based approach to precisely estimate the vertex position. If the fit fails, or if the updated radial position is estimated to be outside of the SCT, or if the reduced vertex goodness of fit

χ^2/N_{DoF} is above the specified threshold, the vertex seed is rejected.

initial estimate seed vertex criteria
$r_{\text{vtx}}^{\text{init}} < 563 \text{ mm}$
$ d_o^{\text{wrt init SV}} < 100 \text{ mm}$
$ z_o^{\text{wrt init SV}} < 50 \text{ mm}$
precision fit seed vertex criteria
$r_{\text{vtx}}^{\text{fit}} < 563 \text{ mm}$
$\chi^2/N_{\text{DoF}} > 5$
LLP decay compatibility criteria
hits required outside and forbidden inside seed position
$\cos(\phi^{(1)} - \phi_{\vec{r}}) > -0.8$ and $\cos(\phi^{(2)} - \phi_{\vec{r}}) > -0.8$
$\cos(\phi^{\text{sum}} - \phi_v) > -0.8$

Table 3.7: Selection requirements for two-track seed vertices, both before and after precision fitting. The hit pattern requirements are discussed in more detail in the text. In the azimuthal angular criteria, “(1)” and “(2)” refer to the two tracks in the seed vertex, “ \vec{r} ” refers to the pointing vector of the seed vertex, and “sum” refers to the vector sum of the two-track momenta of the seed vertex. Both the pointing vector and the two-track momentum vector sum are defined further in the text.

The two-track vertex seeds and their constituent tracks are then required to pass both a hit pattern consistency check and additional kinematic cuts to ensure vertex seeds and tracks are compatible with a long-lived particle decay. The hit pattern requirement verifies the hit patterns of both tracks are consistent with the position of the seed vertex, where consistency is defined by the following criteria, based on the expectation that tracks should travel outwards, not inwards, from the vertex:

- tracks are forbidden to have hits in the inner detector layers with smaller radii than the corresponding vertex seed position;
- tracks are required to have hits in the inner detector layers with larger radii than the corresponding vertex seed position;

- tracks are required to have at least one hit in the next inner detector layer immediately after the corresponding vertex seed position.

In the case of a vertex located very close to an inner detector layer boundary or of tracks traversing disabled modules, the above consistency criteria are relaxed. The hit pattern consistency criteria for two example seed vertices are illustrated in Figure 3.25. The kinematic

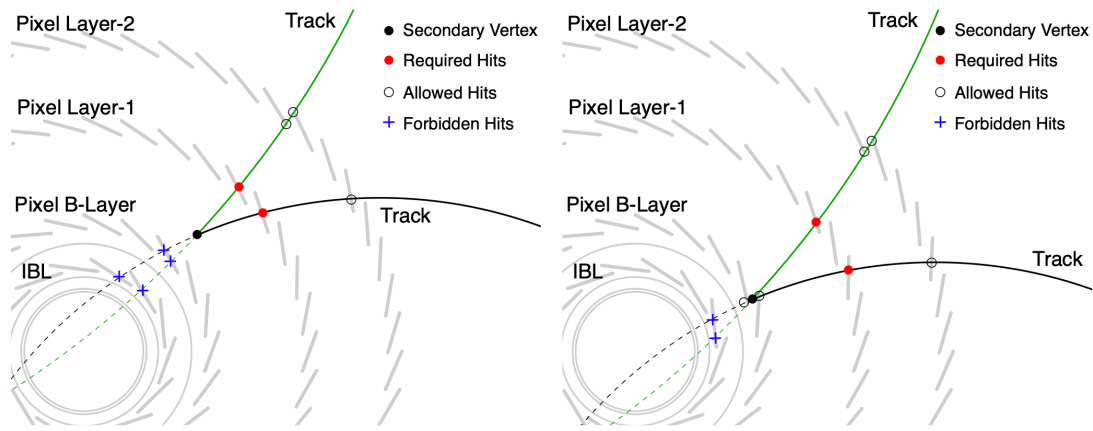


Figure 3.25: Schematic illustrating the hit pattern consistency requirements for a two-track seed vertex and its associated tracks, depicted for two example cases in the Pixel detector's transverse plane [107]. Left: The vertex seed (black) is located between the Pixel's B-layer and Layer 1. Its associated tracks are required to have hits (red) on the next outer layer (i.e. Layer 1), are allowed but not required to have hits (white) on any further outer layer (i.e. Layer 2), and are forbidden to have hits (blue) on any inside layers (i.e. the IBL or the B-layer). Right: Since the vertex is located very close to the B-layer, the associated track criteria are relaxed to allow hits on the nearby layer (i.e. the B-layer), whether inside or outside the vertex seed position, but they still require hits on the next outer layer (i.e. Layer 1) and forbid hits on the inner layers (i.e. the IBL).

selections are applied based on the vertex pointing vector $\vec{r} = \vec{r}(r_v, z_v, \phi_v)$, defined as the relative position of the fitted two-track vertex with respect to the PV, and on the vector sum of the two-track momenta $\vec{p}^{\text{sum}} = \vec{p}^{\text{sum}}(p_T^{\text{sum}}, \eta^{\text{sum}}, \phi^{\text{sum}})$ to remove vertex seeds and tracks pointing backwards to the PV. Cuts are placed on the relative azimuthal angle difference between the pointing vector and each associated track in order to reject vertices seeded by

randomly crossing tracks pointing backwards to the PV, as well as between the pointing vector and the two-track sum momentum vector in order to reject vertices with momenta pointing backwards to the PV.

The third step in the vertex reconstruction algorithm is multi-track vertex forming and track rearrangement. The combinations of all two-track vertex seeds are used to form n-track vertices. Two-track vertices sharing common tracks, which come about when multiple tracks from a common LLP decay are used to form different two-track seeds or a single track is used multiple times in different seeds, are iteratively combined into all possible multi-track vertices based on an incompatibility graph. The incompatibility graph approach works to form n-track vertices from sets of tracks that are all compatible with each other by extracting all fully incompatible tracks from the event. The set of all incompatible track pairs are represented as an incompatibility graph, as shown in Figure 3.26, with the tracks represented by nodes. The track pairs that are incompatible with each other for vertex seeding are represented by connected lines, or edges. The graph is solved and compatible tracks are extracted by removing the minimum number of fully incompatible nodes, and their associated edges, such that only fully-isolated, or compatible, nodes remain. These remaining isolated tracks are then fitted as a single candidate n-track vertex.

At this point, after multi-track vertices have been formed using the incompatibility graph method, tracks can still be associated to multiple vertex candidates. Such ambiguities are

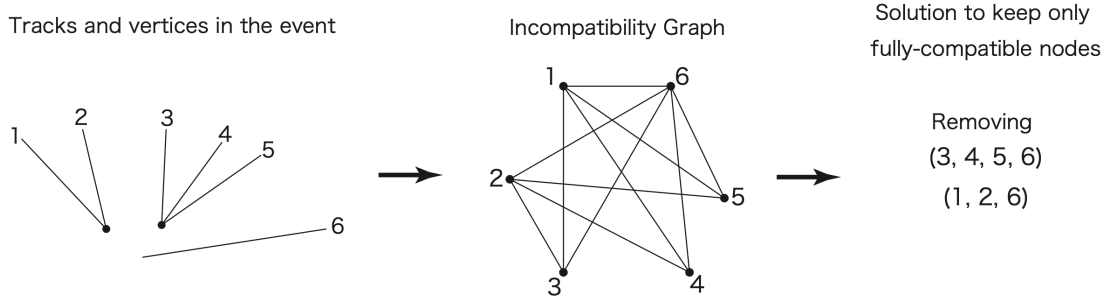


Figure 3.26: Schematic illustrating the incompatibility graph method for finding n-track vertices [105]. Left: The set of tracks and associated vertices in the event. Center: the incompatibility graph formed by connecting track pairs with incompatible two-track seed vertices. Right: The sets of fully-incompatible tracks whose removal leaves behind only fully isolated tracks, compatible for n-track vertex formation.

resolved by iteratively rearranging tracks to optimize their goodness of fit to the vertices until all tracks are maximally associated to a single secondary vertex. This process is known as “track rearrangement” and proceeds as follows:

- the track with the most number of associated vertices is identified, and the goodness of fit of that track with respect to each of its associated vertices is calculated;
- the associated vertex to which the track has the worst goodness of fit χ^2 is identified; if the χ^2 value of the worst-associated vertex is larger than some specified threshold, the track is removed from that vertex, and the procedure is repeated;
- otherwise, if the χ^2 value of the worst-associated vertex is smaller than the threshold, the distance significance and number of shared tracks between all vertices sharing the track of interest are calculated; if the shared vertex positions are compatible within 10σ , where σ is the uncertainty of the distance between the vertices, calculated as the quadrature sum of the covariance matrices of the vertex fits, or if the shared vertices share at least two tracks, the vertices are merged;
- otherwise, if no shared vertices are able to be merged for the track of interest, the track is removed from the worst-associated vertex;
- the procedure repeats until all tracks associated to at most one vertex.

The penultimate step in the vertexing algorithm is vertex merging. The previous steps of the vertexing algorithm may accidentally split vertices, reconstructing a single LLP decay as multiple distinct vertices. These “split” vertices can be recombined, or merged, by sequentially passing them through a set of merging algorithms, starting with attempting to combine the lowest-track-multiplicity vertex, which is the most likely vertex to be incorrectly reconstructed, with all higher-track-multiplicity vertices, from highest to lowest, and increasing the track multiplicity of the vertex of interest at each iteration. The set of merging algorithms tested for each vertex are as follows:

- merge by shuffling: the smaller vertex (with lower track multiplicity) is seeded with the position of the larger (with higher track multiplicity) and refit; if the updated position is compatible with the position of the larger vertex, the two vertices are merged;
- magnetic merging: the tracks from the larger vertex are iteratively associated to the smaller vertex, and the smaller vertex is refit, seeded by the position of the larger vertex; if compatible with the larger vertex position, the two vertices are merged;
- wild merging: all tracks from both the larger and smaller vertices are combined into a single vertex, and the new vertex is fit with the position of the original larger vertex; if the refit vertex is compatible with the larger vertex position, the two vertices are merged;
- final / proximity merging: the remaining vertices within 1 mm of each other are forced to merge, regardless of compatibility.

In the merging algorithms presented above, vertices are considered “compatible” and merged if their positions are within 10σ of one another. The algorithms are tested in order,

and if any one algorithm succeeds for a particular vertex, no subsequent algorithm is tested for that vertex. After merging, all vertices are refit.

The final step in secondary vertex reconstruction is track attachment. At this stage in the vertexing algorithm, some tracks that stem from the LLP decay may not yet be associated to the reconstructed vertex. This can happen if the track fails either the initial seed selection criteria or the hit pattern consistency check or some other earlier step of the reconstruction algorithm. The vertex kinematics, like track multiplicity and invariant mass, can be improved by attaching the currently unassociated tracks that are compatible with the vertex. Such “associated” tracks are required to pass additional criteria, listed in Table 3.8, with looser hit requirements than those placed on selected tracks. Associated tracks are required

$p_T > 1 \text{ GeV}$
$\chi^2/N_{\text{DoF}} < 5$
$ d_o^{\text{wrt SV}} $ -significance < 5
$ z_o^{\text{wrt SV}} $ -significance < 5
relaxed hit pattern consistency requirement

Table 3.8: Preselection requirements for associated tracks used in reattachment step.

to have transverse momentum p_T of at least 1 GeV, a reduced goodness of fit χ^2/N_{DoF} of less than 5, transverse and longitudinal impact parameter significances with respect to the secondary vertex, $|d_o^{\text{wrt SV}}|$ -significance and $|z_o^{\text{wrt SV}}|$ -significance, of less than 5, and a modified hit pattern requirement. The hit pattern consistency check is relaxed for the associated tracks, requiring the presence of hits in layers outside the vertex position only. As tracks

are only allowed to be associated to a single secondary vertex, the attachment procedure is attempted beginning with the highest-track-multiplicity vertex, and once a track is attached, it is no longer considered for attachment to any other vertex. After each attachment attempt, the vertex is refit, and if the reduced vertex goodness of fit χ^2/N_{DoF} is less than 20, the track is attached to the vertex.

Finally, after all possible tracks have been re-attached and all other steps of secondary vertex reconstruction have finished, a last fit of the vertex is performed and all track parameters with respect to the secondary vertex are recalculated. The track parameters with respect to the secondary vertex are then used to compute the vertex parameters, with the vertex mass computed assuming the charged pion mass for all tracks.

3.4.2.2.1 SECONDARY VERTEX TRACK CLEANING Initial validation studies of the secondary vertex reconstruction algorithm uncovered an anomalous asymmetry in the azimuthal angle φ distribution of the DV associated tracks with d_o values roughly corresponding to the radial positions of the Pixel layers. This issue, as demonstrated in Figure 3.27, was found to be due to a bug in the track attachment step related to the simplified track extrapolation method used. To mitigate the issue, an offline cleaning procedure has been recommended, where problematic tracks are removed from the vertices and the vertex kinematics are recomputed using the remaining tracks. Additionally, the cleaning procedure recommends removing associated tracks with $d_o < 2 \text{ mm}$ to exclude attachment of prompt

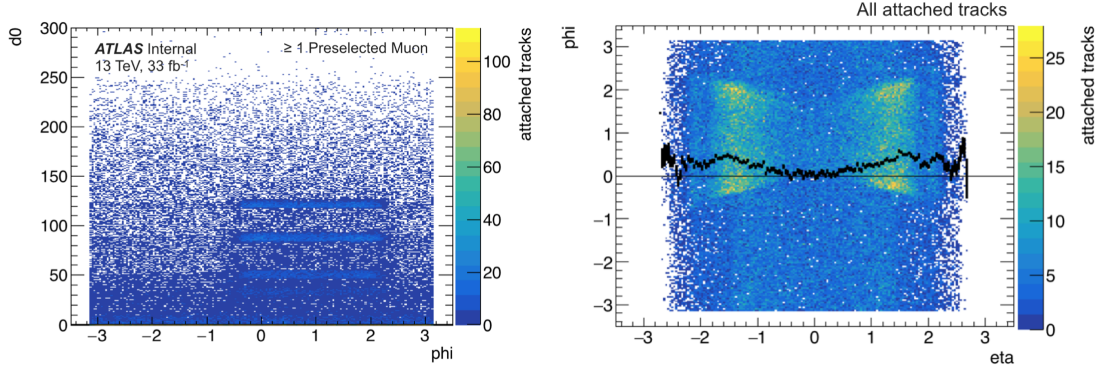


Figure 3.27: Azimuthal angle ϕ distribution of associated tracks in 2016 data [108]. Left: Associated track transverse impact parameter d_0 as a function of azimuthal angle ϕ . Right: Associated track azimuthal angle ϕ as a function of pseudorapidity η , with the average ϕ outlined in black. A clear excess is visible for associated tracks with positive ϕ , particularly where the d_0 values correspond to radial positions of the Pixel layer.

tracks to the vertex. In short, associated tracks are removed in the cleaning procedure if they have the following transverse impact parameter values:

- $|d_0| < 2$ mm;
- $26.0 < |d_0| < 39.0$ mm;
- $46.0 < |d_0| < 56.5$ mm;
- $83.5 < |d_0| < 93.5$ mm;
- $117.5 < |d_0| < 128.0$ mm;

where the center of each interval corresponds to the radial position of a Pixel layer.

3.4.2.2.2 SECONDARY VERTEX RECONSTRUCTION PERFORMANCE Before using the secondary vertexing algorithm in analysis, it is important to understand its reconstruction performance, which is studied using the following three benchmark LLP models:

- long-lived neutralinos: a simplified SUSY model where pair-produced gluinos cascade decay to two quarks and a neutralino, assumed to be the lightest supersymmetric particle, and the neutralino decays to a triplet of light quarks via off-shell squarks; the squark and gluino masses are set to 3 and 2.4 TeV, respectively, and the neutralino has a mass between 50 and 2350 GeV and a lifetime of 300 mm; this model yields high-track-multiplicity hadronic DVs;
- Higgs portal: a hidden-sector model where a SM Higgs boson is produced together with a W boson, and the Higgs boson decays to a pair of BSM pseudoscalars α , each of which obtains a long lifetime by decaying to bottom quarks through an off-shell Higgs boson; the pseudoscalar has a mass of 55 GeV and a lifetime of 100 mm; this model yields multiple nearby DVs reconstructed as a result of the B -hadron lifetime;
- heavy neutral leptons (HNLs): a BSM model where the HNL N has small mixings with the light neutralinos and thus long lifetimes; N decays to a neutrino and two muons and has a mass of 15 GeV and a lifetime of 100 mm; this model yields low-track-multiplicity DVs in conjunction with lepton pairs.

The Feynman diagrams for the above benchmark models are shown in Figure 3.28.

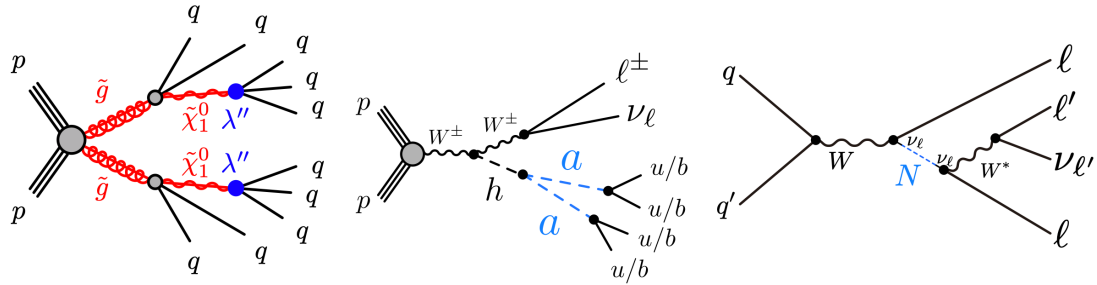


Figure 3.28: Feynman diagrams for benchmark LLP models used in VSI performance studies [107]: long-lived neutralinos (left), Higgs portal (center), and heavy neutral leptons (right).

The secondary vertex reconstruction efficiency is evaluated based on truth matching, or the association of reconstructed vertices to truth signal LLP decays. The relative distance

between vertices is not a sufficient measure of a truth match, since many LLP decays contain short-lived particles that displace the reconstructed vertex from the LLP position. This effect is illustrated in Figure 3.29. Instead, it is more effective to evaluate the truth match

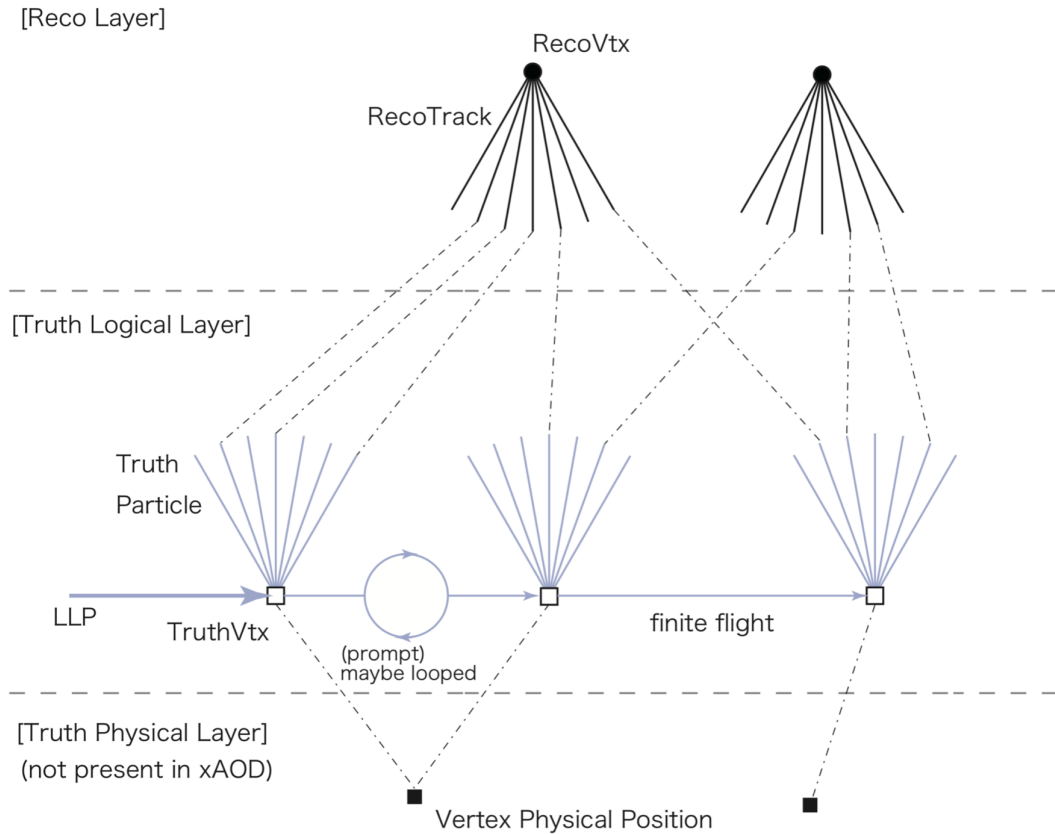


Figure 3.29: Schematic illustrating an example of how reconstructed vertex locations may be displaced from their corresponding truth vertex positions, which may be displaced from their corresponding physical positions [109].

based on the composition of the the reconstructed DV in terms of the constituent tracks corresponding to the descendants of the LLP decay, where a descendant is any particle in the LLP decay chain. It is important to perform truth matching based on descendants,

rather than direct daughters, since LLP decays can involve hadronization, resulting in many intermediate virtual particles in the decay chain. A track- p_T -weighted match score s is defined for a given reconstructed secondary vertex v and LLP decay l , as such:

$$s(v, l) \equiv \frac{\sum_{\substack{i \in \text{tracks} \in v \\ (\text{$p_T^{(i)}$ | descendant of LLP decay l})}} p_T^{(i)}}{\sum_{i \in \text{tracks} \in v} p_T^{(i)}} \quad (3.13)$$

The denominator sum is taken over all tracks in the reconstructed DV, while the numerator sum is taken over all tracks in the reconstructed DV that are matched to truth particles in the LLP decay chain, where the matching between tracks and truth particles is based on a score weighted according to shared detector hits between track and truth particle trajectories. The match score s represents the fraction of secondary vertex tracks that are matched to LLP decay products, and the LLP decay is considered “reconstructed”, or a reconstructed vertex is considered “truth-matched”, in the performance studies presented in this section if the match score is greater than 0.5.

The reconstruction efficiency is defined as the fraction of truth LLP decays that correspond to reconstructed vertices, based on the matching criteria defined above. The separate effects from the tracking and vertexing algorithms can be distinguished by factorizing the total reconstruction efficiency into several terms: $\epsilon^{\text{tot}} = \mathcal{A} \cdot \epsilon^{\text{alg}} = \mathcal{A} \cdot \epsilon^{\text{seed}} \cdot \epsilon^{\text{core}}$.

The acceptance \mathcal{A} is defined as the ratio of LLP decays with at least two reconstructed

tracks to reconstructible LLP decays. A reconstructed track from an LLP decay is an outgoing charged particle with $p_T > 1 \text{ GeV}$ matched to a reconstructed track. A reconstructible LLP decay is one that passes the following fiducial requirements:

- $r < 563 \text{ mm}$ and $|z| < 2720 \text{ mm}$, corresponding to an LLP decay within the silicon detector;
- at least two outgoing charged particles with $p_T > 1 \text{ GeV}$ in the decay chain, corresponding to an LLP decay capable of being seeded by the vertexing algorithm and having tracks capable of being reconstructed by the tracking algorithms.

The acceptance is essentially the rate of reconstructible decays, or the fraction of reconstructible LLP decays with a sufficient number of reconstructed constituent tracks to potentially be reconstructed as a secondary vertex, and provides a measure of the track reconstruction efficiency.

The total reconstruction efficiency ε^{tot} is defined as the ratio of reconstructed LLP decays to reconstructible LLP decays, that is, the fraction of reconstructible LLP decays with match scores above 0.5 to reconstructed vertices. The algorithmic efficiency ε^{alg} is defined as the ratio of the total reconstruction efficiency to the acceptance, or the ratio of reconstructed LLP decays to reconstructible LLP decays with at least two reconstructed tracks, and is essentially a measure of the vertexing performance alone, without the effects of the tracking performance. The seed efficiency $\varepsilon^{\text{seed}}$ is the ratio of the LLP decays with at least two reconstructed selected tracks to reconstructible LLP decays with at least two reconstructed tracks and measures the seed track selection efficiency. The core efficiency $\varepsilon^{\text{core}}$ is

defined as the ratio of the algorithmic efficiency to the seed efficiency, or the ratio of reconstructed LLP decays to reconstructible LLP decays with at least two reconstructed selected tracks, and provides a measure of the pure vertex reconstruction efficiency.

The acceptance and the seed, core, and total efficiencies for the three LLP models presented above are shown in Figure 3.30.

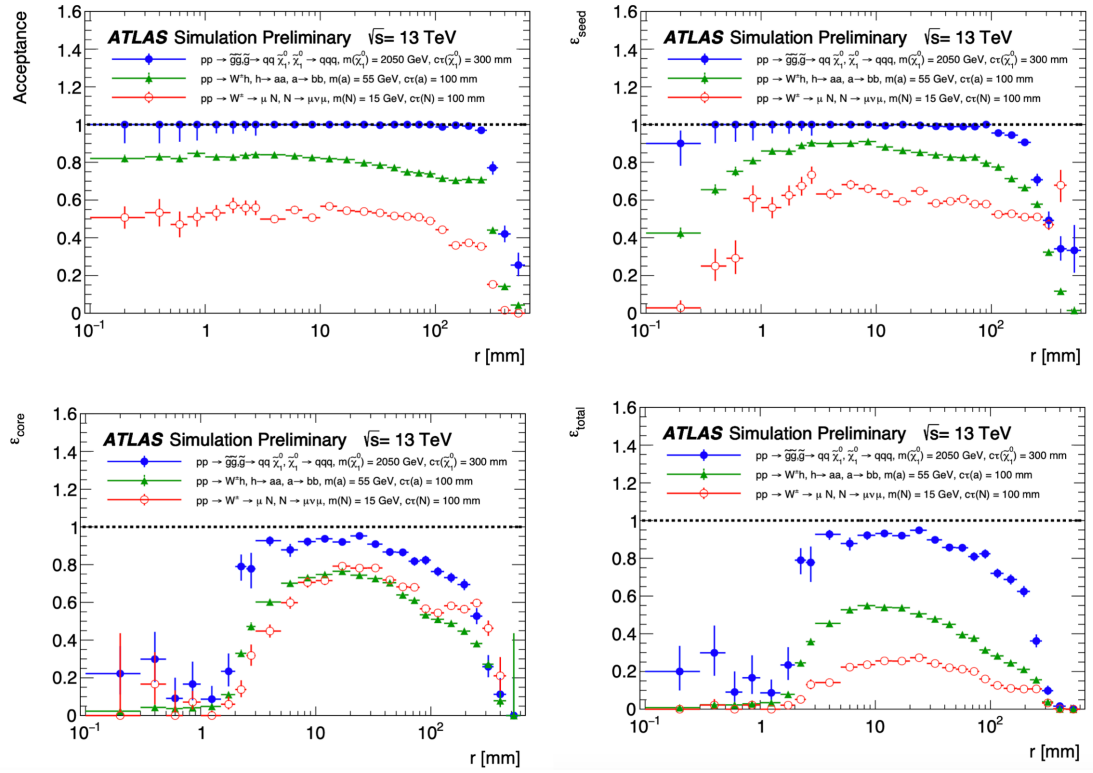


Figure 3.30: Factorized terms of the secondary vertex reconstruction efficiency, including the acceptance \mathcal{A} (top left), the seed efficiency $\varepsilon_{\text{seed}}$ (top right), the core efficiency $\varepsilon^{\text{core}}$ (bottom left), and the total reconstruction efficiency ε^{tot} (bottom right), as a function of the LLP decay radius r for the three BSM models presented above [107].

The acceptance and efficiencies are seen to decrease with the radial displacement of the

vertex production position, particularly beyond $r = 300$ mm, where the minimum hit requirement in the LRT tracking algorithm tends to fail, resulting in a loss of efficiency in the LRT tracking algorithm at large r . Since fewer tracks are reconstructed farther out, there is a lower chance for such tracks to successfully form vertex candidates. The efficiency is also directly related to the track multiplicity, with fewer outgoing particles resulting in a lower probability of a sufficient number of tracks for vertex formation being reconstructed.

3.4.3 JET RECONSTRUCTION

A hard parton produced in the detector undergoes immediate fragmentation and hadronization and appears as a narrow, collimated stream of energetic hadrons. A jet is then a singular reconstruction object encompassing this group of particles and characterizing the initial parton behind their production. Jets are reconstructed by running clustering algorithms over a set of input four-vectors, with inputs being calorimeter energy deposits, charged particle tracks, or simulated stable particles. After reconstruction, jets are calibrated to correct their energy scales and account for various effects using a series of steps.

Jets are defined at the experiment level by the jet algorithms used to cluster them. A jet algorithm, or jet finder, runs over all particles in the event and outputs jet objects according to a set of rules dictating how the particles in the parton showers are grouped together into jets. Jet algorithms are designed to adhere to the following common criteria in order to enable direct comparisons between theory and experiment and to ensure the jets defined by

the algorithms are theoretically sound and experimentally achievable [110]:

- easily implementable in experimental analysis and in theoretical calculation;
- definable at any order of perturbation theory;
- yielding a finite cross section at any perturbation order that is relatively insensitive to hadronization.

The most common class of jet algorithm used in current experiments is the sequential recombination, or cluster-type, algorithm, which uses a distance metric d_{ij} to recursively combine nearby particles together [111] in the following steps:

1. calculate the distance d_{ij} between all particle pairs i, j ;
2. identify the pair i, j that minimizes d_{ij} ;
3. if the minimum d_{ij} is below a given threshold, combine i and j into a single pseudojet and repeat steps 1-3;
4. if no further pairs have a distance below threshold, declare all remaining particles to be jets and terminate the algorithm.

The distance metric used in the three main sequential recombination algorithms (k_t , Cambridge/Aachen, and anti- k_t) is defined as

$$d_{ij} = \min(k_{T_i}^{2p}, k_{T_j}^{2p}) \frac{\Delta R_{ij}^2}{R^2}, \quad (3.14)$$

where $\Delta R_{ij} \equiv \sqrt{(\varphi_i - \varphi_j)^2 + (\eta_i - \eta_j)^2}$ is the angular distance between particles i and j , R is the radius of the jet cone in $\eta - \varphi$ space, k_{T_i} (k_{T_j}) is the transverse momentum of

particle i (j), and p determines the sequential recombination algorithm type. The case of $p = 0$ corresponds to the Cambridge/Aachen algorithm, where only the angular distance between particles, and not their momenta, is considered. The k_t algorithm is specified by the $p = +1$ case, where soft particles are clustered first, and the anti- k_t algorithm is specified by the $p = -1$ case, where hard particles are clustered first.

The anti- k_t jet clustering algorithm [II2] takes any type of four-momentum object as input and produces relatively circular jets contained within cones of radius R whose boundaries are resilient to soft radiation due to the nature of clustering soft particles around hard particle seeds. Such jets are experimentally convenient, as they reduce sensitivity to noise and ease calibration. Thus, the anti- k_t algorithm is the default jet clustering algorithm used at ATLAS.

3.4.3.1 TOPOLOGICAL CELL CLUSTERING

While jet reconstruction algorithms can take any set of four-vectors as inputs, the primary signals used as inputs in ATLAS jet reconstruction are clusters of topologically connected calorimeter cell signals, or “topo-clusters” [II3]. Topo-clusters are fully calibrated three-dimensional objects representing reconstructed particle showers, where the calibration is done at cell-level to the electromagnetic (EM) scale, which correctly reproduces the signal from a single electron, and individual topo-clusters may represent full or fractional showers from single particles or merged shower responses from multiple particles. Calorimeter

cell signals from energies deposited by incoming particles in topologically connected cells are collected into topo-clusters using a three-dimensional clustering algorithm that iteratively adds neighboring cells to a proto-cluster created by a seed. The topological clustering algorithm aims to produce “energy blobs” around significant signals in the calorimeter consistent with reconstructed particle shower energy flow patterns [114]. This is achieved with a growing-volume algorithm, where the topo-clusters are seeded by highly significant calorimeter cell signals, and the seed, growth, and boundary features of the topo-clusters are parametrized by the {S, N, P} thresholds, defined in terms of the cell signal significance

$$\xi_{\text{cell}}^{\text{EM}} = E_{\text{cell}}^{\text{EM}} / \sigma_{\text{noise},\text{cell}}^{\text{EM}}, \quad (3.15)$$

where $E_{\text{cell}}^{\text{EM}}$ is the calorimeter cell signal, and $\sigma_{\text{noise},\text{cell}}^{\text{EM}}$ is the average expected noise in the calorimeter cell, both measured on the EM scale. The cell noise is taken as the quadrature sum of electronic noise and pileup ($\sigma_{\text{noise}} = \sqrt{(\sigma_{\text{noise}}^{\text{electronic}})^2 + (\sigma_{\text{noise}}^{\text{pile-up}})^2}$).

The topo-cluster formation thresholds are defined as follows:

$$\begin{aligned} |E_{\text{cell}}^{\text{EM}}| > S\sigma_{\text{noise},\text{cell}}^{\text{EM}} &\implies |\xi_{\text{cell}}^{\text{EM}}| > S \\ |E_{\text{cell}}^{\text{EM}}| > N\sigma_{\text{noise},\text{cell}}^{\text{EM}} &\implies |\xi_{\text{cell}}^{\text{EM}}| > N \\ |E_{\text{cell}}^{\text{EM}}| > P\sigma_{\text{noise},\text{cell}}^{\text{EM}} &\implies |\xi_{\text{cell}}^{\text{EM}}| > P \end{aligned} \quad (3.16)$$

where S is the primary seed threshold, N is the threshold for growth control, and P is the principal cell filter. The configuration optimized for ATLAS reconstruction, the “4-2-0” algorithm, sets $S = 4$, $N = 2$, and $P = 0$.

Topo-cluster formation then proceeds in a sequence of “seed and collect” steps, which are repeated until all topologically connected cells passing the S and N thresholds and their direct neighbors passing the P threshold are found and clustered:

1. Initial proto-clusters are formed from seed cells with signal significances above the S threshold ($|E_{\text{cell}}^{\text{EM}}| > 4\sigma_{\text{noise},\text{cell}}^{\text{EM}}$), with one seed per proto-cluster.
2. Neighboring cells with signal significances above the N threshold ($|E_{\text{cell}}^{\text{EM}}| > 2\sigma_{\text{noise},\text{cell}}^{\text{EM}}$) are added iteratively to the corresponding proto-clusters, where a neighboring cell is any cell directly adjacent to the proto-cluster in the same calorimeter layer or any cell having partial overlap in the $\eta - \varphi$ plane with the proto-cluster in an adjacent layer. This procedure continues, adding new neighbors to the growing proto-clusters, until no further neighbors with signal significances above the N threshold are found, when the proto-cluster formation stops.
3. Additional neighboring cells with signal significances above the P threshold ($|E_{\text{cell}}^{\text{EM}}| > 0$) are finally added to the proto-cluster. The $P = 0$ configuration used in ATLAS means any cell neighboring a cell with signal significance above the N threshold is added to the proto-cluster, regardless of its energy.

This procedure yields a topo-cluster with a core of highly significant signal cells surrounded by an envelope of less significant signal cells. The resulting topo-clusters contain reconstructed energy, shape, direction, and location information about the incoming particle showers producing the signals found in the calorimeter. The total energy of the topo-cluster is calculated from the sum of the cell signals contained within it, and the directions,

locations, and shapes of the topo-clusters are calculated from the constituent cell energies and locations.

Cluster formation selections are applied to the absolute value of the cell energy, so both positive and negative signals can seed and grow clusters. Negative cell energies arise from fluctuations in pileup and electronic noise. Including these negative cells in the topo-clusters improves the overall noise suppression due to the local cancellations of random upward and downward fluctuations within the cluster, where upward and downward fluctuations are represented by positive and negative energy cells, respectively. The inclusion of negative energy cells also reduces the bias in the reconstructed cluster energy introduced by only including positive signal cell contributions. Jets, however, are only reconstructed from clusters with a net positive energy.

Proto-clusters can initially be formed with more than one local signal maximum, corresponding to multiple particles depositing energy in the calorimeter in close proximity to one another. This often occurs when an initial proto-cluster forms and is too large to provide a good measurement of the particle energy flow. Such proto-clusters are then split between corresponding signal peaks in three dimensions based on their relative distances to each maximum. A local signal maximum is defined as a cell with energy of at least 500 MeV surrounded by at least four neighbors, all with smaller signals, located in certain EM sampling layers. After splitting, cells neighboring more than one maximum are shared between

the two highest-energy nearby proto-clusters, with each cell maximally shared once between at most two clusters and contributing a geometrically-weighted fraction of its energy to each shared cluster, based on the cell's proximity to and the relative energy of each cluster. The geometric weights used in calculating the shared signal between the two clusters are defined as follows:

$$w_{\text{cell},1}^{\text{geo}} = \frac{E_{\text{clus},1}^{\text{EM}}}{E_{\text{clus},1}^{\text{EM}} + rE_{\text{clus},2}^{\text{EM}}} \quad (3.17)$$

$$w_{\text{cell},2}^{\text{geo}} = 1 - w_{\text{cell},1}^{\text{geo}}$$

where $r = \exp(d_1 - d_2)$, d_1 and d_2 are the distances of the cell to the center of gravity of the two clusters, and $E_{\text{clus},1}^{\text{EM}}$ and $E_{\text{clus},2}^{\text{EM}}$ are the energies of the two clusters shared between the cell. The maximal sharing of cells between two proto-clusters is represented by the fact that

$$w_{\text{cell},1}^{\text{geo}} + w_{\text{cell},2}^{\text{geo}} = 1.$$

The cluster kinematics are calculated from a recombination of cell energies and directions: the cluster energy is defined as the sum total of the cluster cell energies; the cluster direction is the signal-weighted barycenter; and the cluster mass is taken to be zero.

3.4.3.2 RECONSTRUCTED JETS AT ATLAS

Jets at ATLAS are reconstructed with the anti- k_t algorithm of radius $R = 0.4$ or $R = 1.0$ for small-R or large-R jets, respectively. Small-R jets are the default at ATLAS and are used

to find hadrons produced in the detector, as they capture most of the shower energy and correspond roughly to a single parton. Large- R jets are used to study jet substructure in order to identify hadronic decays of heavy boosted objects or to study the inner structure of the jet, as they capture more detailed shower information. Reconstructed jets are required to have $p_T > 7 \text{ GeV}$ to be reconstructed by the anti- k_t algorithm.

EMTopo jets at ATLAS are jets reconstructed from topo-clusters measured at the electromagnetic scale. Truth jets are reconstructed from stable simulated MC generator particles measured at the particle-level scale. The recombination scheme used at ATLAS is the “E-scheme”, or four-vector recombination, where jet kinematics are calculated from the summation of the constituent four-vectors, yielding massive jets [115]. Reconstructed jet energy scales differ from those of the corresponding truth jets due to reconstruction and pileup effects, so a multi-stage calibration procedure is applied to bring the reconstructed scale closer to the truth.

3.4.3.3 JET CALIBRATION

After reconstruction, EM-scale calorimeter jets are calibrated in both simulation and data to correct their four-momenta to those of truth jets reconstructed at the particle level in order to account for energy losses in the detector and differences between simulated and real physics events using the jet energy scale (JES) calibration scheme. This calibration scheme is a multistep procedure using both MC-based and *in situ* techniques to correct reconstructed

jet energies such that they correspond to those of the associated stable truth particles within them [II6–II8]. The MC-based steps calibrate reconstructed simulated jets to truth jets, correcting for effects from pileup, jet fragmentation, jet reconstruction, and detector features, and the *in situ* steps calibrate reconstructed jets in data to reconstructed jets in MC, correcting for differences in jet response between data and simulation due to imperfect detector descriptions used in MC.

The JES calibration scheme, as illustrated in Figure 3.31, is performed through the following series of consecutive stages, as summarized below:

1. origin correction: recalculates jet four-momentum to point to the primary vertex instead of the detector center, without altering the jet energy;
2. pileup correction: removes excess jet energy due to pileup using an event-level area-based subtraction and a residual MC-based correction;
3. absolute JES calibration: corrects jet four-momentum to particle-level scale using MC-based absolute jet energy scale and η calibrations;
4. global sequential calibration: improves energy calibration and overall resolution by minimizing differences in calorimeter response based on jet flavors and energy deposits using information from all areas of the detector;
5. *in situ* calibration: corrects jets in data to account for differences between data and simulation by comparing to well-measured reference objects.

3.4.3.3.1 ORIGIN CORRECTION The first step in calibration is the origin correction, which redirects the jet to point to the hard scatter primary vertex rather than the geometrical center of the detector. This correction improves the jet η resolution, measured from the

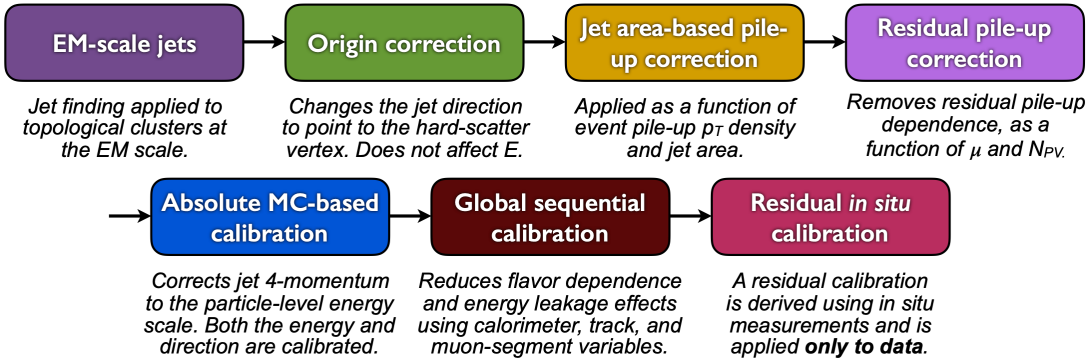


Figure 3.31: JES calibration steps for EM-scale calorimeter jets [118].

difference between the reconstructed and truth jets in simulation, but does not change the energy of the jet.

3.4.3.3.2 PILEUP CORRECTION The next step is the pileup correction, which removes the pileup contribution to the reconstructed jet energy in two stages: an area-based subtraction followed by a residual correction derived from simulation.

In-time and out-of-time pileup add energy roughly uniformly throughout the event, increasing the overall jet energy measured by the calorimeter during jet reconstruction. This excess jet momentum generated by the pileup in the event is subtracted from each jet according to its area, using the area-based correction

$$p_T^{\text{area}} = \rho \times A, \quad (3.18)$$

where ρ is the median energy density, and A is the jet area.

The median energy density, or pileup momentum density, ϱ is calculated from the median of the jet p_T density distribution in the $\eta - \varphi$ plane, where the p_T density of a single jet is defined as the jet p_T over the jet area \mathcal{A} . The distribution of jets used in calculating the median energy density are clustered with the k_t algorithm with radius $R = 0.4$ and are reconstructed only from positive-energy topo-clusters with $|\eta| < 2.5$ and no minimum p_T threshold. The k_t algorithm, rather than the anti- k_t algorithm, is used here for its sensitivity to soft particles. The median of the transverse momentum density distribution is chosen to mitigate the effects of high- p_T hard scatter jets in the tails of the distribution.

The jet area \mathcal{A} is measured by the jet finding algorithm using the ghost association method, where infinitely soft “ghosts” randomly and densely distributed in η and φ are added to the event before jet reconstruction begins and then clustered together with the real particles in the event into jets [119]. As the ghost particles carry infinitesimal momentum, they do not affect the overall properties of the final jets produced from the ghost-included clustering. The area is then measured from the relative number of ghost particles associated to the jet after clustering: $\mathcal{A} = N_g / v_g$, where N_g is the number of ghost particles contained in the jet and v_g is the areal number density of the ghost particles.

The pileup contribution to the jet energy is not fully described by the median p_T density described above, since it is only calculated in the central region of the detector. Therefore, an additional residual correction must be applied after the initial area-based pileup subtraction.

tion in order to remove the remaining dependence of the jet momentum on the amount of pileup in the event, particularly in the forward region of the detector. The residual p_T dependence is measured as the difference in momentum between reconstructed and truth jets, geometrically matched within $\Delta R = 0.3$, in bins of η_{det} , where η_{det} is the jet η pointing from the geometrical detector center, as a function of the number of primary vertices per event N_{PV} , which characterizes the in-time pileup, and as a function of the average number of interactions per event μ , which characterizes the out-of-time pileup. The dependence on each is seen to be approximately linear, with the slopes of the linear fits defining the correction coefficients α and β used in the residual pileup subtraction, where

$$\begin{aligned}\alpha(\eta_{\text{det}}) &= \frac{\partial p_T}{\partial N_{\text{PV}}}(\eta_{\text{det}}), \\ \beta(\eta_{\text{det}}) &= \frac{\partial p_T}{\partial \mu}(\eta_{\text{det}}),\end{aligned}\tag{3.19}$$

and the residual pileup correction is defined as

$$p_T^{\text{residual}} = \alpha \times (N_{\text{PV}} - 1) + \beta \times \mu.\tag{3.20}$$

The pileup-corrected transverse momentum after area-based and residual pileup subtraction is

tions is therefore:

$$p_T^{\text{corr}} = p_T^{\text{reco}} - p_T^{\text{area}} - p_T^{\text{residual}} = p_T^{\text{reco}} - \xi \times A - \alpha \times (N_{\text{PV}} - 1) - \beta \times \mu \quad (3.21)$$

The pileup dependence of the jet p_T before and after the pileup corrections are applied is shown in Figure 3.32.

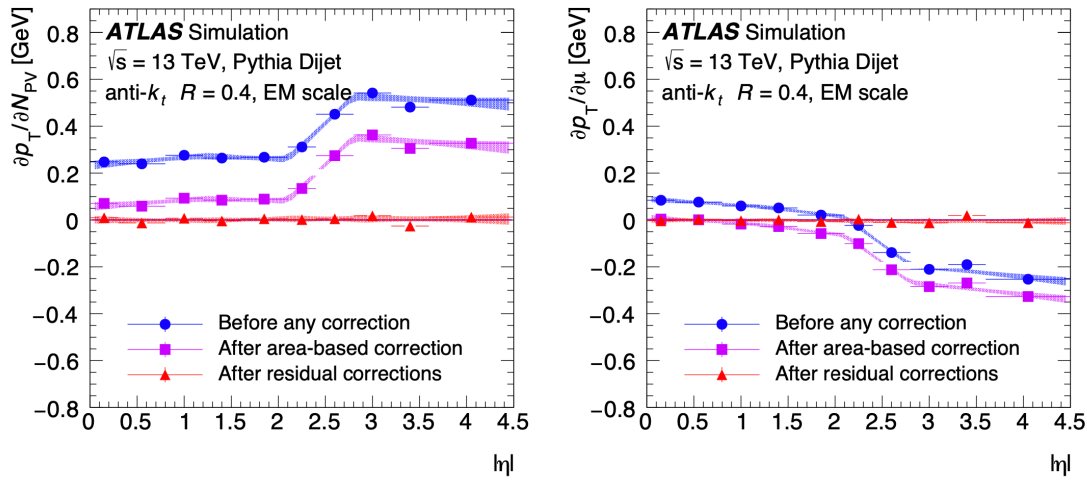


Figure 3.32: In-time (left) and out-of-time (right) pileup dependence of jet p_T as a function of $|\eta|$ before the pileup correction (blue), after the area-based pileup subtraction (purple), and after the residual pileup calibration (red) [118].

3.4.3.3.3 ABSOLUTE JES CALIBRATION The absolute jet energy scale and η calibration step uses MC-based corrections to bring the reconstructed jet four-momentum closer to the truth-level energy scale and to account for biases in the reconstruction of the jet η caused by transitions between different calorimeter regions with different technologies and granularities. These corrections are derived from simulation using isolated reconstructed jets

matched to isolated truth jets within $\Delta R = 0.3$.

The JES correction is derived from the ratio of the reconstructed jet energy to the truth jet energy. The average energy response \mathcal{R} , defined as the mean of a Gaussian fit to the $E^{\text{reco}}/E^{\text{truth}}$ jet distribution and calculated in bins of E^{truth} and η_{det} , is parametrized as a function of E^{reco} , with the corrections to E^{reco} derived from E^{truth} using a numerical inversion procedure. The absolute JES calibration factor is then taken as the inverse of this response.

The γ correction is derived from the difference between the reconstructed and truth jet γ , parametrized as a function of E^{truth} and η_{det} , and with the corrections to E^{reco} derived from E^{truth} using the same numerical inversion procedure as before. The γ calibration corrects the jet γ and p_T only, not the full four-momentum, as in other calibration steps.

After the absolute JES and γ calibration step, EM-scale jets are considered to be at the EM+JES scale.

3.4.3.3.4 GLOBAL SEQUENTIAL CALIBRATION The global sequential calibration (GSC) step is then used to account for differences in the calorimeter response and in the jet reconstruction algorithm due to the particle composition of the jet and the energy distribution in the calorimeter, both of which vary between quark- and gluon-initiated jets. Quark-initiated jets generally penetrate further into the calorimeter, as they contain hadrons with a harder p_T spectrum and a more centrally concentrated energy distribution, whereas gluon-

initiated jets tend to contain hadrons with a higher multiplicity, a softer p_T spectrum, and a wider energy distribution, resulting in a lower calorimeter response. The GSC thus aims to minimize these differences between jet flavors using information from the inner detector, the muon spectrometer, and the calorimeter in order to remove the remaining dependence of the JES on the longitudinal and transverse features of the jet and to improve the overall JES resolution.

Four-momentum corrections are applied independently and sequentially for each of the following five GSC observables:

1. f_{tileo} = fraction of jet energy in first layer of hadronic tile calorimeter ($|\eta_{\text{det}}| < 1.7$);
2. f_{LAr_3} = fraction of jet energy in third layer of EM LAr calorimeter ($|\eta_{\text{det}}| < 3.5$);
3. n_{trk} = number of tracks with $p_T > 1$ GeV ghost-associated to jet ($|\eta_{\text{det}}| < 2.5$);
4. \mathcal{W}_{trk} = average p_T -weighted transverse distance in $\eta - \phi$ plane from jet center to all tracks of $p_T > 1$ GeV ghost-associated to jet ($|\eta_{\text{det}}| < 1.5$);
5. n_{segments} = number of muon track segments associated to jet ($|\eta_{\text{det}}| < 2.7$).

Each correction effectively removes the dependence of the jet energy response on the corresponding observable without altering the overall energy scale at each stage. Observables (1) and (2) measure the penetration of the jet, (3) and (4) measure the particle multiplicity and transverse profile of the jet, and (5) measures the response of high- p_T jets not fully contained in the calorimeter.

3.4.3.3.5 IN SITU CALIBRATION The final calibration step uses *in situ*, or real data, events to account for any remaining differences between the jet response in data and MC due to imperfect descriptions of the detector geometry, material, and response in simulation.

The calibration is derived by comparing jets to well-measured reference objects in order to quantify the differences in jet response between data and MC.

The response $\mathcal{R}_{\text{in situ}}$ is defined as the average ratio of the jet p_{T} to the reference object p_{T} , binned in the reference object p_{T} . $\mathcal{R}_{\text{in situ}}$ is proportional to the response of the calorimeter to jets at the EM+JES scale. The ratio $c = \mathcal{R}_{\text{in situ}}^{\text{data}} / \mathcal{R}_{\text{in situ}}$ provides an estimate of the ratio of the JES in data to that in MC. This ratio is then transformed into a function of the probe jet p_{T} through numerical inversion in order to derive the additional correction factor to be applied to reconstructed jets in data.

The following *in situ* calibration methods are applied, with the resulting calibration constants derived in each method statistically combined into a final overall *in situ* calibration covering the full detector:

1. eta-intercalibration: corrects the energy scale of forward jets using well-measured central jets in dijet events;
2. $Z(\gamma) + \text{jet}$: corrects the energy scale of central jets using well-calibrated $Z(\gamma)$ objects that decay to electron or muon pairs, allowing for the p_{T} response of a recoiling jet to be measured;
3. multijets balance (MJB): corrects the energy scale of central high- p_{T} jets recoiling against a system of well-calibrated low- p_{T} multijets.

3.4.3.4 JET QUALITY SELECTION

After calibration of the jet energy scale, a quality selection is applied to the calibrated jets in order to suppress pileup jets and remove bad, or fake, jets.

While the event-level energy contribution from pileup is subtracted from the signal jets during JES calibration, local fluctuations in pileup activity can produce further pileup jets that still need to be accounted for. These pileup jets can be discriminated from the jets produced in the hard scatter process with the jet vertex tagger (JVT) tool [120], a two-dimensional likelihood function representing the relative probability for a jet to be of signal type. The JVT likelihood is constructed from two variables, corrJVF and R_{p_T} , as defined below:

$$\text{corrJVF} = \frac{\sum_k p_T^{\text{trk}_k}(\text{PV}_o)}{\sum_l p_T^{\text{trk}_l}(\text{PV}_o) + (\sum_{n \geq 1} \sum_l p_T^{\text{trk}_l}(\text{PV}_n)) / (k \cdot n_{\text{trk}}^{\text{PU}})}$$

$$R_{p_T} = \frac{\sum_k p_T^{\text{trk}_k}(\text{PV}_o)}{p_T^{\text{jet}}}, \quad (3.22)$$

where $\sum_k p_T^{\text{trk}_k}(\text{PV}_o)$ is the scalar sum- p_T of the tracks associated to the jet and produced in the hard scatter interaction, $p_T^{\text{PU}} = \sum_{n \geq 1} \sum_l p_T^{\text{trk}_l}(\text{PV}_n)$ is the scalar sum- p_T of the tracks associated to the jet and produced in any pileup interaction, $n_{\text{trk}}^{\text{PU}}$ is the total number of pileup tracks in the event, $k = 0.01$ is a scaling factor that corrects for the linear increase of $\langle p_T^{\text{PU}} \rangle$ with $n_{\text{trk}}^{\text{PU}}$, and p_T^{jet} is the transverse momentum of the jet. The corrJVF, R_{p_T} , and JVT distri-

butions are peaked at zero for pileup jets and tending towards one for hard scatter jets, as illustrated in Figure 3.33. Therefore, low- p_T jets with JVT values below a certain threshold are discarded.

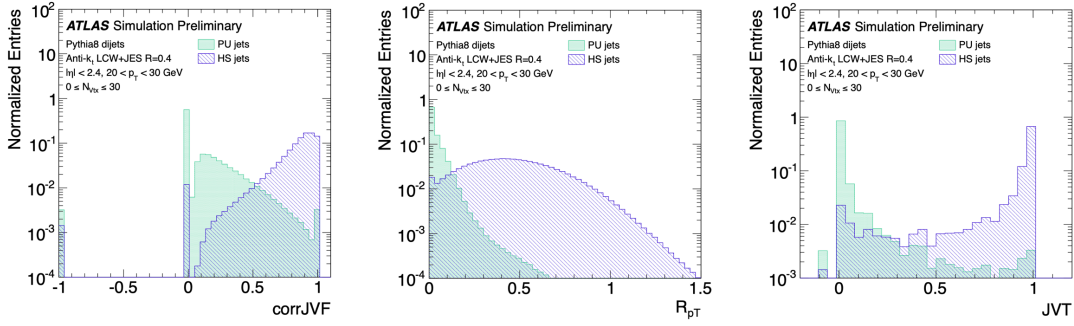


Figure 3.33: Distributions of corrJVF (left), R_{pT} (center), and JVT (right) for pileup and hard scatter jets with p_T between 20 and 30 GeV [120].

Events can also contain bad quality or fake jets originating from sources other than collisions, such as beam induced backgrounds from muons produced in proton interactions with the detector material upstream of the interaction point, cosmic ray muons produced in the atmosphere, and noisy LAr calorimeter cells not accounted for in data quality monitoring. A jet cleaning procedure is thus implemented to identify and reject these background jets through a set of quality selection criteria, based on signal pulse shapes in the LAr calorimeters, energy ratios, and tracks, optimized to discriminate between good and bad jets [121].

The jet cleaning procedure defines two working points: `LooseBad` and `TightBad`, with the `LooseBad` criteria defined for high good jet efficiency and high fake jet rejection and

the `TightBad` criteria defined for slightly lower good jet efficiency but much higher fake jet rejection. A jet is tagged as `LooseBad` if it satisfies any of the following criteria:

- $f_{\text{HEC}} > 0.5$ and $|f_Q^{\text{HEC}}| > 0.5$ and $\langle Q \rangle > 0.8$;
- $|E_{\text{neg}}| > 60 \text{ GeV}$;
- $f_{\text{EM}} > 0.95$ and $|f_Q^{\text{LAr}}| > 0.8$ and $\langle Q \rangle > 0.8$ and $|\eta| < 2.8$;
- $f_{\max} > 0.99$ and $|\eta| < 2$;
- $f_{\text{EM}} < 0.05$ and $f_{\text{ch}} < 0.05$ and $|\eta| < 2$;
- $f_{\text{EM}} < 0.05$ and $|\eta| \geq 2$;

where f_{HEC} and f_{EM} are the fractions of jet energy deposited in the HEC and EM calorimeters, respectively; f_{\max} is the maximum energy fraction deposited in any single calorimeter layer; f_{ch} is the jet charged fraction, equal to the ratio of the scalar sum- p_T of the tracks from the PV to the jet p_T ; $\langle Q \rangle$ is the average jet quality, defined as the energy-squared-weighted average of the pulse quality of the calorimeter cells $Q_{\text{cell}}^{\text{LAr}}$ in the jet; f_Q^{HEC} and f_Q^{LAr} are the fractions of energy in the HEC and LAr calorimeter cells, respectively, with poor pulse quality; and $|E_{\text{neg}}|$ is the energy sum of all the cells with negative energy. The first two criteria identify jets produced from sporadic noise bursts in the HEC, the third identifies jets produced from noise in the EM calorimeter, and the last three identify jets produced from hardware issues, beam-induced background, and cosmic muon showers.

A jet is tagged as `TightBad` if it satisfies any of the `LooseBad` criteria or if it satisfies the additional selection $f_{\text{ch}}/f_{\max} < 0.1$ for $|\eta| < 2.4$. A jet is tagged as a `Loose` jet if it is not

tagged as a `LooseBad` jet, and a jet is tagged as a `Tight` jet if it is not tagged as a `TightBad` jet. The efficiency of the jet quality selection is measured using a tag-and-probe method in dijet events enriched with good jets, with the tag jet required to pass the `Tight` criteria and to be back-to-back with the probe jet. The jet quality selection efficiency is over 99.9% for `Loose` jets and over 99.5% for `Tight` jets across all jet η and is over 99.5% for `Loose` jets and over 95% for `Tight` jets across all p_T , as illustrated in Figure 3.34.

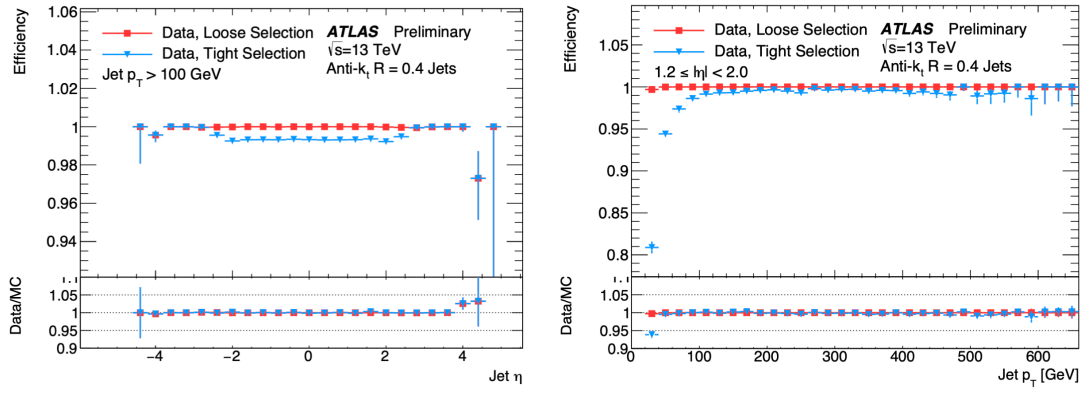


Figure 3.34: Jet cleaning efficiency for `Loose` (red) and `Tight` (blue) selections as a function of jet η (left) and p_T (right) GeV [120].

4

Emerging Jets Search

The ongoing search for an emerging jets signal at ATLAS Run 2 is presented here. The emerging jets signature consists of pair-produced TeV-scale mediators, each decaying to a SM quark and a dark quark, and resulting in a four-jet final state, with two jets having properties characteristic of a jet emerging from the decays of long-lived dark pions in the dark sector, in conjunction with a multitude of displaced vertices in the event. The analysis is

to be performed on 139 fb^{-1} of proton-proton collision data at $\sqrt{s} = 13 \text{ TeV}$ recorded at ATLAS between 2015 and 2018. The search is based on identifying long-lived dark particles, with millimeter to centimeter lifetimes, with displaced decays within calorimeter jets; such long-lived particle decays can be reconstructed in the inner detector as secondary vertices and associated to nearby jets. The high jet multiplicity and hard p_T spectrum of the signal provides some immediate discrimination from the QCD multijet background, but background reduction remains the largest obstacle to the search for this rare and small-strength process. A set of benchmark signal models are used to study the sensitivity of the detector to the emerging jets signal and to design the analysis selections. This novel search was developed as the first of its kind at ATLAS in Run 2.

4.1 SIGNAL MODEL

Emerging jets arise as new reconstruction objects in models with a confining hidden sector and a shared asymmetry between dark and baryonic matter, known as dark QCD. The dark QCD model consists of a dark gauge group and a new TeV-scale matter field, charged under both QCD and dark QCD, that generates the shared asymmetry and relates the two running gauge couplings such that the dark confinement scale is comparable to that of QCD at the GeV scale. The hidden sector of dark QCD contains a dark proton, the lightest dark baryon, that acts as the dark matter candidate, along with a plethora of unstable

particles, with dark mesons that decay to the visible sector with large and varying displacements, leading to the emerging jets signal. Here, the dark mesons are taken to decay to SM quarks with lifetimes of order millimeters to centimeters in order for most of the decays to occur inside the inner detector, enabling the corresponding displaced vertices and outgoing tracks to be reconstructed at ATLAS. Generally, a dark QCD model can produce emerging jets if it includes a large hierarchy between the mediator mass and dark sector scale, a strong coupling in the hidden sector to produce a large track multiplicity, and macroscopic decay lengths of the dark sector hadrons into the visible sector.

The dark QCD model considered in this analysis is that of a confining hidden sector with a non-Abelian $SU(N_d)$ gauge symmetry, where $N_d \geq 2$ is the number of dark colors, with n_f dark quarks, where n_f is the number of dark quark flavors, and the dark quarks q_d are fundamentals of $SU(N_d)$. The parameters defining the dark sector are the dark confinement scale Λ_d , which sets the approximate mass of the dark hadrons, and the mass of the pseudo-Goldstone boson, or dark pion π_d , both of which are of order 1 to 10 GeV. Dark baryon number is conserved, leading to a stable dark proton, but no such dark meson conserved charge exists, allowing dark mesons to decay to SM particles. The heavy scalar mediator X_d , a bifundamental under both QCD and dark QCD, connects the visible and dark sectors. It can be pair-produced via gluon fusion or quark-antiquark annihilation and then decays to a right-handed down-type SM quark and a dark quark via a Yukawa coupling (see

Figure 2.4), resulting in a four-jet final state with two QCD jets and two emerging jets. The collider phenomenology is dominated by dark meson production, since dark baryon production is suppressed in QCD-like theories, and all heavier meson resonances are expected to rapidly decay to dark pions, which then decay to down-type quarks.

In this analysis, five simplified benchmark signal models are investigated in order to examine the phenomenology of the emerging jets signal over a range of dark sector mass scales. These benchmarks are referred to henceforth as Model A, Model B, Model C, Model D, and Model E. Each represents a simplified model of the dark QCD sector in the context of the Hidden Valley model phenomenology [122]. The particle content of the simplified dark sector includes the scalar mediator, dark quarks, dark gluons, dark pions, and dark rhos. This limited hadron content stems from a simplified dark sector fragmentation, which produces only dark scalar mesons and dark vector meson resonances, but no dark baryons. Motivated by QCD, the dark rho masses are taken to be larger than the dark confinement scale, and the dark pion masses are taken to be smaller than the dark confinement scale, such that the dark vectors rapidly decay to the dark pions before they decay to SM particles.

The benchmark models are defined by the following parameters:

- the number of dark colors N_d , which defines the dimension of the dark gauge group;
- the number of dark quark flavors n_f , where the dark quarks are the fundamental representations of the dark gauge group;

- the $n_f \times 3$ matrix of Yukawa couplings between the right-handed down-type SM quarks and the dark quarks;
- the mediator width;
- the dark sector confinement scale Λ_d , which dictates the approximate mass of the dark hadrons;
- the dark quark masses m_{q_d} , with one per dark quark flavor;
- the dark rho mass m_{ρ_d} ;
- the dark pion mass m_{π_d} ;
- the scalar mediator mass m_{X_d} ;
- the dark pion lifetime $c\tau_{\pi_d}$.

In the benchmarks considered in the analysis, the following assumptions are made:

- the dark gauge group has three dark colors $N_d = 3$, seven dark flavors $n_f = 7$, and a QCD-like spectrum;
- all Yukawa couplings are negligible except for the coupling to the down quark (i.e. all dark pions decay to down quarks);
- the scalar mediator width is small compared to the detector mass resolution: $\Gamma_{X_d} = 10 \text{ GeV}$;
- all dark quarks are mass degenerate, with the mass equal to the dark confinement scale;
- the dark pion mass is equal to one half of the dark quark mass and one fourth of the dark rho mass.

The dark pion mass m_{π_d} , dark pion lifetime $c\tau_{\pi_d}$, and mediator mass m_{X_d} are then left as free parameters. The benchmark models represent the potential dark sector energy scales and are defined by the dark pion mass and related dark confinement scale. The other free parameters, the mediator mass and dark pion lifetime, are then varied for each model to generate the signal grid spanning the parameter space. The mediator mass is fluctuated around 1 TeV, and the dark pion lifetime is spread across values within the range of the detector sensitivity.

Table 4.1 lists the parameters for each benchmark model used in the Emerging Jets search. The models span the range of the dark QCD sector scale, with Models A, B, and C representing the intermediate mass regimes, Model D representing the very high mass regime, and Model E representing the very low mass regime. Heavier dark sectors produce more visible hadrons per dark pion decay, or larger track multiplicities per displaced vertex, and shorter average dark pion transverse decay distances, since lighter states are more boosted on average and are therefore more likely to decay outside of the calorimeter and thus not be clustered into jets, for a fixed mediator mass and dark pion lifetime. Additionally, the dark pion multiplicity is inversely related to the mass of the model. Therefore, Model D corresponds to the upper limit of the search sensitivity, where the emerging jets topology starts to break down, since most of the jet energy is contained in a single massive dark pion, and the signal starts to look more like a standard displaced dijet signature. Meanwhile, Model

E corresponds to the lower limit of the search sensitivity, where the reconstruction capabilities of the ATLAS detector become inefficient, since lighter dark pions yield fewer, softer tracks, making the resulting displaced vertices more challenging to reconstruct.

	Model A	Model B	Model C	Model D	Model E
Λ_d [GeV]	10	4	20	40	1.6
m_{ρ_d} [GeV]	20	8	40	80	3.2
m_{π_d} [GeV]	5	2	10	20	0.8

Table 4.1: Simplified benchmark model parameters for the emerging jets signal.

mediator mass m_{X_d} [GeV]	dark pion lifetime $c\tau_{\pi_d}$ [mm]
1400	300
	150
	75
	20
	5
	2
1000	300
	150
	75
	5
	2
600	300
	150
	20
	2
	1
	0.5

Table 4.2: Scalar mediator masses and dark pion lifetimes defining the emerging jets signal parameter space.

Table 4.2 lists the mediators masses and dark pion lifetimes defining the parameter space of the emerging jets signal. The mediator masses and dark pion lifetimes considered in this search span the theoretically-motivated parameter space, as described above and in Section 2, where a reasonable search sensitivity is expected. Lower mediator masses produce softer jets, so if the mediator mass being considered is too low, there is no means of background discrimination. Meanwhile, the average decay distance traveled by the dark pions is proportional to their lifetimes, with longer lifetimes corresponding to more dark mesons decaying in or outside of the calorimeters. This results in jets with lower p_T and different shapes than usual, since the particles produced from the longest-lived and most energetic dark pions are not included in the reconstructed jets and are thus not counted towards the jet energies. The displaced track and vertex reconstruction algorithms for very short and very long dark pion lifetimes are also highly inefficient. These limitations motivate the ranges of mediator masses and dark pion lifetimes chosen for consideration in the analysis.

For this search, a 90-point signal grid is designed that spans the parameter space defined by the dark sector models, mediator masses, and dark pion lifetimes described above. A signal point is defined by a distinct combination of the model, mediator mass, and dark pion lifetime, where five models, with three mediator masses per model and six different dark pion lifetimes per mediator mass, are considered. Each of the eighteen mediator mass - dark pion lifetime points listed in Table 4.2 is combined with each of the five models described

in Table 4.1 to form the full 90-point signal grid used in the analysis.

The full details of the event generation of the simulated signal samples are described in Section 4.2.2.

4.2 DATA AND MC SAMPLES

The Emerging Jets analysis plans to make use of the full Run 2 ATLAS dataset, reprocessed with nonstandard reconstruction. Monte Carlo simulated samples are also generated for the benchmark signal models in order to optimize signal region definitions, model the expected backgrounds, and estimate the sensitivity of the search. The details of the ATLAS dataset and its processing are described in Section 4.2.1, and the details of the MC sample production are described in Section 4.2.2.

4.2.1 DATA SAMPLES

This analysis uses 139 fb^{-1} of $\sqrt{s} = 13 \text{ TeV}$ pp -collision data, collected by ATLAS during the 2015, 2016, 2017, and 2018 data taking periods. The total integrated luminosity is 36.2 fb^{-1} , 44.3 fb^{-1} , and 58.5 fb^{-1} for 2015+2016, 2017, and 2018, respectively. The uncertainty on the total luminosity is 2.1%, 2.4%, and 2.0% for 2015+2016, 2017, and 2018, respectively, and 1.7% for the full Run-2 dataset. The integrated luminosities and uncertainties are determined as described in [53]. The average mean number of interactions per crossing $\langle\mu\rangle$ is 13.4, 25.1, 37.8, and 36.1 for data-taking years 2015, 2016, 2017, and 2018, respectively, and 33.7

for the full Run 2 dataset. The peak $\langle\mu\rangle$ is approximately 25, 50, 65, and 70 for the 2015, 2016, 2017, and 2018 data, respectively, as illustrated in Figure [3.3](#).

The data for the Emerging Jets analysis is collected with jet triggers, as described in [3.2.4](#), with the lowest unprescaled four-jet triggers used to select signal events and a heavily prescaled single jet trigger used to select background events, which is then reconstructed using the LLP-specialized Large Radius Tracking and secondary vertexing algorithms, as described in Sections [3.4.1.2](#) and [3.4.2.2](#), respectively, to improve sensitivity to the displaced tracks and vertices from LLP decays characteristic of the signal. Such reconstruction is CPU-intensive and requires a particular data-flow, as described below.

4.2.1.1 DATA-FLOW

The data-flow at ATLAS is a sequential processing of the dataset to smaller size and more specific contents, where the size and contents of the dataset is reduced at each step by selecting events and objects of interest to specific physics groups and analyses with tighter criteria as the processing progresses. A particular data-flow using the specialized `DRAW_RPVLL` and `DAOD_RPVLL` streams is implemented for R-parity violating and long-lived particle, or RPVLL, searches to increase sensitivity to displaced signatures.

Since the displaced track and vertex reconstruction algorithms required by RPVLL analyses are computationally expensive, only a subset of the full `physics_Main` dataset is reconstructed with these specialized LLP algorithms in order to reduce the number of events

being processed and thereby reduce CPU consumption. `RAW` events from `physics_Main` are first filtered with RPVLL-specific selections to the `DRAW_RPVLL` stream. `DRAW_RPVLL` events are then reconstructed with Large Radius Tracking and secondary vertexing and saved to the `DAOD_RPVLL` stream, where the `DAOD_RPVLL` format is a specialized AOD format including additional information produced in the nonstandard reconstruction algorithms. RPVLL reconstruction is performed as a central reprocessing of the dataset, where the `RAW` information from the detector that is to be processed with standard reconstruction is filtered and saved to be reprocessed with RPVLL reconstruction at a later date. The full Run 2 dataset, reprocessed with `DRAW_RPVLL` filtering and `DAOD_RPVLL` reconstruction, is to be used in this analysis.

The `DAOD_RPVLL` datasets are then processed further to `DAOD_EXOT23` derivations, where a derivation or `DAOD` is a derived AOD, and finally to n-tuples to further reduce the sample size at each step by applying more analysis-specific selections. Derivations are processed officially at ATLAS with the ATLAS software framework `Athena`, and n-tuples are produced offline with `EmergingJetsAnalysis`, the ROOT- and EventLoop-based analysis code framework for the Emerging Jets analysis group.

The data-flow described above is summarized as follows:

`RAW (physics_Main) → DRAW_RPVLL → DAOD_RPVLL → DAOD_EXOT23 → EJs`
n-tuples .

4.2.1.1.1 DRAW_RPVLL Reconstructing events with the Large Radius Tracking and secondary vertexing algorithms required by this search is quite computationally expensive and is only necessary for a relatively small group of analyses. As such, the computational resources required for this special reconstruction can be reduced by filtering the events to be run over. Events relevant to long-lived particle searches are selected from the full ATLAS dataset with a collection of filters that define the selection criteria based on the needs of the analyses that use them. The filters, each unique to a specific LLP analysis and specifying selections based on basic triggers and standard physics object kinematics, are run over RAW events in the the `physics_Main` stream at Tier-0 throughout the year, and events passing any of the defined filters are saved in RAW format to the `DRAW_RPVLL` stream for later reprocessing. This filtering reduces the size of the data to be reprocessed with nonstandard reconstruction algorithms to around 5 – 10% of the full `physics_Main` dataset.

The filter rates for a representative run in 2018 are shown in Figure 4.1, with the rate breakdown per filter per lumi-block shown on the left and the overall rate as a function of the instantaneous luminosity shown on the right, where the filter rate is defined as the rate of events selected by the `DRAW_RPVLL` filters, or the number of `DRAW_RPVLL` events divided by the number of `physics_Main` events, divided by the time covered by the lumi-block. The rate of each individual filter in a given lumi-block is represented by a different color and stacked on top of one another, while the overall rate for the entire stream is

shown in black. The sum of the individual filter rates is larger than the overall rate, as some events can be selected by more than one filter. The overall `DRAW_RPVLL` rate is directly dependent on the instantaneous luminosity.

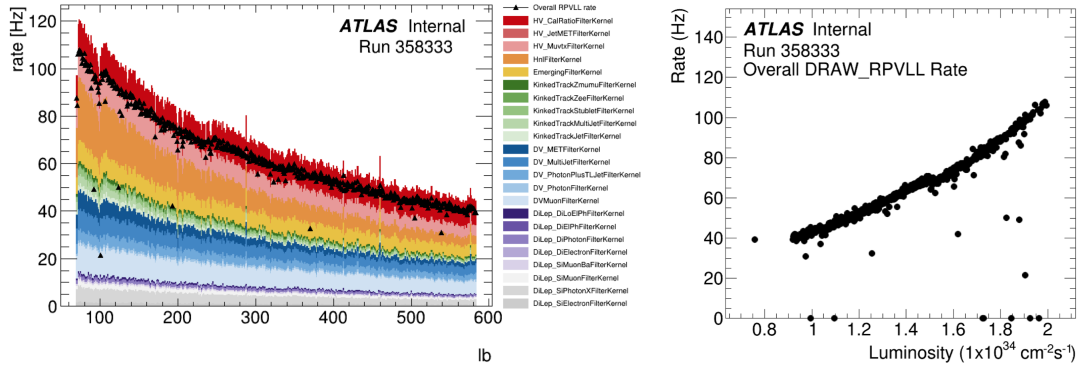


Figure 4.1: The rate of events selected by the `DRAW_RPVLL` filters for a representative run (Run 358333) in 2018. Left: the stacked rates of each individual filter as a function of lumi-block, with the overall rate of the stream shown in black. Right: the overall filter rate as a function of instantaneous luminosity.

Figure 4.2 displays the filter rates for a representative set of runs throughout 2017, with the fraction of the total stream occupied by each individual filter per run shown on the left and the stacked individual filter rate per run shown on the right. The rate peaks at the beginning of the run when the instantaneous luminosity is maximal and decreases throughout the run as the luminosity decreases.

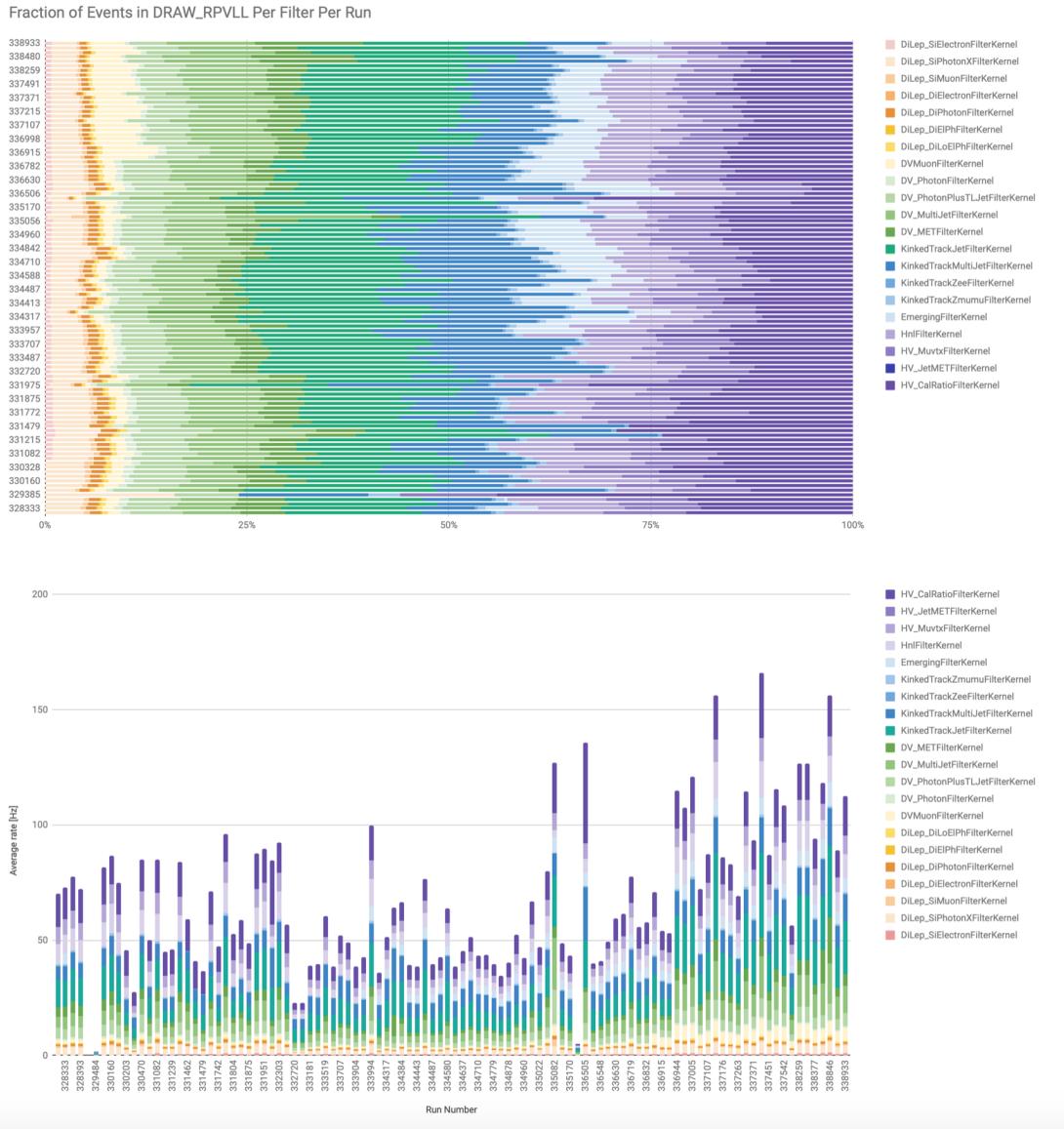


Figure 4.2: DRAW_RPVLL filter rates for a representative set of runs in 2017. Top: the fraction of the total DRAW_RPVLL stream occupied by each individual filter per run. Bottom: the stacked individual filter rates per run.

The average `DRAW_RPVLL` rate as a function of the average $\langle \mu \rangle$ throughout 2017 is illustrated in Figure 4.3, where the average `DRAW_RPVLL` rate is defined as the number of `DRAW_RPVLL` events divided by the number of `physics_Main` events times the average `physics_Main` rate of the run. The average rate increases approximately exponentially with the pileup, in part because standard quality requirements and calibrations are not defined at filter level; thus, selections are kept loose to maintain high signal efficiency, as well as to allow for data-driven background estimates, and are therefore not necessarily robust against pileup.

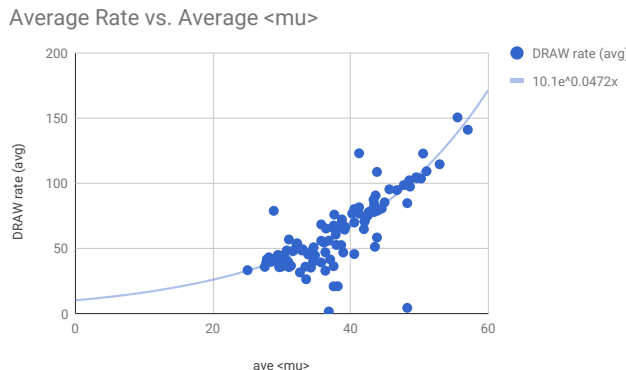


Figure 4.3: The average overall `DRAW_RPVLL` rate in 2017 as a function of average $\langle \mu \rangle$. The rate increases approximately exponentially with pileup.

Throughout data-taking, the average overall rate of the `DRAW_RPVLL` stream is attempted to be kept under around 30 Hz, but with increased pileup, this limitation becomes increasingly difficult to meet and was often exceeded during Run 2, as evidenced in Figure 4.3. Many efforts were taken between data-taking periods in 2017 and 2018 to tighten the

filter selections and reduce the `DRAW_RPVLL` rates in the face of heavy pileup conditions.

The `Emerging` filter, developed specifically for the Emerging Jets search, defines the event selections applied for use in the EJs analysis. Two sets of selections are included in the filter to collect four-jet events for performing the signal search and dijet events for estimating backgrounds, as described below:

- four-jet signal selections: the filter selects emerging jet signal-like events passing the lowest unprescaled four-jet trigger and containing at least four jets with $p_T > 120$ GeV and $|\eta| < 2.5$; the specific four-jet triggers included in the filter are:
 - `HLT_4j90`;
 - `HLT_4j100`;
 - `HLT_4j110`;
 - `HLT_4j120`;
 - `HLT_4j130`;
 - `HLT_4j140`;
 - `HLT_4j150`;
- dijet background selections: the filter also selects dijet background events passing a heavily prescaled single-jet trigger and containing at least two jets with $p_T > 120$ GeV and $|\eta| < 2.5$; the specific single-jet trigger used in the filter is:
 - `HLT_j110`.

The jet- p_T and $-|\eta|$ thresholds are implemented to correspond to the offline analysis cuts and to keep the filter rate relatively low.

Further details on the `DRAW_RPVLL` stream, including the filtering code package and the work done to monitor the stream rates, can be found in Appendix [B](#).

4.2.1.1.2 DAOD_RPVLL Once events are filtered through the `DRAW_RPVLL` stream, the data is reconstructed with nonstandard algorithms specific to LLPs and output in the `DAOD_RPVLL` format, a specialized AOD format containing additional information from LLP reconstruction, namely large- d_{o} tracks from Large Radius Tracking added to the standard track container and new `VrtSecInclusive` vertex containers from secondary vertexing. These additions are included on top of the standard contents of the AOD, where the AOD, or Analysis Data Object, format is the common analysis format output by reconstruction, readable in ROOT, and containing event and physics object information in the form of “xAOD” objects.

4.2.1.1.3 DAOD_EXOT23 The next step in data processing is the production of derivations from `DAOD_RPVLL` datasets in order to further reduce the size of the data, apply necessary “AOD-fix” corrections, and append additional required information.

As many physics groups need to be able to run over data samples frequently throughout the course of developing and running the analyses in order to add new variables and cuts, fix bugs, update combined performance (CP) group recommendations, and apply systematics, analysis-specific derivations are produced centrally as the intermediate format between full data samples and analysis-level n-tuples. A derivation, or `DAOD`, which stands for “derived AOD”, is of the same output format as an AOD, containing xAOD objects, but is of

a significantly reduced size and contains less information. The derivation production step reduces the dataset size by removing irrelevant information, with a set of selections applied based on the needs of the physics analyses using the corresponding derivations. Additional information not centrally available in the original AODs can also be added in this step.

The four main operations used to build derivations from the full data are illustrated in Figure 4.4 and summarized below:

- skimming: the removal of whole events from the dataset; skimming can only be processed on certain quantities, namely unique single values for given objects returnable by simple methods, such as object kinematics or trigger decisions;
- thinning: the removal of whole objects from events within the dataset, while retaining the rest of the event;
- slimming: the removal of variables from objects uniformly across events in the dataset, while retaining the rest of the object; slimming can either remove individual variables or whole collections of objects; most derivations utilize smart slimming, or the centralized slimming of xAOD collections based on common requirements among analyses, which saves all basic variables needed for analysis and those required by CP tools for a given object type and removes the rest from the given collection; extra variables can be included individually on top of the smart-slimmed containers as needed;
- augmentation: the addition of new information to the dataset not found in the original input; augmentation can take place in one of two ways:
 1. the decoration of existing reconstruction objects with additional information, known as “dressing”;
 2. the addition of new reconstruction object containers, such as custom on-the-fly jet collections built with modified algorithms and restored collections that were removed in AOD reduction.

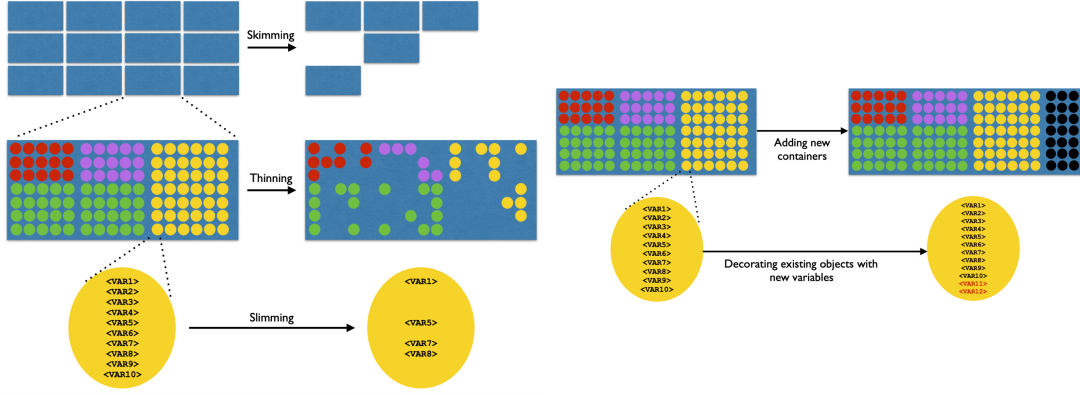


Figure 4.4: Schematics of the four major DAOD operations to build derivations from full data. The skimming, thinning, and slimming operations (left) are used to remove unneeded information and to reduce the overall size of the dataset, and the augmentation step (right) is used to add needed information to objects or events not available in the original dataset [123].

This analysis uses the DAOD_EXOT23 derivation, designed specifically for the Emerging Jets search and based off of the SUSY-DV DAOD_SUSY15 derivation. The derivation skims the data based on a set of four-jet and single-jet triggers, thins the track particles based on momentum, slims away the unneeded object types, like leptons, photons, and missing energy, and adds multiple truth jet types.

The DAOD_EXOT23 derivation first skims the data by selecting events passing any of the below list of triggers, with the four-jet triggers designed to target four-jet signal-like events and the single-jet triggers designed to target dijet background-like events:

- Four-jet triggers for EJs signal:
 - HLT_4j90
 - HLT_4j100
 - HLT_4j110
 - HLT_4j120
 - HLT_4j130
 - HLT_4j140
 - HLT_4j150
- Single-jet triggers for dijet backgrounds:
 - HLT_j15
 - HLT_j25
 - HLT_j35
 - HLT_j45
 - HLT_j55
 - HLT_j60
 - HLT_j85
 - HLT_j100
 - HLT_j110
 - HLT_j150
 - HLT_j175
 - HLT_j200
 - HLT_j260
 - HLT_j300
 - HLT_j320
 - HLT_j340
 - HLT_j360
 - HLT_j380
 - HLT_j400
 - HLT_j420
 - HLT_j440
 - HLT_j450
 - HLT_j460
 - HLT_j480
 - HLT_j500
 - HLT_j520

Next, the track particle container is thinned, removing tracks with $p_T < 0.5 \text{ GeV}$.

Then, truth jet containers are added to the derivations during MC production. Standard truth jets, which are slimmed away by default during AOD production, are restored, and custom truth dark jets are built on-the-fly. Truth dark jets are built by clustering dark truth particles with the anti- k_t algorithm for radius $R = 0.4$ and $R = 1.0$. For details on the reconstruction of truth dark jets, see Appendix C.

Finally, the slimming of the data is applied, saving only the below jet, b-jet, track, primary vertex, secondary vertex, and truth (in the case of MC production) containers to the final derivation output:

- Smart slimming containers:
 - `AntiKt4EMTopoJets`
 - `AntiKt4LCTopoJets`
 - `AntiKt4EMPFlowJets`
 - `BTagging_AntiKt4EMTopo`
 - `BTagging_AntiKt4EMPFlow`
 - `InDetTrackParticles`
 - `PrimaryVertices`
- All-variable slimming containers:
 - `AntiKt4EMTopoJets`
 - `AntiKt4LCTopoJets`
 - `AntiKt4EMPFlowJets`
 - `BTagging_AntiKt4EMTopo`
 - `BTagging_AntiKt4EMPFlow`
 - `InDetTrackParticles`
 - `PrimaryVertices`
 - `VrtSecInclusive_SecondaryVertices`
 - `VrtSecInclusive_SecondaryVertices_Leptons`
 - `VrtSecInclusive_All2TrksVertices`
 - `TruthParticles`
 - `TruthEvents`
 - `TruthVertices`
 - `AntiKt4TruthJets`
 - `AntiKt4TruthDarkJets`
 - `AntiKt10TruthDarkJets`

The objects of the smart slimming containers have some of their less commonly necessary associated variables removed, as described above, while the objects in the all-variable slimming containers retain all of their associated variables.

Full derivation details can be found in the DAOD_EXOT23 code on gitlab [[124](#)].

4.2.1.1.4 N-TUPLES Flat n-tuples are then produced from derivations with analysis-specific code to include objects and variables of interest to the search. Tools, calibrations, and common object selections as recommended by combined performance groups are applied at this stage to the xAOD objects and saved to the n-tuples for analysis.. The n-tuples for this analysis are generated with `EmergingJetsAnalysis` , a ROOT- and EventLoop-based analysis code framework developed specifically for the Emerging Jets search, the code of which can be found on gitlab [[125](#)].

4.2.1.1.5 DATA QUALITY Finally, poor quality events are filtered out offline. Monitoring algorithms are run during reconstruction to assess the quality of the data based on detector hardware and software conditions in any given lumi-block of a run. Flags associated to the quality of the data are then fed to Good Runs Lists (GRLs), which are XML files listing each run and the range of quality lumi-blocks in each. Analyses read in GRLs to determine which parts of the data are usable and which should be discarded.

4.2.2 MONTE CARLO SAMPLES

Simulated Monte Carlo samples are produced for use in the analysis to study the sensitivity of the detector to long-lived particle decays and emerging jet objects, to define signal objects and signal regions, to estimate the efficiencies of physics object reconstruction and signal event selection, and to validate the background estimation techniques.

4.2.2.1 MC SIGNAL SAMPLES

Signal samples are produced for the simplified benchmark models in the defined signal grid, as described in Section 4.1. As event generation is CPU intensive, at the time of writing, 36 of the 90 signal grid points have been officially produced and are currently available for use in the analysis.

Signal events are generated and parton showering and hadronization are simulated with the Hidden Valley model implementation [126, 127] of PYTHIA 8.230 [80], which simulates the production and dynamics of the dark sector with a running dark coupling. The hard scatter process is simulated using the NNPDF23LO PDF set [128, 129], which is fit with the neural network approach developed by the NNPDF collaboration and uses a global data set including LHC data from ATLAS and CMS in 2010 and 2011. The modeling of the parton showering, hadronization, and multiparticle interaction is optimized with the A14 (ATLAS 2014) tune [73].

The Hidden Valley (HV) model refers to a general class of models containing a new confining gauge group in a light hidden sector, or the valley, which is decoupled from the visible SM sector at some relatively low energy and contains light particles charged under the hidden sector and neutral under the visible sector, as well as a communicator between the two sectors which is coupled to both. Valley particles form HV-neutral bound states, some of which can decay to SM particles with observable lifetimes. The signal model described in [4.1](#) is one such HV scenario, where the dark sector corresponds to the hidden sector, or hidden valley. The HV is indirectly detectable through the effects of hidden sector radiation on the kinematic distributions of the recoiling visible particles.

The HV implementation in **Pythia** is designed to study such recoil effects. In the **Pythia** HV model, traditional showering is extended to include the new hidden sector radiation, which is interleaved with the normal QED and QCD radiation. Additional QCD-like hadronization is also implemented in the hidden sector. The HV hadronization is somewhat simplified, disregarding HV baryons and producing only pseudoscalar and vector HV mesons. The HV model contains the following properties and particle content:

- the $SU(N_v)$ gauge group, where N_v is the number of HV colors;
- twelve (12) HV partners to the SM fermions, F_v , each of which is charged under both the visible and hidden sectors, couples flavor-diagonally to the corresponding SM field, and has the same charge and color as its SM partner;
- the HV gauge boson, which is the massless HV gluon g_v ;

- n_{flav} copies of the HV quark q_v , which is a massive particle charged only under the hidden sector, where all q_v species are identical except for their flavor;
- flavor-diagonal and off-diagonal HV pions π_v , which are spin-0 HV mesons that can decay back to the SM;
- flavor-diagonal and off-diagonal HV rhos ρ_v , which are spin-1 HV mesons that can decay back to the SM

The HV fermion partners F_v are pair-produced via gluon fusion or quark-antiquark annihilation: $gg \rightarrow F_v \bar{F}_v$ or $q\bar{q} \rightarrow F_v \bar{F}_v$. The produced F_v will then radiate SM and HV gluons and eventually decay to its SM partner and the HV quark: $F_v \rightarrow f q_v$.

In the signal models generated for this analysis, the HV partner of the down quark, D_v , is taken to be the TeV-scale scalar mediator X_d , with spin = 0, charge = 1/3, and width = 10 GeV, which decays to a down quark and an HV, or dark, quark. The mass of the mediator is a free parameter determined by the signal grid point, with the masses under consideration listed in Table 4.2.. The number of HV colors N_v , corresponding to the number of dark QCD colors N_d , is set to three, and the number of HV quark species n_{flav} , corresponding to the number of dark flavors n_f , is set to seven. Such values are chosen to produce a QCD-like hidden sector. To simulate QCD-like behavior in the hidden sector, the HV gauge coupling is allowed to run to first order, with the beta function based on the number of HV colors and quark flavors. The running coupling option is a new option added to recent PYTHIA releases, motivated by the work of the emerging jets theorists [17], to replace the default fixed HV coupling, which does not accurately reproduce a QCD-like hidden

sector. The running HV coupling, including the development of its implementation in the Pythia HV model and the motivation for its use in generating the signal models, is discussed in more detail in Section [4.2.2.1.1](#) below.

By default, only flavor-diagonal HV mesons are allowed to decay, since the HV mediator is assumed to be a vector, and the off-diagonal HV mesons carry HV charge, so they should be stable. In the dark QCD signal models studied here, however, a scalar mediator is considered, in which case the HV charge is not a conserved quantum number. Therefore, all of the HV mesons are allowed to decay. Moreover, it is reasonable to assume the couplings of the diagonal and off-diagonal HV mesons are roughly the same size; thus, both the diagonal and off-diagonal HV mesons of a single type are set to have the same decay channels with the same lifetimes. The HV rho is taken to promptly decay to two HV pions with branching ratio (BR) of 0.999 and to two down quarks with BR of 0.001, and the HV pion is set to decay to two down quarks with BR of 1.0 and a macroscopic lifetime of order millimeters to centimeters. The lifetime of the HV pion is a free parameter set by the signal point under consideration, with potential values listed in Table [4.2](#).

The HV quark mass is set to the HV confinement scale Λ_v , which is set to two times the HV pion mass; the HV rho mass is set to be four times the HV pion mass; and the HV pion mass is a free parameter set by the GeV-scale benchmark model, as listed in Table [4.1](#).

The ATLAS default $c\tau$ limit for generator stable particles is turned off to allow for the

HV pions to decay at the generator level. Otherwise, they would be considered stable by **Pythia** and passed off to **Geant4** to be decayed, which does not know how to handle them, and they would therefore remain stable throughout the simulation.

Additionally, a truth-level filter is applied to the signal samples during event generation such that the only events generated are those with four truth jets with $p_T > 100 \text{ GeV}$ and $|\eta| < 2.7$. This is done to increase statistics for signal points with otherwise low signal selection efficiency. The truth-level cuts are chosen to reflect the cuts applied in the **Emerging DRAW_RPVLL** filter, with the selection values for the truth objects loosened slightly relative to the corresponding reconstruction objects to avoid throwing away signal events.

Simulated signal MC samples are currently prepared for 36 representative points of the full 90-point signal grid, which is comprised of five benchmark models, three mediator masses, and eight dark pion lifetimes, with six lifetimes per model - mediator mass point, as described in Section 4.1. The parameter space occupied by the full signal grid and by the currently available subset of signal points is shown in Figure 4.5. The 36 points of the signal sub-grid are chosen to span the full signal grid as much as possible.

The 36 available signal points and the number of events generated for each point are listed in Table 4.3, along with their production cross sections and generator filter efficiencies, as calculated in **Pythia**. The production cross section increases with decreasing scalar mediator mass and is independent of the benchmark model, while the generator filter ef-

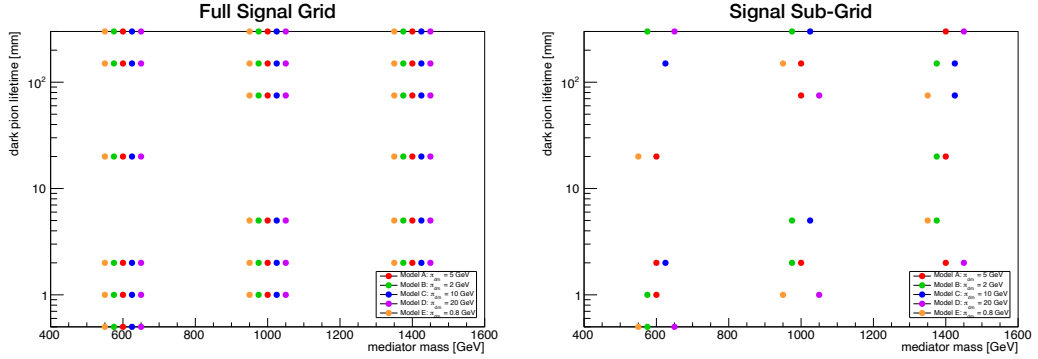


Figure 4.5: The full 90-point signal grid (left) and 36-point signal sub-grid (right) in dark pion lifetime - mediator mass parameter space. Points are shown for Model A (red), Model B (green), Model C (blue), Model D (purple), and Model E (orange). The full grid is designed to span the parameter space, and the sub-grid is chosen to include a representative set of models, mediator masses, and dark pion lifetimes within the full grid.

ficiency decreases with decreasing scalar mediator mass. Both parameters are independent of the dark pion lifetime. Different numbers of events are generated for each Monte Carlo campaign, where separate MC campaigns are used for different data taking years in order to reproduce the ATLAS geometry and LHC performance during each year, with MC16a, MC16d, and MC16e corresponding to data taking years 2015+2016, 2017, and 2018, respectively.

After event generation, the signal samples are processed with full simulation and digitization and with special RPVLL reconstruction, as described in Sections 3.3 and 3.4, respectively, producing the same output DAOD_RPVLL format as for real data. Finally, the MC samples are processed through to the same derivations and ntuples as produced for data, described above.

Signal Point				Number of Events			Metadata	
DSID	Model	m_{X_d}	$c\tau_{\pi_d}$	MC16a	MC16d	MC16e	Cross-Section [nb]	Gen. Filter Efficiency
312001	A	1400	300	99,000	118,000	160,000	1.0785×10^{-6}	0.93601
312004	A	1400	20	60,000	80,000	100,000	1.0786×10^{-6}	0.93528
312006	A	1400	2	50,000	60,000	80,000	1.0791×10^{-6}	0.93595
312008	A	1000	150	80,000	100,000	130,000	1.5195×10^{-5}	0.86813
312009	A	1000	75	60,000	70,000	100,000	1.5191×10^{-5}	0.86835
312011	A	1000	2	60,000	70,000	100,000	1.5180×10^{-5}	0.86679
312015	A	600	20	99,000	120,000	160,000	4.2962×10^{-4}	0.60561
312016	A	600	2	100,000	120,000	159,000	4.3019×10^{-4}	0.60450
312017	A	600	1	220,000	280,000	360,000	4.3009×10^{-4}	0.60564
312020	B	1400	150	100,000	120,000	160,000	1.0777×10^{-6}	0.94283
312022	B	1400	20	60,000	80,000	99,000	1.0783×10^{-6}	0.94249
312023	B	1400	5	50,000	60,000	79,000	1.0783×10^{-6}	0.94287
312025	B	1000	300	120,000	146,000	199,000	1.5190×10^{-5}	0.88997
312028	B	1000	5	70,000	90,000	119,000	1.5216×10^{-5}	0.89052
312029	B	1000	2	60,000	70,000	100,000	1.5208×10^{-5}	0.88949
312031	B	600	300	150,000	190,000	242,000	4.3017×10^{-4}	0.67869
312035	B	600	1	200,000	250,000	300,000	4.3013×10^{-4}	0.67772
312036	B	600	0.5	200,000	250,000	300,000	4.3042×10^{-4}	0.67886
312038	C	1400	150	100,000	120,000	159,000	1.0784×10^{-6}	0.94193
312039	C	1400	75	78,000	100,000	129,000	1.0779×10^{-6}	0.94363
312043	C	1000	300	119,000	150,000	196,000	1.5197×10^{-5}	0.86652
312046	C	1000	5	99,000	130,000	170,000	1.5183×10^{-5}	0.86615
312050	C	600	150	200,000	250,000	300,000	4.3074×10^{-4}	0.57394
312052	C	600	2	320,000	400,000	530,000	4.2297×10^{-4}	0.57309
312055	D	1400	300	98,000	120,000	160,000	1.0791×10^{-6}	0.96925
312060	D	1400	2	90,000	110,000	148,000	1.0775×10^{-6}	0.96897
312063	D	1000	75	60,000	70,000	100,000	1.5168×10^{-5}	0.90922
312066	D	1000	1	130,000	160,000	220,000	1.5188×10^{-5}	0.90867
312067	D	600	300	410,000	500,000	680,000	4.3001×10^{-4}	0.63178
312072	D	600	0.5	200,000	249,000	299,000	4.3014×10^{-4}	0.63165
312075	E	1400	75	50,000	60,000	80,000	1.0773×10^{-6}	0.94790
312077	E	1400	5	50,000	60,000	80,000	1.0780×10^{-6}	0.94723
312080	E	1000	150	60,000	80,000	100,000	1.5184×10^{-5}	0.90574
312084	E	1000	1	120,000	150,000	200,000	1.5197×10^{-5}	0.90591
312087	E	600	20	100,000	119,000	160,000	4.3053×10^{-4}	0.72697
312090	E	600	0.5	110,000	140,000	180,000	4.3026×10^{-4}	0.72834

Table 4.3: The 36-point signal sub-grid. The signal point is defined by the benchmark model, the mediator mass, and the dark pion lifetime and is labeled by the dataset identifier (DSID). The pair production cross section of the scalar mediator is shown, as well as the efficiency of the four-truth-jet generator filter applied, both of which are calculated in Pythia during the event generation.

4.2.2.1.1 HV RUNNING COUPLING The running hidden sector gauge coupling was not available in PYTHIA at the start of the analysis. Initially, a locally modified version of PYTHIA was used to generate private test samples before the necessary modifications were added globally to a new PYTHIA release and used in the official MC samples produced at ATLAS.

In the original implementation of PYTHIA used in the analysis, prior to release 8.230, the hidden sector gauge coupling in the Hidden Valley model is a fixed parameter with no mechanism available to allow it to run and a confinement scale instead mimicked by the explicit dark quark masses. In earlier releases, the HV implementation is thus manually modified to enable a running HV gauge coupling option. The first private studies of the analysis are performed with a modified version of PYTHIA 8.183 [130], adapted to include a QCD-like HV confinement scale and a running HV gauge coupling that evolves, based on the numbers of HV colors and flavors, according to the one-loop beta function. The running coupling in the Hidden Valley is applied analogously to the running coupling in QCD in the PYTHIA timelike final-state showering algorithm.

Eventually this feature was included in a later PYTHIA release and available for use in official MC production within the ATLAS simulation framework. Full, official MC samples used for the bulk of the analysis are produced with PYTHIA 8.230, with the running HV coupling included as a feature, as described above. Validation studies of the HV running

coupling implementation in an official PYTHIA release are presented in Appendix D.

It is vital to include the running HV coupling, versus a fixed coupling, to reproduce QCD-like behavior in the hidden sector. A fixed coupling does not accurately reproduce QCD-like events and yields more spherical events, with the energy distributed spherically throughout the detector around the collision point, rather than in jet-like conical structures, as is characteristic of QCD-like models. This effect is quantified most discernibly through two observables: orphan p_T and jet girth.

The orphan p_T is defined as the sum- p_T of particles not clustered into hard jets:

$$\text{orphan } p_T = \sum_i p_T^i - \sum_i (p_T^i \mid \text{constituent of hard jet}), \quad (4.1)$$

where the first sum is over all particles in the event, and the second sum is over all particles in the event that are constituents of a hard jet with p_T above some threshold. The orphan p_T essentially quantifies the amount of leftover p_T in the event that is not confined inside jets.

The jet girth is defined as the p_T -weighted and normalized angular distribution of particle constituents within the jet:

$$\text{girth} = \frac{I}{p_T^{\text{jet}}} \sum_i p_T^i \Delta R_i, \quad (4.2)$$

where p_T^{jet} is the jet transverse momentum, the sum is over all constituents of the jet, and ΔR_i is the angular distance of the constituent from the jet axis.

In Figures 4.6 and 4.7, the orphan p_T and jet girth, respectively, are compared between events generated with a fixed gauge coupling and a running gauge coupling in the modified PYTHIA 8.183 version described above for a single signal point. A value of 0.7 is chosen for the fixed gauge coupling to most accurately reproduce the running coupling events in terms of the hadron multiplicity.

A fixed coupling produces events with more orphan energy and broader jets than those produced with a running coupling. This translates to the fixed-coupling events being more spherical and having more energy spread around the detector than running-coupling events, which emit partons in jet-like structures, as the dark QCD theory dictates. The effect of the fixed coupling on the orphan p_T is not as obvious here as in events producing only emerging jets, i.e. through a Z' mediator, as illustrated in Reference [17], since the dark sector gauge coupling has no effect on the visible sector or the QCD jets. The effect of the dark gauge coupling on the shape of the jets, however, is immediately apparent, particularly for the truth-level emerging jets. A “truth emerging jet” is defined as a truth jet matched to a good dark jet, where a match is considered if the truth jet is within $\Delta R < 0.3$ of a dark jet with $p_T > 30 \text{ GeV}$. The p_T cut implemented on the dark jets is designed to ignore poorly clustered dark jets consisting of a single constituent.

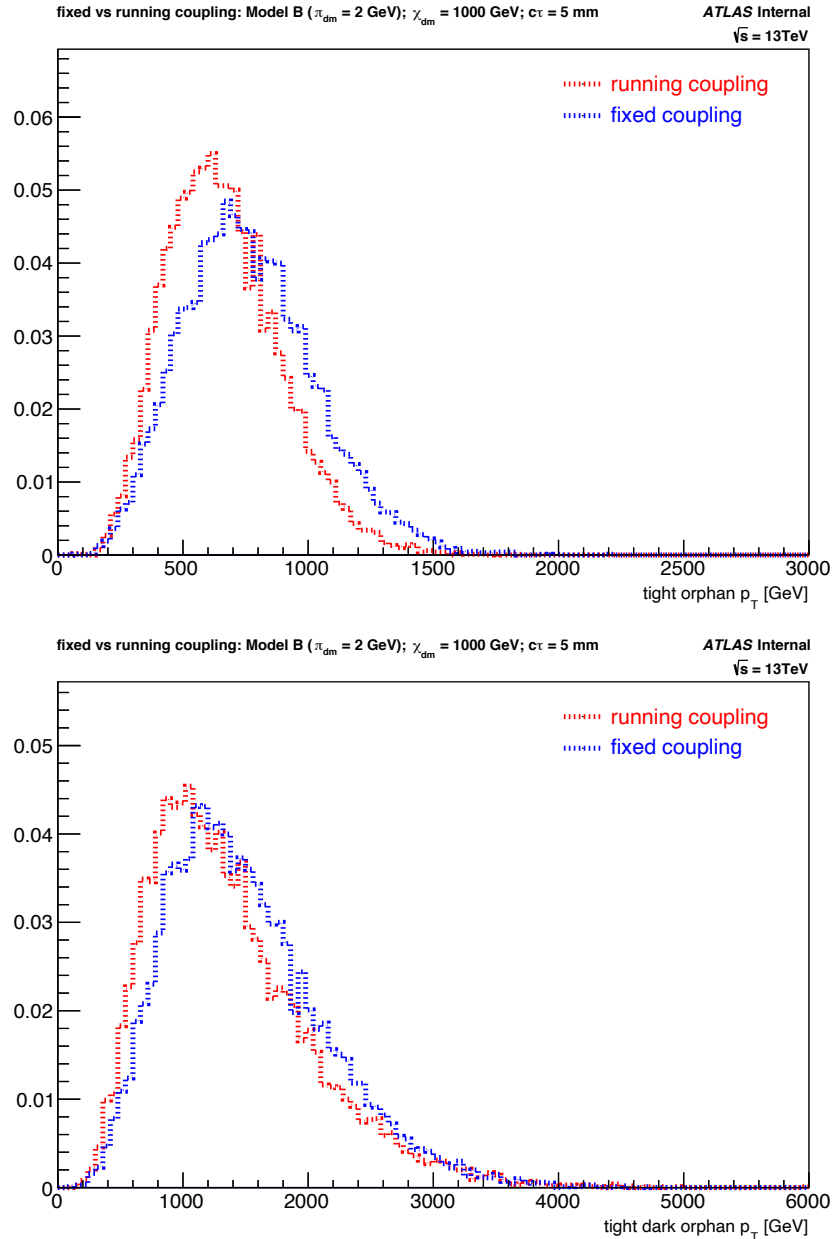


Figure 4.6: The orphan p_T in the visible (top) and dark (bottom) sectors, calculated as the amount of visible or dark truth particle p_T in the event not contained in visible or dark truth jets with $p_T > 200$ GeV, respectively, in events generated with a fixed gauge coupling of 0.7 (blue) and a running gauge coupling (red) in modified Pythia 8.183 for Model B, $m_{X_d} = 1000$ GeV, $c\tau_{\pi_d} = 5$ mm signal events.

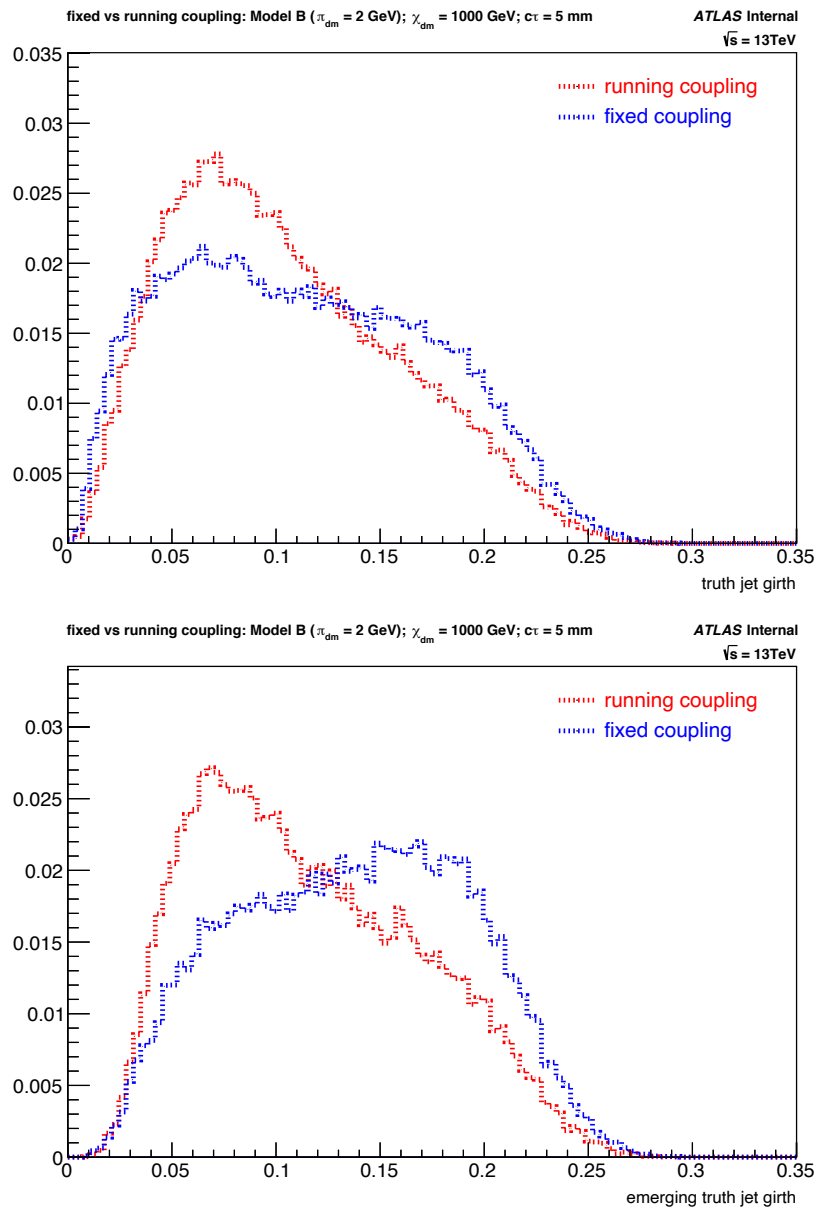


Figure 4.7: The girth, or p_T -weighted width, of the inclusive truth jets (top) and the emerging truth jets (bottom) in events generated with a fixed gauge coupling of 0.7 (blue) and a running gauge coupling (red) in modified Pythia 8.183 for Model B, $m_{X_d} = 1000$ GeV, $c\tau_{\pi_d} = 5$ mm signal events.

4.2.2.1.2 TRUTH SIGNAL DISTRIBUTIONS Truth studies are performed to analyze the kinematic properties of the signal model prior to the effects of detector simulation in order to investigate the potential selection criteria and validate the event generation before large production of events with full simulation and specialized reconstruction. Truth observables are those produced at the generator level.

The signature under consideration in the Emerging Jets analysis is two QCD jets and two emerging jets, or four high- p_T jets with associated displaced vertices, corresponding to the decays of long-lived dark pions. The kinematic properties of the scalar mediator, dark quark, dark pion, and dark rho determine the overall distributions of the signal event, with the dark pion decays being of particular importance, as they primarily dictate the features of the outgoing emerging jets and displaced vertices in the event.

Plots are presented below illustrating the truth-level kinematics of the signal samples for the different benchmark models, mediator masses, and dark pion lifetimes of the signal grid. All distributions are normalized to unity to display differences in shapes, rather than scales, between signal points. For plots comparing distributions between benchmark models and mediator masses at a single lifetime, $c\tau = 150$ mm signal points are used. In these studies, produced from private truth derivations for all signal points in the full grid, offline selections are applied to match those of the generator filter, requiring events to contain four truth jets with $p_T > 100$ GeV and $|\eta| < 2.7$.

4.2.2.1.2.1 DARK PION DECAYS The number of dark pions produced per event for all models and mediator masses at a single lifetime is shown in Figure 4.8. The dark pion multiplicity depends inversely on the mass scale of the model, with higher multiplicities for lower model mass scales, and directly on the mediator mass, with more dark pions produced from heavier mediators.

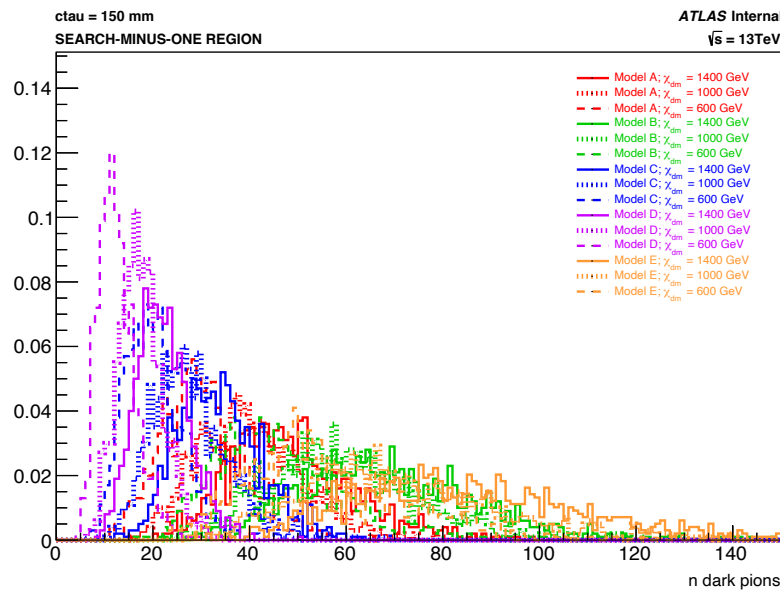


Figure 4.8: The number of dark pions produced per event for Models A, B, C, D, and E, scalar mediator masses 1400, 1000, and 600 GeV, and dark pion lifetime 150 mm. The dark pion multiplicity is directly proportional to the mediator mass, indirectly proportional to the model mass scale, and independent of the dark pion lifetime.

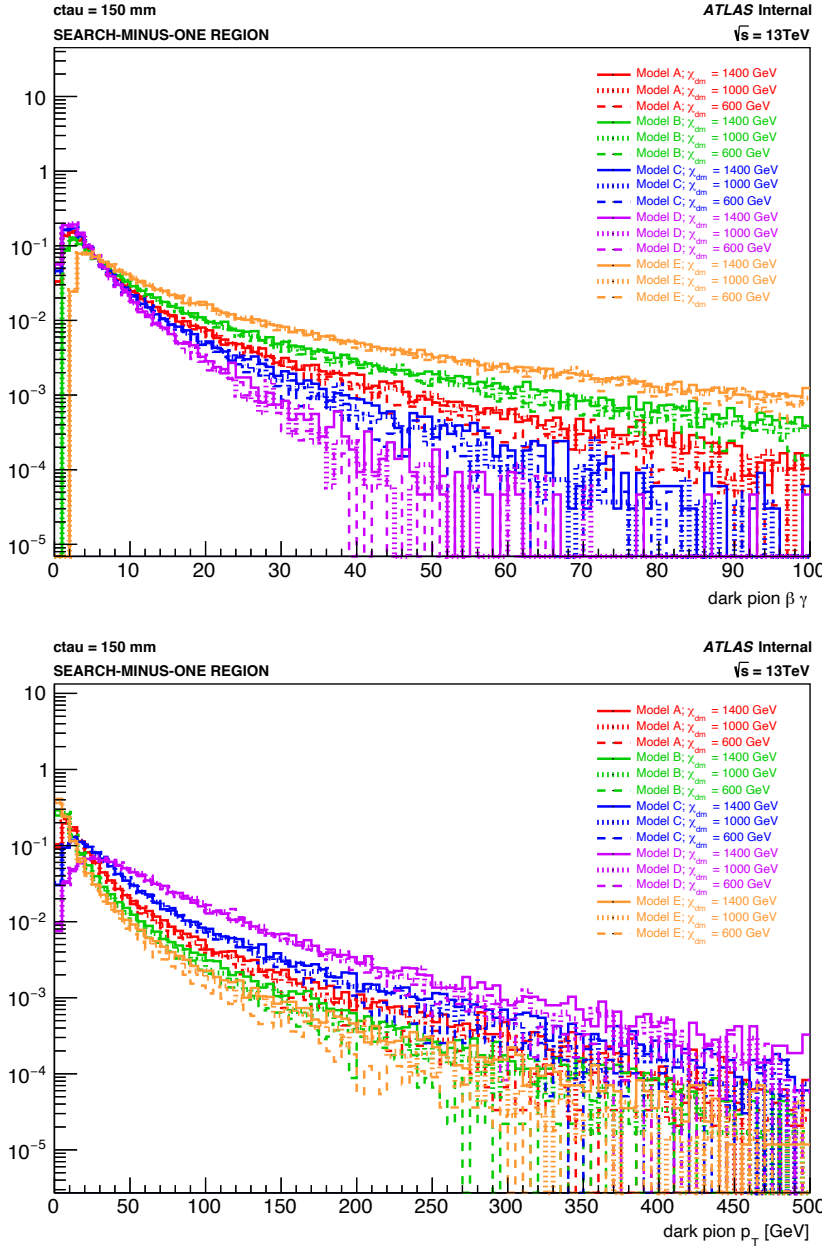


Figure 4.9: The dark pion $\beta\gamma$ (top) and p_T (bottom) for Models A, B, C, D, and E, scalar mediator masses 1400, 1000, and 600 GeV, and dark pion lifetime 150 mm.

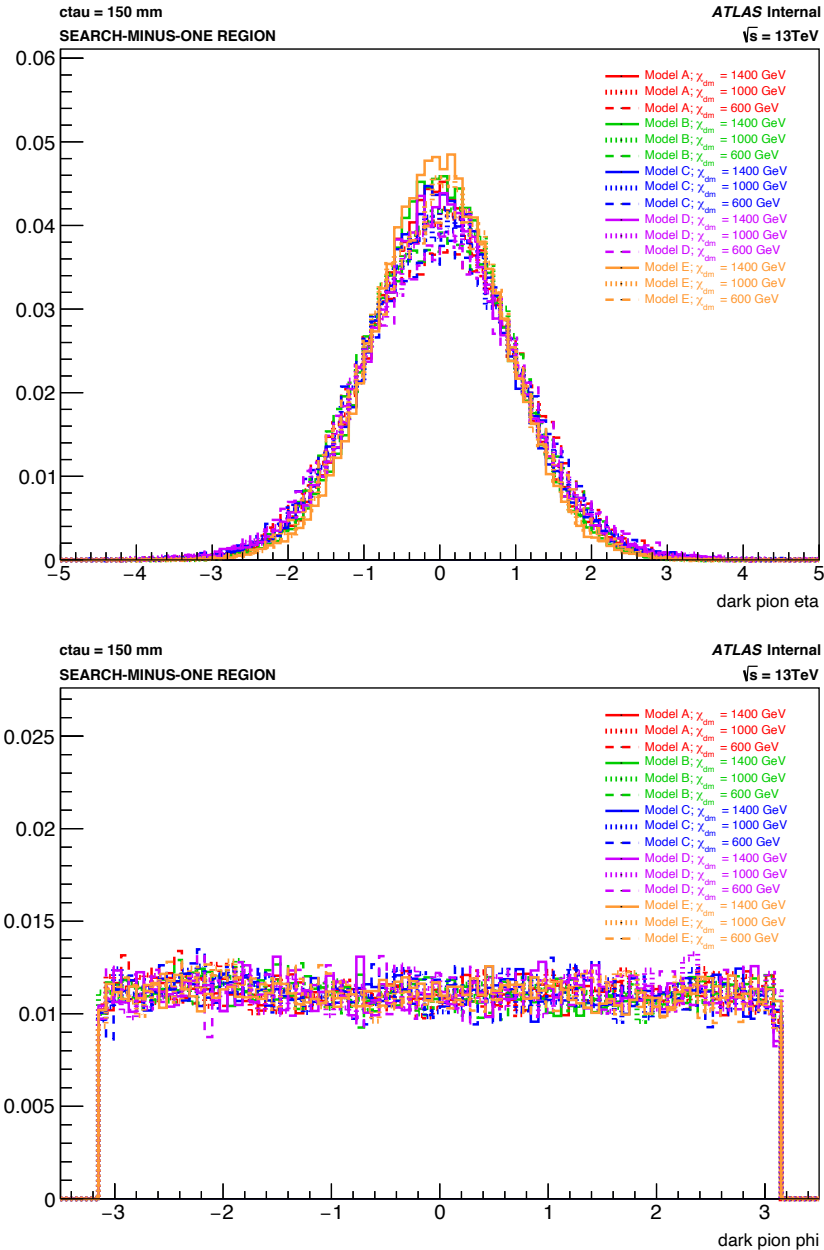


Figure 4.10: The dark pion γ (top) and ϕ (bottom) distributions for Models A, B, C, D, and E, scalar mediator masses 1400, 1000, and 600 GeV, and dark pion lifetime 150 mm.

Figure 4.9 displays the dark pion boost factor $\beta\gamma$ and transverse momentum p_T for all signal models and mediator masses at a single lifetime, where $\beta\gamma = p/m$. Dark pions with lower masses from lower mass models tend to be more boosted and thus have larger $\beta\gamma$ values. Conversely, dark pions with higher masses tend to have larger transverse momenta. Both the dark pion $\beta\gamma$ and p_T are minimally dependent on the mediator mass, with slightly larger values of each for larger mediator masses, and are independent of the dark pion lifetime.

The η and ϕ distributions of the dark pion for a single lifetime are shown in Figure 4.10. Both are symmetric and relatively independent of the signal point parameters, as expected. A minimal model and mediator mass dependency is observed in η , with slightly narrower distributions for lighter models and mediator masses.

4.2.2.1.2.2 DARK PION DECAY VERTICES The number of dark pion decay vertices is shown for all five models at a single mediator mass and lifetime and for a single model and mediator mass at six different lifetimes in Figure 4.11.

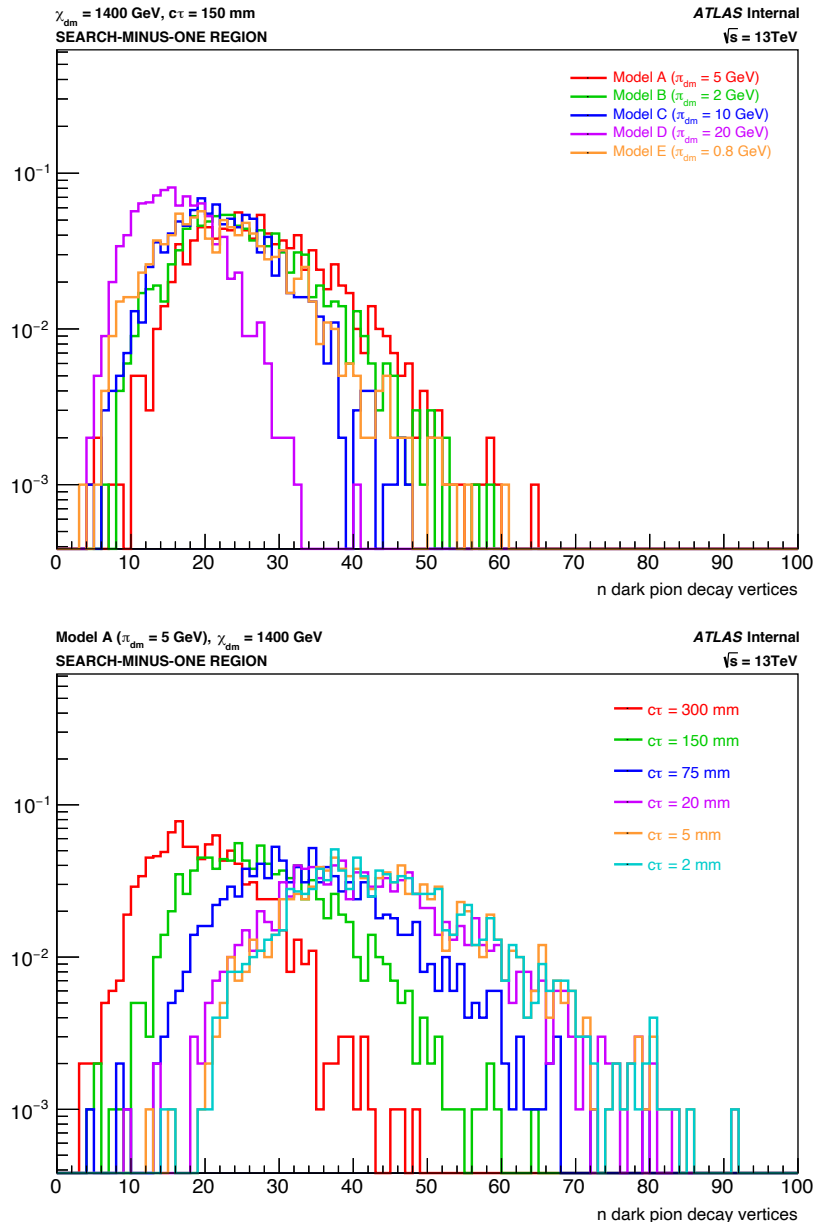


Figure 4.11: The number of dark pion decay vertices within the SCT. Top: the model dependency of the dark pion decay vertex multiplicity, shown for 1400-GeV mediator mass and 150-mm lifetime points. Bottom: the lifetime dependency of the dark pion decay vertex multiplicity, shown for 1400-GeV mediator mass points in Model A.

For the truth studies presented here, dark pion decays are required to occur within the SCT such that they have the potential of being reconstructed; therefore, fiducial volume cuts of $r < 563$ and $|z| < 2720$ mm are applied to the dark pion decay vertices. This fiducial volume cut is responsible for the observed dependency of the dark pion decay vertex multiplicity on the dark pion lifetime, despite the dark pion multiplicity being the same across all lifetimes. Dark pions with longer lifetimes are more likely to decay outside of the silicon detector and are thus less likely to be reconstructed as displaced vertices by the secondary vertexing algorithm. Like the dark pion multiplicity, the dark pion decay vertex multiplicity is directly related to the mediator mass and inversely related to the model mass scale.

The model and lifetime dependencies of the transverse and longitudinal positions, r and z , of the dark pion decay vertex are shown in Figure 4.12. The r and z decay positions follow exponentially falling distributions, with the observed spread in z a consequence of the size of the beam spot, which averages around 50 mm [131]. For the same dark pion lifetime across different models, the dark pion decay vertices in lighter models are slightly further displaced in both r and z , since the lighter dark pions tend to be more boosted and thus travel further distances before decaying, as a particle's mean decay length is given by $\langle \Delta L \rangle = \beta \gamma c \tau$. For the same model across different lifetimes, the transverse and longitudinal decay positions are directly dependent on the dark pion lifetime, with decays from larger lifetime dark pions being further displaced, as expected. The displaced decay vertex

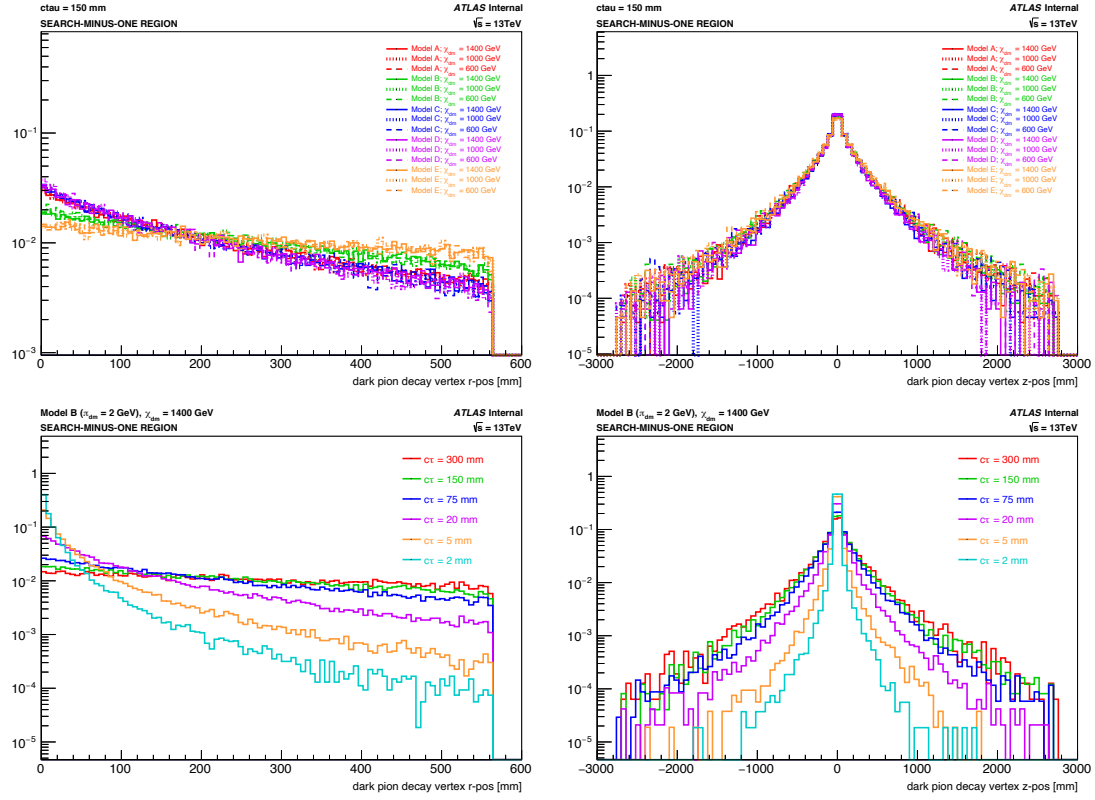


Figure 4.12: The transverse (left) and longitudinal (right) positions of the dark pion decay vertices. Top: the model dependency of the dark pion decay vertex position for 150-mm lifetime points. Right: the lifetime dependency of the dark pion decay vertex position for 1400-GeV mediator mass points in Model B.

position is independent of the mediator mass.

The opening angle of the dark pion decay vertex, defined as the maximum angular distance between any two outgoing particles, is shown in Figure 4.13 for all models and mediator masses at a single lifetime. The opening angle is directly related to the mass of the model, with heavier models producing wider dark pion decays, which in turn produce wider jets.

Figure 4.14 shows the number of dark pion decay vertex descendants and the invariant

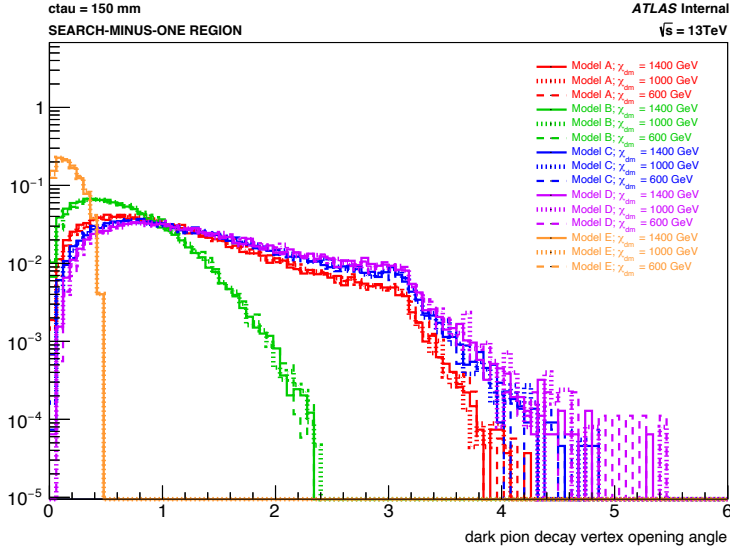


Figure 4.13: The maximum angular distance between any two outgoing particles from a dark pion decay vertex for 150-mm lifetime points.

mass of the decay vertex. A descendant is any charged particle in the dark pion decay chain with $p_T > 1 \text{ GeV}$, representing a decay product that is capable of being reconstructed as an inner detector track by the standard tracking and LRT algorithms. As such, descendants are also interchangeably referred to as “reconstructible descendants”. The invariant mass of the decay vertex is calculated from the four-vector sum of the reconstructible descendants. The number of descendants and the invariant mass are directly dependent on the model mass and independent of both the mediator mass and dark pion lifetime. The invariant mass distribution in each model is centered around the corresponding dark pion mass, as expected.

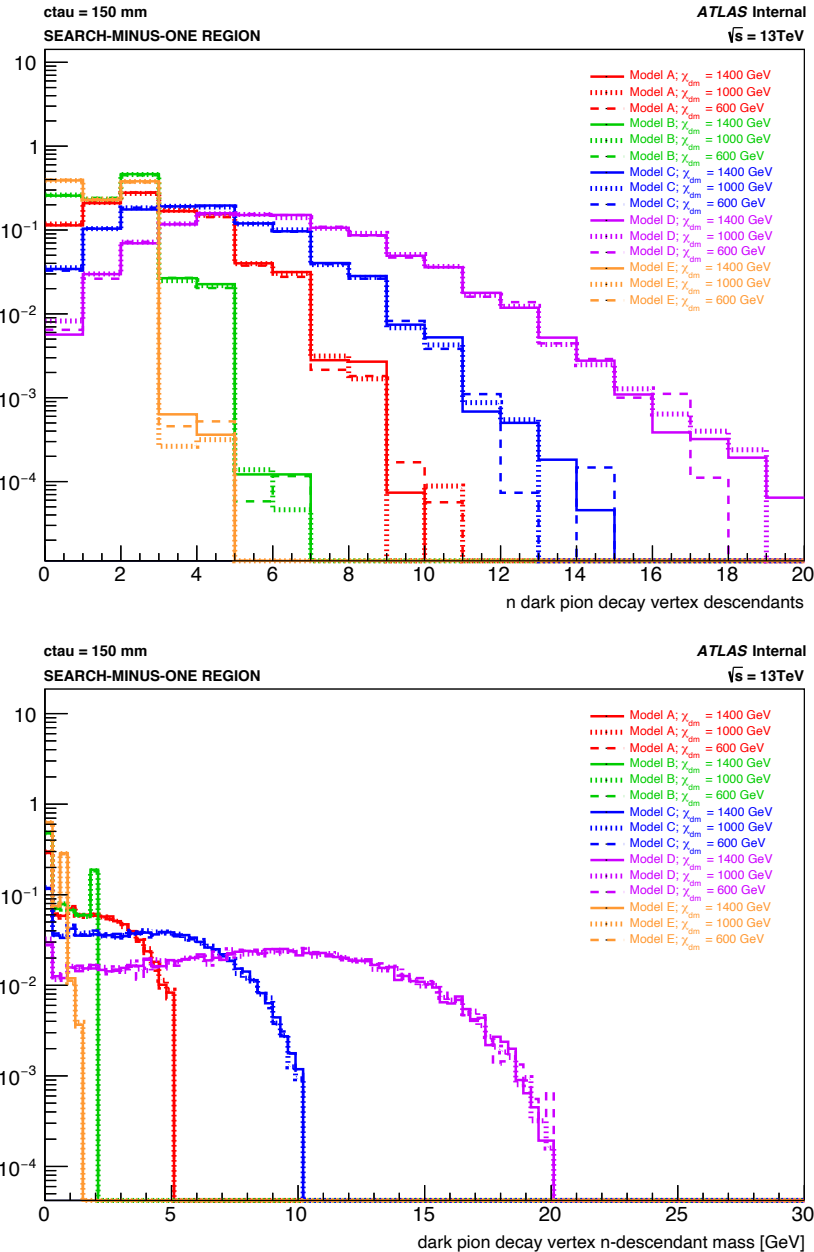


Figure 4.14: Top: the number of reconstructible descendants stemming from the dark pion decay vertex. Bottom: the invariant mass of the dark pion decay vertex descendants. Distributions are shown for all models and mediator masses at a single lifetime.

4.2.2.1.2.3 DARK PION DECAY VERTEX DESCENDANTS The reconstructible descendants of the dark pion decay vertex represent displaced truth tracks that could be reconstructed in the inner detector. The p_T , η , and ϕ distributions of the descendants are shown in Figures [4.15](#) and [4.16](#).

The transverse momentum is minimally dependent on the model mass, with heavier masses producing slightly higher- p_T descendants, and inversely related to the lifetime, with larger lifetimes producing somewhat lower-momentum descendants. The $|\eta|$ and ϕ distributions of the dark pion are relatively independent of changes across all signal parameters.

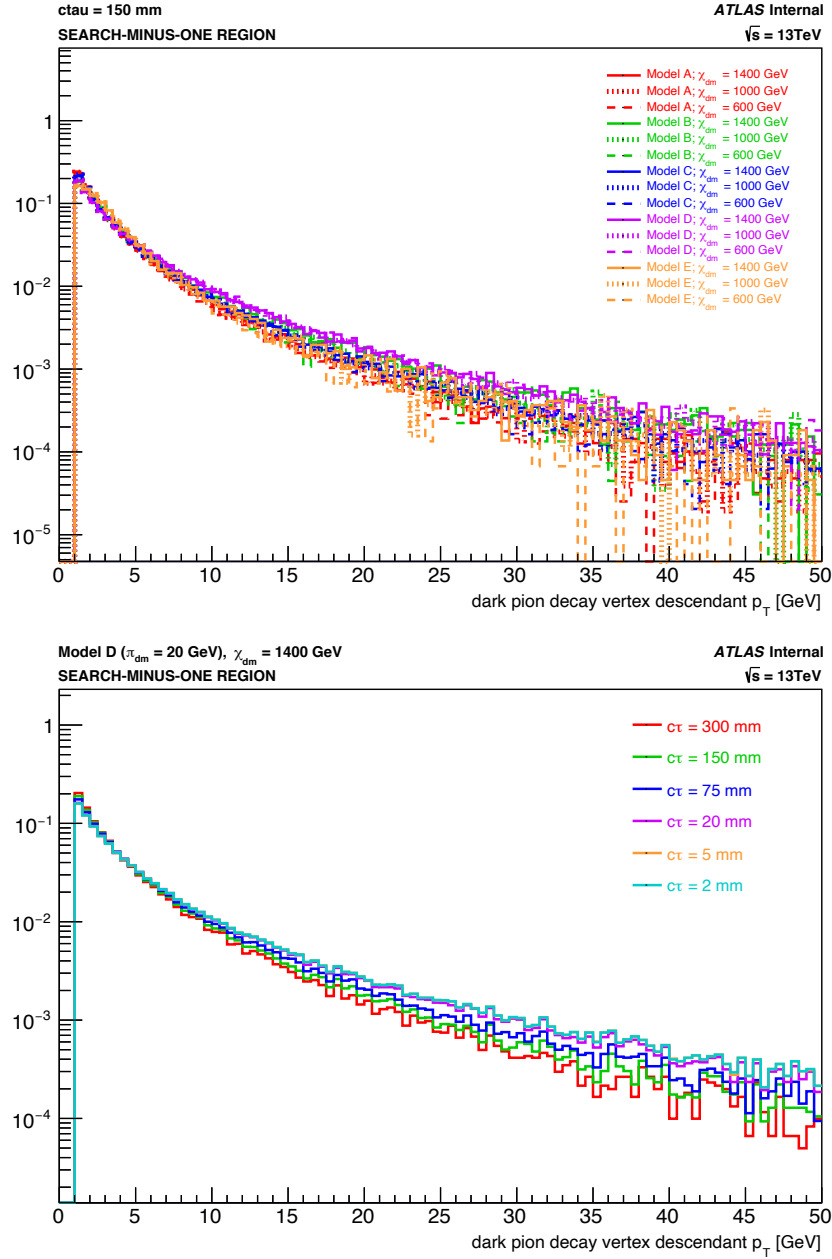


Figure 4.15: The p_T of the dark pion decay vertex descendants for all models and mediator masses at $c\tau = 150 \text{ mm}$ (top) and for all lifetimes in Model D with mediator mass 1400 GeV (bottom).

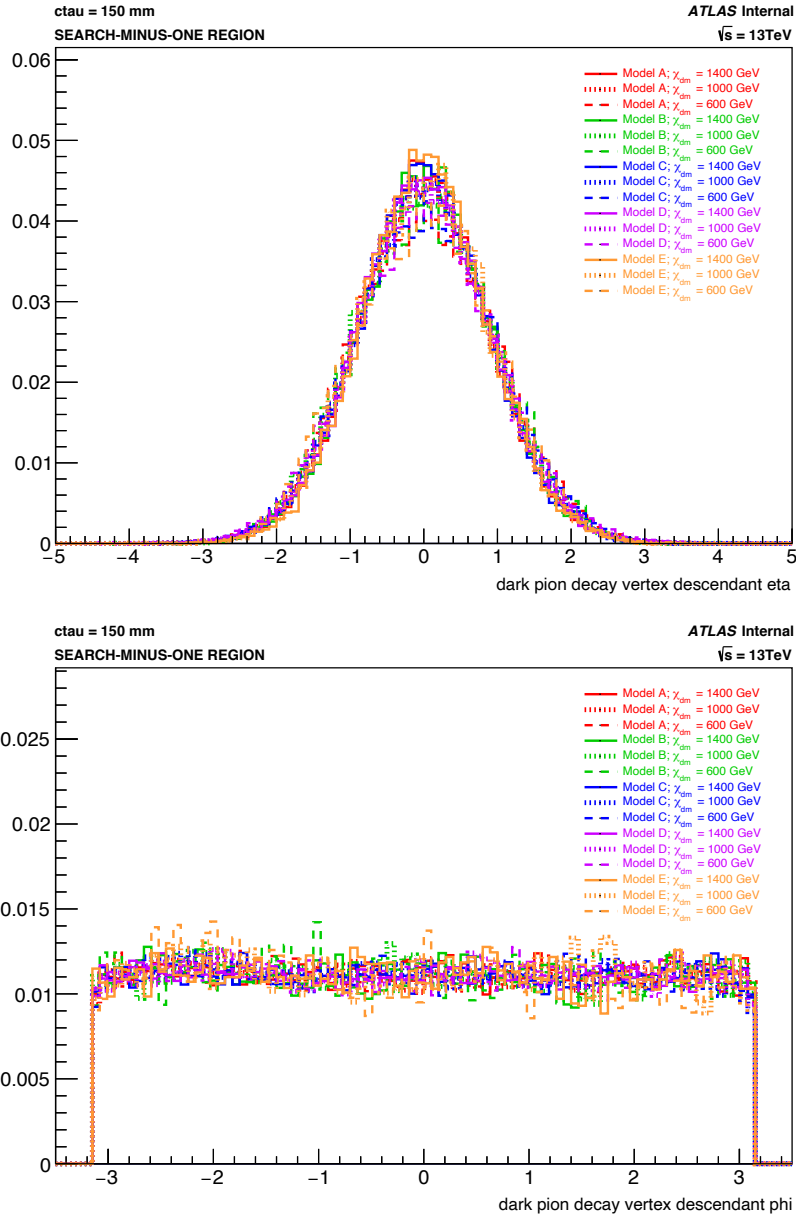


Figure 4.16: The dark pion decay vertex descendant γ (top) and ϕ (bottom) distributions for all models and mediator masses at $c\tau = 150 \text{ mm}$.

The transverse and longitudinal impact parameters, d_o and z_o , of the dark pion decay descendants are shown in Figure 4.17. The truth impact parameters are approximated from the decay vertex position and the angle between the descendant and vertex as follows:

$$\begin{aligned} d_o &\approx r \sin \Delta\phi, \\ z_o &\approx r / \tan \vartheta, \end{aligned} \tag{4.3}$$

where r is the transverse position of the decay vertex, $\Delta\phi$ is the azimuthal angle between the descendant four-momentum and the vertex pointing vector from the decay vertex to the primary vertex, and ϑ is the polar angle of the vertex pointing vector.

For the same dark pion lifetime across different models, the transverse impact parameter of the descendants is directly dependent on the mass scale, with heavier models producing descendants with larger $|d_o|$ values. This is a consequence of the decay vertex opening angle dependency on the model mass, with lighter models producing descendants more parallel to the direction of the vertex pointing vector. The longitudinal impact parameter is independent of the model mass. Both the transverse and longitudinal impact parameters are directly dependent on the dark pion lifetime, with larger lifetimes producing descendants with larger impact parameters, as expected.

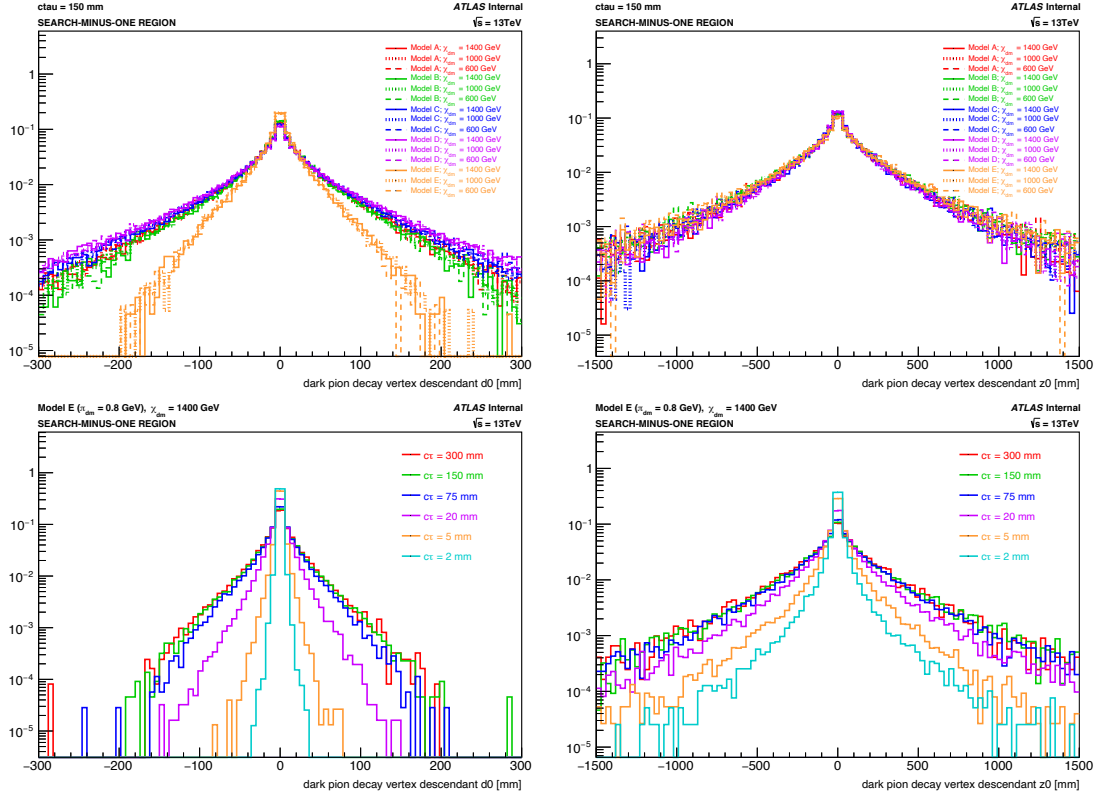


Figure 4.17: The transverse (left) and longitudinal (right) impact parameters of the dark pion decay descendants. Top: the model dependency of the descendant impact parameter for 150-mm lifetime points. Bottom: the lifetime dependency of the descendant impact parameters for 1400-GeV mediator mass points in Model E.

4.2.2.1.2.4 TRUTH JETS The numbers of visible and dark truth jets per event and the numbers of constituents per visible and dark truth jet are shown in Figure 4.18. The number of truth jets in both the visible and dark sector increases with increasing model and mediator mass and is independent of the dark pion lifetime. Conversely, the number of dark jet constituents decreases with increasing model mass but still increases with increasing mediator mass, since the dark pion multiplicity is inversely related to the model mass and directly related to the mediator mass. The number of visible truth jet constituents is also directly dependent on the mediator mass and varies between models but not with any discernible pattern. The numbers of visible and dark jet constituents are also independent of the dark pion lifetime.

The numbers of truth emerging jets per event and constituents per truth emerging jet are shown in Figure 4.19. The dependencies of the numbers of emerging jets and emerging jet constituents on the model scale and the mediator mass are the same as those of the dark jets.

Figures 4.20 and 4.21 show the truth jet p_T , η , and ϕ distributions. The transverse momentum is shown for the inclusive truth jets and for the dark jets across all models and mediator masses at a single lifetime, as well as for the emerging jets across all models at a single mediator mass and lifetime and in Model C alone, in order to separately demonstrate the model and mediator mass dependency. The p_T is inversely related to the model mass scale

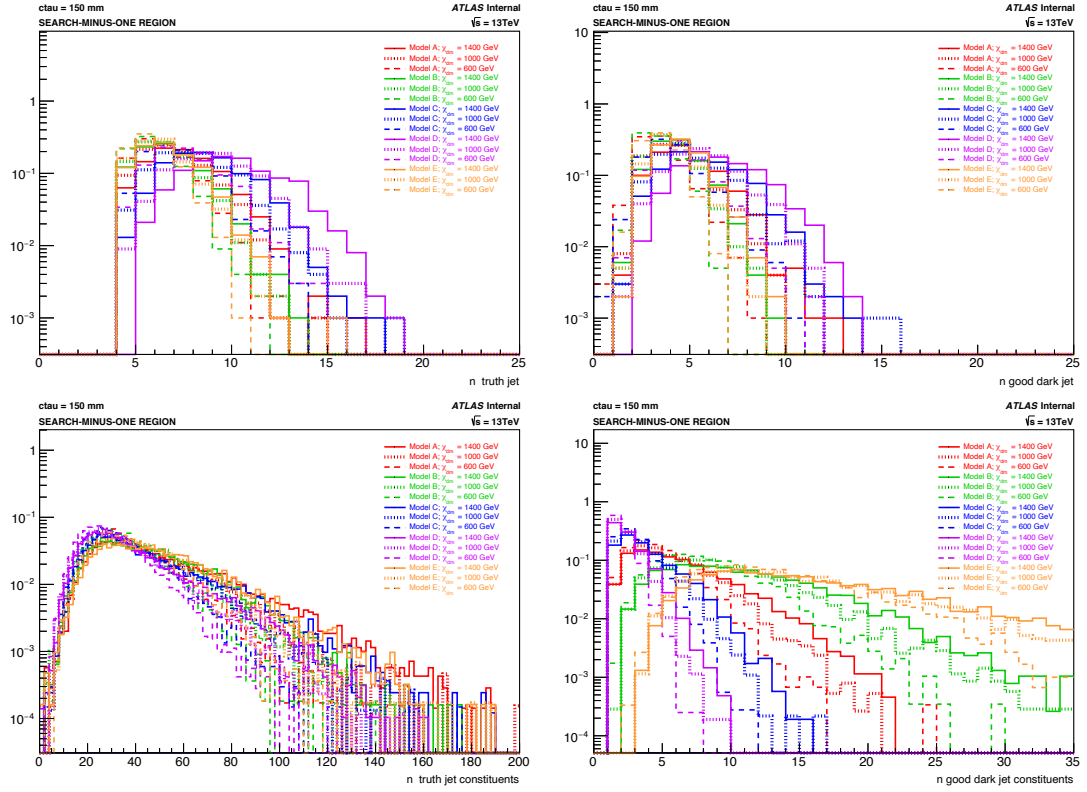


Figure 4.18: The number of truth visible (left) and dark (right) jets per event (top) and constituents per jet (bottom). Distributions are shown comparing all models and mediator masses at a single lifetime of 150 mm.

and directly related to the mediator mass, as expected, since heavier mediators should produce higher- p_T objects, and lower-mass models produce more dark pions, which contribute to the emerging jet. The truth jet η and ϕ distributions are symmetric and independent of the model parameters.

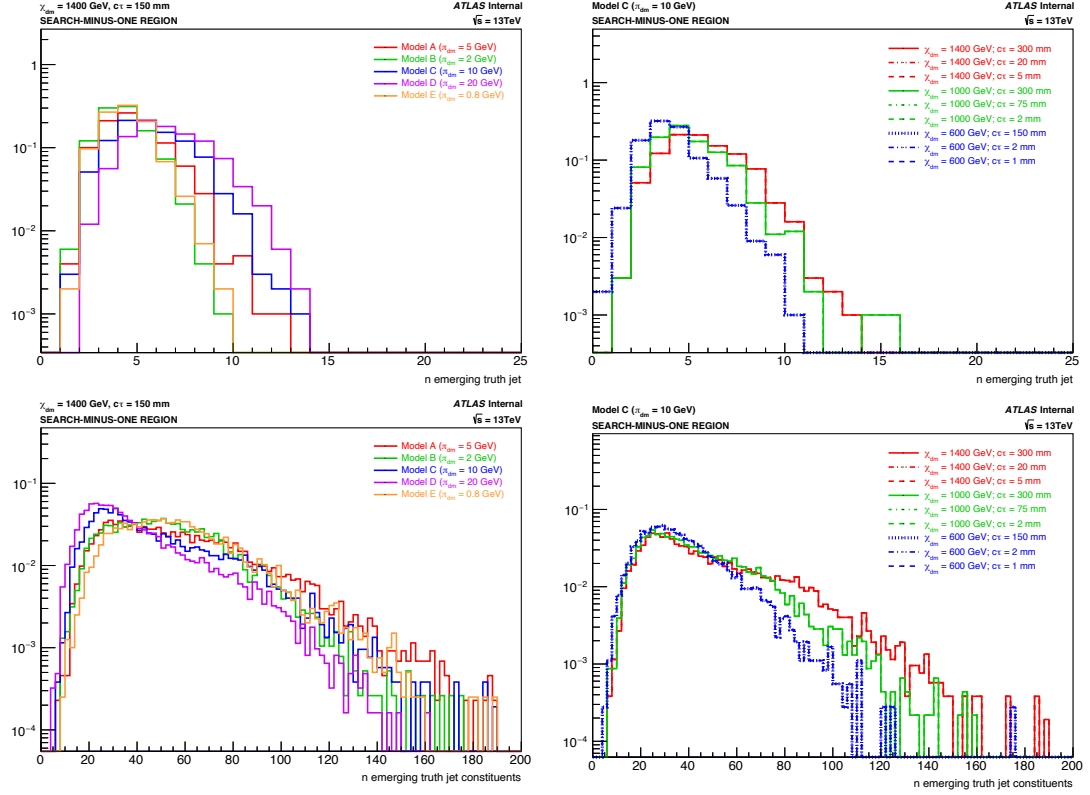


Figure 4.19: The number of truth emerging jets per event (top) and constituents per jet (bottom) for all models at 1400-GeV mediator mass and 150-mm lifetime (left) and for Model C (right).

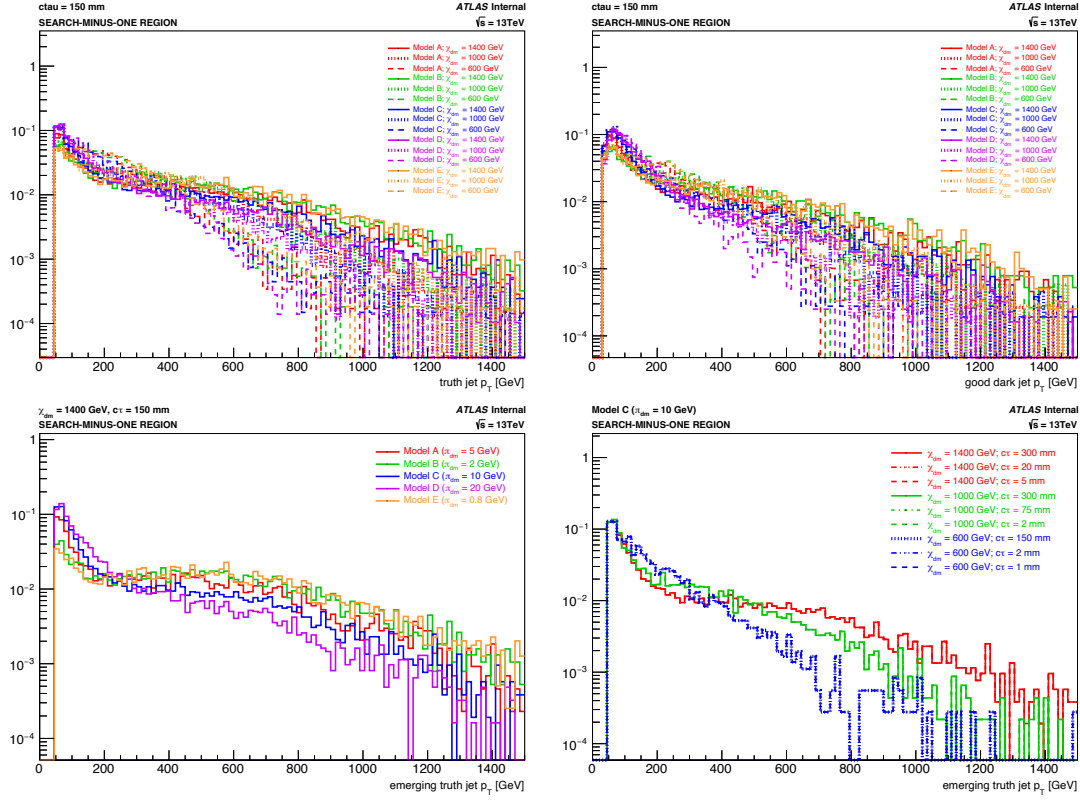


Figure 4.20: The transverse momentum of the truth jets (top left) and dark jets (top right) across all models and mediators masses at a single lifetime and of the emerging jets across all models at 1400-GeV mediator mass and 150-mm lifetime (bottom left) and for Model C (bottom right).

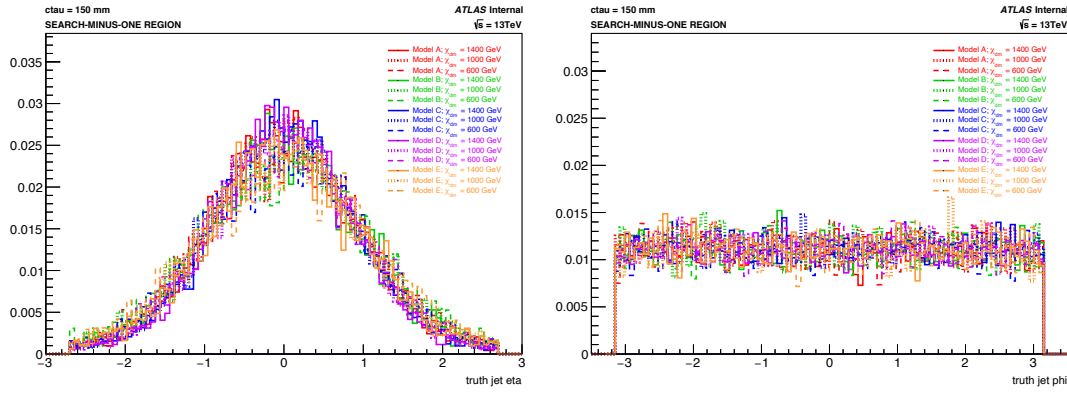


Figure 4.21: The truth jet η and ϕ distributions for all models and mediator masses at a lifetime of 150 mm.

The girth distributions of the truth QCD jets and truth emerging jets are shown in Figure 4.22. Here, a “truth QCD jet” is a visible truth jet not matched to a truth dark jet. The QCD jet girth is independent of the signal point parameters, as expected, and the emerging jet girth directly depends on the model mass scale, with heavier models producing wider emerging jets, as a consequence of the dark pion decay vertex opening angle, as discussed above. The girth is also inversely related to the mediator mass, with heavier mediators producing slightly narrower jets, and is independent of the dark pion lifetime.

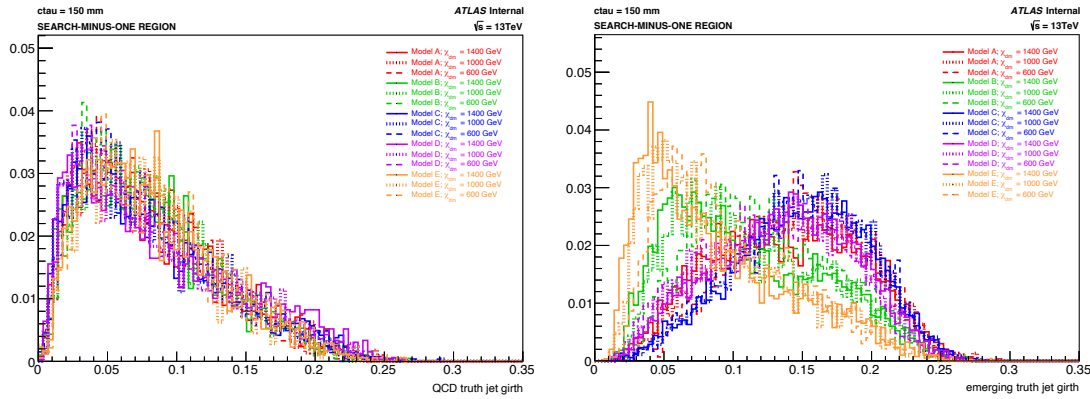


Figure 4.22: The truth emerging (left) and truth QCD (right) jet girth for 150-mm lifetime points.

Finally, the numbers of associated dark pion decay vertices and descendants per truth emerging and QCD jet for a single dark pion lifetime are shown in Figure 4.23, and the numbers of dark pion decay vertices and descendants per truth emerging jet for various lifetimes in Models D and E with a 1400-GeV mediator mass are shown in Figure 4.24.

A vertex or descendant is associated to a jet if it is within $\Delta R < 0.6$. As expected, more dark pion decay vertices and descendants are found around emerging jets than around

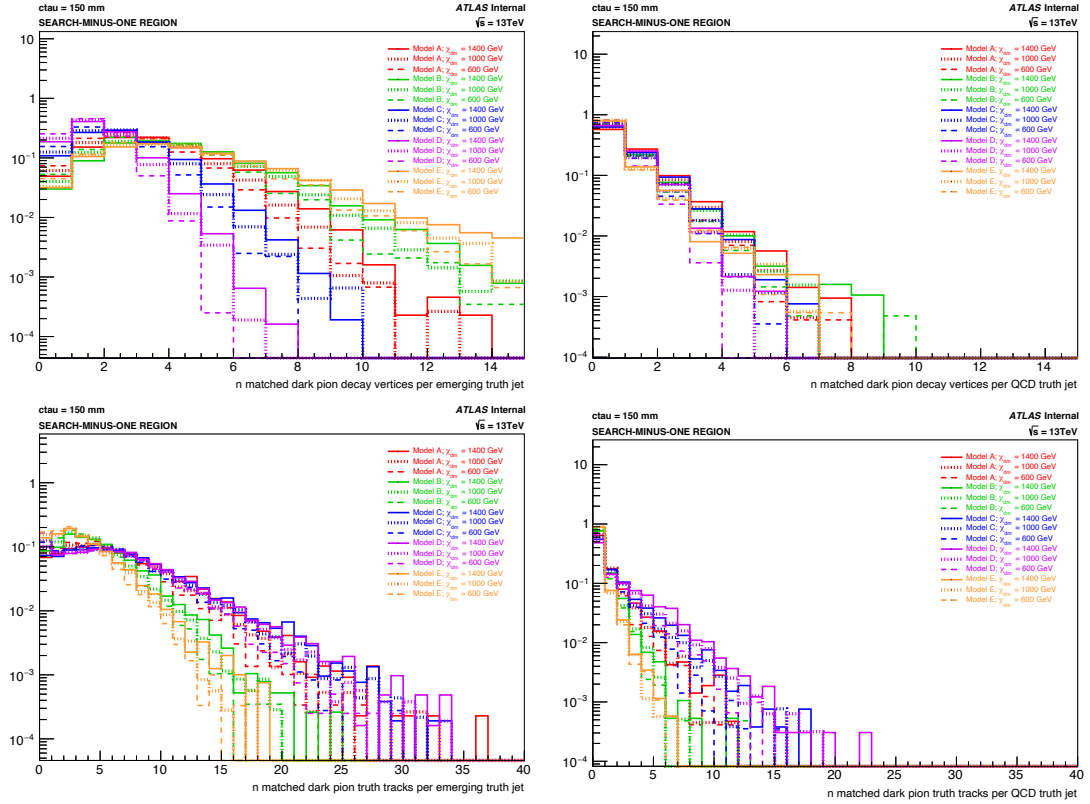


Figure 4.23: The number of matched dark pion decay vertices (top) and dark pion decay descendants (bottom) per truth emerging (left) and truth QCD (right) jet across all models and mediator masses at 150-mm dark pion lifetime.

QCD jets. Lower model mass scales produce larger numbers of jet-associated vertices and smaller numbers of jet-associated descendants, consistent with the overall model dependency of the event-level vertex and descendant multiplicity. Similarly, the distributions are minimally dependent on the mediator masses, with higher mediator masses producing slightly larger numbers of jet-associated displaced vertices and descendants. The numbers of vertices and descendants associated to emerging jets are also inversely related to the dark pion lifetime, as longer lifetime dark pions are more likely to decay outside the inner detec-

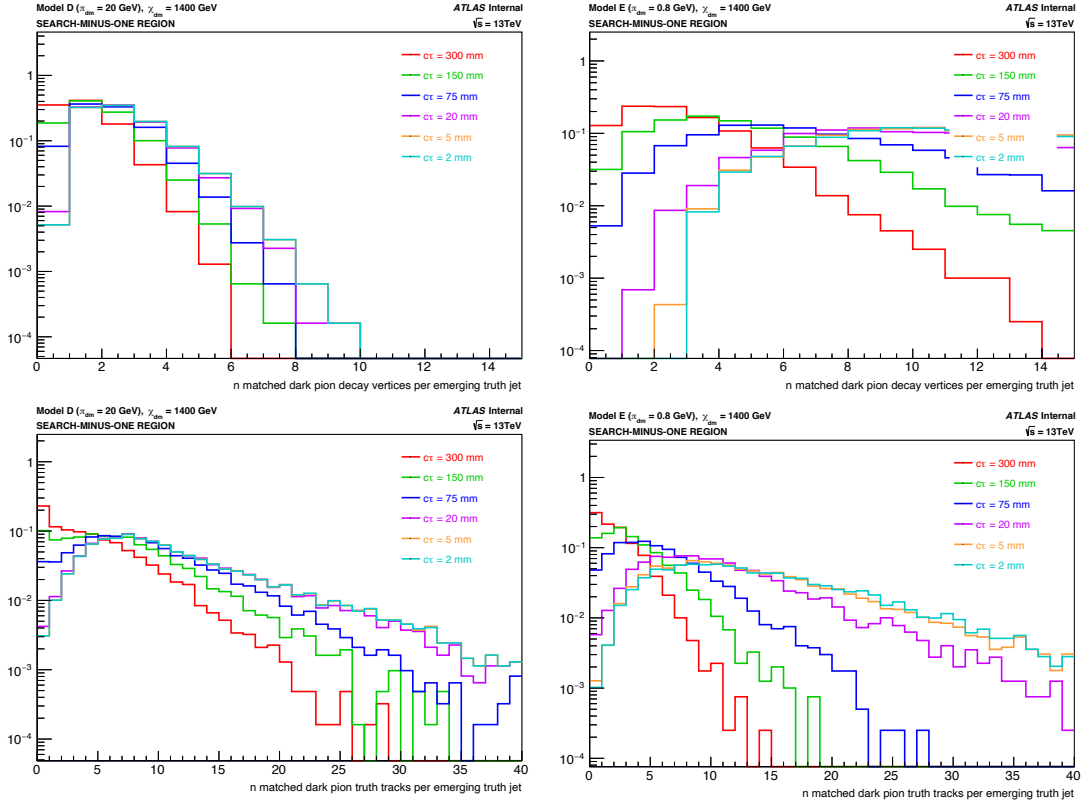


Figure 4.24: The number of matched dark pion decay vertices (top) and dark pion decay descendants (bottom) per truth emerging jet in Model D (left) and Model E (right) at 1400-GeV mediator mass.

tor or calorimeter and thus not be associated to jets.

4.2.2.2 MC BACKGROUND SAMPLES

Background samples are produced for QCD dijet events using the PYTHIA event generator, the NNPDF23LO PDF, and the A14 tune. PYTHIA dijet samples are generated in slices of leading jet p_T and labeled JZXW, where X ranges from 0 to 12 and denotes the sample slice, which represents the range of transverse momentum within which the leading jet must fall.

Each slice is then weighted individually such that when all slices are combined the overall p_T distribution is smooth and falling. The PYTHIA dijet slicing in leading jet p_T [GeV] is:

- JZ₀W: 0 - 20
- JZ₁W: 20 - 60
- JZ₂W: 60 - 160
- JZ₃W: 160 - 400
- JZ₄W: 400 - 800
- JZ₅W: 800 - 1300
- JZ₆W: 1300 - 1800
- JZ₇W: 1800 - 2500
- JZ₈W: 2500 - 3200
- JZ₉W: 3200 - 3900
- JZ₁₀W: 3900 - 4600
- JZ₁₁W: 4600 - 5300
- JZ₁₂W: 5300 - 7000

At the time of the writing, only the JZ₄W slice in campaigns MC16a and MC16d is available with the dedicated RPVLL reconstruction setup necessary for the analysis. This slice is used to design and validate the background estimation technique and to aid in defining the signal selections. The number of events generated, the cross section, and the filter efficiency of the JZ₄W slice with RPVLL reconstruction are listed in Table [4.4](#).

Background Slice		Number of Events			Metadata	
DSID	JZXW Slice	MC16a	MC16d	MC16e	Cross-Section [nb]	Gen. Filter Efficiency
361024	JZ4W	1,000,000	1,000,000	-	2.5463×10^2	5.3137×10^{-4}

Table 4.4: The Pythia dijet JZ4W background MC sample with RPVLL reconstruction. The production cross section and generator filter efficiency are calculated in Pythia.

4.3 SIGNAL SELECTIONS

The aim of the Emerging Jets analysis is to select signal events containing the specific signature characteristic of the simplified models presented in Section 4.1. The set of criteria used to select the signal events defines the signal region, which is optimized for high signal efficiency and background rejection in order to maximize the statistical significance of the signal. The selection criteria used to isolate the signal region are presented below.

4.3.1 SELECTION OVERVIEW

The signal selections used in this analysis are designed to be as model independent as possible in order to be maximally inclusive to any new BSM physics channels with hadronic long-lived particles yielding multijet plus displaced vertex signatures. The emerging jets signal is used as the benchmark for this search, but selections are designed to target the general topology of emerging-jet-like events, rather than being optimized to maximize the efficiency for a particular model, with the expectation that the search may be potentially applicable to other related models in the future. Some tentative selections are proposed to identify

emerging-like jets in the event, but it is presumed these cuts can be loosened or removed as needed, i.e. in related searches, without significant impact on the overall result.

Selection of events for use in the analysis proceeds through a series of successive steps. First, a set of loose preselections is applied to select a sufficient number of events and physics objects with which to perform background studies and to design and optimize the full analysis. Initial search and validation regions are defined to separately study signal-like and background-like events and to investigate and validate further selections used to define the final signal region. The validation region is used specifically to compare data and simulation in order to validate the observables on which cuts are to be applied are well modeled in Monte Carlo. Finally, a tight full selection is applied to remove additional background and further isolate the signal. A summary of the full event selection, including the loose preselections defining the search and validation regions and the tight selections defining the tentative signal region, is shown in Table 4.5 and outlined below. Detailed descriptions of the object and event selections are provided in the subsequent sections.

EVENT PRESELECTION:		Sec. 4.3.2
Skimming	DRAW_RPVLL and DAOD_EXOT23 selections (Sec. 4.2.1.1)	
Event cleaning	removal of corrupted events due to detector problems (calorimeter noise bursts and data corruption; SCT recovery)	
Good Runs Lists	removal of events in bad-quality lumi-blocks	
Jet cleaning	rejection of events with LooseBad ($p_T > 20 \text{ GeV}$ and $ \eta < 2.8$) jets	
Hard scatter	≥ 1 PV with ≥ 2 outgoing tracks	
Baseline objects	≥ 2 baseline jets (Sec. 4.3.3)	
REGION SELECTION:		Sec. 4.3.4
SEARCH		
Trigger	lowest unprescaled four-jet	single-jet
	2015: HLT_4j100	
	2016: HLT_4j100	
	2017: HLT_4j120	
	2018: HLT_4j120	
Jet cut	$N_{\text{jet}} \geq 4$ $p_T > 120 \text{ GeV}$ and $ \eta < 2.5$	$2 \leq N_{\text{jet}} < 4$
N leading jet cut	$H_T^{\text{NJet}} > 1000 \text{ GeV}$	-
DV SELECTION:		Sec. 4.3.5
VALIDATION		
Loose selection	$N_{\text{DV}} \geq 2, 3, 4$ Material Map veto and track cleaning $r < 300 \text{ mm}$ and $ z < 300 \text{ mm}$ $\chi^2/N_{\text{DoF}} < 5$ and $m > 0.7 \text{ GeV}$	
Medium selection	Loose + $p_T > 2.5 \text{ GeV}$	
Tight selection	Medium + minimum track impact parameter and associated error cuts	
EJ SELECTION:		Sec. 4.3.6
$N_{\text{EJ}} \geq 0, 1, 2$		
Loose selection	$p_T > 200 \text{ GeV}$, $ \eta < 2.0$, $m > 25 \text{ GeV}$ $p_T^{N_{\text{sv}}} > 5 \text{ GeV}$ and $N_{\text{jet-trk}}^{N_{\text{sv}}} > 2$	
Tight selection	Loose + $p_T^{N_{\text{sv}}} > 7.5 \text{ GeV}$ and $N_{\text{jet-trk}}^{N_{\text{sv}}} > 4$	
NJETX SELECTION:		Sec. 4.3.7
$X^{\text{NJet}} > Y$		
$\text{NJet} = \text{leading four-jet or dijet system}$		

Table 4.5: The set of consecutive cuts applied to select signal events for the Emerging Jets analysis. Skimming selections are applied to data but not to Monte Carlo samples. DV, EJ, and NJetX selections are applied to the search region but not to the validation region. The signal region is currently still under construction, so all tentative DV and EJ selection working points and potential N_{DV} , N_{EJ} , and X^{NJet} requirements used to build the final signal region are listed.

Events are processed from filtered derivations into analysis-specific n-tuples and then refined into regions isolating the signal. The event preselection consists of the DRAW_RPVLL filter and DAOD_EXOT23 derivation selections described in Section [4.2.I.I.1](#) and [4.2.I.I.3](#), respectively, along with requirements on the quality of the data, the presence of a hard scatter primary vertex, and the number of jets passing loose quality cuts. Events are then separated into orthogonal search and validation regions defined by jet triggers and multiplicities and saved to n-tuples.

The search region is a precursor to the signal region and is designed to provide a region of phase space where signal-like events can be studied before the final signal region selections are applied. Search region events are required to pass the lowest unprescaled four-jet trigger, contain at least four jets with certain transverse momentum and pseudorapidity, and pass a loose cut on the scalar sum- p_T of the four leading jets. The values of the jet- p_T and $-\eta$ cuts are chosen to be near the plateau regions and within the pseudorapidity coverage of the four-jet triggers. The four-jet sum- p_T cut is implemented to reduce the contribution from QCD background. An additional “search-minus-one” subregion that excludes the four-jet sum- p_T requirement is also defined to increase statistics while still remaining orthogonal to the validation region. The validation region is designed to study the background, compare variables to data, and validate the cuts applied to the signal region. Validation region events are required to pass a heavily prescaled single-jet trigger and contain at

least two but less than four jets with the same transverse momentum and pseudorapidity requirements as applied to the jets in the search region. The selections applied ensure the two regions are mutually exclusive, with the search region being signal-rich with four-jet events and the validation region being background-rich with dijet events.

Finally, events in the search region are required to pass additional offline selections on the number of displaced vertices N_{DV} , the number of emerging jets N_{EJ} , and some event-level observable related to the four leading jets X^{NJet} , like the scalar sum- p_{T} ($H_{\text{T}}^{\text{NJet}}$), to be included in the signal region. The signal region is currently being optimized to reduce background and maximize signal sensitivity across all models, mediator masses, and dark pion lifetimes, but the final selection is of the following form:

$$N_{\text{DV}}^i + N_{\text{EJ}}^j + X^{\text{NJet}}, \quad (4.4)$$

where N_{DV}^i is the number of displaced vertices, with $i = 2, 3$, or 4 ; N_{EJ}^j is the number of emerging-like jets, with $j = 0, 1$, or 2 ; and X^{NJet} is a leading four-jet or dijet event-level observable, with $X = H_{\text{T}}, p_{\text{T}}, m_{\text{sum}}$, or something similar.

4.3.2 EVENT PRESELECTION

The event preselection consists of skimming selections specific to RPVLL analyses, as well as a set of quality criteria common among all ATLAS analyses. The initial skimming cri-

teria is defined by the dedicated filter and derivation selections of the RPVLL data flow described in Section [4.2.1.1](#). The only data events used in the analysis are those passing the filters defining the `DRAW_RPVLL` stream, which preselects a subset of relevant events over which to run the specialized large-radius track and secondary vertex reconstruction algorithms, and the subsequent related skimming selections of the analysis-dedicated derivation. The `Emerging` filter targets four-jet signal-like events passing the lowest unprescaled four-jet triggers and dijet background-like events passing a heavily prescaled single-jet trigger, but events passing any of the filters comprising the `DRAW_RPVLL` stream are included in the initial skimming. The `DAOD_EX0T23` selections further skim the data by requiring the events explicitly pass the four-jet or single-jet triggers specific to the Emerging Jets analysis and listed in Section [4.2.1.1.3](#). Monte Carlo events are not subject to the skimming preselection criteria.

After skimming of the data, a cleaning procedure is performed to remove poor quality, corrupted, or incomplete data. A set of event-level cleaning criteria is applied to reject events potentially plagued by the following detector problems:

- LAr noise bursts or data corruption
- Tile data corruption
- SCT recovery procedure

Events passing the event cleaning step are then required to be in the Good Runs Lists (GRL), which provides a list of good luminosity blocks within given runs. Any luminosity

block affected by problematic detector conditions is excluded from the list, and any event within one of the bad lumi-blocks not listed in the GRL is rejected. Finally, jet cleaning is applied, as described in Section 3.4.3.4, and events containing any unclean jets are rejected. The `LooseBad` jet cleaning working point is implemented for this analysis, meaning all jets eligible for cleaning must pass the `Loose` jet cleaning criteria, or the event is thrown away. To be eligible for cleaning, a jet must have $p_T > 20 \text{ GeV}$ and $|\eta| < 2.8$. Jet cleaning is implemented to reduce contributions from non-collision backgrounds, and the presence of unclean jets can affect other features of the event, so it is necessary to remove the entire event rather than individual jets during jet cleaning [132].

Additionally, the event must pass the hard scatter criteria of containing at least one primary vertex with at least two tracks. The primary vertex with the largest sum- p_T -squared is taken to be hard scatter vertex, while the rest are considered pileup vertices.

Lastly, at least two baseline jets are required per event, where a baseline jet is defined in Section 4.3.3.1 below.

4.3.3 BASELINE PHYSICS OBJECT SELECTION

Before further processing into analysis regions and ntuples, certain physics objects, i.e. jets and tracks, in the preselected events are required to pass some baseline quality criteria.

4.3.3.1 BASELINE JETS

The analysis uses `EMTopoAntiKt4Jets`, or jets reconstructed using the anti- k_t algorithm,

with distance parameter $R = 0.4$ and topological clusters measured at the electromagnetic scale as inputs, as discussed in Section 3.4.3. Offline, reconstructed jets are calibrated to restore their energies to those of the corresponding truth jets, as described in Section 3.4.3.3.

This calibration is done according to recommendations by the JetEtMiss combined performance group after reconstruction and before jet selection at the n-tuple production stage.

Baseline jets are then required to have $p_T > 50$ GeV and $|\eta| < 2.7$ after calibration. Jets with $20 < p_T < 60$ GeV and $|\eta| < 2.4$ are additionally required to pass the Medium JVT working point ($\text{JVT} > 0.59$), where the JVT is a measure of the likelihood of the jet originating from the hard-scatter, as opposed to a pileup, vertex, as detailed in 3.4.3.4. The JVT cut has the potential to remove displaced jets that do not point back to the primary vertex, but this is not expected to be an issue in this analysis, since the jets considered in this search are subject to higher- p_T selections, beyond the range over which the JVT cuts are applied, further downstream.

4.3.3.2 BASELINE TRACKS

Baseline tracks are required to have $p_T > 1$ GeV and $\chi^2/N_{\text{DoF}} < 50$, in line with the criteria imposed on tracks used in the reconstruction of secondary vertices.

4.3.4 ANALYSIS REGION SELECTION

After event preselection and baseline object selection, events are separated into two orthogonal and intermediate analysis regions defined by jet triggers and multiplicities. Events passing either set of criteria defining either region are saved to n-tuples for further analysis. Subsequent additional selections are applied to the search region at the analysis level to define the final signal region. The search region is defined to loosely isolate the expected signal before the full, tight selections are applied to remove the background. The validation region is defined to isolate the orthogonal region where no signal is expected for the purposes of studying the backgrounds and systematics and of validating the analysis techniques. The trigger selections applied to the search and validation regions are the four-jet and single-jet triggers defined in the DAOD_EXOT23 derivation, respectively.

4.3.4.1 SEARCH REGION

Search region events must pass the lowest unprescaled four-jet trigger for the corresponding year and contain at least four jets with $p_T > 120$ GeV and $|\eta| < 2.5$. Additionally, a cut is placed on the leading four-jet scalar sum- p_T : $H_T^{\text{NJet}} > 1000$ GeV. The H_T^{NJet} cut is applied to reduce background contributions from QCD jets. An additional “search-minus-one” region is also defined with the same selection criteria as the search region except for the H_T^{NJet} requirement in order to provide a loosened search region with increased statistics that is still

orthogonal to the validation region for testing purposes.

4.3.4.1.1 TRIGGER DETAILS An OR of the four-jet trigger list defined in the `Emerging` filter and the `DAOD_EXOT23` derivation is used to select search region events for the analysis. This list contains all relevant unprescaled four-jet triggers that could potentially be the lowest-threshold at any point throughout Run 2:

- `HLT_4j90`
- `HLT_4j100`
- `HLT_4j110`
- `HLT_4j120`
- `HLT_4j130`
- `HLT_4j140`
- `HLT_4j150`

The jet trigger menu evolved significantly throughout Run 2, with the lowest unprescaled four-jet trigger thresholds changing with luminosity and between data-taking years. Additionally, the calibration applied to jet triggers changed between 2016 and 2017, with MC15 and MC16 used in the jet energy scale calibration for data 2017 and 2018, while MC12 was used for 2015 and 2016. As such, the trigger efficiencies in relation to the offline analysis selections must be studied and accounted for separately for each data-taking year.

The triggers used in the analysis are chosen such that they have collected the full luminosity for ATLAS for each year. This corresponds to `HLT_4j100` for 2015 and 2016 and

`HLT_4j120` for 2017 and 2018. Both triggers are not necessarily the lowest- p_T threshold uprescaled triggers for the entire or any part of the year, but they are always enabled and unprescaled and thus collect full data. For instance, `HLT_4j85` is the lowest unprescaled trigger used throughout 2015, but the `Emerging` filter does not capture this trigger, and `HLT_4j100` is also maintained and unprescaled, and thus collecting full data, throughout the year. Similarly, `HLT_4j100` and `HLT_4j120` are the primary and recommended four-jet triggers used in 2016 and 2017, respectively, as they are always maintained and unprescaled and have collected the full luminosity, despite certain periods within these years implementing additional lower-threshold triggers. `HLT_4j120` is the primary, recommended, and lowest unprescaled four-jet trigger in 2018.

The trigger efficiency turn-on curves for `HLT_4j45`, `HLT_4j85`, and `HLT_5j45` as a function of the n th offline jet p_T in 2015 and 2016 are shown in Figure 4.25. These triggers all have 95–100% turn-on values at the n th offline jet p_T of approximately 10 – 15 GeV above the trigger thresholds, meaning they are fully efficient for events with n jets with p_T of 10 – 15 GeV above the corresponding trigger thresholds. Thus, it is assumed the `HLT_4j100` triggers in 2015 and 2016 will also be fully efficient for the 120 GeV offline jet p_T cuts applied in the analysis. With the increased thresholds for the triggers used in 2017 and 2018, however, the selected events will most likely lie within the turn-on region. The resulting trigger inefficiency in this region will thus need to be accounted for in some way. Alternatively, the

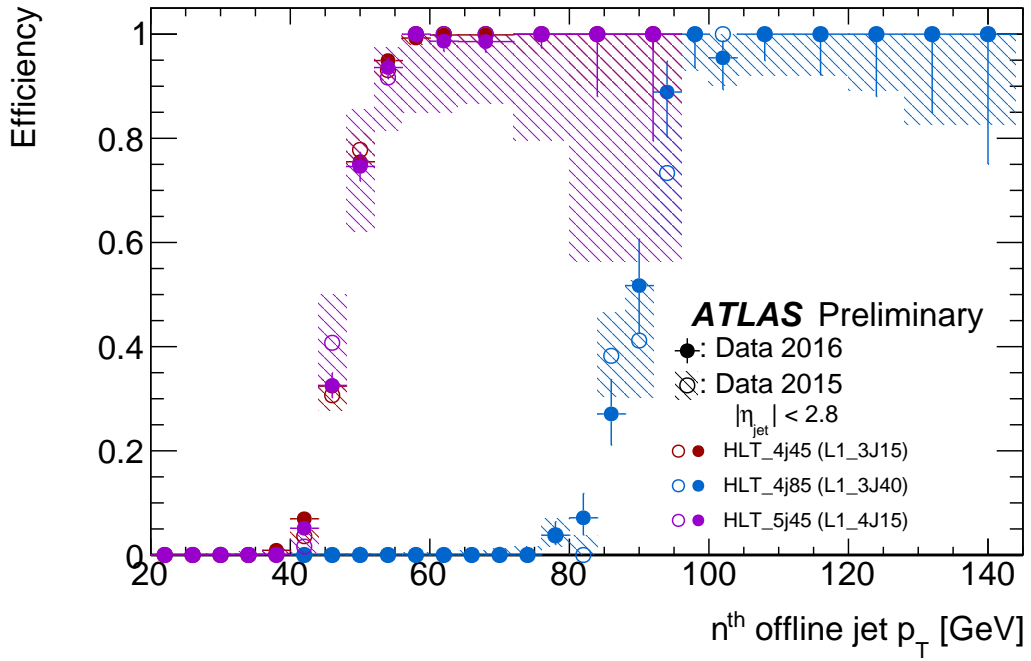


Figure 4.25: Efficiencies for HLT n -jet triggers as a function of the n th leading offline jet p_T in 2015 and 2016 data [133]. HLT _{n} j_x triggers accept events containing n jets reconstructed at L1 with $E_T > x$ GeV and $|\eta| < 2.8$. Additionally, the n leading jets are required to be separated by $\Delta R > 0.6$. The HLT₄j85 four-jet trigger is shown in blue with a 95% turn-on around 95 GeV.

offline jet p_T cuts can be tightened to select events in the trigger plateau where the efficiency is nearly 100%, at the potential cost of some small signal efficiency loss.

4.3.4.2 VALIDATION REGION

Validation region events must pass a single jet trigger and contain at least two but less than four, i.e. two or three, jets with $p_T > 120$ GeV and $|\eta| < 2.5$. No H_T^{Njet} requirement is placed on the validation region. The triggers considered in the validation region are those defined in the single-jet trigger list of the DAOD_EXOT23 derivation (see Section 4.2.1.1.3,

which consists of both heavily prescaled and unprescaled triggers. A heavily prescaled trigger is used to select dijet events in the `Emerging` filter in order to keep the filter rate low, but other potential single jet triggers are included when skimming the derivations and selecting the validation region events in order to increase statistics in this region. As this region is only used for testing and validation and not in the final analysis of the signal, the specific triggers and their prescales are of no consequence to the final result.

4.3.5 DISPLACED VERTEX SELECTION

After the selection of the initial analysis regions, additional selections are applied to the search region to further isolate the signal and remove background objects and events. Events are required to contain some number of displaced vertices (DVs) per event, where a tentative selection requiring between two and four displaced vertices ($N_{\text{DV}} \geq 2, 3, \text{ or } 4$) is proposed. The displaced vertices in the event are required to satisfy certain quality criteria and signal selections designed to eliminate contributions from fakes, as well as to be associated to one of the N_{jet} leading jets in the event. Three tentative working points are defined to select signal DVs for this analysis: `Loose`, `Medium`, and `Tight`. These sets of DV selection criteria have not yet been fully optimized and are subject to further tuning in order to maximize signal DV retention and fake DV rejection, particularly in terms of additional track cleaning and filtering that could be applied to remove bad tracks, which could alter the subsequent vertex-level cuts.

4.3.5.1 DISPLACED VERTEX SELECTION WORKING POINTS

The **Loose**, **Medium**, and **Tight** working points defined for analysis DV selection are listed in Table 4.6 below.

Loose
Material Map veto
Track cleaning
Fiducial volume: $r < 300 \text{ mm}$ and $ z < 300 \text{ mm}$
Quality of fit: $\chi^2/N_{\text{DoF}} < 5$
K-short mass cut: $m > 0.7 \text{ GeV}$
Medium
Loose selections
$p_T > 2.5 \text{ GeV}$
Tight
Medium selections
minimum track $ d_o < 10 \text{ mm}$
minimum track $ z_o < 100 \text{ mm}$
minimum square-root track d_o -error < 0.5
minimum square-root track z_o -error < 1.5

Table 4.6: Loose, Medium, and Tight working points for analysis DV selection. Medium selections are applied on top of Loose selections, and Tight on top of Medium.

In addition to passing one of the working points defined for the analysis, displaced vertices are also required to be associated to one of the N_{jet} leading jets in the event in order to be considered in the final displaced vertex count. Secondary vertices are associated to jets through ΔR matching, where a match is considered if the vertex is within $\Delta R < 0.6$ of the jet center. In the case of multiple nearby jets within the specified angular separation, the vertex is associated to the single closest jet in ΔR .

The displaced vertex selection working points defined above are designed to optimally select signal DVs and reject fake DVs produced from background across all LLP models, without the relatively strict mass and track multiplicity requirements implemented in other ATLAS DV searches. The determination of the selections comprising the working points are detailed below.

The `Loose` DV working point is based on a set of standard selections commonly applied to many RPVLL DV analyses to remove known and easily isolated background sources.

First, all vertices must pass the Material Map veto. DVs are rejected if they are reconstructed inside of material-rich regions of the detector, as determined by a three-dimensional material map [134]. Hadronic interactions with the detector material produce a large source of background displaced vertices with large track multiplicities that are difficult to distinguish from signal long-lived particle decays. Thus, it is necessary to remove DVs found inside regions of the detector material to reduce background contributions from hadronic interactions. A simplified map of the detector material in the analysis fiducial volume is derived from measurements of low-mass, low-track-multiplicity DVs in data and from information about known detector material in simulation. The map is three-dimensional in (r, z, ϕ) , covering $r < 300$ mm, $|z| < 300$ mm, and $-\pi < \phi < \pi$, and indicates the presence or absence of material at a given point in the real detector in Run 2 data and in the simulated detector in MC16 simulation. In designing the map, selections

are applied to remove vertices produced from real LLPs, from random track crossings, and from fake vertices, in order to isolate displaced vertices dominated by hadronic interactions with the detector material. After these selections, a high density of the remaining DVs in any given region is indicative of the presence of material, i.e. bins in Δr , Δz , and $\Delta\phi$ with N_{DV} above some threshold are counted as material. Additional known elements of the detector, like the beam pipe and support tubes, are then added to the map by hand. The locations of the material in the map are then compared to the locations of the displaced vertices to veto DVs produced from hadronic interactions with the detector material. The positions of the detector material and the corresponding displaced vertices rejected by the Material Map veto are shown in Figure 4.26. The veto removes approximately 42% of the analysis fiducial volume.

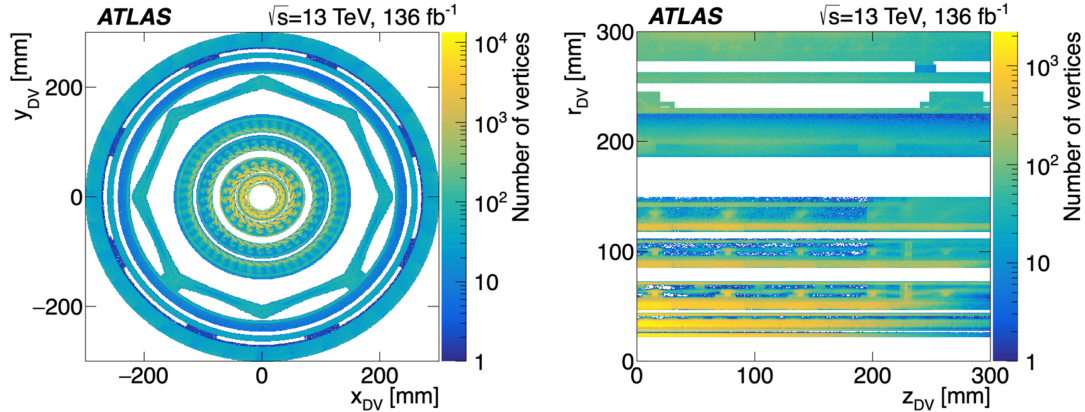


Figure 4.26: The distributions in the $x - y$ (left) and $r - z$ (right) planes of reconstructed displaced vertices rejected by the Material Map veto in 2016-2018 ATLAS data [135]. The locations of the vetoed displaced vertices correspond to regions of material defined in the dedicated Material Map.

Next, the track cleaning procedure detailed in Section [3.4.2.2.1](#) is applied to remove problematic tracks from the reconstructed vertices. The effect of further filtering of poor-quality or poorly-associated tracks, known as track trimming, is being investigated but has not yet been implemented in the current iteration of the analysis. After the removal of the unclean tracks, the kinematic variables of the vertices are recomputed using the remaining clean tracks. Vertices with less than two clean tracks are then rejected. As all vertices are reconstructed with at least two “selected” tracks, and with the current cleaning procedure only removing “associated” tracks added to the vertex during the final track attachment step of reconstruction, the track cleaning potentially alters the vertex observables but does not remove any vertices from the event. With the addition of track trimming in the future, this may not always be the case.

Figure [4.27](#) shows the d_o and ϕ distributions of displaced vertex associated tracks before and after track cleaning in the search-minus-one region of simulated signal and background samples. The cleaning procedure removes associated tracks with certain d_o values corresponding to the radial positions of the Pixel layers and mitigates the observed phi asymmetry resulting from a bug in the secondary vertexing algorithm.

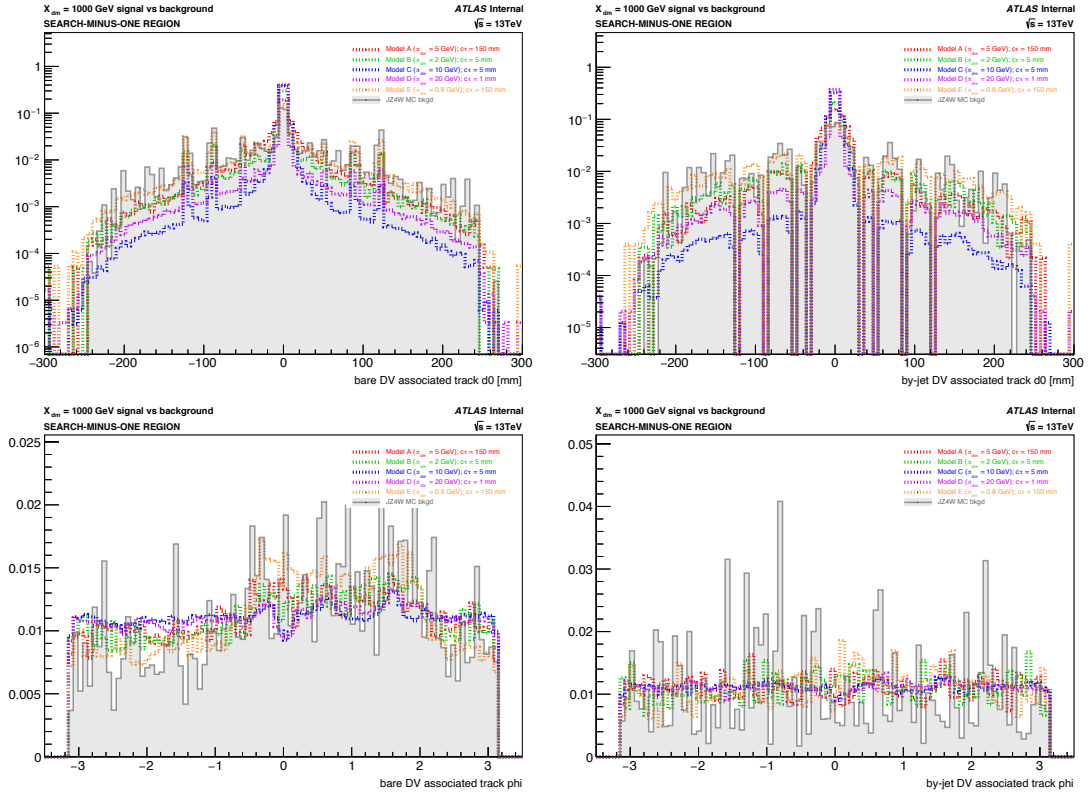


Figure 4.27: The transverse impact parameter d_o (top) and azimuthal angle ϕ (bottom) of the displaced vertices in the search-minus-one region before (left) and after (right) track cleaning. Distributions are shown in color for five signal models with $m_{X_d} = 1000$ GeV and different dark pion lifetimes, as well as in grey for the MC QCD dijet background. No other DV cuts are applied.

Selections are then applied to the position of the vertices, as one can only reasonably expect to efficiently reconstruct good-quality vertices within a certain fiducial volume, defined by $r < 300$ mm and $|z| < 300$ mm and covering the majority of the pixel barrel up to the first layer of the SCT. Displaced vertices outside of this volume are rejected. The radial limit of the fiducial volume is set by the tracking algorithm, as there are not enough hits left in the tracker to efficiently reconstruct tracks with Large Radius Tracking above $r = 300$ mm, and

the longitudinal limit is loosely set by the vertexing algorithm, as the vertex reconstruction efficiency significantly decreases close to edge of the Pixel barrel and beyond.

The radial and longitudinal displacements of the secondary vertex positions before the fiducial volume cut is applied are shown in Figure [4.28](#) for signal and background DVs.

Here, a signal displaced vertex is a reconstructed vertex matched to a reconstructible dark pion decay with $r < 563$ mm, $|z| < 2720$ mm, and two outgoing charged descendants with $p_T > 1$ GeV. For the purposes of identifying discriminating variables between signal and background vertices and investigating the effects of the displaced vertex selections, a very loose matching criteria is applied, where any reconstructed vertex with a nonzero match score is considered a match. The match score is calculated as described in Section [3.4.2.2.2](#).

Similarly, a background displaced vertex is a reconstructed vertex with no match to a dark pion decay. The signal and background vertex distributions are produced from signal and background MC samples, respectively. All vertex variable distributions in this section are normalized to unity to illustrate differences in shape between signal and background.

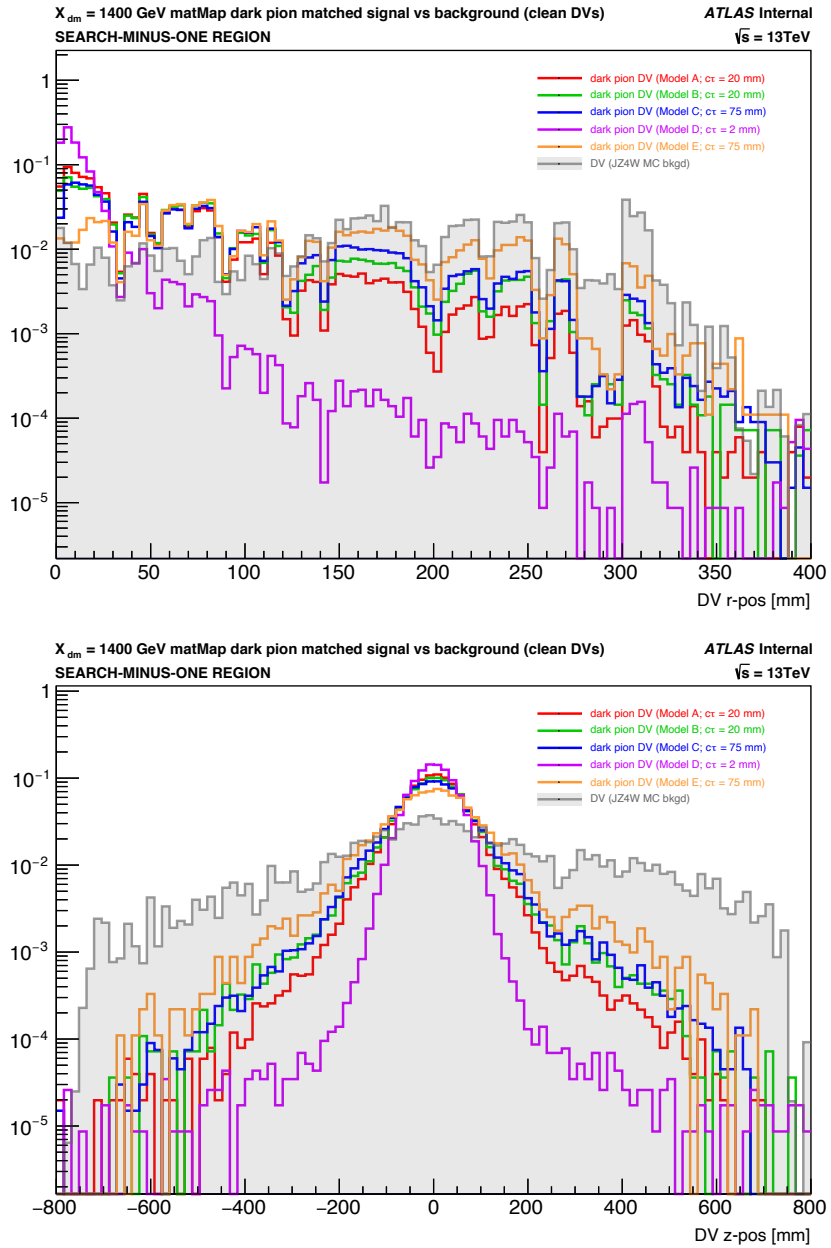


Figure 4.28: The transverse (top) and longitudinal (bottom) displacements of the secondary vertex position, r and z , before the fiducial volume cut is applied in the search-minus-one region. Signal distributions are shown in red (Model A), green (Model B), blue (Model C), purple (Model D), and orange (Model E) for a 1400-GeV mediator mass and three different dark pion lifetimes. The QCD Pythia dijet background distribution is shown in grey. The jagged behavior of the r distribution is a result of the Material Map veto.

While the signal r distributions look very much like background at long lifetime, the background distribution is relatively flat across all r and is much wider than the signal in z , indicative of fake vertices reconstructed from random track crossings throughout the detector. The fiducial selection attempts to remove a significant portion of these fake DVs by rejecting vertices outside of the inner detector volume where the secondary vertex reconstruction is reasonably efficient. Additionally, the material map is only defined in this volume, meaning DVs produced from hadronic interactions with the detector material are not vetoed outside of this fiducial volume.

A cut is also imposed on the reduced goodness of the vertex fit, requiring $\chi^2 / N_{\text{DoF}} < 5$, to remove poorly-fit secondary vertices, which are typical of background DVs.

Finally, a mass cut is applied to remove displaced vertices from k-short decays to charged pions, which provide a small but non-negligible source of Standard Model background. The k-short has a mass of approximately 0.5 GeV and decays with a long lifetime of around 27 mm. The displaced vertices resulting from these decays can be removed by excluding secondary vertices in the k-short mass region, i.e. between 0.45 and 0.55 GeV. To err on the side of increased background reduction, rather than removing just the k-short mass window, all DVs below a certain mass threshold are excluded. To avoid signal loss, the threshold is set to 0.1 GeV below the lowest dark pion mass considered in the benchmark models, and vertices are required to have masses of at least 0.7 GeV.

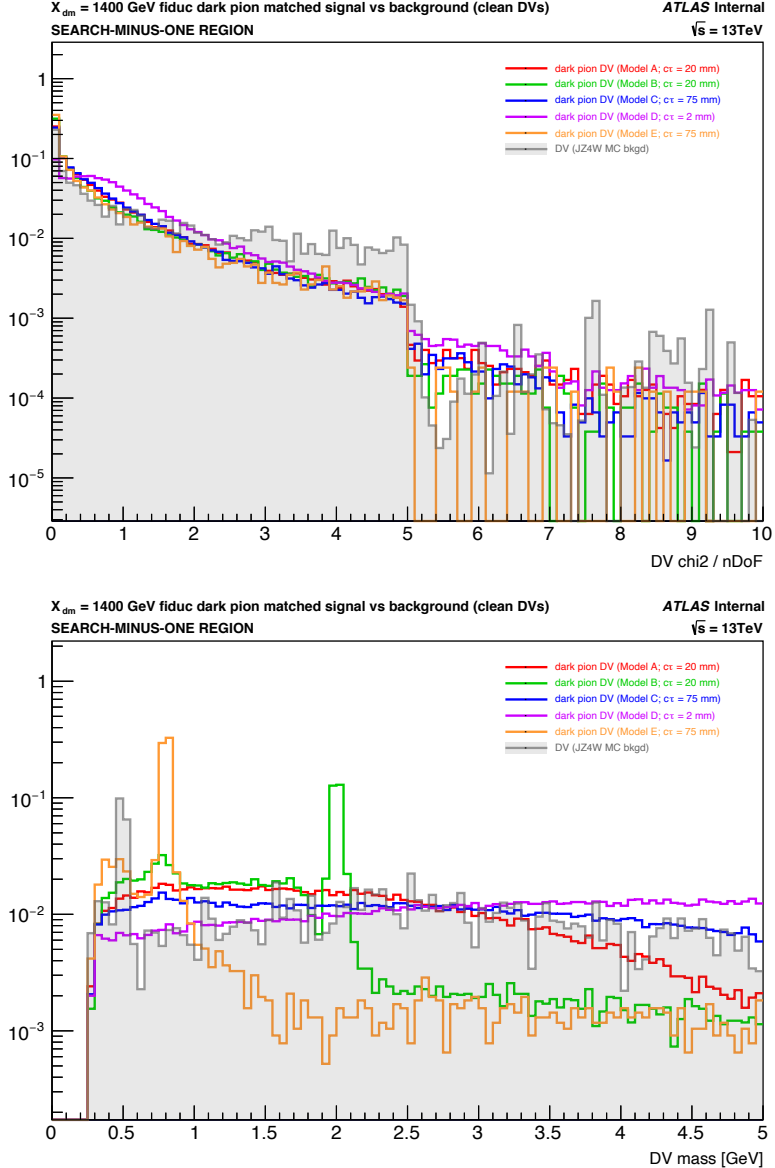


Figure 4.29: The reduced goodness of fit χ^2 / N_{DoF} (top) and mass (bottom) of the signal and background displaced vertices after application of the Material Map veto, the track cleaning procedure, and the fiducial volume selections in the search-minus-one region. Five representative signal points are shown in color for different models and lifetimes and a 1400-GeV mediator mass against the MC background in grey. The mass distribution is zoomed in on the x-axis to show the low-mass behavior, particularly the peak in the background distribution around 0.5 GeV, corresponding to the k-short decay.

The distributions of the secondary vertex χ^2/N_{DoF} and mass in signal and background after the Material Map veto, track cleaning, and fiducial volume selections are shown in Figure 4.29. The background DVs tend to have higher χ^2/N_{DoF} values, and the k-short mass peak is clearly visible in the background mass distribution.

Additional selections are then applied to define the `Medium` and `Tight` working points, based on further comparisons between signal vertices matched to LLP decays and unmatched background DVs. Cuts are imposed with the intent to minimize signal loss and maximize background reduction. After the `Loose` selections are applied, the displaced vertices are dominated by fakes produced from random track crossings. These fake vertices tend to have low mass and low track multiplicity. Unfortunately for the search at hand, the displaced vertices of the Emerging Jets signal also tend to be low-mass and low-multiplicity, particularly in the lower-mass benchmark models, so it is necessary to consider alternative discriminating variables to define additional displaced vertex selections. The `Medium` and `Tight` selections are designed to maximize the fake vertex rejection, or the fraction of unmatched vertices failing the DV selections, while keeping the signal vertex selection efficiency, or fraction of signal vertices passing the DV selections, as high as possible, for the purpose of effectively reducing the background to zero after applying the N_{DV} event-level signal selection. At this point, extensive optimization has not been performed, and more emphasis has been placed on background rejection than signal efficiency. Further optimiza-

tion could be performed to increase sensitivity to certain signal points or to boost the signal efficiency overall, but the working points defined below are currently adequate selections to reduce background while retaining relatively sufficient signal.

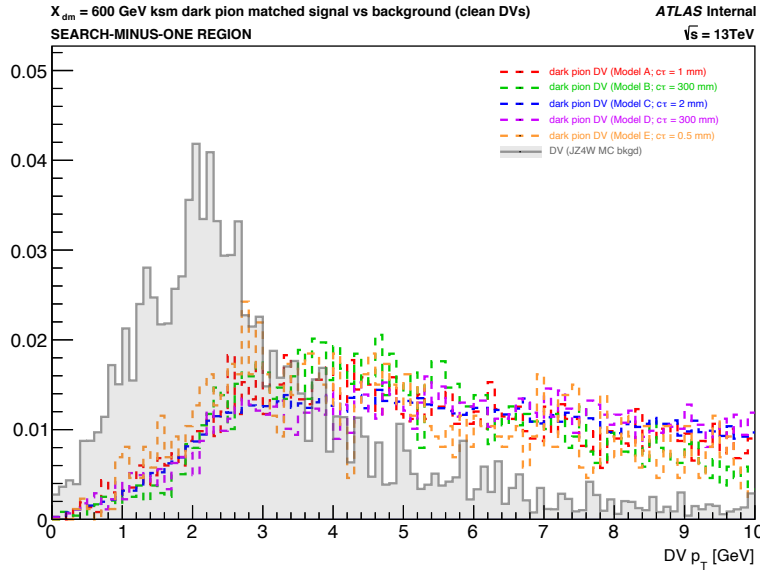


Figure 4.30: The displaced vertex p_T distribution in 600-GeV mediator mass signal and dijet background after Loose selections are applied in the search-minus-one region. The transverse momentum of the vertex is calculated from the sum of the four-momentum of the constituent tracks, and the distribution is zoomed in on the x -axis to highlight the behavior at low- p_T .

The Medium DV selection working point applies a p_T cut on top of the Loose selections. The vertex p_T is calculated from the constituent track four-momentum sum. Since background vertices tend to have few tracks and low mass, they are also expected to be low- p_T , and cutting on the transverse momentum of the vertex provides more freedom in the applied selection over the mass, which is very low for some signals, and the track multiplicity,

which is a discrete variable. The vertex p_T thus provides a reasonable handle to remove background DVs without significantly affecting the signal, as shown in Figure 4.30, and vertices are required to have $p_T > 2.5 \text{ GeV}$

The Tight DV selection working point then applies cuts on the minimum of the vertex track impact parameters and their uncertainties on top of the Medium selections. Background vertices are often formed from random track crossings from large-radius tracks reconstructed with the LRT algorithm, which implements very loose impact parameter cuts and thus yields high fake rates, so background DVs are more likely to be constituted of tracks with large impact parameters and large related uncertainties, indicative of fake tracks. While signal DVs are also expected to be highly displaced and thus have large impact parameters, particularly for models with very long lifetimes, the minimum of the impact parameters of the tracks constituting the vertex is seen to be larger in background than in signal. Thus, vertices with minimum transverse and longitudinal impact parameters of all constituent tracks above some threshold are rejected. Similarly, vertices with minimum square-root error on the transverse and longitudinal impact parameters of all constituent tracks above some threshold are rejected in order to remove vertices comprised primarily of likely fake tracks, where the error is the standard deviation of the measured track impact parameter. Tight displaced vertices are required to have minimum track $|d_o| < 10 \text{ mm}$, minimum track $|z_o| < 100 \text{ mm}$, minimum square-root track d_o -uncertainty < 0.5 , and minimum

square-root track z_0 -uncertainty < 1.5 . Figure 4.31 illustrates the difference in the minimum track impact parameter and square-root error distributions between signal and background vertices.

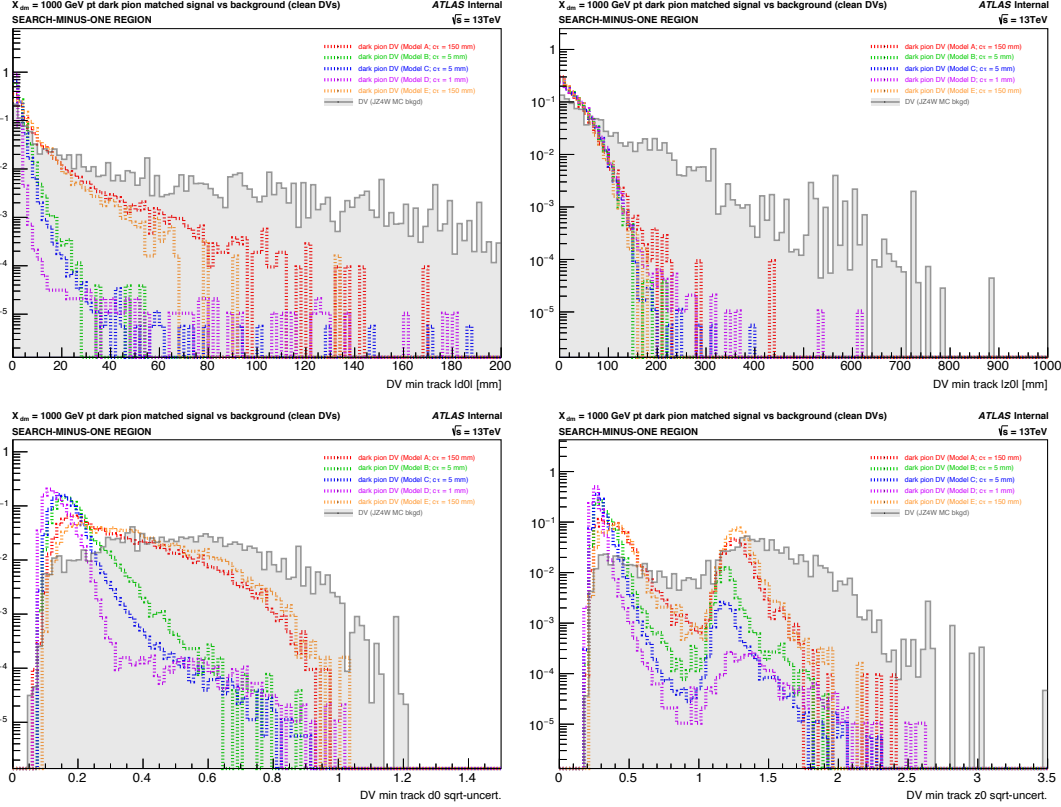


Figure 4.31: The minimum track transverse (left) and longitudinal (right) impact parameter (top) and corresponding square-root uncertainty (bottom) of MC signal and background displaced vertices in the search-minus-one region after Medium selections are applied. The signal distributions are shown in color for five models, various dark pion lifetimes, and a 1000-GeV scalar mediator. The QCD dijet background is shown in grey.

Finally, vertices passing one of the above defined selection working points are also required to be associated to one of the N_{jet} leading jets in the event, where $N_{\text{jet}} = 4$ in the search region and $N_{\text{jet}} = 2$ or 3 in the validation region. This selection is designed to exploit

the emerging jets topology of the signal, where multiple displaced vertices are expected to be inside of a single jet cone, whereas background vertices are more likely to be randomly distributed throughout the detector and not associated to any single jet object.

The overall effect of the displaced vertex selection criteria described above can be understood by studying the resulting vertex-level and event-level yields and efficiencies, as compared between signal and background.

The cumulative effect of each individual displaced vertex selection on the overall vertex count and efficiency of the signal and background is illustrated in the vertex-level cutflow shown in Figure 4.32. Each bin in the cutflow represents the number or fraction of total vertices in all events in the search-minus-one region passing the corresponding cut and all previous cuts. While the count and efficiency decreases with each cut for both the signal and background, the displaced vertex selection efficiency decreases more slowly for signal than for background, indicating the cuts target background vertices more often than signal vertices, as intended. The ratio of the signal to background, displayed underneath the cutflow, increases with each successive cut, with the exception of the final requirement of association to a leading jet.

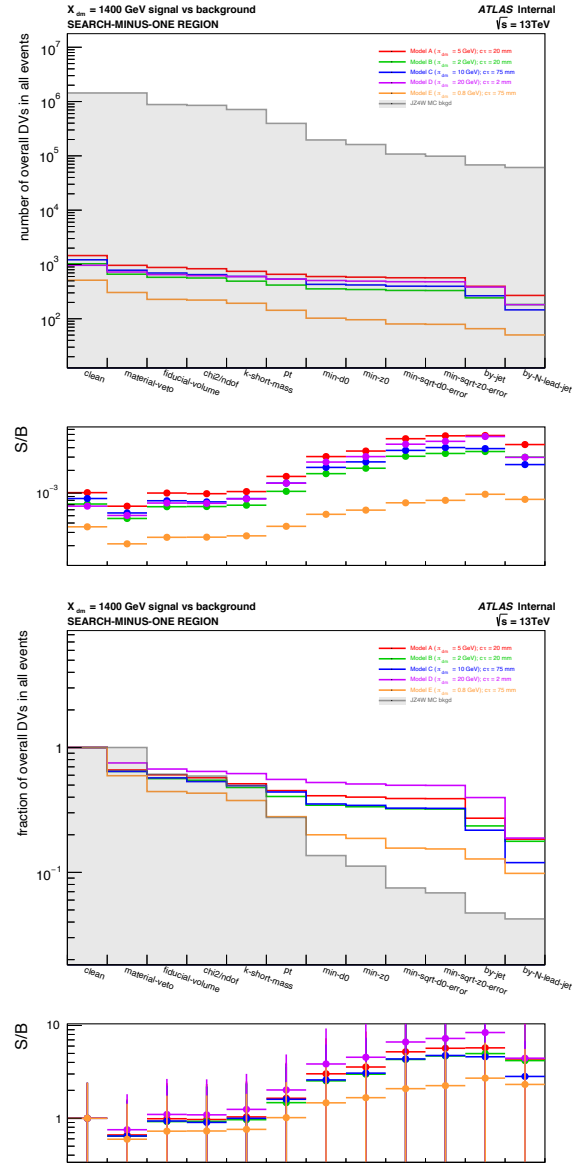


Figure 4.32: The vertex-level cutflow (top) and cutflow efficiency (bottom) for the individual displaced vertex selections, showing the number and fraction of total vertices in all events in the search-minus-one region passing each successive cut, respectively. The cutflows are compared between five signal models and the MC background. The bottom panels show the signal-to-background ratios of each bin. The cuts are designed to maximally reduce the background while maintaining signal efficiency. The background samples used in this study have the Material Map veto applied at the n-tuple level; hence, its effect on the background vertices is not evident from the cutflow.

An alternative “by-jet” selection, where the vertex is only required to be associated to any jet in the event, but not necessarily a leading jet, is seen to offer a higher signal efficiency than the “by-N-lead-jet” selection and a maximum signal-to-background ratio when combined with all other previous selections. As such, it may be beneficial to loosen the final DV jet-association in order to boost the signal efficiency.

The event-level cutflows for the N_{DV} selection are shown in Figure 4.33, comparing 600-GeV, 1000-GeV, and 1400-GeV mediator-mass signal events to background for the **Loose**, **Medium**, and **Tight** displaced vertex selection working points with the by-leading-jet requirement. Each cutflow bin shows the number of weighted events in the search-minus-one region surviving the respective N_{DV} selection, where N_{DV} is the number of displaced vertices required per event, and MC events are weighted by the production cross-section and the generator filter efficiency and scaled to full Run 2 luminosity. Additionally, the background MC events are weighted according to the jet p_{T} slice. Unless otherwise stated, all MC events referred to throughout the remainder of the thesis are weighted accordingly. The background effectively goes to zero for $N_{\text{DV}} > 6$, $N_{\text{DV}} > 5$, and $N_{\text{DV}} > 3$ with the **Loose**, **Medium**, and **Tight** working points, respectively. The signal vertex yield suffers in the low-mass models and for extreme dark pion lifetimes, whether very short or very long, and is lowest for the **Tight** DV selection working point.

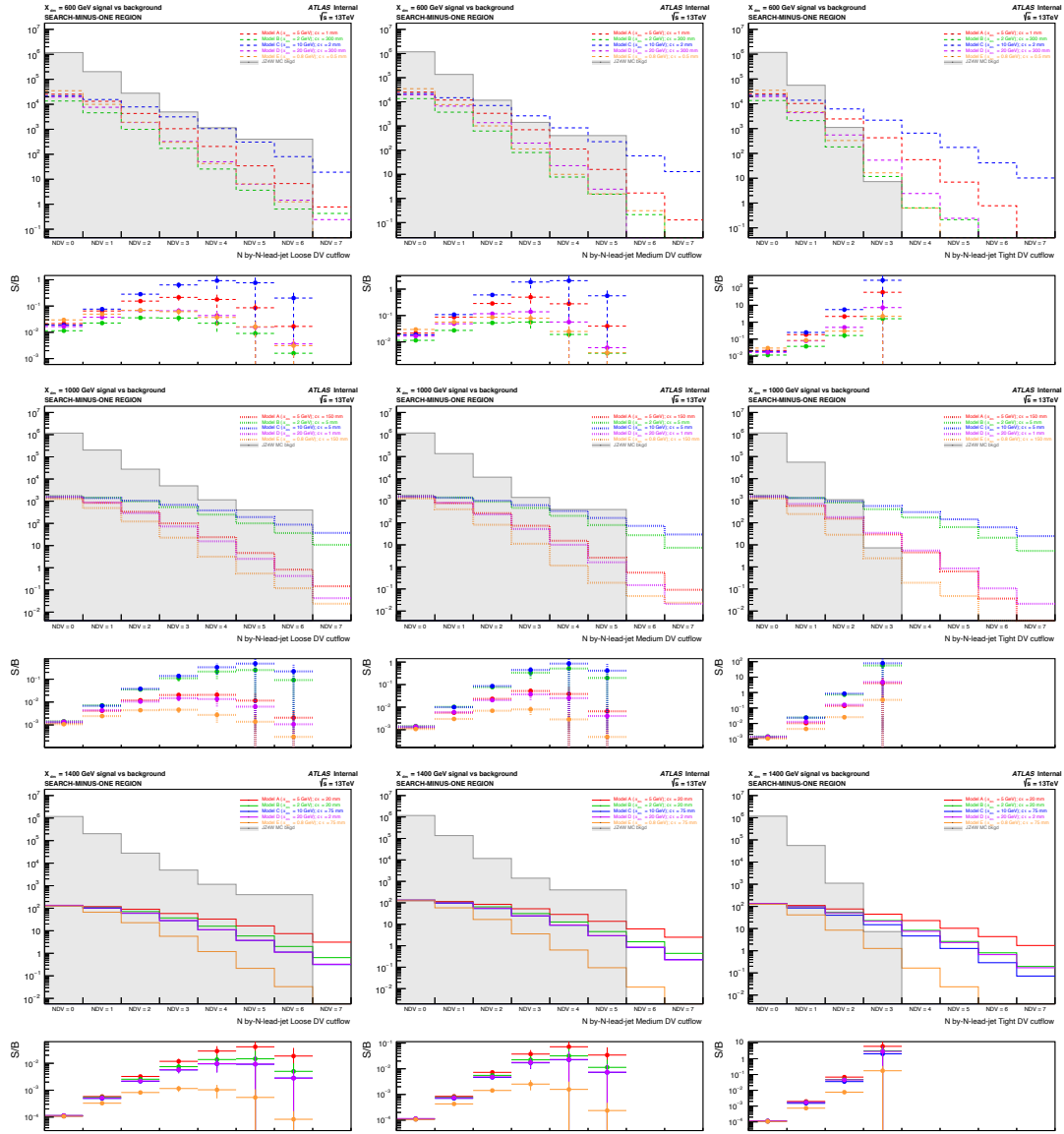


Figure 4.33: The event-level N_{DV} cutflows for by-N-lead-jet Loose (left), Medium (center), and Tight (right) DVs in 600-GeV (top), 1000-GeV (middle), and 1400-GeV (bottom) signal samples versus a QCD dijet background sample. Each bin displays the number of events in the search-minus-one region containing at least the number of vertices specified by the N_{DV} selection. The bottom panels show the ratio of signal to background events in each bin with nonzero background.

The N_{DV} event-level cutflows comparing **Loose**, **Medium**, and **Tight** vertices selected with the by-N-lead-jet requirement to those selected with the by-jet requirement are shown in Figure 4.34 for 1000-GeV mediator-mass signal versus background. The by-jet requirement increases the signal yield somewhat over the by-N-lead-jet requirement for all working points, but it also significantly increases the background yield for the **Loose** and **Medium** working points. For the **Tight** working point, the background is overall relatively unaffected, going to zero for $N_{\text{DV}} > 3$ regardless of whether the jets to which the displaced vertices are associated are the leading jets in the event. As such, the jet association requirement can be loosened when used in conjunction with the **Tight** working point for selecting displaced vertices in order to increase the overall signal efficiency, if need be.

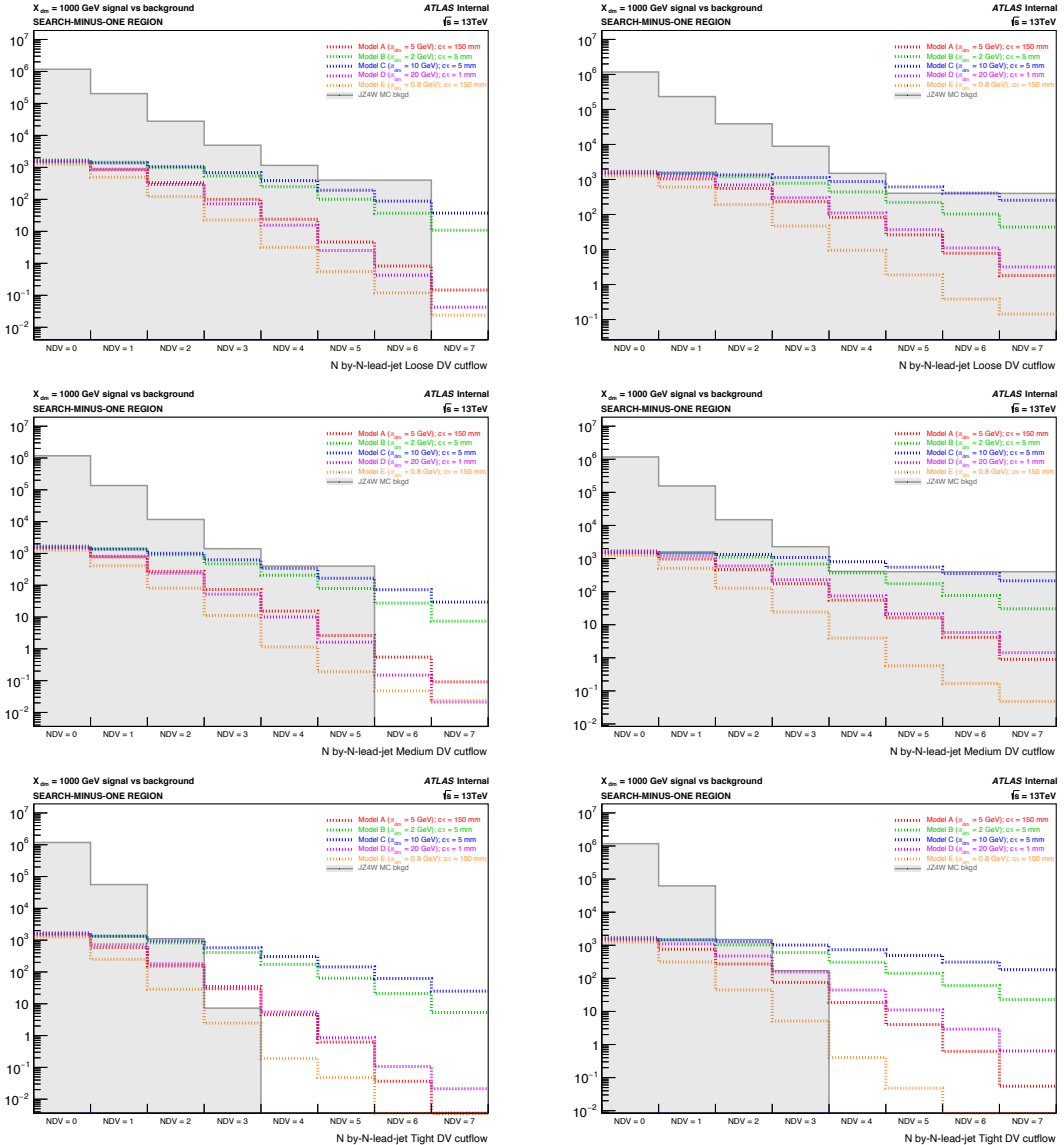


Figure 4.34: The event-level N_{DV} cutflows for by-N-lead-jet (left) and by-jet (right) Loose (top), Medium (middle) and Tight (bottom) DVs in 1000-GeV signal samples versus a QCD dijet background sample. Each bin displays the number of events in the search-minus-one region containing at least the number of vertices specified by the N_{DV} selection.

4.3.5.2 DISPLACED VERTEX RECONSTRUCTION EFFICIENCY

The displaced vertex reconstruction efficiency in the context of the emerging jets simplified signal models is presented below. The efficiency for reconstructing displaced vertices is dependent on the tracking efficiency for reconstructing charged particles as tracks and on the secondary vertexing efficiency for reconstructing tracks as displaced vertices. To extract the individual effects of the tracking and secondary vertexing algorithms on the overall displaced vertex reconstruction efficiency for the emerging jets signal, the tracking and vertexing efficiencies are studied separately, following the methodologies introduced in Sections [3.4.1.2.1](#) and [3.4.2.2.2](#), respectively, where the general performances of the algorithms are discussed in the context of a few representative RPVLL models.

4.3.5.2.1 TRACKING EFFICIENCY The track reconstruction efficiency is defined as the fraction of signal truth particles matched to reconstructed tracks, where a truth-track pair is considered a match if the hit-based matching probability score is at least 0.5. The same fiducial selections as those presented in Table [3.5](#) are applied to truth particles in order to target signal particles that can reasonably be expected to be reconstructed as tracks in the inner detector. These fiducial selections require the truth particles under consideration to have $p_T > 1 \text{ GeV}$ and $|\eta| < 2.5$, to be produced at a radial distance from the IP of $r < 440 \text{ mm}$, to be electrically charged, and to be a descendant of the long-lived dark pion.

As discussed in the LRT performance section above, the overall track reconstruction efficiency is known to deteriorate as the displacement of the track from the interaction point increases. Figure 4.35 shows the inclusive tracking efficiency for five representative EJs signal points as a function of the truth particle production radius r and the truth particle transverse impact parameter $|d_o|$. The inclusive tracking efficiency is the fraction of truth particles reconstructed as tracks by either the standard or large-radius tracking algorithm and accounts for all reconstructed tracks, regardless of the specific tracking algorithm used to reconstruct them.

For all signal points, the inclusive tracking efficiency begins to degrade around $r = 50$ mm, with an efficiency between 80% and 100% for $r \approx 50$ mm to $r \approx 100$ mm and between 60% and 80% for $r \approx 100$ mm to $r \approx 300$ mm. Once r approaches 300 mm, the tracking efficiency drops significantly to only 30% and quickly dissipates above this radial limit. Similarly, the tracking efficiency consistently decreases as a function of $|d_o|$, approaching zero as $|d_o|$ approaches 300 mm. The anomalous upticks observed in some of the signal distributions are most likely due to low statistics in their tails. The efficiency varies somewhat between signal points, with the inclusive tracking efficiencies for heavier models and shorter lifetimes being higher, as heavier points are more likely to produce higher- p_T tracks, and shorter lifetimes are more likely to produce less displaced tracks, for which the track reconstruction is more efficient.

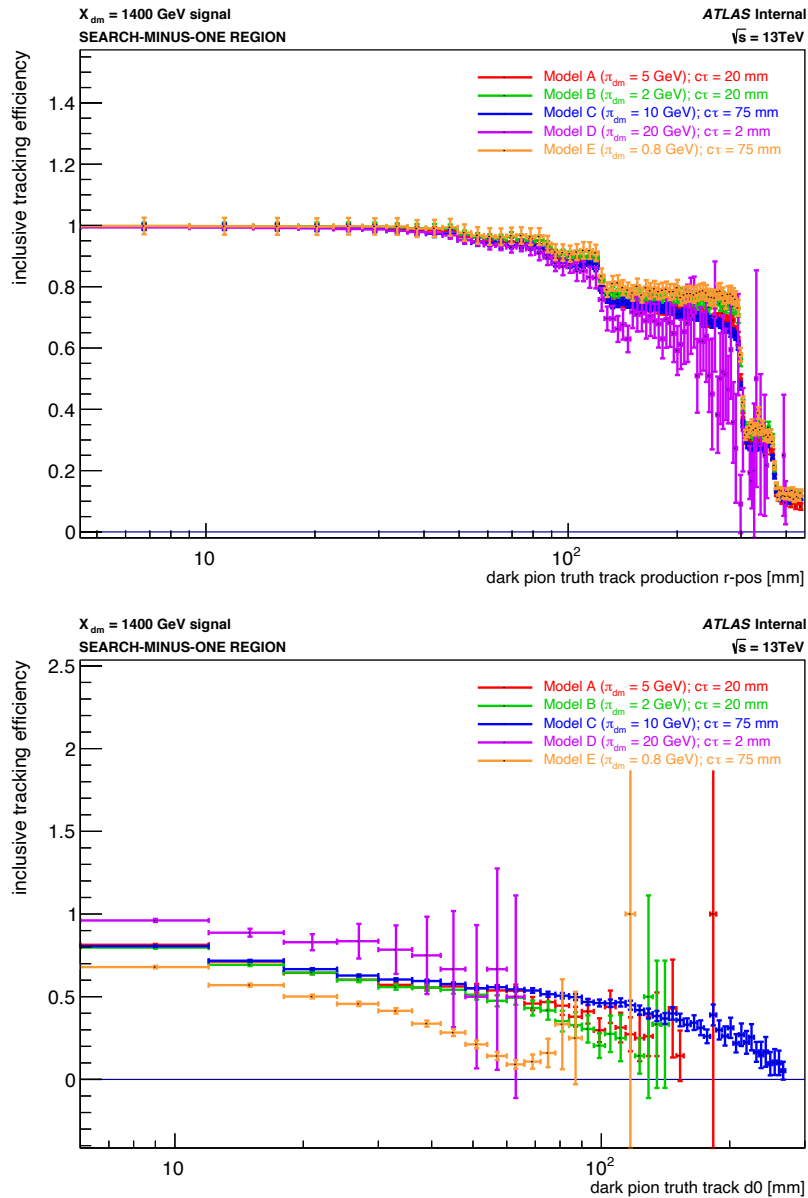


Figure 4.35: Inclusive tracking efficiency as a function of truth particle production radius r (top) and truth particle transverse impact parameter $|d_0|$ (bottom) for five 1400-GeV mediator-mass signal models with different lifetimes.

The inclusive tracking efficiency is a combination of the standard tracking efficiency and the large-radius tracking efficiency, which are additive. The standard tracking efficiency, or the fraction of truth particles matched to tracks reconstructed by the standard tracking algorithm, is highest for prompt tracks and decreases with increasing radial distance from the IP of the position where track is produced. Alternately, the large-radius tracking efficiency, or the fraction of truth particles matched to tracks reconstructed by the Large Radius Tracking algorithm, is lowest for prompt tracks and increases as the production radius grows larger. The separate inclusive, standard, and large-radius tracking efficiencies for four different signal points of distinct models and lifetimes are shown in Figure [4.36](#).

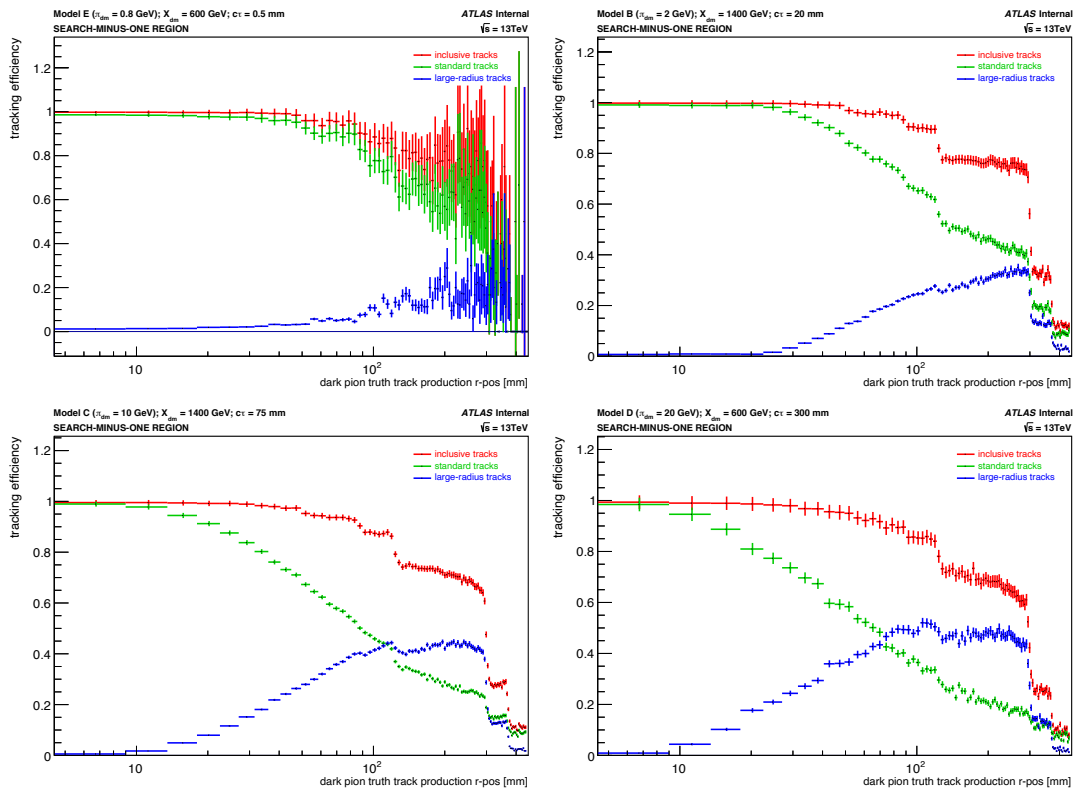


Figure 4.36: Inclusive (red), standard (green), and large-radius (blue) tracking efficiencies as a function of track production radius r for dark pion $c\tau = 0.5 \text{ mm}$ (top left), 20 mm (top right), 75 mm (bottom left), and 300 mm (bottom right) in Models E, B, C, and D, respectively.

For short lifetimes, where most tracks are produced with small production radius r , the track reconstruction is dominated by the standard tracking algorithm, and the large-radius tracking efficiency remains low across the range of r . As the lifetime of the signal LLP increases and more tracks are further displaced, the standard tracking efficiency decreases further and faster and the large-radius tracking compensates accordingly. For longer lifetimes across the same models, the inclusive tracking efficiency is somewhat lower, though the effect is very small, i.e. only a few percent.

The inclusive, standard, and large-radius tracking efficiencies for two different lifetimes in Models A and B are shown in Figure 4.37. Below $|d_0| = 10$ mm, the standard tracking algorithm is responsible for the majority of the track reconstruction, but above this threshold, which corresponds to the transverse impact parameter cut applied in standard track reconstruction, the reconstruction is immediately overtaken by the large-radius tracking algorithm.

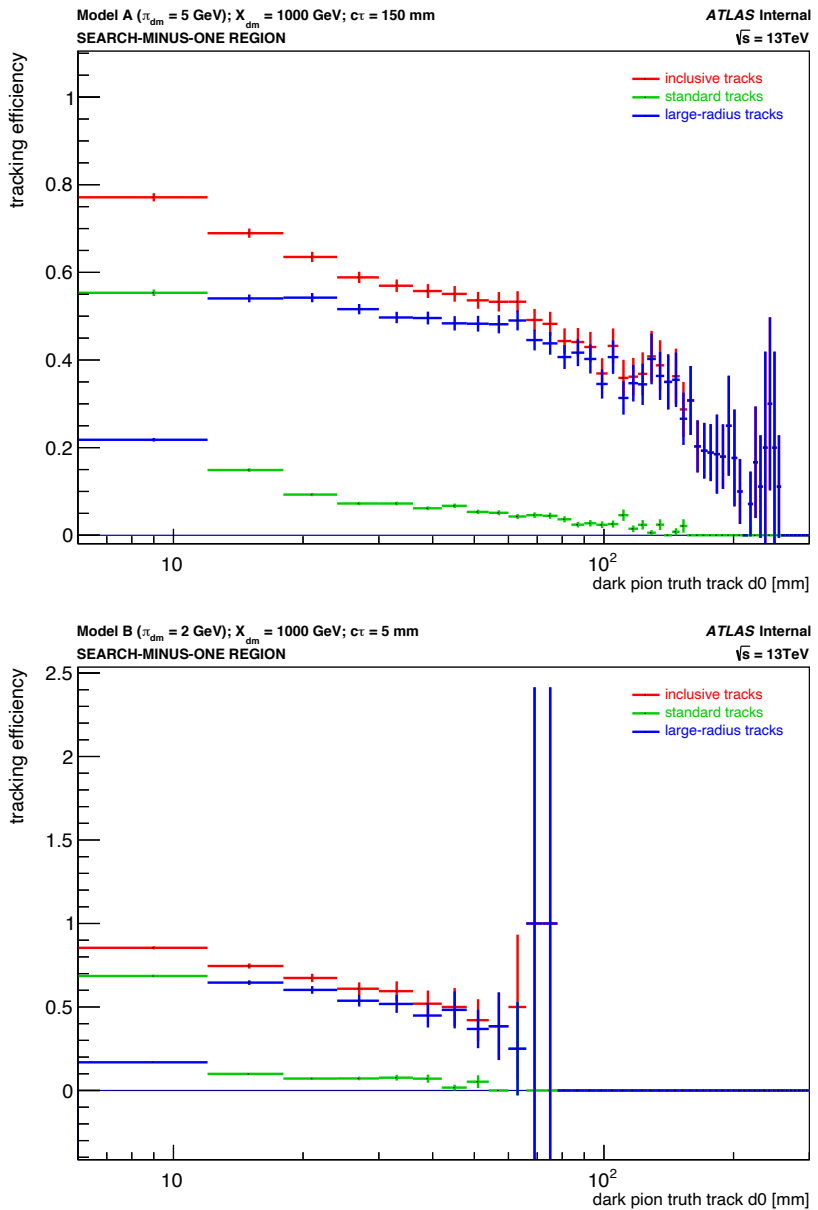


Figure 4.37: Inclusive (red), standard (green), and large-radius (blue) tracking efficiencies as a function of track transverse impact parameter d_0 for dark pion $c\tau = 150 \text{ mm}$ (top) and 5 mm (bottom) in Models A and B, respectively, with a 1000-GeV mediator-mass.

Figure 4.38 displays the inclusive tracking efficiency as a function of pileup, or the average number of interactions $\langle\mu\rangle$. For signal points with low lifetimes, which are primarily reconstructed with the standard tracking algorithm, the tracking efficiency is robust against pileup, while the efficiency for long-lifetime points, where the LRT algorithm dominates, degrades with increased pileup. The longer the lifetime, the greater the effect.

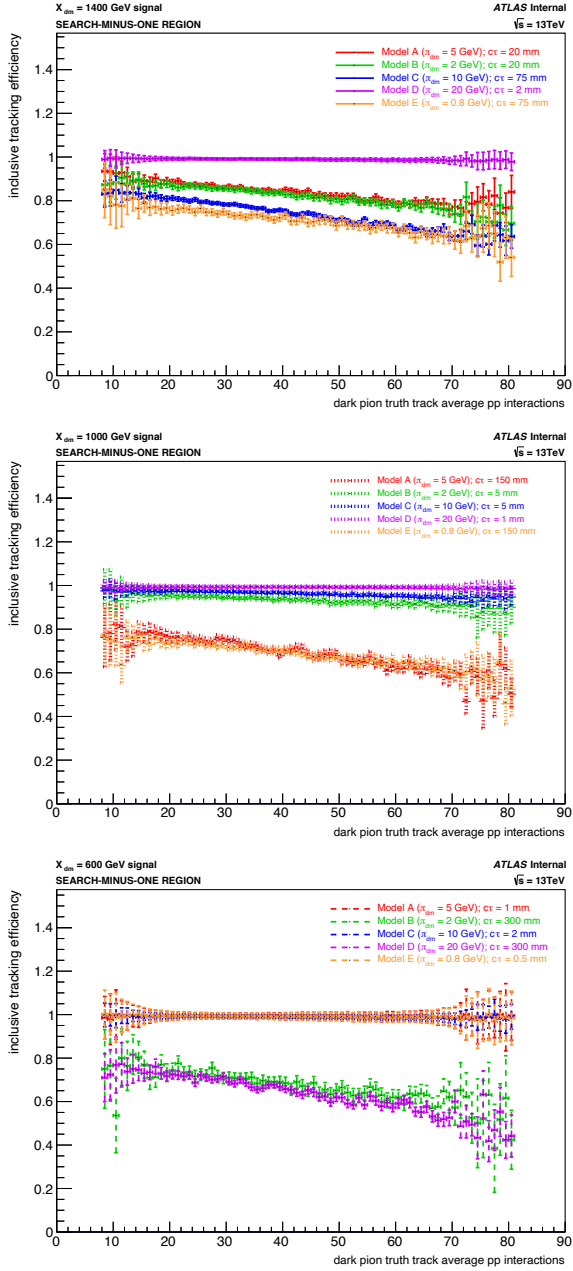


Figure 4.38: Inclusive tracking efficiency as a function of average number of pp interactions $\langle\mu\rangle$ for 1400-GeV (top), 1000-GeV (middle), and 600-GeV (bottom) mediator mass signal points over various models and dark pion lifetimes.

4.3.5.2.2 VERTEXING EFFICIENCY The vertex reconstruction efficiency is defined as the fraction of signal truth LLP decays matched to reconstructed displaced vertices, where the matching procedure between LLP decays and reconstructed secondary vertices is the same as that presented in the earlier DV performance section. That is, each LLP-DV pair is assigned a track- p_T -weighted match score s representing the probability the reconstructed vertex tracks are primarily correspondent to the truth particles produced from the LLP decay. For a truth LLP decay to be considered a match to a reconstructed vertex, the match score is required to be $s > 0.5$. As is evident in Figure 4.39, which displays the distribution of non-zero match scores between long-lived dark pions decays and reconstructed vertices in various EJs signal models, the majority of vertices satisfy this requirement.

The dark pion decays under consideration in studying the reconstruction efficiency are required to be “reconstructible”, with $r < 563$ mm, $|z| < 2720$ mm, and at least two outgoing charged particles with $p_T > 1$ GeV in the decay chain, in order to target truth vertices that decay within the silicon detector and that produce enough reconstructible tracks to seed the vertex.

The separate effects of the tracking and vertexing algorithms on the overall reconstruction efficiency as a function of the radial vertex position r are illustrated in Figure 4.40.

The top left plot shows the average number of tracks per reconstructible dark pion decay within the analysis fiducial volume of $r < 300$ mm and $|z| < 300$ mm, or “reconstructible

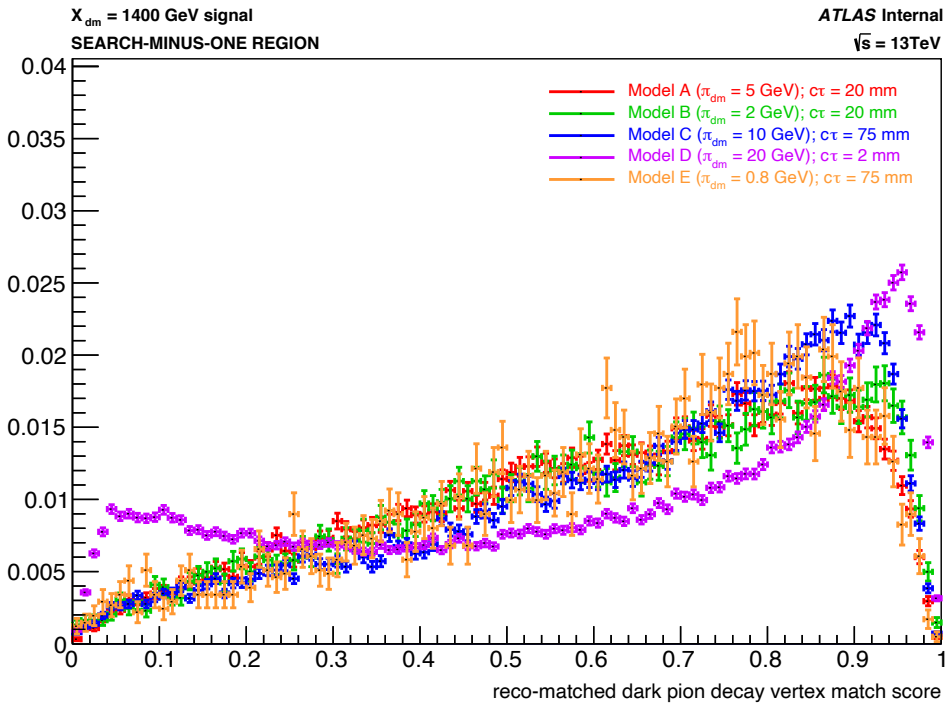


Figure 4.39: Match score s between truth LLP decays and reconstructed secondary vertices in five representative EJs signal models with various dark pion lifetimes.

fiducial” dark pion decay. The number of truth tracks, or reconstructible descendants, is shown in red, representing the maximum number of tracks available from the LLP decay to be reconstructed into a displaced vertex. The number of reconstructed truth tracks, or reconstructible descendants matched to reconstructed tracks, is shown in green, representing the maximum number of tracks reconstructed by the tracking algorithms and available for use in the vertexing algorithm. The loss of efficiency from the track reconstruction is indicated by the decrease in average number of tracks between the truth and reconstructed

truth track distributions. The number of vertexed truth tracks, or reconstructed truth tracks associated to a matched reconstructed vertex, is shown in blue, representing the average number of tracks per reconstructed displaced vertex. The difference between the average number of reconstructed and vertexed truth tracks indicates the loss of efficiency from the secondary vertex reconstruction separate from the track reconstruction.

The average number of **Loose**, **Medium**, and **Tight** vertexed truth tracks, or reconstructed truth tracks associated to a matched reconstructed vertex passing the **Loose**, **Medium**, and **Tight** working points, respectively, are also shown in magenta, orange, and cyan. The reduction in the number of tracks from the vertexed truth track distribution represents the loss of efficiency from the displaced vertex signal selections. The primary difference in the radial distribution is due to the application of the Material Map veto. The average fraction of truth tracks that are reconstructed and vertexed is shown in the plot on the top right.

The bottom left plot shows the average mass per reconstructible fiducial dark pion decay, where the mass is calculated from the sum-four-momentum of the associated truth tracks, reconstructed truth tracks, and vertexed truth tracks, as defined above. The average fraction of the LLP decay mass from reconstructed and vertexed truth tracks is shown in the plot on the bottom right.

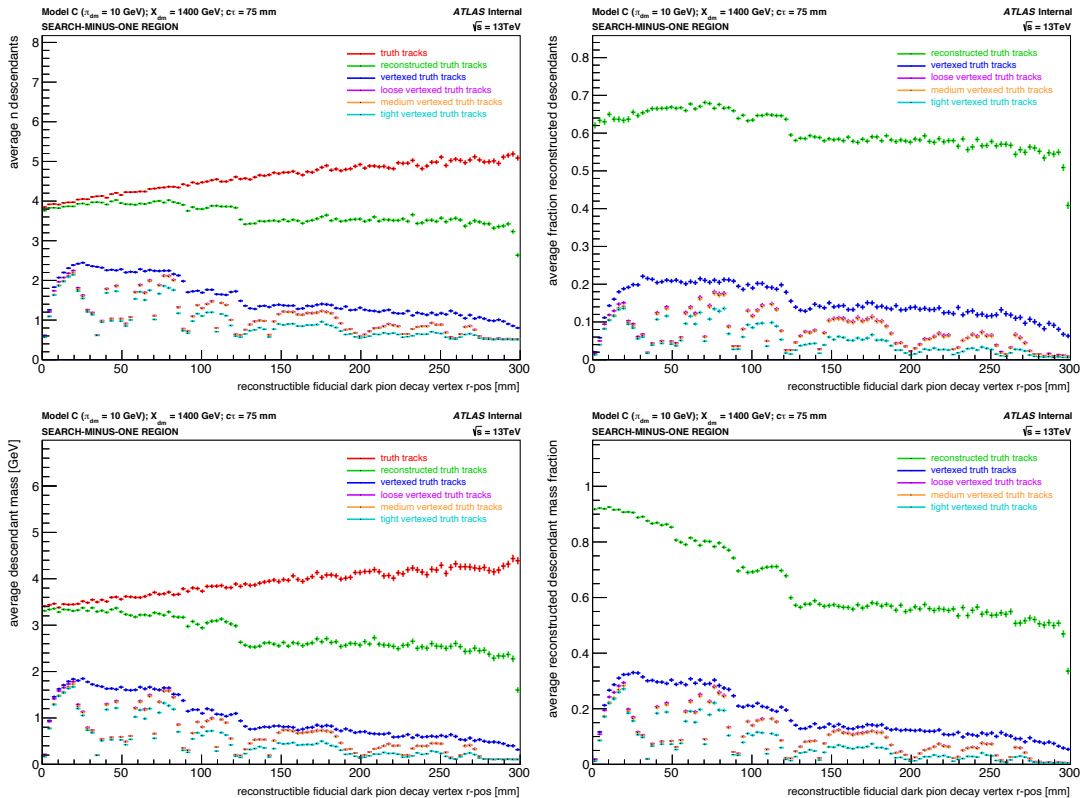


Figure 4.40: Separate effects on overall vertex reconstruction efficiency from tracking and vertexing algorithms in EJs signal Model C with $m_{X_d} = 1400 \text{ GeV}$ and $c\tau = 75 \text{ mm}$. Top left: the average number of truth (red), reconstructed truth (green), vertexed truth (blue), Loose vertexed truth (magenta), Medium vertexed truth (orange), and Tight vertexed truth (cyan) tracks per reconstructible fiducial dark pion decay as a function of the truth vertex decay radius. Top right: the average fraction of truth tracks that are reconstructed by the standard and large-radius tracking algorithms (green), vertexed by the secondary vertexing algorithm (blue), and selected by the Loose (magenta), Medium (orange), and Tight (cyan) DV analysis working points. Bottom left: the average mass of the reconstructible fiducial dark pion decay, calculated from truth tracks, reconstructed truth tracks, vertexed truth tracks, and Loose, Medium, and Tight vertexed truth tracks. Bottom right: the average mass fraction from reconstructed, vertexed, and Loose, Medium, and Tight vertexed truth tracks.

The total secondary vertex reconstruction efficiency is factorized into independent terms that separately characterize the distinct effects of the tracking and vertexing algorithms, as discussed in Section 3.4.2.2.2, where the displaced vertexing performance is described. The total vertex reconstruction efficiency is defined as follows:

$$\varepsilon^{\text{tot}} = \mathcal{A} \cdot \varepsilon^{\text{alg}} = \mathcal{A} \cdot \varepsilon^{\text{seed}} \cdot \varepsilon^{\text{core}}, \quad (4.5)$$

where \mathcal{A} is the acceptance, $\varepsilon^{\text{alg}} = \varepsilon^{\text{seed}} \cdot \varepsilon^{\text{core}}$ is the algorithmic efficiency, $\varepsilon^{\text{core}}$ is the core efficiency, and $\varepsilon^{\text{seed}}$ is the seed efficiency.

The acceptance \mathcal{A} is the fraction of reconstructible dark pion decays with two reconstructed truth tracks, which provides a measure of the impact of the tracking algorithm on the total vertex reconstruction efficiency. The effect of the vertexing algorithm is contained in the algorithmic efficiency ε^{alg} , which is the ratio of the number of reconstructible dark pion decays matched to a reconstructed displaced vertex with match score $s > 0.5$ to the number of dark pion decays in acceptance. The algorithmic efficiency can be further factorized into terms that separately account for the seed vertex track selection efficiency and for the pure vertex reconstruction efficiency: the seed efficiency and the core efficiency, respectively. The seed efficiency $\varepsilon^{\text{seed}}$ is the fraction of dark pion decays in acceptance with two selected truth tracks, and the core efficiency $\varepsilon^{\text{core}}$ is the number of reconstructible dark pion decays with a reconstructed DV match divided by the number of reconstructible dark

pion decays with two selected truth tracks, where a selected truth track is one matched to a reconstructed track selected for seeding during secondary vertex reconstruction. The total efficiency ε^{tot} is then the fraction of reconstructible dark pion decays that are matched to a reconstructed displaced vertex.

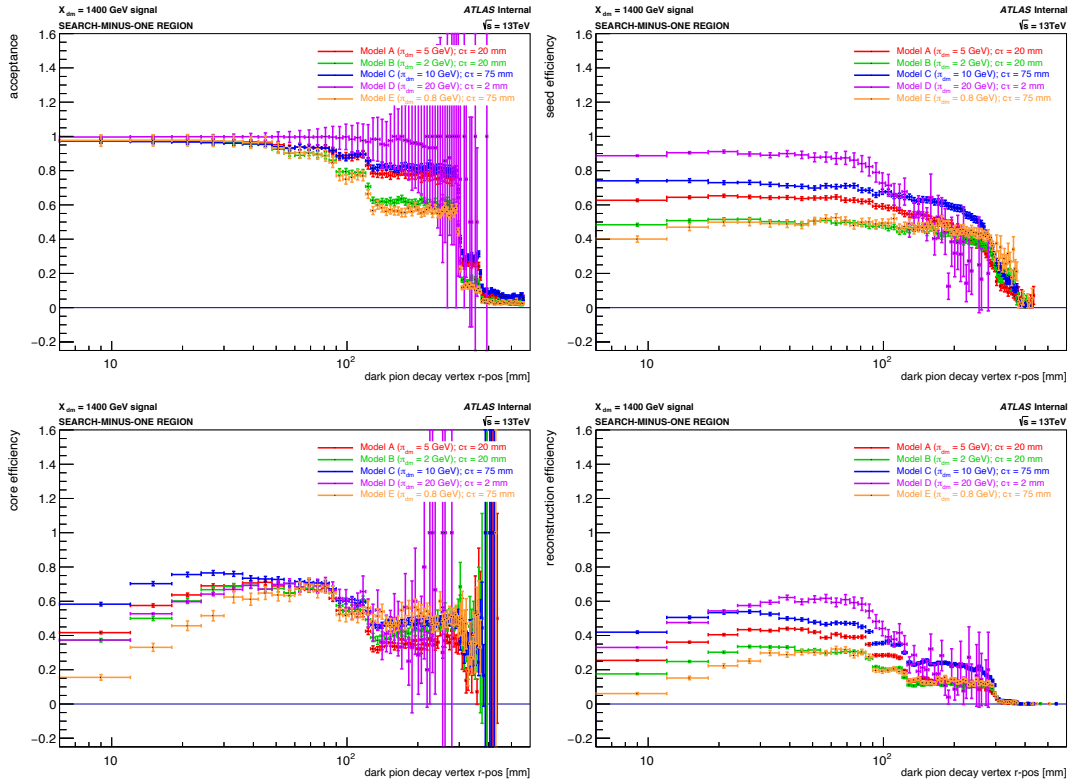


Figure 4.41: The vertex reconstruction efficiency as a function of radial position r for displaced dark pion decays in five representative EJs signal models with various lifetimes. The factorized components of the overall efficiency are shown: the acceptance (top left), seed efficiency (top right), core efficiency (bottom left), and total efficiency (bottom right).

The acceptance, seed efficiency, core efficiency, and total efficiency are shown as a function of the radial position r of the dark pion decay in Figure 4.41. No cuts, other than the necessary track cleaning to resolve the phi asymmetry, are applied to the matched recon-

structed vertices in these inclusive reconstruction efficiency studies.

The acceptance is minimally dependent on lifetime, with larger lifetime points having slightly lower acceptances, as the tracking efficiency slightly degrades with lifetime. A more significant dependence is observed on the mass of the model, with the acceptance in lighter models degrading faster with r compared to heavier models, where the acceptance remains close to one throughout $r < 300$ mm. This effect is illustrated in Figure 4.42, where the acceptance is compared between different lifetime points across a single model in each plot.

The seed efficiency is also primarily dependent on the mass of the model, with heavier models producing dark pion decay vertices with larger track multiplicities, increasing the probability of at least two high-quality tracks being successfully reconstructed and selected for secondary vertexing.

The core efficiency provides a measure of the vertexing fitting efficiency given a set of constituent tracks, separate from the efficiency of the track reconstruction. The low efficiency at $r < 10$ mm, as seen in Figure 4.43, is a consequence of the $|d_o| > 2$ mm cut applied to the vertex seed tracks. After an initial increase in efficiency above this threshold, the core efficiency degrades with increasing r above $r \approx 50 - 100$ mm. This degradation with the radial vertex position is related to the LRT efficiency, which decreases with large r , resulting in fewer available tracks for use in reconstructing vertices with large radial displacements.

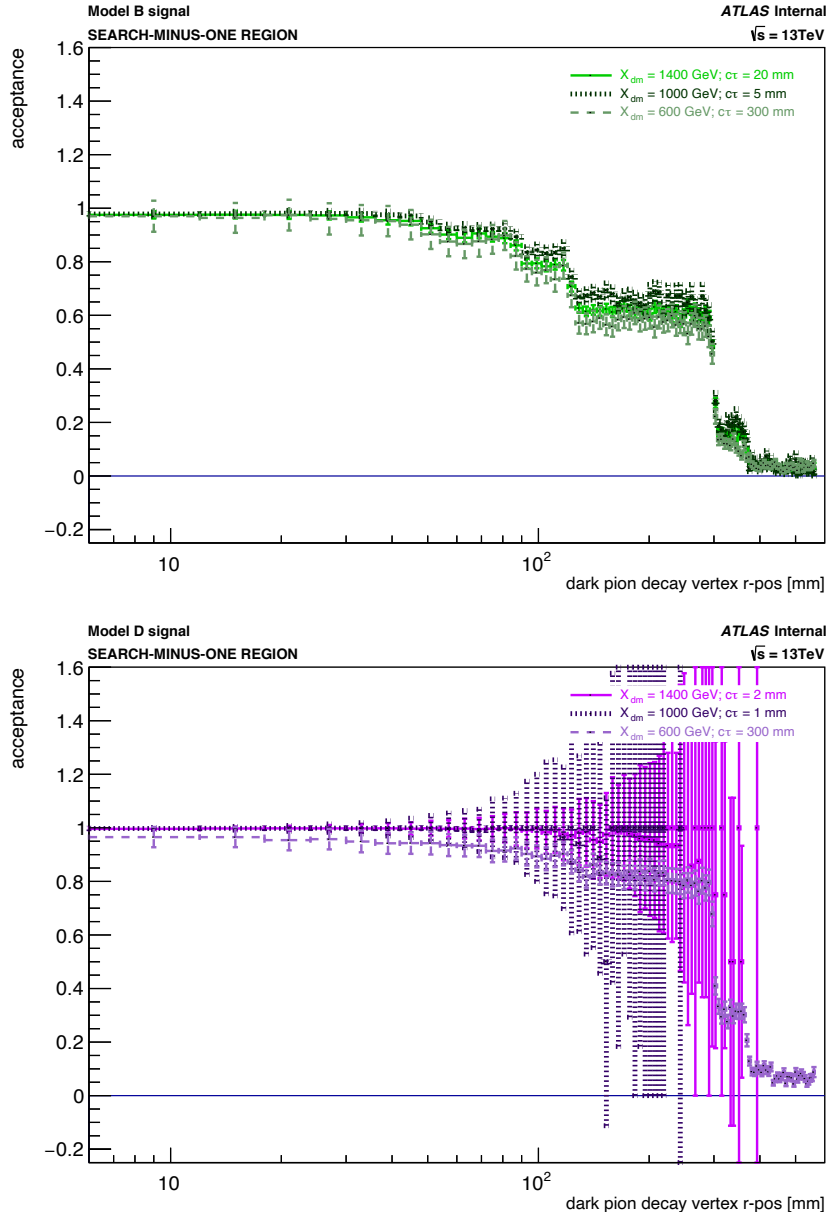


Figure 4.42: The vertex acceptance as a function of the dark pion decay's radial displacement r for Model B (top), with a 2-GeV dark pion, and Model D (bottom), with a 20-GeV dark pion. The acceptance is less dependent on the radial position of the vertex for heavier models.

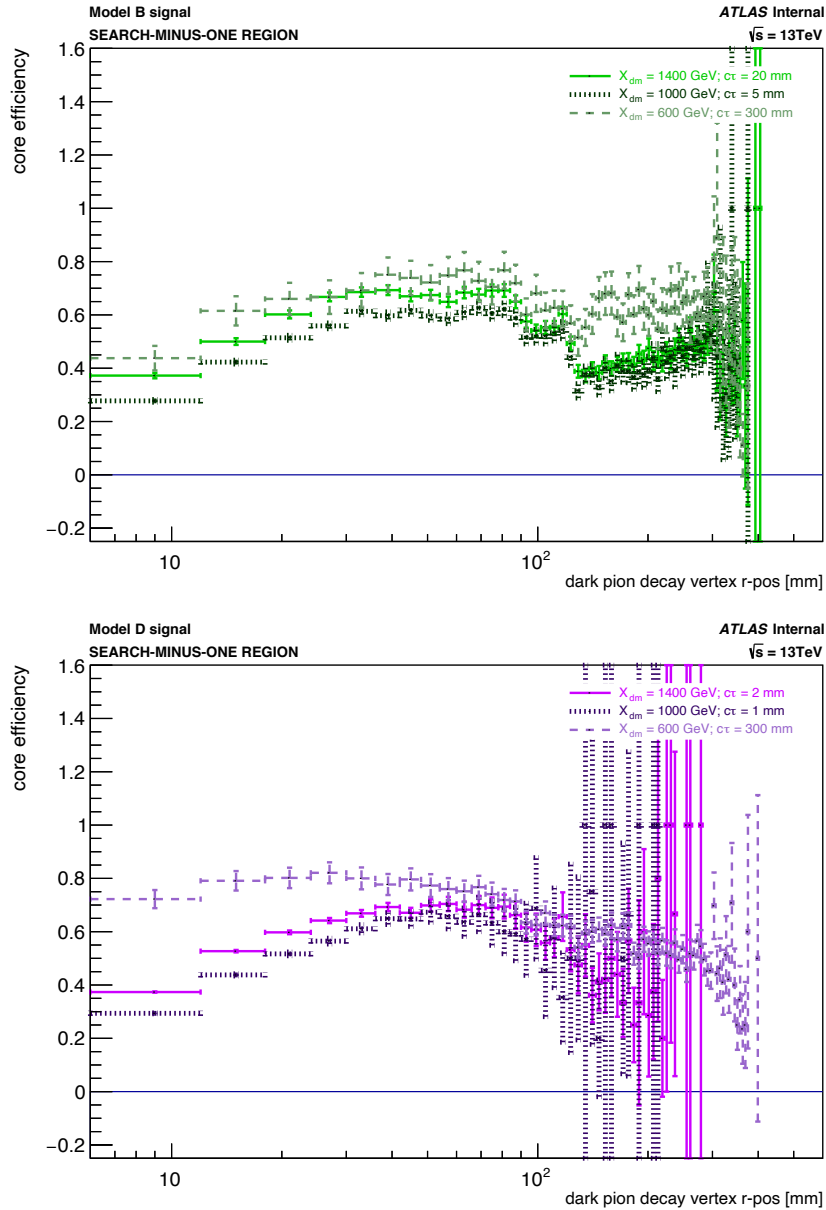


Figure 4.43: The core vertex efficiency of the dark pion decay as a function of radial position r for Model B (top) and Model D (bottom). The core efficiency is higher for dark pions with longer lifetimes and degrades with increasing radial displacement above $r \approx 50 - 100 \text{ mm}$.

The core efficiency is lowest for short dark pion lifetimes, as such vertices are more likely to fail the kinematic cuts applied during two-track vertex finding designed to remove displaced vertex seeds pointing back to the primary vertex. The initial increase in efficiency with increasing r observed for all signals is likely also due to these PV cuts, as the farther the secondary vertex is from the primary vertex, the less likely it is to be mistakenly associated to the PV.

The algorithmic efficiency is directly dependent on the vertex mass and on the number of selected tracks, as depicted in Figure 4.44, with higher efficiencies for vertices with larger masses and larger selected track multiplicities. As the average displaced vertex mass and track multiplicity is relatively low for the signal models under consideration, the overall vertexing efficiency for the Emerging Jets search is considerably lower than in some other RPVLL analyses.

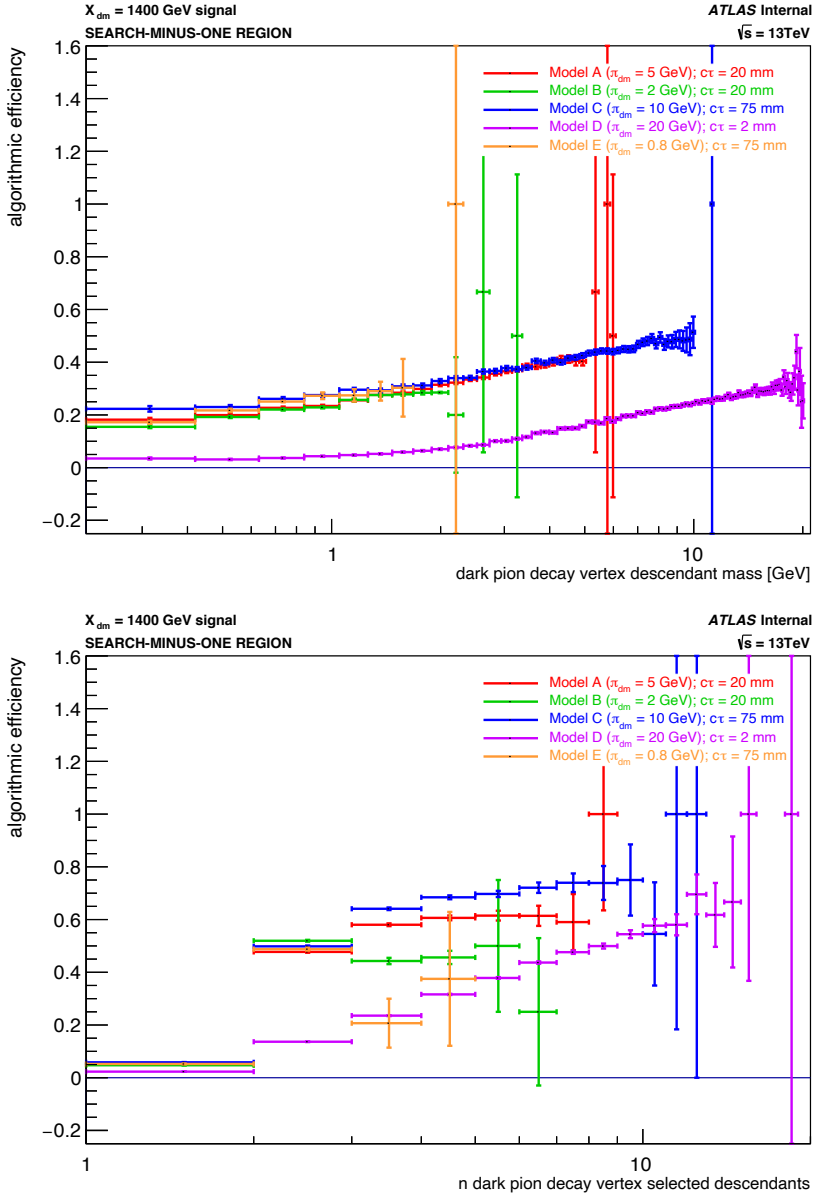


Figure 4.44: The algorithmic vertex efficiency as a function of dark pion decay vertex mass (left) and number of selected tracks (right) for five representative EJs signal models with $X_{dm} = 1400 \text{ GeV}$. The efficiency of the vertexing algorithm increases with the LLP decay mass, calculated from the sum-four-momentum of the constituent truth tracks, and with the number of selected tracks produced in the LLP decay.

The acceptance, seed efficiency, core efficiency, and total efficiency are shown as a function of the average number of pp interactions $\langle\mu\rangle$ in Figure 4.45. The acceptance degrades with increased pileup for dark pion decays with lifetimes of $c\tau = 5$ mm and above as a consequence of the inefficiency of the Large Radius Tracking algorithm at high pileup. Between the lowest and highest pileup conditions considered, the acceptance loss is between $\approx 10\%$ and 20% for long-lifetime dark pion decays. The seed efficiency loss with increasing pileup is more significant and occurs even for dark pion decays with small lifetimes of 2 mm and below, with losses between $\approx 25\%$ and 40% . The core efficiency, however, is observed to be independent of pileup and suffers no loss in high $\langle\mu\rangle$ environments.

The signal vertex reconstruction efficiency is also calculated for vertices passing the analysis selection working points. The same definitions for the total efficiency and its factorized components are applied, but the dark pion decays under consideration are required to pass the reconstructible decay criteria and be within the analysis fiducial volume, and the matched displaced vertices are required to pass the `Loose`, `Medium`, and `Tight` signal selections, separately. The signal acceptance, seed efficiency, core efficiency, and total efficiency for the `Loose` selection working point are shown in Figure 4.46. The signal acceptance and signal seed efficiency are independent of the matched reconstructed vertex and are thus the same for all three DV selection working points.

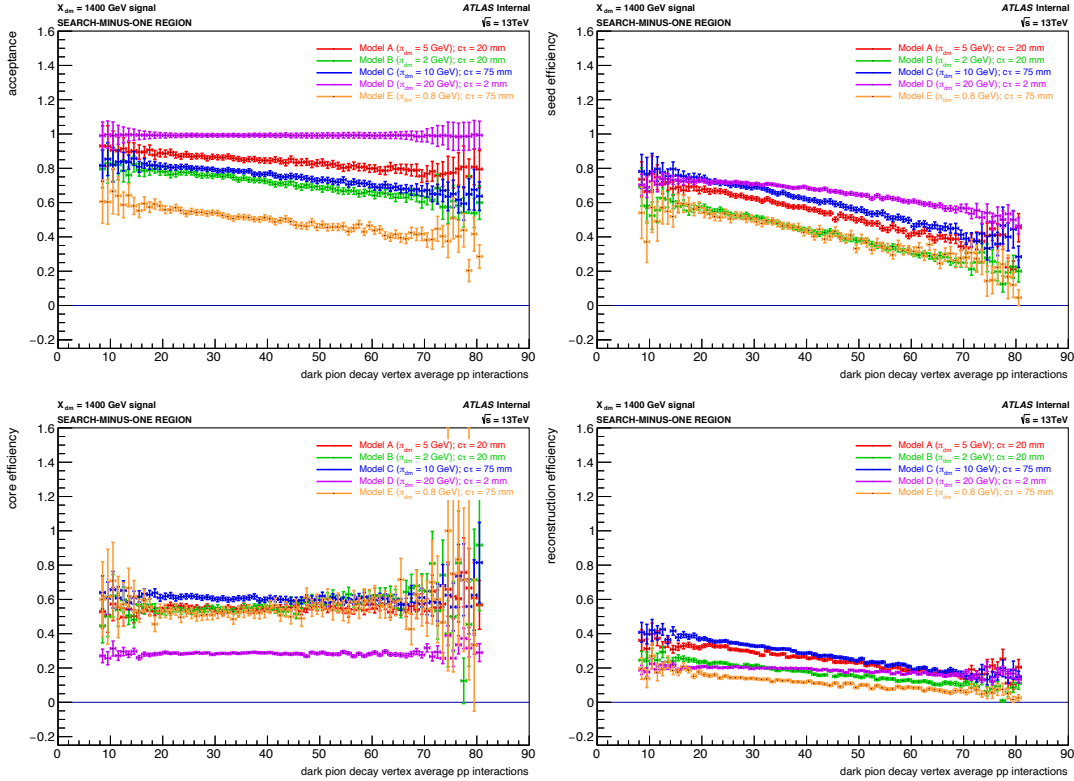


Figure 4.45: The dark pion decay vertex acceptance (top left), seed efficiency (top right), core efficiency (bottom left), and total reconstruction efficiency (bottom right) as a function of the average number of interactions $\langle \mu \rangle$ for various EJs signal samples.

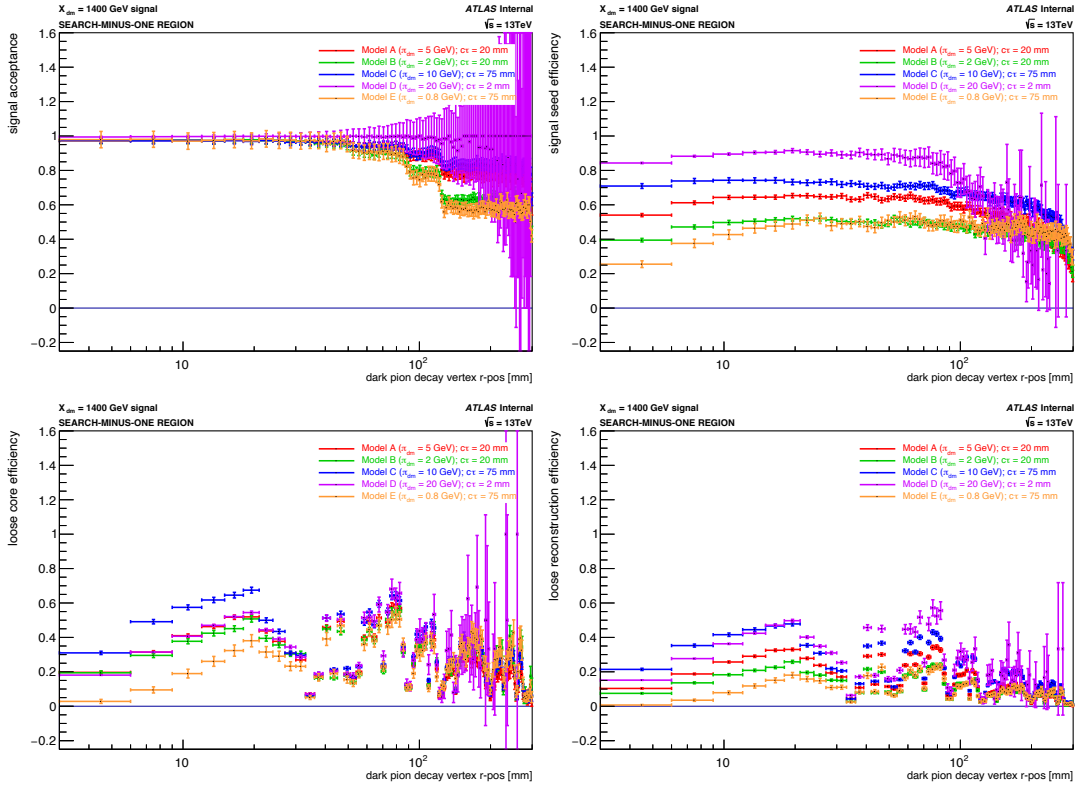


Figure 4.46: The signal acceptance (top left), signal seed efficiency (top right), Loose core efficiency, and Loose total reconstruction efficiency for dark pion decays as a function of the truth vertex radial-position r . The signal acceptance and seed efficiency are calculated from truth dark pion decays within the analysis fiducial volume, and the Loose core and total efficiencies are calculated from matched reconstructed displaced vertices passing the Loose DV selection working point.

The **Loose** vertex selections result in a loss of total efficiency of approximately 10% compared to the inclusive vertex reconstruction efficiency presented above. The loss of efficiency between the **Loose** and **Tight** vertex selection working points is only a few percent. The total reconstruction for all inclusive vertices and for vertices passing the **Loose**, **Medium**, and **Tight** selections are compared in Figure 4.47.

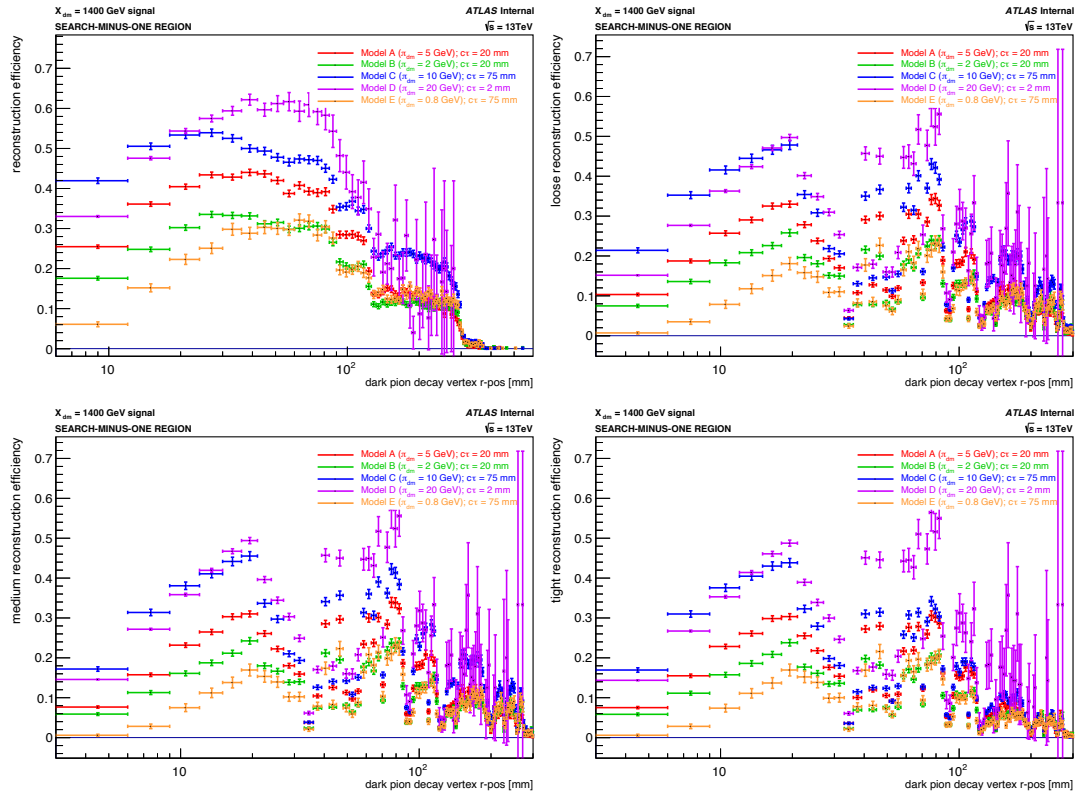


Figure 4.47: The total dark pion decay reconstruction efficiency as a function of radial position r for all (top left), Loose (top right), Medium (bottom left), and Tight (bottom right) reconstructed displaced vertices.

4.3.6 EMERGING JET SELECTION

Signal events are further required to contain some number of “emerging” jets (EJs) satisfying certain criteria designed to discriminate emerging-like jets from QCD-like jets in the event, where a tentative selection requiring between zero and two emerging jets ($N_{\text{EJ}} \geq 0, 1,$ or 2) is proposed. Omitting the event-level emerging jet multiplicity cut, or implementing an $N_{\text{EJ}} = 0$ selection, would maintain the model independence of the search and the efficiency of the signal, but requiring $N_{\text{EJ}} > 0$ aids in reducing the QCD background, which is large and presents the biggest challenge to the search. The studies to construct a set of cuts defining an emerging jet object and to optimize the event-level signal region selection on the emerging jet multiplicity is ongoing, but two preliminary working points are currently defined to select signal EJs for this analysis: **Loose** and **Tight**. These working points are tentative and may need further tuning before implementation in the final signal selections, and the overall N_{EJ} requirement is still to be optimized in combination with the other event-level signal region cuts, i.e. the number of displaced vertices and the N_{jet} -leading jet variable, if further background rejection is required.

4.3.6.1 EMERGING JET SELECTION WORKING POINTS

The **Loose** and **Tight** working points defined for analysis EJ selection are listed in Table 4.7 and summarized below.

Loose
$p_T > 200 \text{ GeV}$
$ \eta < 2.0$
$m > 25 \text{ GeV}$
$\not{p}_T^{N_{\text{sv}}} > 5 \text{ GeV}$
$N_{\text{jet-trk}}^{N_{\text{sv}}} > 2$
Tight
Loose selections
$\not{p}_T^{N_{\text{sv}}} > 7.5 \text{ GeV}$
$N_{\text{jet-trk}}^{N_{\text{sv}}} > 4$

Table 4.7: Loose and Tight working points for analysis EJ selection. Tight selections are applied on top of Loose selections, and the N_{sv} superscript refers to the system of secondary vertices passing one of the DV working points matched to the jet.

The emerging jet selection working points defined above are designed to optimally target signal jets originating from dark pion decays within dark jets and separate them from standard QCD jets in order to maximize background rejection with minimal signal loss. To identify discriminating variables between emerging-like signal and QCD-like background jets and investigate the effects of the emerging jet selections, jets matched to truth dark jets (see Appendix C) in MC signal samples are compared to unmatched jets in the MC background sample. A jet is considered to have a truth dark jet match if it is within $\Delta R < 0.3$ of a dark jet with $p_T > 30 \text{ GeV}$, if it is also matched to a truth jet that is matched to the same dark jet, where the same ΔR matching requirement is implemented, and if the leading ghost parton associated to the jet is a down quark. The additional requirements beyond the base ΔR matching to the dark jet are implemented to ensure the reconstructed jet is associated with a dark jet of good quality. In order to avoid bias from comparing against a single dijet

background slice, the jet distributions are analyzed in a subregion of the search region corresponding to the JZ₄W leading jet p_{T} slice, known as the “JZ₄W-slice-search” region. Events are required to pass all of the search region selections and to have the leading jet in the event with p_{T} between 400 and 800 GeV.

The dark-matched signal jets are observed to be slightly harder and more central than the unmatched background jets. Therefore, cuts are imposed on the jet transverse momentum, pseudorapidity, and invariant mass, requiring emerging jets to have $p_{\text{T}} > 200$ GeV, $|\eta| < 2.0$, and mass > 25 GeV. These three cuts are collectively known as the “hard” jet selections and are illustrated in Figure 4.48, where the distributions are normalized to unity to highlight differences in shape between signal and background. Distributions are shown only for the four leading jets in the event.

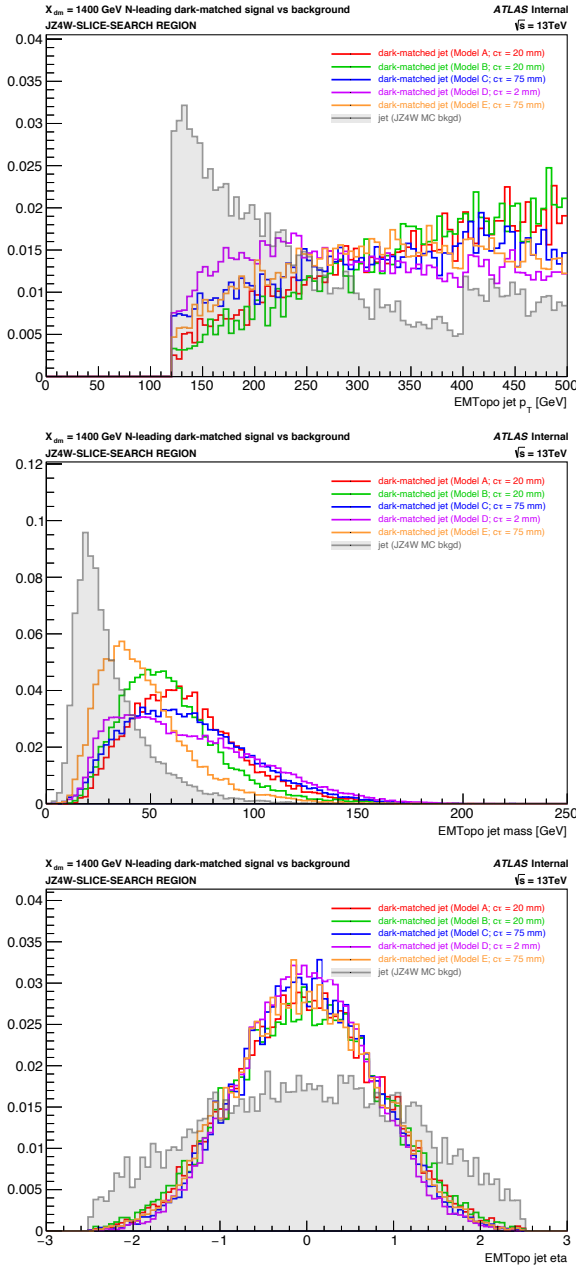


Figure 4.48: The p_T (top), invariant mass (middle), and η (bottom) distributions for dark-matched leading jets in the 1400-GeV mediator mass signal and unmatched leading jets in the JZ4W dijet background in the JZ4W-slice-search region, where “leading” refers to any of the four leading jets in the event. The transverse momentum distribution is zoomed in on the x -axis to highlight the behavior at low p_T .

Additionally, emerging jets are expected to have a number of secondary vertices associated to them, corresponding to the multiple dark pion decays characterizing their topology. Because the selections imposed on the signal displaced vertices already require they be associated to a leading jet, and an event-level cut on the number of displaced vertices is already implemented, applying an emerging jet cut on the associated secondary vertex multiplicity per jet would be relatively redundant. Instead, alternate variables related to the number of associated secondary vertices are used to isolate signal jets containing multiple vertices. First, a cut is placed on the transverse momentum part of the four-vector sum of the momenta of the secondary vertices matched to the jet, where a vertex is considered a match if it is within $\Delta R < 0.6$ of the jet, requiring the emerging jet to have $p_T^{N_{sv}} > 5 \text{ GeV}$. Next, a cut is imposed on the number of secondary vertex jet tracks associated to the jet, where the sum is taken over all tracks associated to the matched secondary vertices that are also independently matched to the jet within $\Delta R < 0.6$, requiring the emerging jet to have $N_{\text{jet-trk}}^{N_{sv}} > 2$. These variables, depicted in Figure 4.49, both target jets with inherently larger secondary vertex multiplicities while providing more flexibility in the designation of the cut values. The secondary vertex selections are applied separately for each of the DV signal selection working points, defining `Loose-SV` (LSV), `Medium-SV` (MSV), and `Tight-SV` (TSV) emerging jet selections. Collectively, these “SV” jet selections together with the hard jet selections described above make up the `Loose EJ` selection working point.

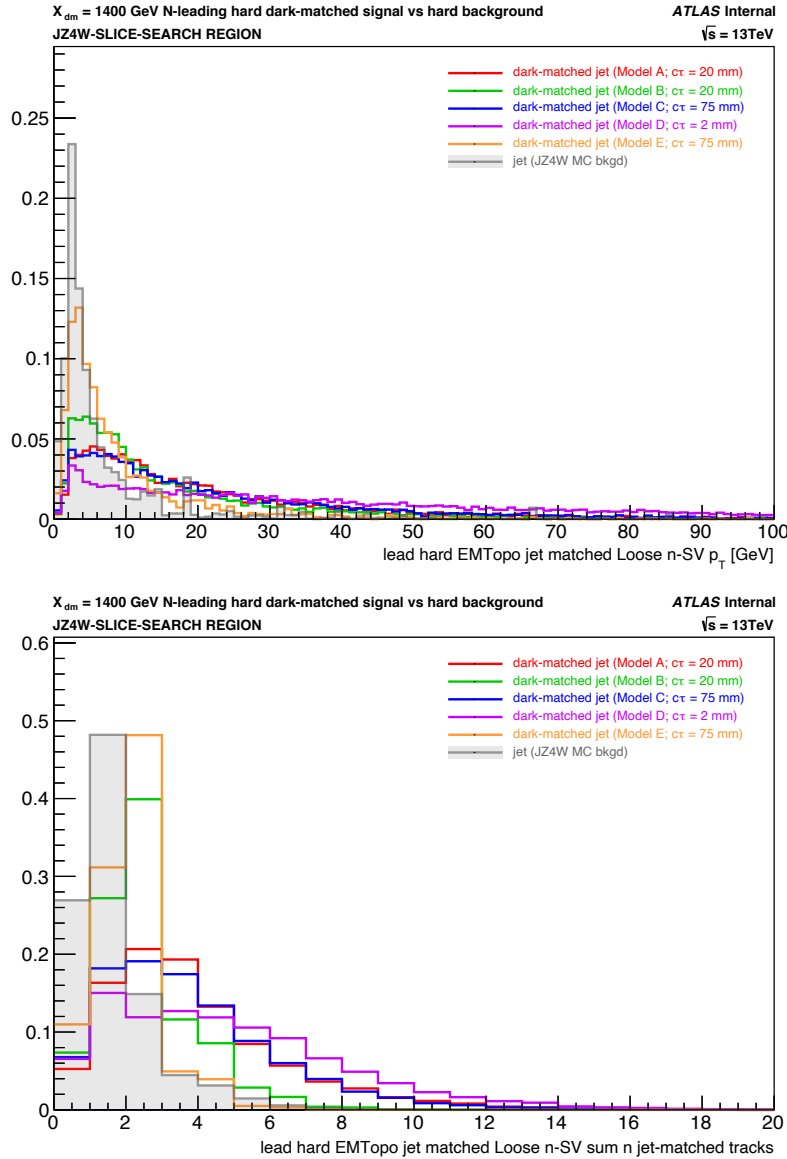


Figure 4.49: The transverse momentum (top) and number of jet-matched tracks (bottom) of the secondary vertices associated to the dark-matched leading jets in the 1400-GeV mediator mass signal and to the unmatched leading jets in the JZ4W dijet background. The secondary vertex transverse momentum $p_T^{N_{SV}}$ is calculated from the sum of the four-momentum of all matched secondary vertices per jet, and the secondary vertex jet track multiplicity $N_{jet-trk}^{N_{SV}}$ is the sum of jet-matched tracks associated to the all matched vertices per jet. Distributions are shown for the four leading jets in the event in the JZ4W-slice-search region after the hard jet selections have been applied.

The **Tight** EJ selection working point then applies tightened $p_T^{N_{sv}}$ and $N_{jet-trk}^{N_{sv}}$ cuts, requiring the emerging jet to have $p_T^{N_{sv}} > 7.5 \text{ GeV}$ and $N_{jet-trk}^{N_{sv}} > 4$.

The intent of the emerging jet selection criteria defining the **Loose** and **Tight** working points is to maximize the EJ efficiency, or the fraction of dark-matched signal jets passing the EJ selections, and the **QCD** jet rejection, or the fraction of unmatched background jets failing the EJ selections. The cumulative effect of each individual EJ selection on the overall count and efficiency of emerging-like jets in the signal and **QCD**-like jets in the background is illustrated in the jet-level cutflow shown in Figure 4.50. Each bin in the cutflow represents the number or fraction of total N_{jet} -leading jets in all events in the JZ4W-slice-search region passing the corresponding cut and all prior cuts, where only the emerging-like jets among the four leading jets in the event are counted in the signal, and only the **QCD**-like jets among the four leading jets in the event are counted in the background.

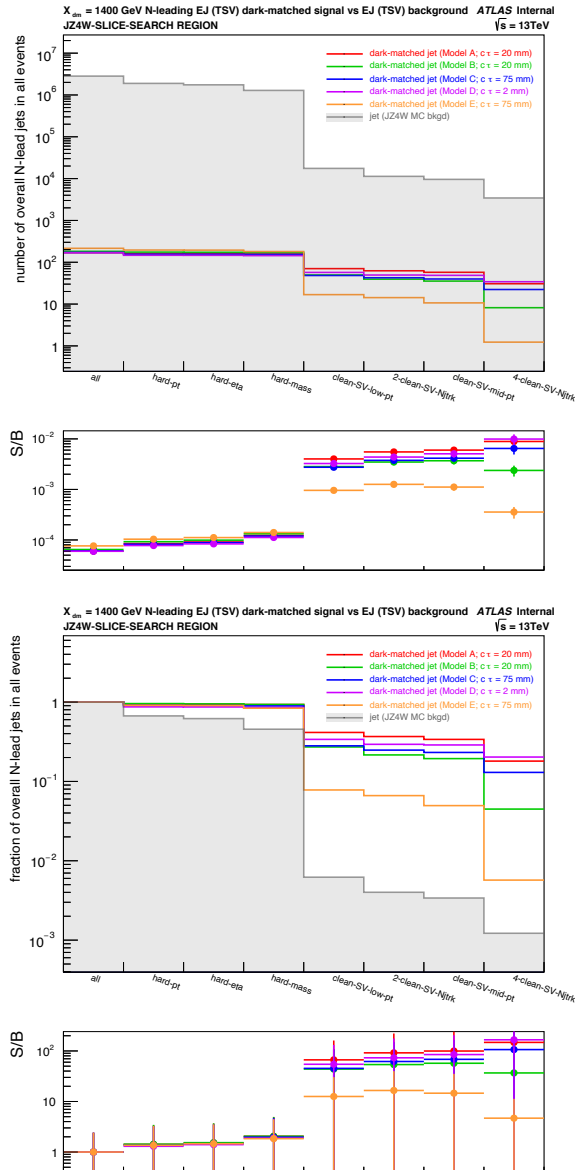


Figure 4.50: The jet-level cutflow (top) and cutflow efficiency (bottom) for the individual emerging jet selections, showing the number and fraction of total N_{jet} -leading jets in all events in the JZ4W-slice-search region passing each successive cut, respectively. The cutflows are compared between dark-matched leading jets in five signal models and unmatched leading jets in the MC background. The bottom panels show the signal-to-background ratios of each bin. The cuts are designed to maximally reduce the background while maintaining the signal efficiency.

While the count and efficiency decreases with each cut for both the dark-matched signal and unmatched background jets, the emerging jet selection efficiency decreases more slowly for signal than for background, indicating the cuts target background QCD jets more often than signal emerging jets, as intended. Specifically, the background efficiency decreases significantly with the first SV-related cut, which is designed to target the multiple displaced vertex topology characteristic of emerging jets. The ratio of the signal to background, displayed underneath the cutflow, increases with each successive cut, with the exception of the final tight $N_{\text{jet-trk}}^{N_{\text{sv}}}$ cut for low-mass models.

The event-level cutflows for the N_{EJ} selection are shown in Figure 4.51, comparing 600-GeV, 1000-GeV, and 1400-GeV mediator mass signal events to background for `Loose` and `Tight` emerging jet selection working points with `Loose` associated secondary vertices. Each cutflow bin shows the number of events in the JZ4W-slice-search region surviving the respective N_{EJ} selection, where N_{EJ} is the number of emerging jets required per event. No requirement is placed on whether the emerging jet is one of the four leading jets, but the hard- p_{T} cut included in the EJ selection almost guarantees that it is. The background goes to zero for $N_{\text{EJ}} > 1$ with both the `Loose` and `Tight` working points, regardless of the DV working point used for the associated secondary vertex cuts. While the `Loose` selection boasts higher signal efficiencies for all samples over the `Tight` selection and appears to be sufficient to reduce the QCD background, further comparisons must be done with the

full set of PYTHIA dijet slices, when available, to ensure the N_{EJ} selections with the current working points are truly adequate in terms of rejecting the background.

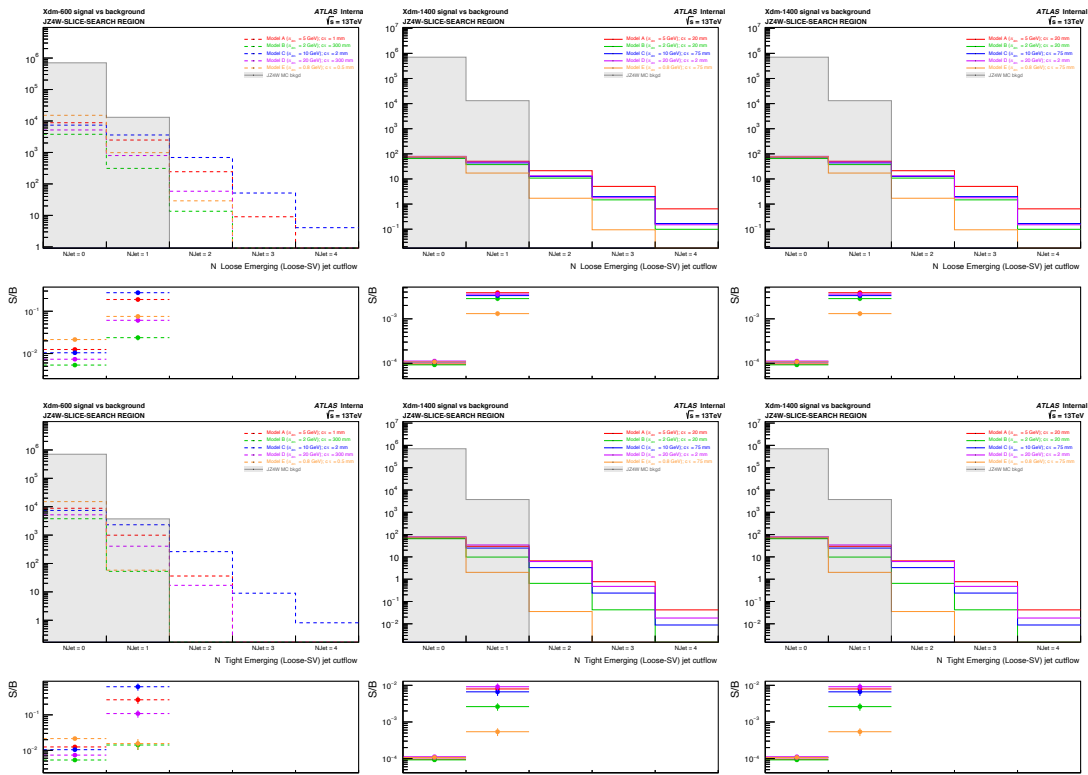


Figure 4.51: The event-level N_{EJ} cutflows for Loose (top) and Tight EJs with Loose associated secondary vertex selections in 600-GeV (left), 1000-GeV (center), and 1400-GeV (right) signal samples versus a QCD dijet background sample. Each bin displays the number of events in the JZ4W-slice-search region containing at least the number of emerging jets specified by the N_{EJ} selection. The bottom panels show the ratio of signal to background events in each bin with nonzero background.

4.3.7 LEADING N-JET SELECTION

Finally, events are required to pass some leading N-jet observable (NJetX) threshold to further reduce the QCD background. A number of potential NJetX variables X^{NJet} related to the leading four-jet system or to a dijet system among the four leading jets are considered for the final signal selection. This leading N-jet selection is still to be optimized, both alone and in conjunction with the other N_{EJ} and N_{DV} cuts defining the signal region. All prospective NJetX variables currently being examined are listed and briefly described below. A range of possible selection thresholds for each NJetX variable is also proposed to investigate the effect of the selection on the overall signal efficiency and background rejection and to determine the cut variable and value that maximizes the signal to background ratio. The set of potential NJetX variables and the corresponding ranges of possible cut values defining the leading N-jet selections are chosen to target signal events with signal-like jets originating from pair-produced scalar mediators and distinguish them from background QCD dijet events. This is achieved by studying the distributions in signal and background and determining the thresholds that maximize the discrimination between the two. The following NJetX selections, showing promising discrimination between signal and background, are proposed:

- $H_{\text{T}}^{\text{NJet}} > 1200 - 1500 \text{ GeV}$
- $p_{\text{T}}^{\text{NJet}} > 100 - 200 \text{ GeV}$

- $m_{\text{sum}}^{\text{NJet}} > 120 - 175 \text{ GeV}$
- $p_T^{\text{NJetJJ}} > 350 - 700 \text{ GeV}$
- $p_T^{\text{NJetJJ,max-dR}} > 300 - 600 \text{ GeV}$
- $p_T^{\text{NJetJJ,avg}} > 350 - 525 \text{ GeV}$
- $H_T^{\text{NJetJJ,max}} > 750 - 1200 \text{ GeV}$
- $m_{\text{sum}}^{\text{NJetJJ,max}} > 60 - 125 \text{ GeV}$
- $H_T^{\text{NJetJJ,min}} > 500 - 800 \text{ GeV}$
- $m_{\text{sum}}^{\text{NJetJJ,min}} > 50 - 100 \text{ GeV}$
- $p_T^{\text{NJetJJ,max-}p_T} > 500 - 900 \text{ GeV}$
- $H_T^{\text{NJetJJ,max-}p_T} > 600 - 1000 \text{ GeV}$
- $m_{\text{sum}}^{\text{NJetJJ,max-}p_T} > 50 - 100 \text{ GeV}$

The H_T^{NJet} , p_T^{NJet} , and $m_{\text{sum}}^{\text{NJet}}$ observables are measurements of the system of the four leading jets in the event, where H_T^{NJet} is the scalar sum- p_T of the four leading jets, p_T^{NJet} is the p_T of the four-vector sum of the four leading jets, and $m_{\text{sum}}^{\text{NJet}}$ is the scalar sum of the invariant masses of the four leading jets. The remaining NJetX observables are measures of some dijet system within the leading four-jet system.

The p_T of the nominal dijet system, p_T^{NJetJJ} , is defined as the average of the two dijet pairs among the four leading jets with the smallest difference in invariant mass between them. It is expected that the invariant mass distribution of this dijet system should approximately reproduce the scalar mediator mass in the signal, as each mediator produces a pair of jets; thus,

probing this dijet system could serve as a viable method of tagging events with signal-like jets. It is observed that the transverse momentum of this dijet system serves as a superior discriminator between signal and background events over the invariant mass.

The p_T of the maximum- ΔR dijet system, $p_T^{\text{NJetJJ,max-dR}}$, is defined as the average of the two dijet pairs among the four leading jets with the largest angular distance between them. Similar to the expectation that the dijet pairs stemming from the pair-produced scalar mediators should have approximately the same invariant mass, it is also reasonable to expect they may be produced relatively back-to-back and thus have a large angular distance between them. Therefore, the maximum- ΔR dijet system can also provide a measure of discrimination between signal and background events, with the p_T distribution yielding the most prominent difference.

The $p_T^{\text{NJetJJ,avg}}$ observable is the p_T of the average dijet system, where the average is taken over all possible jet pair combinations among the four leading jets. The $H_T^{\text{NJetJJ,max}}$ and $m_{\text{sum}}^{\text{NJetJJ,max}}$ observables are the scalar sum- p_T and scalar sum-invariant-mass of the dijet system with the maximum invariant mass among the four leading jets in the event. Analogously, $H_T^{\text{NJetJJ,min}}$ and $m_{\text{sum}}^{\text{NJetJJ,min}}$ are the scalar sum- p_T and scalar sum-invariant-mass of the dijet system with the minimum invariant mass, and $p_T^{\text{NJetJJ,max-}p_T}$, $H_T^{\text{NJetJJ,max-}p_T}$, and $m_{\text{sum}}^{\text{NJetJJ,max-}p_T}$ are the p_T , scalar sum- p_T , and scalar sum-invariant-mass of the dijet system with the maximum transverse momentum. These NJetX dijet variables were determined

via observation of their discriminating power between signal and background events in MC.

The distributions for a few promising discriminating NJetX variables in the JZ₄W-slice-search region are shown in the figures below, with H_T^{NJet} , $m_{\text{sum}}^{\text{NJet}}$, and p_T^{NJet} depicted in Figure 4.52 and $H_T^{\text{NJetJJ,max-}p_T}$, $m_{\text{sum}}^{\text{NJetJJ,max-}p_T}$, and $p_T^{\text{NJetJJ,max-}p_T}$ depicted in Figure 4.53. The distributions, normalized to unity to illustrate distinctions in shape between signal and background, are shown for 1400-GeV mediator mass signal samples, where the NJetX variable distributions peak at higher values and differ more widely from the QCD background. In the search region, where higher- p_T leading jets are included, the signal distributions are peaked at even higher values and the separation between signal and background is slightly larger, particularly for the high-mediator-mass models.

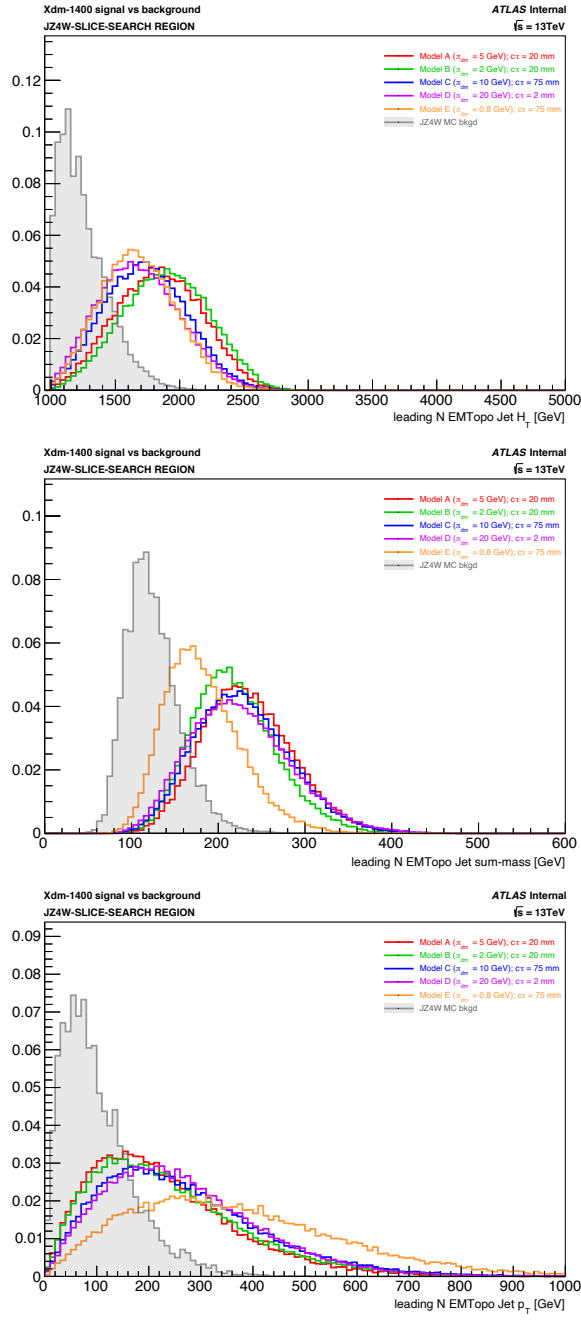


Figure 4.52: The H_T^{NJet} (top), $m_{\text{sum}}^{\text{NJet}}$ (middle), and p_T^{NJet} (bottom) distributions for 1400-GeV mediator mass signal events and JZ4W dijet background events in the JZ4W-slice-search region. The observables are calculated from the system of the four leading jets in the event.

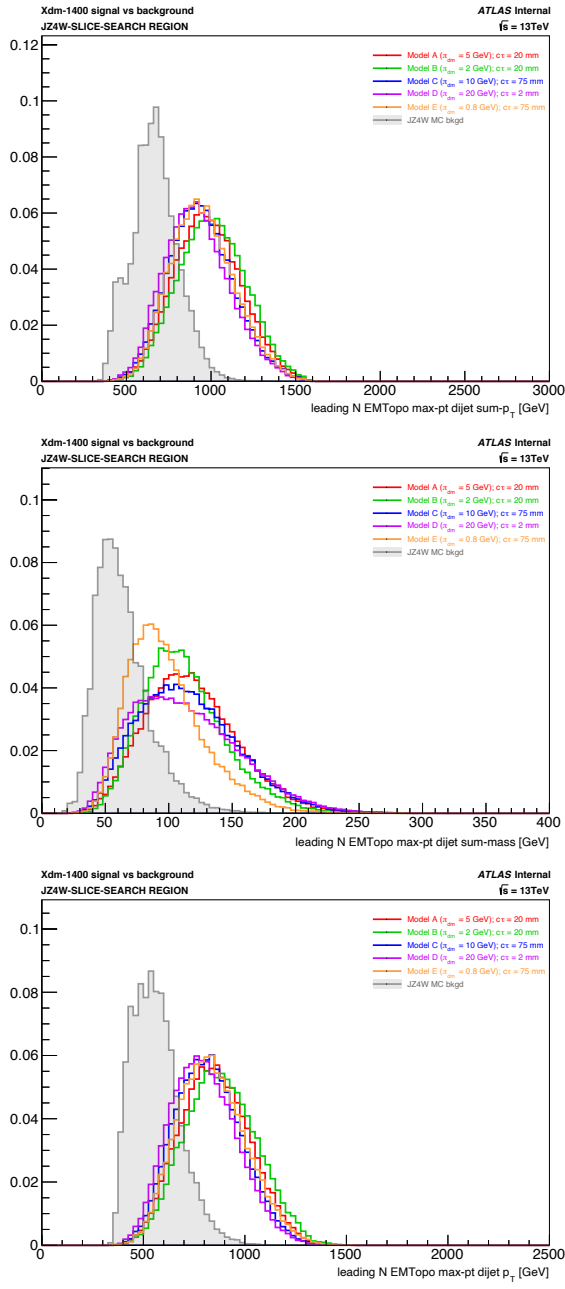


Figure 4.53: The $H_T^{\text{NJetJJ}, \text{max-}p_T}$ (top), $m_{\text{sum}}^{\text{NJetJJ}, \text{max-}p_T}$ (middle), and $p_T^{\text{NJetJJ}, \text{max-}p_T}$ (bottom) distributions for 1400-GeV mediator mass signal events and JZ4W dijet background events in the JZ4W-slice-search region. The observables are calculated from the dijet system with the maximum p_T among the four leading jets in the event.

Event-level cutflows and cutflow efficiencies for the H_T^{NJet} and $H_T^{\text{NJetJJ,max-}p_T}$ selections are shown in Figures 4.54 and 4.55, respectively, comparing 600-GeV, 1000-GeV, and 1400-GeV mediator mass signal events to MC background across the corresponding ranges of proposed cut values. Each cutflow bin represents the number or fraction of JZ4W-slice-search region events passing the respective NJetX selection, where an event passes the selection if it has X^{NJet} above the specified threshold. While the efficiency is minimally affected with the increase in X^{NJet} threshold for the 1400-GeV signal, the lower mediator mass signal suffers from a more significant loss of efficiency, as expected. Regardless, the signal-to-background ratio, displayed underneath the cutflow, increases with each successive cut value, indicating the tightest NJetX cuts can be implemented to maximally reduce the background without complete loss of sensitivity to the signal, even in the low-mediator-mass models.

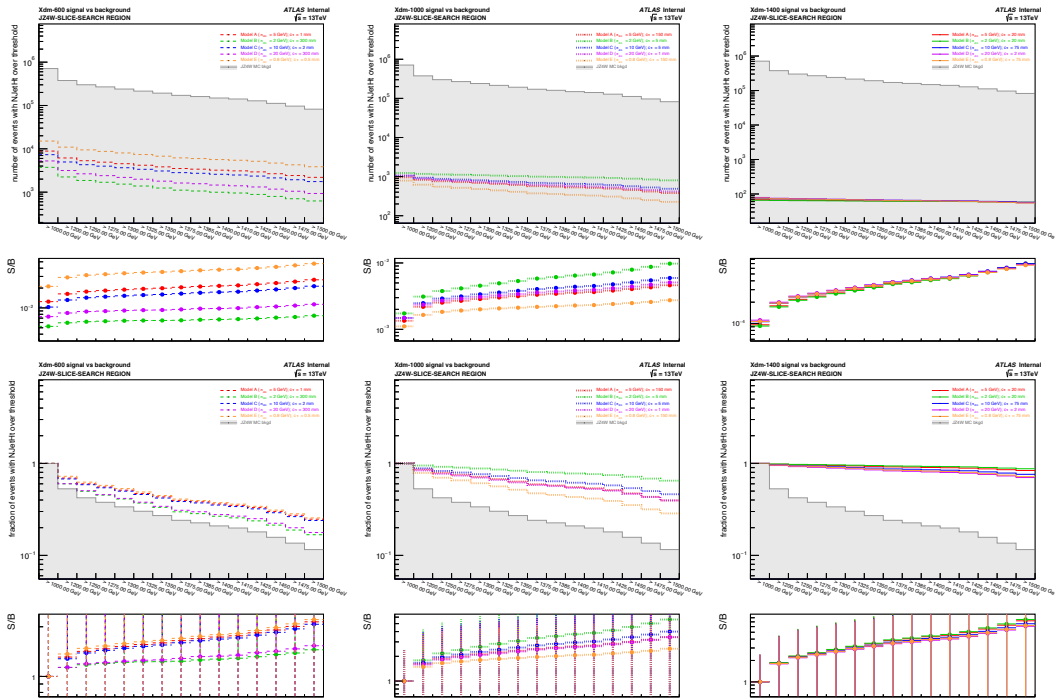


Figure 4.54: The event-level NJetX cutflow (top) and cutflow efficiency (bottom) for $X^{\text{NJet}} = H_T^{\text{NJet}}$ in 600-GeV (left), 1000-GeV (center), and 1400-GeV (right) signal versus QCD dijet background in the JZ4W-slice-search region. Each bin displays the number or fraction of events in the region with H_T^{NJet} above the specified selection threshold. The bottom panel shows the ratio of signal to background events in each bin.

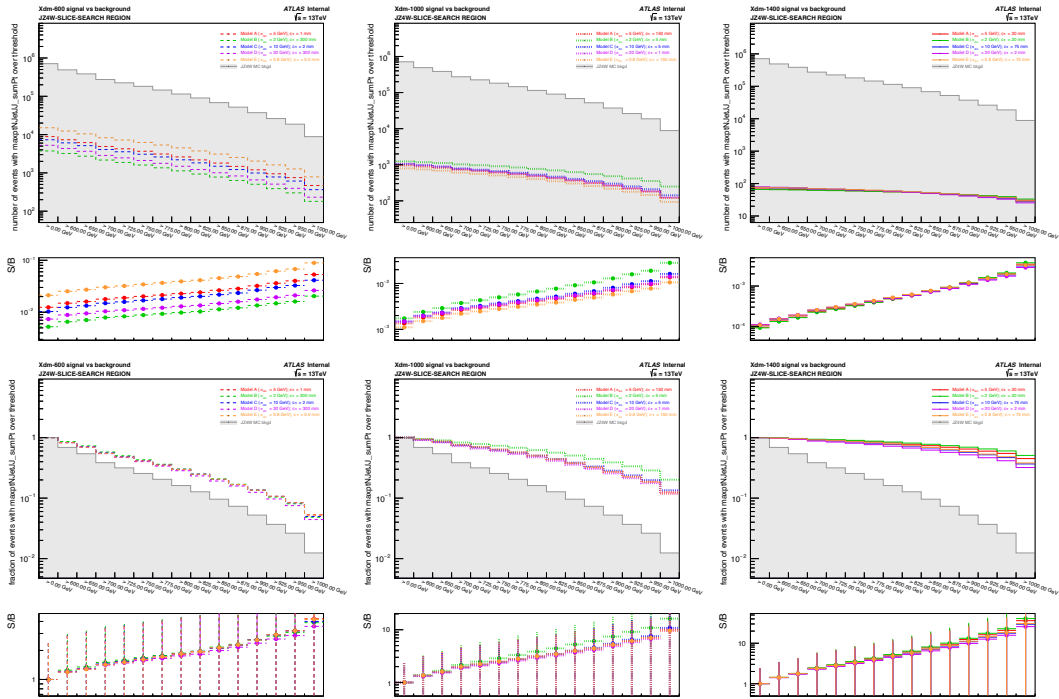


Figure 4.55: The event-level NJetX cutflow (top) and cutflow efficiency (bottom) for $X^{\text{NJet}} = H_{\text{T}}^{\text{NJetJJ}, \text{max-}p_{\text{T}}}$ in 600-GeV (left), 1000-GeV (center), and 1400-GeV (right) signal versus QCD dijet background in the JZ4W-slice-search region. Each bin displays the number or fraction of events in the region with $H_{\text{T}}^{\text{NJetJJ}, \text{max-}p_{\text{T}}}$ above the specified selection threshold. The bottom panel shows the ratio of signal to background events in each bin.

4.3.8 OVERALL EVENT CUTFLOW AND SIGNAL EFFICIENCY

The overall event counts and efficiencies for a representative set of $N_{\text{EJ}} + N_{\text{DV}} + X^{\text{NJet}}$ signal region selections are presented below.

The search region signal event cutflows for $X^{\text{NJet}} = H_T^{\text{NJetJJ,max-}p_T}$ and a combination of N_{EJ} and N_{DV} selections in 1400-GeV signal samples and MC background are shown in Figures 4.56, 4.57, and 4.58. Each figure contains cutflows for $N_{\text{EJ}} = 0$ and 1 for the **Loose EJ** working point in combination with $N_{\text{DV}} = 2, 3$, and 4, with the **Loose**, **Medium**, and **Tight DV** working points illustrated separately in Figures 4.56, 4.57, and 4.58, respectively. Each cutflow bin represents the number of search region events passing the corresponding signal selection and all previous selections. The first bin contains all events in the search region, the second bin contains the number of search region events passing the N_{EJ} selection, and the third contains those passing both the N_{EJ} and N_{DV} selections. The last three bins contain the number of search region events passing the combined $N_{\text{EJ}}, N_{\text{DV}}$, and X^{NJet} selections, where the fourth, fifth, and sixth bins correspond to the lowest, central, and highest elements of the proposed range of cut values.

Implementing a **Loose** emerging jet cut of $N_{\text{EJ}} \geq 1$ minimally reduces the overall event count in the signal samples but significantly reduces the background event count in the signal region, resulting in the background effectively going to zero earlier in the sequence of signal event selections or when it otherwise would not, depending on the specific N_{DV} .

and X^{NJet} selections applied in combination, versus the $N_{\text{EJ}} = 0$ selection. For $N_{\text{DV}} \geq 4$ with **Medium** and **Tight** DV working points, the N_{EJ} selection is not required to eliminate the MC background. The **Tight** DV $N_{\text{DV}} \geq 3$ selection can also sufficiently remove the MC background without the N_{EJ} cut, depending on the subsequent NJetX selection. The low-mass-model and extreme-lifetime signal points are the most heavily impacted by the N_{EJ} selection, which also yields lower signal efficiencies for lower mediator mass samples.

The event-level cutflows comparing $N_{\text{EJ}} = 1$ signal cuts using **Loose** and **Tight** emerging jet selections in the search region are shown in Figure 4.59 for the **Loose** DV working point and $X^{\text{NJet}} = H_{\text{T}}^{\text{NJetJJ,max-}p_{\text{T}}}$. Tightening the emerging jet selection working point can aid in reducing or even eliminating the background, depending on the N_{DV} and NJetX selections applied in combination, with very little impact on the overall signal efficiency, with the low-mediator-mass, low-mass-model, and extreme-lifetime signal points suffering the most signal loss from the tighter EJ working point.

Figure 4.60 shows the signal event cutflow in the search region for $N_{\text{EJ}} = 2$, $N_{\text{DV}} = 2$, and $X^{\text{NJet}} = H_{\text{T}}^{\text{NJetJJ,max-}p_{\text{T}}}$ in 1400-, 1000-, and 600-GeV signal samples versus QCD dijet MC background, using the **Loose** DV selection working point and comparing the event count between the **Loose** and **Tight** emerging jet selection working points. Requiring two emerging jets, regardless of the working point used to define the emerging jet selection, sufficiently eliminates the MC background, but the signal efficiency suffers immediately

and severely for some signal points, particularly for the **Tight** EJ working point. Given that combinations of other signal cuts with looser N_{EJ} selections can effectively reduce the background while retaining more sensitivity to the signal, the $N_{\text{EJ}} = 2$ cut is likely tighter than necessary for the final signal region.

The full signal region event count and efficiency cutflows for a representative $N_{\text{EJ}} + N_{\text{DV}} + X^{\text{NJet}}$ selection in 1400-, 1000-, and 600-GeV signal samples versus the QCD di-jet MC background is depicted in Figure 4.61, where $N_{\text{EJ}} = 1$, $N_{\text{DV}} = 3$, $X^{\text{NJet}} = H_{\text{T}}^{\text{NJet}}$, and the **Loose** EJ and **Medium** DV working points are implemented. Each cutflow bin represents the number or fraction of events passing the respective signal selection used in the analysis and all previous selections. The first bin contains the initial number or fraction of events generated in the MC sample, and the second bin contains that after the derivation skimming. Unlike the data, Monte Carlo samples are not skimmed at the derivation level. Bins three through six correspond to the remaining event preselections, with the data quality event cleaning and GRL selections excluded, as they are irrelevant to MC. Bins seven through eleven correspond to the search region selections, while the last five bins correspond to the N_{EJ} , N_{DV} , and low-, middle-, and high- X^{NJet} selections defining the final signal region. The signal samples are minimally impacted by the initial preselections and search region selections, with only the 600-GeV signal suffering from any real loss of efficiency after the $H_{\text{T}}^{\text{NJet}} > 1000$ GeV search region cut. The final N_{EJ} , N_{DV} , and X^{NJet} signal

region selections serve to dramatically reduce the background with smaller effect on the signal.

The potential signal regions defined by the proposed $N_{\text{EJ}} + N_{\text{DV}} + X^{\text{NJet}}$ selections are still to be optimized to identify the most promising signal region resulting in maximal signal efficiency and background rejection.

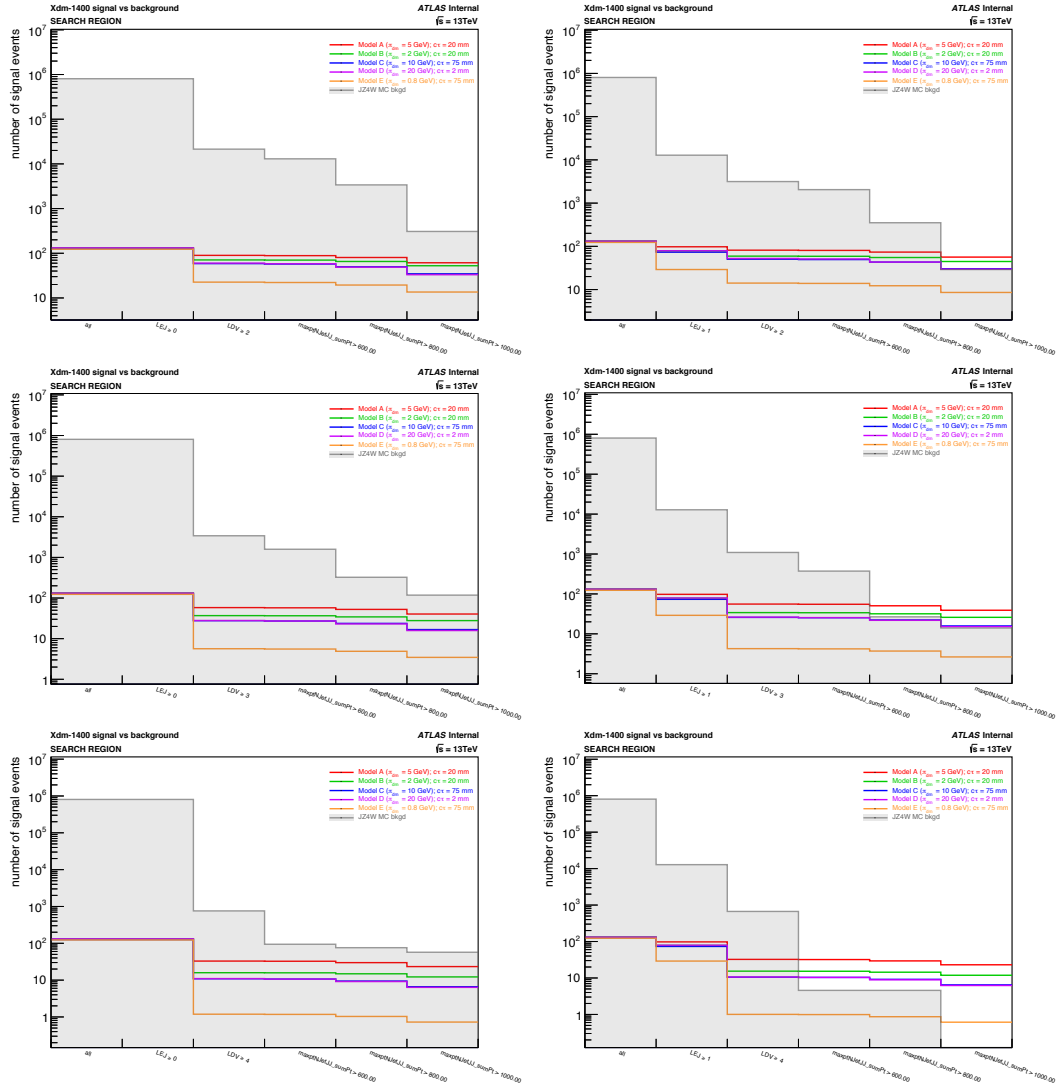


Figure 4.56: The signal event cutflow for $N_{EJ} = 0$ (left) and $N_{EJ} = 1$ (right), with the Loose EJ working point, in combination with $N_{DV} = 2$ (top), $N_{DV} = 3$ (middle), and $N_{DV} = 4$ (bottom), with the Loose DV working point, and $X^{N\text{Jet}} = H_T^{\text{NJetJJ}, \text{max-}p_T}$ in 1400-GeV signal versus QCD dijet background in the search region. Each bin displays the number of events in the search region passing the respective signal selection and all previous selections.

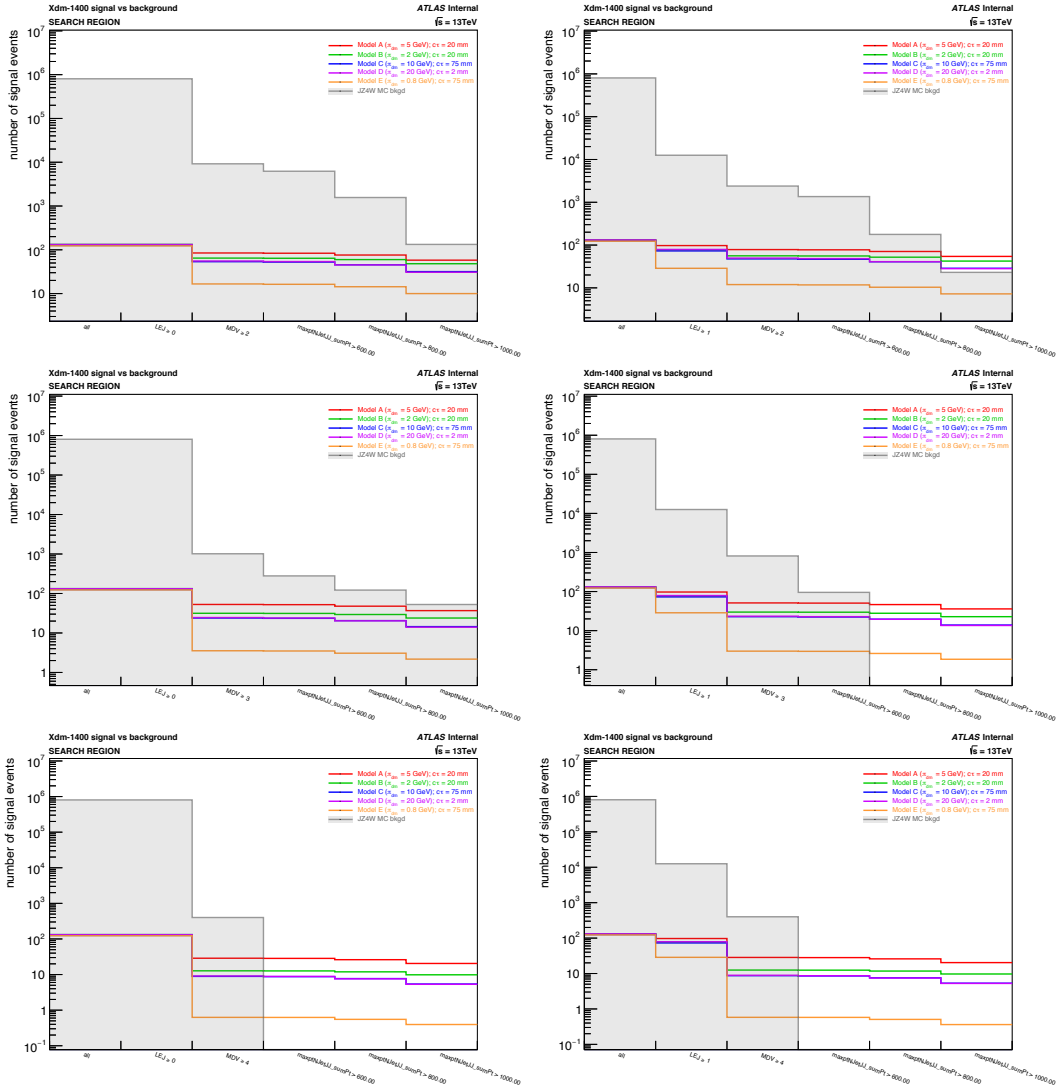


Figure 4.57: The signal event cutflow for $N_{EJ} = 0$ (left) and $N_{EJ} = 1$ (right), with the Loose EJ working point, in combination with $N_{DV} = 2$ (top), $N_{DV} = 3$ (middle), and $N_{DV} = 4$ (bottom), with the Medium DV working point, and $X^{N\text{Jet}} = H_T^{\text{NJetJJ}, \max p_T}$ in 1400-GeV signal versus QCD dijet background in the search region. Each bin displays the number of events in the search region passing the respective signal selection and all previous selections.

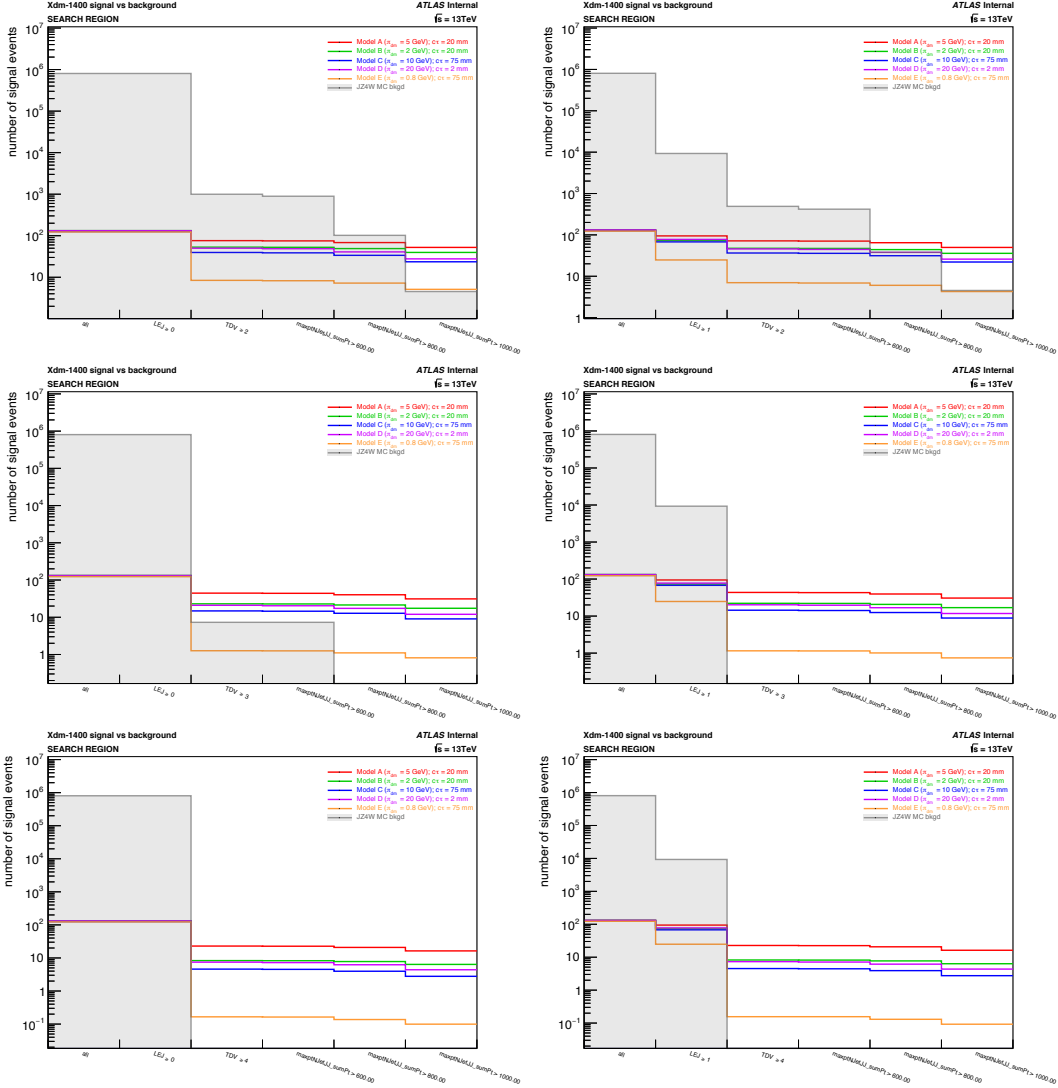


Figure 4.58: The signal event cutflow for $N_{EJ} = 0$ (left) and $N_{EJ} = 1$ (right), with the Loose EJ working point, in combination with $N_{DV} = 2$ (top), $N_{DV} = 3$ (middle), and $N_{DV} = 4$ (bottom), with the Tight DV working point, and $X^{N\text{Jet}} = H_T^{\text{NJetJJ}, \text{max-}p_T}$ in 1400-GeV signal versus QCD dijet background in the search region. Each bin displays the number of events in the search region passing the respective signal selection and all previous selections.

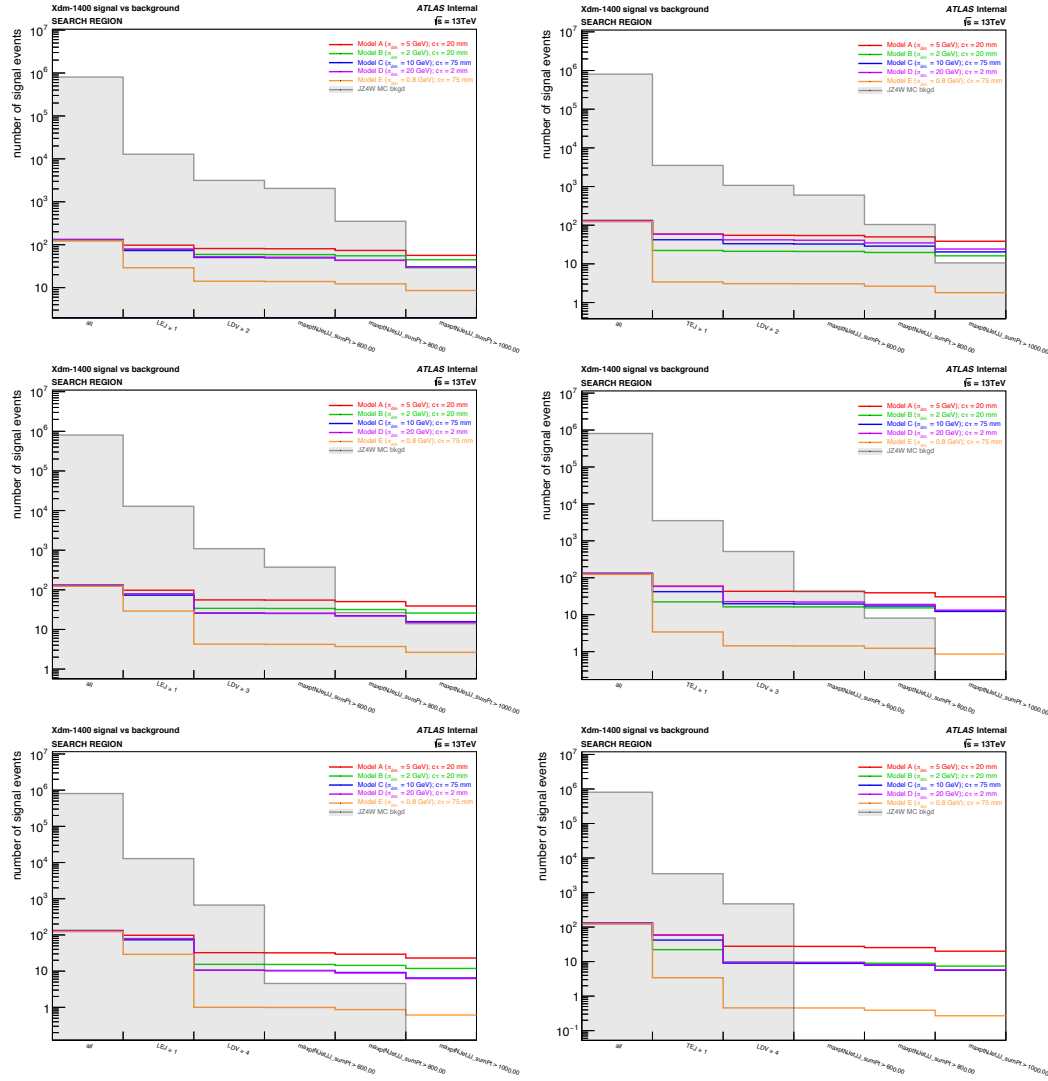


Figure 4.59: The signal event cutflow for $N_{\text{EJ}} = 1$, with the Loose (left) and Tight (right) EJ working points, in combination with $N_{\text{DV}} = 2$ (top), $N_{\text{DV}} = 3$ (middle), and $N_{\text{DV}} = 4$ (bottom), with the Loose DV working point, and $X^{\text{NJet}} = H_{\text{T}}^{\text{NJetJJ}, \text{max}p_{\text{T}}}$ in 1400-GeV signal versus QCD dijet background in the search region. Each bin displays the number of events in the search region passing the respective signal selection and all previous selections.

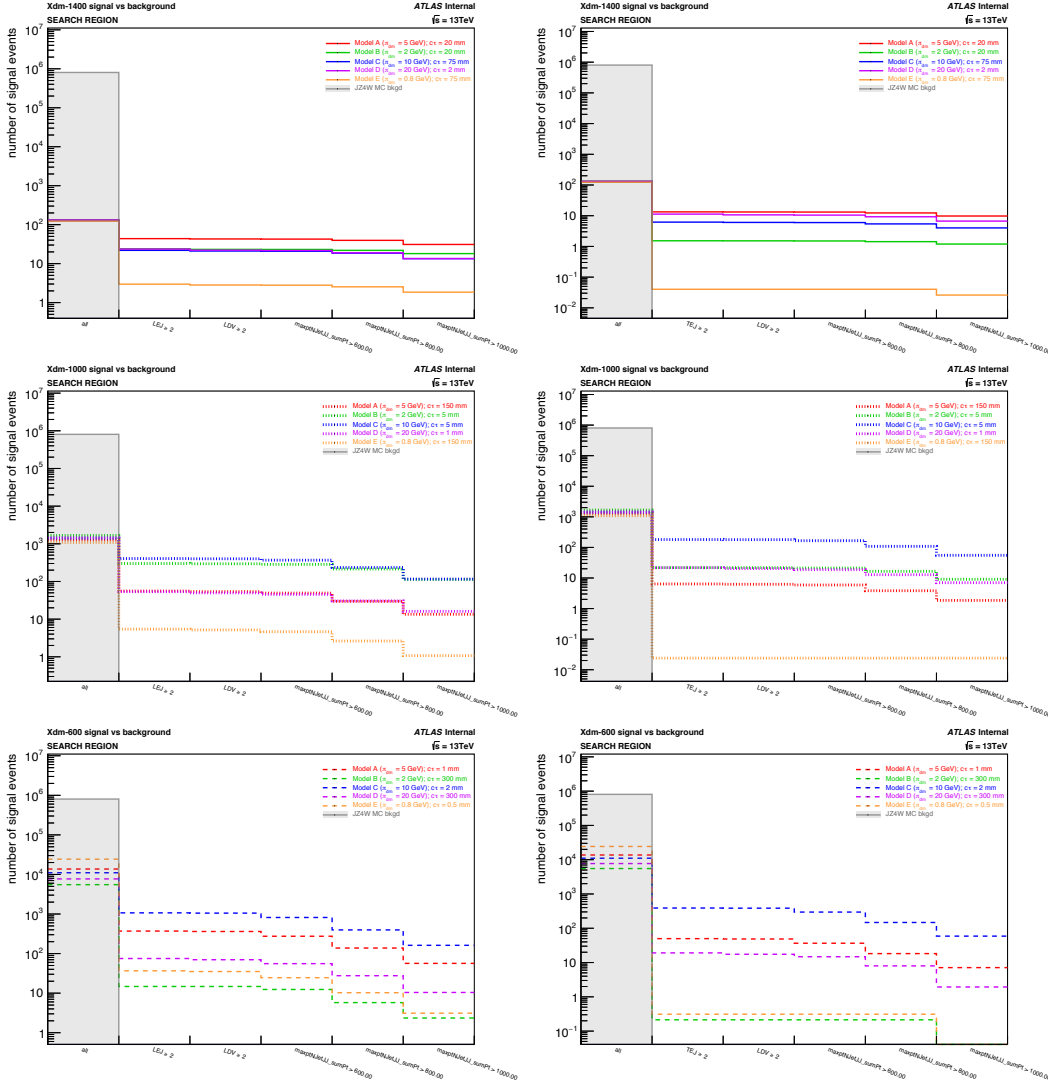


Figure 4.60: The signal event cutflow for $N_{\text{EJ}} = 2$ (left), with the Loose (left) and Tight (right) EJ working points, in combination with $N_{\text{DV}} = 2$, with the Loose DV working point, and $X^{\text{NJet}} = H_T^{\text{NJetJJ,max-}p_T}$ in 1400-GeV (top), 1000-GeV (middle) and 600-GeV (bottom) signal versus QCD dijet background in the search region. Each bin displays the number of events in the search region passing the respective signal selection and all previous selections.

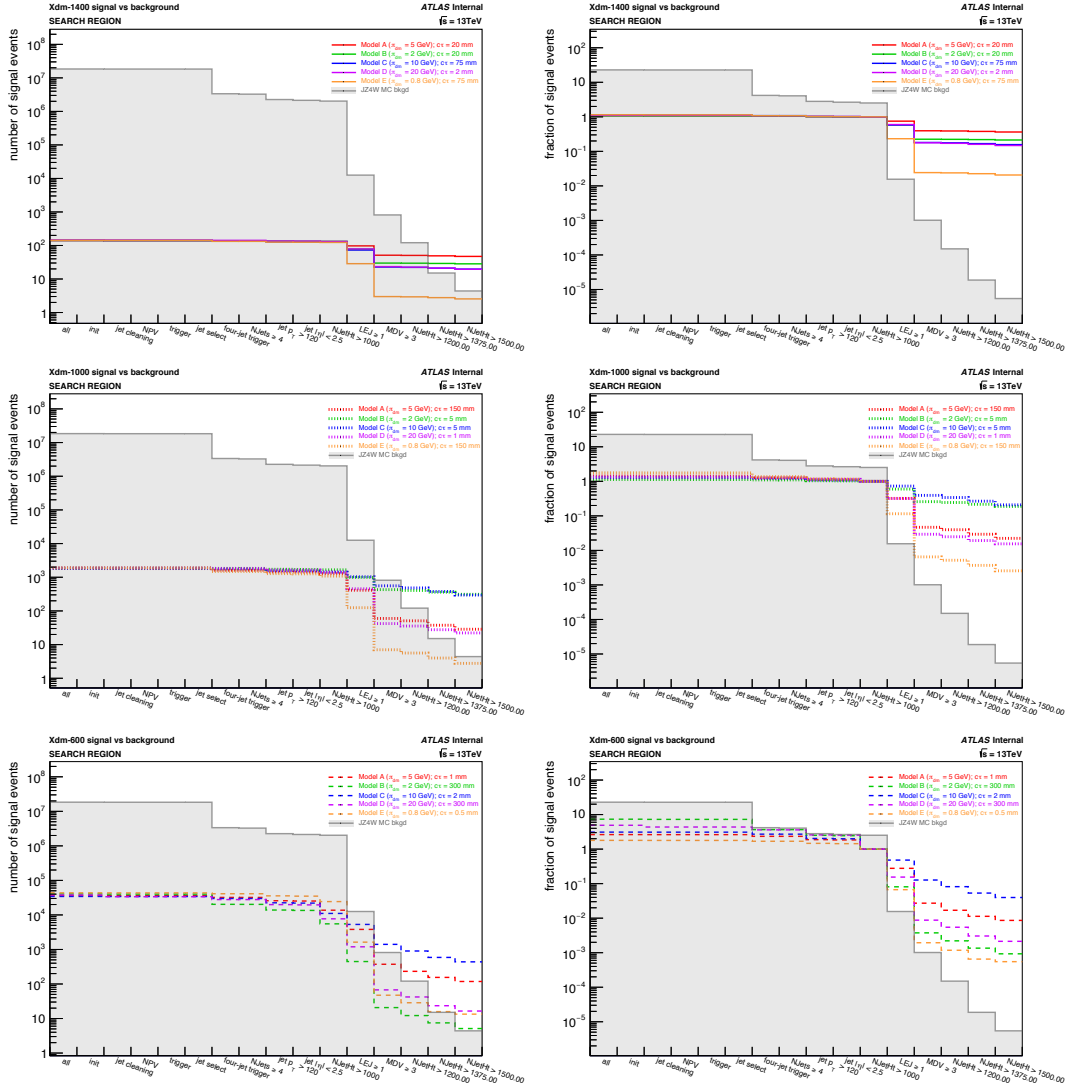


Figure 4.61: The full signal event count (left) and efficiency (right) cutflow for $N_{EJ} = 1$, with the Loose EJ working point, in combination with $N_{DV} = 3$, with the Medium DV working point, and $X^{N_{\text{Jet}}} = H_T^{N_{\text{Jet}}}$ in 1400-GeV (top), 1000-GeV (middle) and 600-GeV (bottom) signal versus QCD dijet background. Each bin displays the number or fraction of events in the MC sample passing the respective signal selection and all previous selections.

4.4 BACKGROUND ESTIMATION

The major background process contributing to the Emerging Jets analysis is Standard Model QCD multijets, which can yield four high- p_T jets that mimic the signal. Events from such SM QCD multijet processes can also result in signal-like displaced vertices that are produced from background sources but pass the DV signal selections. These background sources producing signal-like DVs include hadronic interactions, where particles interact with the detector and produce displaced vertices, primarily inside regions of the detector material, and randomly crossing tracks, where random unassociated tracks cross and are accidentally reconstructed as displaced vertices. The DV signal selections discussed in Section 4.3 remove a large portion of these fake vertices, while the remaining fakes are encompassed within the larger SM QCD multijet background. The overall background contribution to the signal region can thus be estimated for a single inclusive process to yield a single overall background prediction.

To estimate the background contribution from the SM QCD multijet process to the final signal region, the ABCD method is used, which is a data-driven background estimation technique that predicts the number of background events in the signal region through the application of a transfer factor, measured from the number of observed events in the associated control regions. The underlying assumption behind the ABCD method is that the variables used to define the relevant signal and control regions are uncorrelated, and

the estimation method is validated by comparing background predictions to observed data in a dedicated validation ABCD plane. The ABCD method is also used in this analysis to validate the background rejection is sufficiently high for the set of potential signal region selections before determining the ultimate signal cuts. A dedicated “shifted validation region (VR)” ABCD method is developed for this purpose, in order to estimate the amount of data in the signal region without unblinding the search region.

4.4.1 OVERVIEW OF ABCD METHOD

The ABCD method implements a two-dimensional ABCD plane where the signal and background are separated into four regions: A, B, C, and D, defined by two independent selections forming part of the final signal region definition. These two selections are placed on two uncorrelated observables that form the x - and y -axes of the ABCD plane. Region A is the signal region, where events pass both selections, and B, C, and D are the control regions, which are designated by inverting the two signal selections and are ideally rich in the background processes being estimated and mostly free from signal. The ABCD regions are as follows:

- Region A: $x > X$ and $y > Y$;
- Region B: $x > X$ and $y < Y$;
- Region C: $x < X$ and $y > Y$;
- Region D: $x < X$ and $y < Y$;

where x and y are the observables defining the x - and y axes of the ABCD plane, and X

and Y are the selection values used to separate the plane into regions. The cuts are chosen to preferentially select signal events in the signal region and to have minimal contamination from the signal events in the control regions. Assuming a blinded analysis, the number of events in A is unknown but can be predicted from the number of events recorded in the control regions, with the goal of the ABCD method being to estimate the number of non-signal events in the signal region.

The basic method, or the standard arithmetic approach, calculates the expected background contribution to the final signal region as follows:

$$N_A^{\text{bkgd}} = N_B^{\text{bkgd}} \times N_C^{\text{bkgd}} / N_D^{\text{bkgd}}, \quad (4.6)$$

where N_R^{bkgd} is the number of background events in region R . The underling assumption of the ABCD method is the condition that $N_C^{\text{bkgd}} / N_D^{\text{bkgd}} = N_A^{\text{bkgd}} / N_B^{\text{bkgd}}$, which is satisfied if the observables defining the ABCD plane are sufficiently independent of one another for the background distribution under consideration. The ratio $N_C^{\text{bkgd}} / N_D^{\text{bkgd}} = m$ is known as the transfer factor (TF), which represents the ratio of events passing the signal selection applied to one of the observables defining the x - and y -axes of the ABCD plane to the events failing the same selection. Assuming the two observables are uncorrelated, the ratio of events passing to those failing one ABCD selection should not change as a function of the second selection, meaning $\text{TF} = N_C^{\text{bkgd}} / N_D^{\text{bkgd}} = N_A^{\text{bkgd}} / N_B^{\text{bkgd}}$. The transfer

factor should ideally be measured in a region of pure background as free from signal as possible, so the basic ABCD method assumes all events recorded in regions B, C, and D are due to background processes only. This assumption is often a safe one, particularly in BSM and exotics searches, where the signal processes under consideration are rare and the signal strength is sufficiently small such that any signal contribution to the control regions can be deemed negligible. In the case where the signal contamination can not be ignored, an alternative likelihood fit ABCD method can be implemented to estimate the background instead.

The likelihood-based approach involves fitting a statistical model constructed with the underlying assumption of the basic ABCD method about the relationship of the background distribution between different regions. The basic ABCD method assumption can be expressed as

$$\tilde{N}_A = \tilde{m}\tilde{N}_B, \tilde{N}_C = \tilde{m}\tilde{N}_D, \quad (4.7)$$

where a tilde represents a free parameter in the fit, and \tilde{m} is the transfer factor of the ABCD method. The likelihood for observing the data $\{N_A, N_B, N_C, N_D\}$ is then given by

$$L(\{N_A, N_B, N_C, N_D\} | \tilde{N}_B, \tilde{N}_D, \tilde{m}) = \text{Poisson}(N_A + N_B + N_C + N_D | \tilde{N}_{\text{total}}) \times \\ \prod_{N_A} \frac{\tilde{m}\tilde{N}_B}{\tilde{N}_{\text{total}}} \prod_{N_B} \frac{\tilde{N}_B}{\tilde{N}_{\text{total}}} \prod_{N_C} \frac{\tilde{m}\tilde{N}_D}{\tilde{N}_{\text{total}}} \prod_{N_D} \frac{\tilde{N}_D}{\tilde{N}_{\text{total}}}, \quad (4.8)$$

where $\tilde{N}_{\text{total}} = \tilde{m}\tilde{N}_B + \tilde{N}_B + \tilde{m}\tilde{N}_D + \tilde{N}_D$. In the case of a fit performed on blinded data where the number of events in A is unavailable, N_A is removed from the model, and the likelihood for observing the blinded data $\{N_B, N_C, N_D\}$ is

$$L(\{N_B, N_C, N_D\} | \tilde{N}_B, \tilde{N}_D, \tilde{m}) = \text{Poisson}(N_B + N_C + N_D | \tilde{N}_{\text{blind total}}) \times \\ \prod_{N_B} \frac{\tilde{N}_B}{\tilde{N}_{\text{blind total}}} \prod_{N_C} \frac{\tilde{m}\tilde{N}_D}{\tilde{N}_{\text{blind total}}} \prod_{N_D} \frac{\tilde{N}_D}{\tilde{N}_{\text{blind total}}}, \quad (4.9)$$

where $\tilde{N}_{\text{blind total}} = \tilde{N}_B + \tilde{m}\tilde{N}_D + \tilde{N}_D$. The probability of the observed data is thus the product of the probabilities of observing each event in the respective region multiplied by the overall Poisson probability of observing the total number of events.

The ABCD background estimation method can be validated by applying the same method, whether the standard arithmetic or likelihood-based approach, in a dedicated ABCD validation plane that is free of signal and where the data is safely unblinded. The validation plane, with regions A', B', C', and D', is defined by inverting an earlier analysis cut to exclude signal events and then applying the same two selections defining the nominal ABCD plane; the background yield in A' is estimated using the other three primed regions; and the prediction for the number of events in A' is compared directly to observation. The relative uncertainty between the predicted and observed values of $N_{A'}$ in the validation plane can be taken as a systematic uncertainty on the background estimate if the values do not agree.

4.4.2 PROPOSED ABCD PLANES AND METHOD

The ABCD plane used to estimate the SM QCD multijet background for the EJs analysis is defined by two axes representing two discriminating observables: one, the y -axis, representing the displaced vertex multiplicity, and the other, the x -axis, representing the properties of the N_{jet} leading jets in the event, as these are the two defining characteristics of the EJs signal and thus optimally discriminate between the signal and background distributions. The y -axis delineates categories of events based on the value of the N_{DV} observable, or the number of displaced vertices passing the DV working point selections and nearby to leading jets, splitting events into a DV signal region (DV SR) and a DV control region (DV CR), and the x -axis defines categories of events based on the value of the X^{NJet} observable, splitting events into an NJetX signal region (NJetX SR) and an NJetX control region (NJetX CR), where both N_{DV} and X^{NJet} are defined in Section 4.3 above. The two observables defining the DV \times NJetX ABCD plane are shown to be uncorrelated in Figure 4.62, where the average value of N_{DV} is plotted as a function of X^{NJet} for a set of representative N_{DV} and X^{NJet} signal variables in data and MC QCD dijet background in the validation region. The average number of displaced vertices per event is constant with respect to X^{NJet} for all potential N_{DV} and X^{NJet} observables, indicating the two variables are independent of each other for the background process being estimated. Any correlation that may exist in the signal is irrelevant to the success of the method, although no correlation is observed there either.

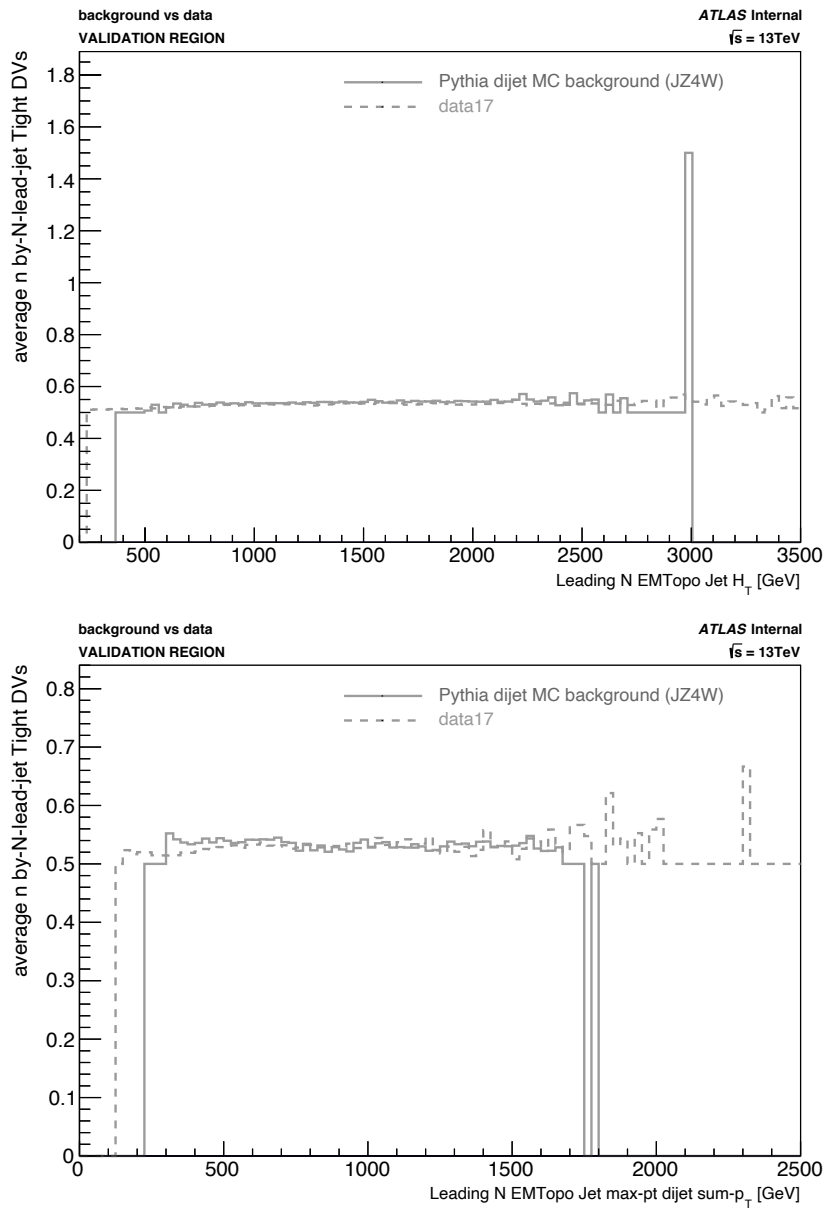


Figure 4.62: The average number of Tight displaced vertices per event as a function of $H_T^{N\text{Jet}}$ (left) and $H_T^{N\text{JetJJ},\text{max-}p_T}$ (right) in the JZ4W Pythia dijet MC background slice and in a subset of 2017 data in the validation region. No correlation is observed between N_{DV} and either $X^{N\text{Jet}}$ observable for any DV selection working point. The sharp spike in simulation in the $H_T^{N\text{Jet}}$ distribution is due to low statistics for high- p_T jet events in the JZ4W slice.

The $\text{DV} \times \text{NJetX}$ ABCD plane is applied on top of all other signal selections preceding the N_{DV} and X^{NJet} cuts and thus consists of four regions determined by the range of DV multiplicity and NJetX selection values defining the proposed signal regions, with the signal and control regions specified by whether the N_{DV} and X^{NJet} observables representing the x - and y -axes are above or below the designated signal thresholds. The four regions are chosen such that A is dominated by signal and B, C, and D are dominated by background, with A and B containing events with signal-like NJetX properties and C and D having background-like NJetX properties, and A and C having signal-like DV multiplicities and B and D having background-like DV multiplicities. The A, B, C, and D regions of the $\text{DV} \times \text{NJetX}$ ABCD plane are defined below:

- Region A: $N_{\text{DV}} \geq Y$ and $X^{\text{NJet}} > X \rightarrow \text{DV SR} \times \text{NJetX SR}$, containing events passing both the N_{DV} and X^{NJet} signal selection thresholds, where the displaced vertices included in the DV count pass the DV working point signal selections and are nearby to leading jets; this region is intended to isolate the signal as much as possible, given the discriminating power of the corresponding selections defining the ABCD plane, and corresponds to the top-right quadrant;
- Region B: $N_{\text{DV}} < Y$ and $X^{\text{NJet}} > X \rightarrow \text{DV CR} \times \text{NJetX SR}$, containing events with N_{DV} below threshold and X^{NJet} above threshold, which corresponds to the bottom-right quadrant;
- Region C: $N_{\text{DV}} \geq Y$ and $X^{\text{NJet}} < X \rightarrow \text{DV SR} \times \text{NJetX CR}$, containing events passing the N_{DV} selection and failing the X^{NJet} selection, corresponding to the top-left quadrant;
- Region D: $N_{\text{DV}} < Y$ and $X^{\text{NJet}} < X \rightarrow \text{DV CR} \times \text{NJetX CR}$, containing events

with both the N_{DV} and X^{NJet} values below threshold, corresponding to the bottom-left quadrant, where the background is primarily isolated;

where A is the signal region, and B, C, and D are the control regions.

The event-level signal and background distributions in a representative set of potential ABCD planes are shown in Figures [4.63](#) and [4.64](#), illustrating the discriminating power of the DV \times NJetX signal selections between signal and background and the number of expected events in each of the four resulting regions. One set of potential N_{DV} and X^{NJet} cut values that primarily isolates the background with region D is shown in each plot. The ABCD plane is defined on top of all preceding signal selections defining the search region, as well as the N_{EJ} cut, meaning A represents the final signal region for a given set of N_{DV} and X^{NJet} selections. Currently, the ABCD plane and background estimates have only been investigated for the case of $N_{\text{EJ}} = 0$, but the background rejection and overall signal significance can potentially be improved by implementing a nonzero N_{EJ} cut in the future, if need be.

The initial background estimates are performed with the basic ABCD method, but the distributions in the ABCD plane show obvious signal contamination in the control regions, particularly for low-mediator-mass signals, where the discrimination between signal and background is less significant, that may require implementing a likelihood-based approach instead. The signal contamination is observed to be larger for some DV \times NJetX planes than for others, and the addition of a nonzero N_{EJ} cut may also serve to decrease or even

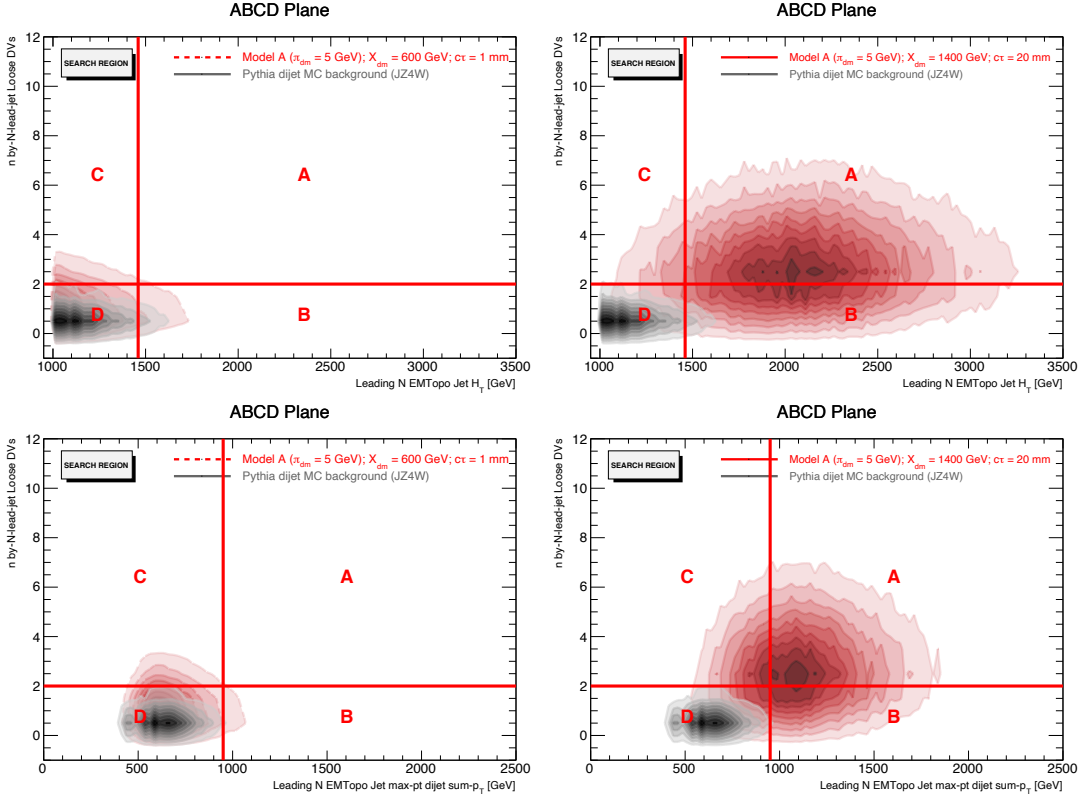


Figure 4.63: The Model A signal and background distributions in the DV \times NJetX ABCD plane for $N_{\text{DV}} = 2$, with the Loose DV working point, versus H_T^{NJet} (top) and $H_T^{\text{NJetJJ}, \text{max-}p_T}$ (bottom) in 600-GeV (left) and 1400-GeV (right) mediator mass signal samples and the JZ4W Pythia dijet MC background. The red lines represent the N_{DV} and X^{NJet} cut values implemented to separate the plane into signal region A and control regions B, C, and D, which are labeled in red.

mostly remove the signal contributions to the observed events in the control regions, so the need for a likelihood-based approach, if any, will depend largely on the final signal region chosen for the analysis. Additionally, the signal strength is very small overall compared to the background, and the signal contamination in the control regions is thus much smaller than it appears in the ABCD plane plots, being at most of order 10^{-3} , so it may even be safe to regard the signal contamination as negligible and implement the basic arithmetic method

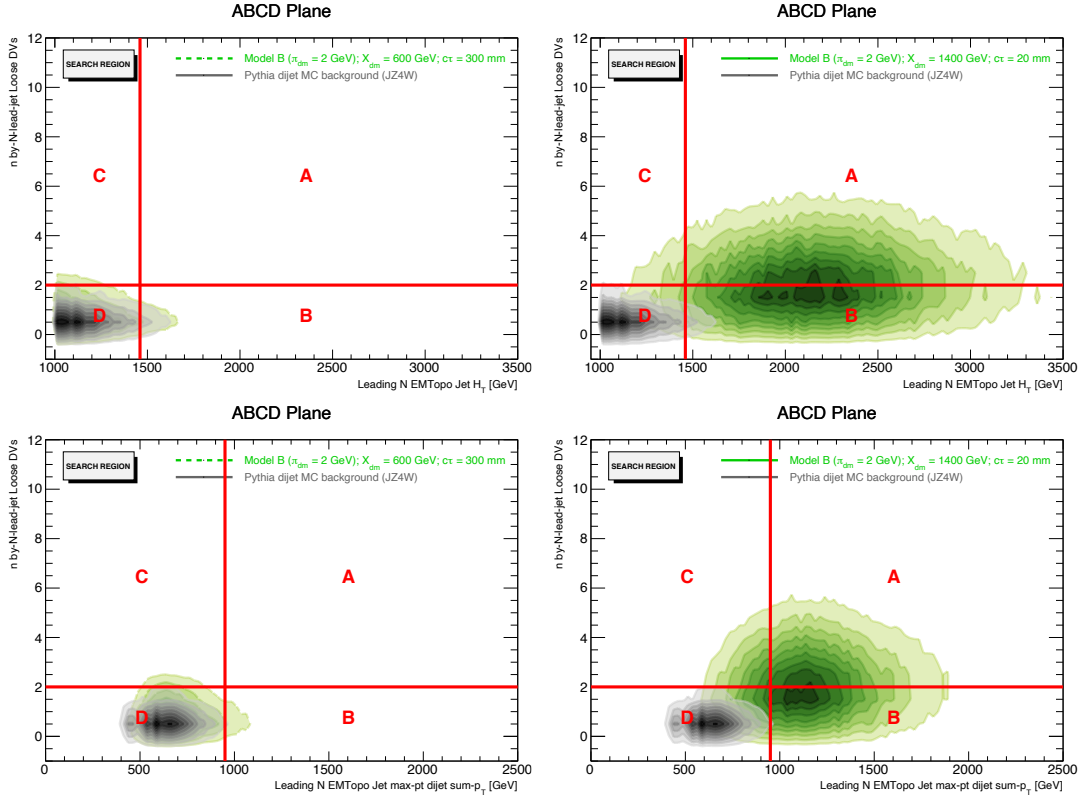


Figure 4.64: The Model B signal and background distributions in the DV \times NJetX ABCD plane for $N_{\text{DV}} = 2$, with the Loose DV working point, versus $H_{\text{T}}^{\text{NJet}}$ (top) and $H_{\text{T}}^{\text{NJetJJ}, \text{max-}p_{\text{T}}}$ (bottom) in 600-GeV (left) and 1400-GeV (right) mediator mass signal samples and the JZ4W Pythia dijet MC background. The red lines represent the N_{DV} and X^{NJet} cut values implemented to separate the plane into signal region A and control regions B, C, and D, which are labeled in red.

for the final background estimate, regardless of the chosen signal region. Either way, only initial estimates have been performed so far, using the basic ABCD method, in order to get a rough prediction of the background yield in the eventual signal region, and full estimates with full data are still to be done, with the final method used yet to be fully determined.

At this point, the initial background estimates are performed with the basic ABCD method over MC dijet background samples, primarily for the purpose of aiding in final-

izing and validating the signal region, making sure the final signal cuts sufficiently reject enough background events in region A before they are officially implemented. In order to cross-check the rough estimates predicted from the MC background distributions without accidentally unblinding the data in the signal region before it is finalized, a dedicated method is developed to estimate the number of background events in A using shifted validation region data, as described in the following section.

4.4.3 SHIFTED VALIDATION REGION METHOD

In the current state of the analysis, the definitive signal region is yet to be finalized, as the determination of the final SR depends greatly on the overall background rejection. It is essential to ensure the eventual SR defined for official use in the analysis sufficiently rejects background such that there is some measurable excess of signal over background. Since the available MC background samples are not guaranteed to entirely accurately represent the data, due to possible MC mismodeling and the use of a single dijet slice, a cross-check on the initial rough estimates performed with MC background is required using the data itself. As the search region currently contains tentative signal regions of unknown size and shape, applying the standard ABCD method to data in the search region could result in accidentally probing the eventual signal region while performing estimates for the background yield in the other potential signal regions, which may encompass the final SR, thus unintentionally looking inside the signal region and partially unblinding the analysis.

In order to avoid this, a dedicated method, referred to as the “shifted validation region (VR) ABCD method”, is developed to perform ABCD background estimates with data using the observed events in region D alone of the search region ABCD plane, along with the observed events in the primed regions of the validation plane after the data has been shifted with a scale factor to reproduce the expected search region background distributions. As the validation plane is free from signal, and region D should be dominated by background, this method allows a way to roughly estimate the data yield in A without relying on any information from regions that may contain significant signal, thereby minimizing the risk of bias while the final SR is still being constructed.

The shifted VR ABCD method is outlined below:

1. Shift the data in the ABCD validation plane by applying a scale factor SF that effectively reproduces the expected search region distribution. The scale factor is determined by comparing the known MC background distributions in the search and validation regions.
2. Count the number of events in the A', B', C', and D' regions of the shifted validation plane.
3. Count the number of events in region D of the nominal search plane.
4. Calculate the ratio between the number of events in region D and the number of shifted events in region D':

$$N_D^{\text{ratio}} = N_D^{\text{search}} / N_{D'}^{\text{shifted validation}}. \quad (4.10)$$

It is assumed that regions B' and C' should scale similarly to B and C as D' to D between the shifted validation and search regions, since the N_{DV} and X^{NJet} observables

are uncorrelated.

5. Multiply the number of shifted events in B' and C' by N_D^{ratio} to approximate the number of events in B and C:

$$\begin{aligned} N_B^{\text{search}} &= N_{B'}^{\text{shifted validation}} \times N_D^{\text{ratio}} \\ N_C^{\text{search}} &= N_{C'}^{\text{shifted validation}} \times N_D^{\text{ratio}}. \end{aligned} \quad (4.\text{II})$$

6. Estimate the number of events in the signal region by applying the standard ABCD method using the number of events in the control regions approximated from the shifted validation plane:

$$N_A^{\text{search}} = N_B^{\text{search}} \times N_C^{\text{search}} / N_D^{\text{search}}, \quad (4.\text{I2})$$

where N_D^{search} is counted directly from observation, and N_B^{search} and N_C^{search} are approximated from the shifted event counts in B' and C' and the shifted VR ratio N_D^{ratio} , as described above.

The validation ABCD plane is defined by implementing the same x - and y -axis observables as for the nominal ABCD plane on top of the validation region described in Section 4.3.4.2, where the signal cut on the number of jets is inverted, requiring less than four jets in the event, to exclude signal events. The scale factor SF is applied to the x -axis distribution, representing the NJetX observable, as this distribution is expected to differ significantly between the validation and search regions due to the difference in number of leading jets per event in each region. The scale factor is calculated separately for each potential X^{NJet} variable used for the respective ABCD plane by dividing the mean values of the corresponding distributions in the JZ4W-slice-validation and -search regions for the MC dijet background

slice:

$$SF = \mu_{\text{NJetX}}^{\text{search}} / \mu_{\text{NJetX}}^{\text{validation}} \quad (4.13)$$

This scale factor is then applied to the respective validation region distribution in the data.

The shifted VR ABCD method is illustrated in Figure 4.65, where the H_T^{NJet} validation region distribution is shown before and after a scale factor of $4/3$ is applied against the nominal search region distribution for the JZ4W MC background, along with the event-level distribution in the DV \times NJetX ABCD plane before and after the VR shift. The scale factor effectively reproduces the search region distribution from the validation region distribution for the MC background sample and is expected to do so for the data, as well, since the shapes of the MC background and data distributions in the validation region generally agree. The ABCD plane distributions illustrated in Figure 4.65 do not apply any DV working point selections, but only the X^{NJet} distribution is scaled in the shifted VR ABCD method, as the N_{DV} distribution is not expected to significantly change between the validation and search regions, so the efficacy of the method should not change with the implementation of the DV signal selections.

At this point in the analysis, the shifted VR ABCD method has been developed and minimally tested, but is yet to be fully implemented over data for rough estimates.

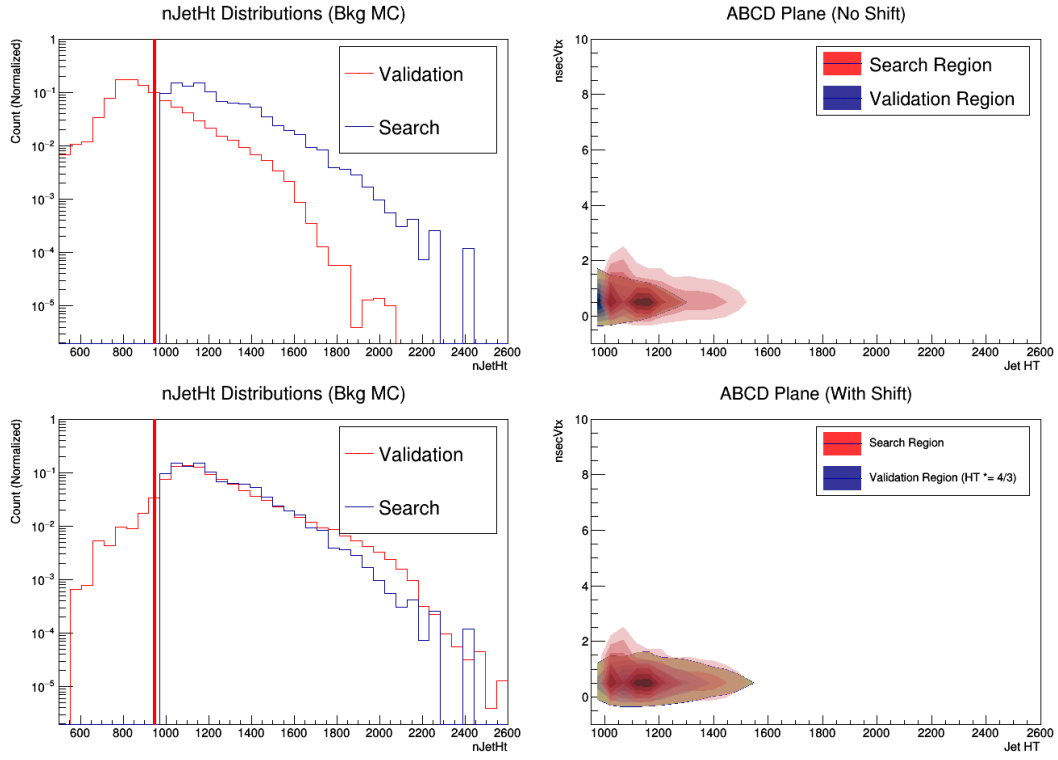


Figure 4.65: An illustration of the shifted VR ABCD method: the H_T^{NJet} distributions (left) and $N_{\text{DV}} \times H_T^{\text{NJet}}$ ABCD plane distributions (right) of the JZ4W Pythia dijet MC background sample before (top) and after (bottom) the application of a scale factor of $SF = 4/3$ to the validation region events against the search region events.

4.4.4 VALIDATION OF BACKGROUND ESTIMATION METHOD

The performance of the ABCD background estimation method implemented in the analysis must also be validated, which is achieved by comparing the number of predicted to observed events in the dedicated validation ABCD plane, which is defined by inverting one of the analysis cuts and is equal to the validation region defined in Section 4.3.4.2 above.

Initial validation studies are performed with the MC PYTHIA dijet background sample

and a subset of the data in the validation plane, and an official validation will be performed with full data in the near future, once the ultimate SR is finalized, in order to determine a systematic uncertainty on the final background estimate. The agreement between prediction and observation for the background yields in A' in the validation ABCD plane vary widely between different signal selection observables and cut values, with the standard ABCD method performing very well for some proposed signal regions and very poorly for others.

The agreement between the estimate and observed background yields can be measured in terms of the standardized difference, or z -score, which quantifies how far away the estimate is from the nominal background yield in terms of the number of standard deviations, or sigmas, between the two values. The z -score for a given data point in a normal distribution is calculated with the following formula: $z = (x - \mu)/\sigma$, where x is the data point of interest, μ is the mean of the distribution, and σ is the standard deviation. In the case of the ABCD background estimate, x corresponds to the measured background yield from the ABCD estimate, μ is the nominal background yield from direct observation, and σ is the square root of the quadrature sum of the statistical and systematic uncertainties of the background estimate. The statistical uncertainty is the standard Poisson uncertainty on the nominal prediction, or the square root of the estimated background yield in A, and the systematic uncertainty is calculated from standard error propagation of the statistical

uncertainties of the observed background yields in B, C, and D. In the case where the background estimate is vastly different from the expected yield, the relative uncertainty, defined as the difference between the predicted and observed background yields divided by the background prediction, can be taken as a systematic uncertainty on the overall background estimate.

The initial validation studies for the background estimation method applied to the $N_{\text{DV}} \times H_T^{\text{NJet}}$ ABCD plane for a representative set of selection values are shown in Tables 4.8 and 4.9, where the background estimates are compared to the observed yields in the A' region of the ABCD validation plane for the MC dijet background and a subset of data, respectively. As the actual number of events in A' is irrelevant to the ABCD method and to the overall background yield in the signal region, and only the agreement between prediction and observation are of interest, only the statndardized difference and relative uncertainty of the background estimate in the validation region, and not the actual estimated or observed values, are listed below.

N_{DV} Selection	H_T^{NJet} Selection	Standardized Difference	Relative Uncertainty
≥ 2 (Loose)	> 1200 GeV	-61.98	0.19
≥ 2 (Loose)	> 1375 GeV	-58.51	0.23
≥ 2 (Loose)	> 1500 GeV	-44.66	0.23
≥ 3 (Loose)	> 1200 GeV	-11.06	0.09
≥ 3 (Loose)	> 1375 GeV	-20.44	0.21
≥ 3 (Loose)	> 1500 GeV	-9.65	0.13
≥ 4 (Loose)	> 1200 GeV	-14.51	0.42
≥ 4 (Loose)	> 1375 GeV	-27.45	1.05
≥ 4 (Loose)	> 1500 GeV	-20.43	0.99
≥ 2 (Medium)	> 1200 GeV	-23.59	0.11
≥ 2 (Medium)	> 1375 GeV	-26.10	0.16
≥ 2 (Medium)	> 1500 GeV	-15.42	0.12
≥ 3 (Medium)	> 1200 GeV	11.73	0.18
≥ 3 (Medium)	> 1375 GeV	-5.76	0.12
≥ 3 (Medium)	> 1500 GeV	-6.22	0.17
≥ 4 (Medium)	> 1200 GeV	-30.31	2.97
≥ 4 (Medium)	> 1375 GeV	-5.29	0.51
≥ 4 (Medium)	> 1500 GeV	-12.77	1.64
≥ 2 (Tight)	> 1200 GeV	-6.60	0.09
≥ 2 (Tight)	> 1375 GeV	-0.18	0.00
≥ 2 (Tight)	> 1500 GeV	-11.28	0.27
≥ 3 (Tight)	> 1200 GeV	-6.57	2.23
≥ 3 (Tight)	> 1375 GeV	-14.80	7.24
≥ 3 (Tight)	> 1500 GeV	-0.16	0.07
≥ 4 (Tight)	> 1200 GeV	0.00	0.00
≥ 4 (Tight)	> 1375 GeV	0.00	0.00
≥ 4 (Tight)	> 1500 GeV	0.00	0.00

Table 4.8: The standardized difference and relative uncertainty of the estimated background yield as compared to the nominal observation in Region A' of the validation ABCD plane for a range of N_{DV} and H_T^{NJet} selections in the JZ4W Pythia dijet MC background sample.

N_{DV} Selection	$H_T^{N\text{jet}}$ Selection	Standardized Difference	Relative Uncertainty
≥ 2 (Loose)	> 1200 GeV	-238.92	0.84
≥ 2 (Loose)	> 1375 GeV	-188.58	0.71
≥ 2 (Loose)	> 1500 GeV	-156.79	0.64
≥ 3 (Loose)	> 1200 GeV	-86.77	0.96
≥ 3 (Loose)	> 1375 GeV	-69.64	0.82
≥ 3 (Loose)	> 1500 GeV	-50.28	0.64
≥ 4 (Loose)	> 1200 GeV	-38.52	1.26
≥ 4 (Loose)	> 1375 GeV	-28.30	0.97
≥ 4 (Loose)	> 1500 GeV	-4.73	0.17
≥ 2 (Medium)	> 1200 GeV	-167.15	0.97
≥ 2 (Medium)	> 1375 GeV	-144.38	0.90
≥ 2 (Medium)	> 1500 GeV	-112.70	0.76
≥ 3 (Medium)	> 1200 GeV	-51.62	1.17
≥ 3 (Medium)	> 1375 GeV	-34.80	0.82
≥ 3 (Medium)	> 1500 GeV	-18.44	0.46
≥ 4 (Medium)	> 1200 GeV	-30.19	2.17
≥ 4 (Medium)	> 1375 GeV	-21.72	1.56
≥ 4 (Medium)	> 1500 GeV	-0.15	0.01
≥ 2 (Tight)	> 1200 GeV	-61.74	0.99
≥ 2 (Tight)	> 1375 GeV	-66.93	1.18
≥ 2 (Tight)	> 1500 GeV	-44.64	0.83
≥ 3 (Tight)	> 1200 GeV	0.00	0.00
≥ 3 (Tight)	> 1375 GeV	0.00	0.00
≥ 3 (Tight)	> 1500 GeV	0.00	0.00
≥ 4 (Tight)	> 1200 GeV	0.00	0.00
≥ 4 (Tight)	> 1375 GeV	0.00	0.00
≥ 4 (Tight)	> 1500 GeV	0.00	0.00

Table 4.9: The standardized difference and relative uncertainty of the estimated background yield as compared to the nominal observation in Region A' of the validation ABCD plane for a range of N_{DV} and $H_T^{N\text{jet}}$ selections in a subset of 2017 data.

While the initial validation studies do not provide a realistic measure of exactly how well the ABCD method performs, as they are only applied to a single JZ4W MC background slice and a small subset of data, an obvious trend is observed where the tighter signal selections produce a more accurate prediction for the background yield in the corresponding signal region, as the tighter selections more effectively discriminate between the signal and background and better isolate the background to the control regions. To accurately quantify the validity of the method and apply a corresponding systematic, the validation studies will need to be performed over the full data once the final signal region is determined.

4.4.5 INITIAL BACKGROUND ESTIMATE RESULTS

Initial estimates for the background yields in region A, as defined in the set of potential DV \times NJetX ABCD planes and the range of corresponding selection values, have been performed with the JZ4W PYTHIA dijet MC background slice. These estimates are not expected to be wholly accurate, but rather to provide a rough approximation of the size of the background in the various potential signal regions in order to aid in optimizing the signal region cuts to be used in the final analysis. The initial estimated and observed background yields in a representative set of signal regions defined by a range of N_{DV} and H_T^{NJet} selections are listed in Table [4.10](#) below.

N_{DV}	H_T^{Njet}	Predicted Events	Observed Events
Selection	Selection	$\pm \text{stat.} \pm \text{syst.}$	$\pm \text{stat.}$
≥ 2 (Loose)	> 1200 GeV	$22239.61 \pm 149.13 \pm 160.57$	22629.08 ± 150.43
≥ 2 (Loose)	> 1375 GeV	$9943.33 \pm 99.72 \pm 58.27$	10323.77 ± 101.61
≥ 2 (Loose)	> 1500 GeV	$4917.48 \pm 70.12 \pm 28.19$	5264.61 ± 72.56
≥ 3 (Loose)	> 1200 GeV	$4029.20 \pm 63.48 \pm 67.00$	3175.12 ± 56.35
≥ 3 (Loose)	> 1375 GeV	$1690.07 \pm 41.11 \pm 22.99$	1315.21 ± 36.27
≥ 3 (Loose)	> 1500 GeV	$812.86 \pm 28.51 \pm 10.53$	636.93 ± 25.24
≥ 4 (Loose)	> 1200 GeV	$1310.68 \pm 36.20 \pm 38.10$	330.12 ± 18.17
≥ 4 (Loose)	> 1375 GeV	$416.20 \pm 20.40 \pm 11.32$	159.90 ± 12.65
≥ 4 (Loose)	> 1500 GeV	$178.14 \pm 13.35 \pm 4.86$	159.90 ± 12.65
≥ 2 (Medium)	> 1200 GeV	$8502.14 \pm 92.21 \pm 97.65$	10698.07 ± 103.43
≥ 2 (Medium)	> 1375 GeV	$4246.50 \pm 65.17 \pm 36.92$	4558.70 ± 67.52
≥ 2 (Medium)	> 1500 GeV	$2145.85 \pm 46.32 \pm 17.60$	2082.39 ± 45.63
≥ 3 (Medium)	> 1200 GeV	$1377.83 \pm 37.12 \pm 39.06$	781.96 ± 28.00
≥ 3 (Medium)	> 1375 GeV	$518.95 \pm 22.78 \pm 12.65$	337.75 ± 18.38
≥ 3 (Medium)	> 1500 GeV	$240.73 \pm 15.52 \pm 5.65$	196.52 ± 14.02
≥ 4 (Medium)	> 1200 GeV	$884.38 \pm 0.00 \pm 0.00$	0.00 ± 0.00
≥ 4 (Medium)	> 1375 GeV	$245.63 \pm 0.00 \pm 0.00$	0.00 ± 0.00
≥ 4 (Medium)	> 1500 GeV	$105.18 \pm 0.00 \pm 0.00$	0.00 ± 0.00
≥ 2 (Tight)	> 1200 GeV	$1200.92 \pm 34.65 \pm 36.45$	904.94 ± 30.08
≥ 2 (Tight)	> 1375 GeV	$416.73 \pm 20.41 \pm 11.32$	632.77 ± 25.15
≥ 2 (Tight)	> 1500 GeV	$236.19 \pm 15.37 \pm 5.60$	194.15 ± 13.94
≥ 3 (Tight)	> 1200 GeV	$0.00 \pm 0.00 \pm 0.00$	14.63 ± 3.82
≥ 3 (Tight)	> 1375 GeV	$0.00 \pm 0.00 \pm 0.00$	14.63 ± 3.82
≥ 3 (Tight)	> 1500 GeV	$0.00 \pm 0.00 \pm 0.00$	14.63 ± 3.82
≥ 4 (Tight)	> 1200 GeV	$0.00 \pm 0.00 \pm 0.00$	0.00 ± 0.00
≥ 4 (Tight)	> 1375 GeV	$0.00 \pm 0.00 \pm 0.00$	0.00 ± 0.00
≥ 4 (Tight)	> 1500 GeV	$0.00 \pm 0.00 \pm 0.00$	0.00 ± 0.00

Table 4.10: The number of predicted and observed background events in Region A of the ABCD plane for a range of N_{DV} and H_T^{Njet} selections, as calculated from initial estimates using the JZ4W Pythia dijet MC background sample.

As expected, the background contribution to the signal region decreases as the selections are tightened, with the implementation of the `Tight DV` working point yielding very few to zero background events. Naturally, the tightened selections also decrease the overall signal efficiency, so the signal significance will also need to be considered in conjunction with the estimated background yield before finalizing the signal region. Moreover, the estimates below are not known to be accurate representations of the expected backgrounds, so the shifted VR ABCD method should also be applied to the full data in the validation region as a secondary rough estimate before determining the final analysis cuts. Once the analysis is completely designed with a finalized signal region, the actual background estimates will need to be performed and validated with the full ATLAS dataset.

5

Conclusion

This thesis has described the basis of the ongoing Emerging Jets search for evidence of new physics producing a signal with four high- p_T jets and multiple leading-jet-associated displaced vertices at ATLAS Run 2 using 139 fb^{-1} of pp collision data at a center-of-mass energy of $\sqrt{13}$ TeV during data-taking years 2015 through 2018.

The overall design of the analysis has been developed and implemented in order to target

signal-like events and discriminate them from SM QCD multijet backgrounds. A dedicated Emerging DRAW_RPVLL filter and a corresponding DAOD_EXOT23 derivation have been developed and applied to the full Run 2 ATLAS dataset in order to process events of interest to the analysis. A custom analysis code framework (`EmergingJetsAnalysis`) was built with which to perform studies and produce ntuples, histograms, and plots specific to the Emerging Jets search, but in a configurable manner for use by other RPVLL analyses. The full signal grid for the Monte Carlo signal samples has been designed, and 36 of the 90 points have thus far been produced for initial use within the analysis. Extensive truth and PYTHIA validation studies were performed during the early stages of the development of the analysis, in order to optimally design the signal grid to cover the full parameter space over which the analysis is expected to have some degree of sensitivity.

The event selections have been carefully designed and investigated, with extensive studies performed over the secondary vertices and leading jets in the event, in order to aid in the development of the potential signal object working point selections and the respective final signal regions, a set of which have been proposed but are still to be optimized. Additionally, the displaced vertex reconstruction efficiency has been studied in detail. An initial background estimation method has been developed and validated, but true estimates can only be made, and the method can only be fully validated, using the entire dataset once the eventual signal region is finalized, at which point the use of a related likelihood-fit ABCD

method will be investigated.

As the final selection for this search has not yet been prepared, and the full signal grid is not yet available, the expected signal yields and efficiencies and the estimated background have not yet been able to be determined, and therefore the estimated reach of the analysis can not yet be calculated. From initial studies, however, it is evident the signal will be small, particularly for the low-mediator-mass, extreme-lifetime, and low-mass-model signal points, and the background will be large, unless stringent cuts are placed on the signal region, which will reduce the overall signal yield even further. As such, the final signal region will need to be carefully optimized to maximally reduce the background contribution while maintaining as much signal efficiency as possible. Much of the design of the analysis has been to define a set of cuts to maximize the discrimination between signal and background objects and events, but the optimal signal region from the set of proposed selections currently in place need still be determined.

The underlying foundation of the Emerging Jets search has been established, but a few remaining steps are necessary before the analysis is complete. The trigger study is still to be performed, as the turn-on curves and efficiencies of the four-jet triggers used to select signal events must be investigated, and any observed inefficiency will need to be accounted for, either by raising the threshold on the jet- p_T signal selection, or by adding a corresponding systematic uncertainty to the final analysis result. Ultimately, the signal selections are still

to be optimized, including the DV and EJ object definitions, and the final signal region still to be determined, as discussed above. This involves implementing the shifted VR ABCD method to validate the initial rough background estimate predicted with the JZ4W MC di-jet slice in each of the potential signal regions. Once the signal selections have been finalized, the last pieces of the analysis can be performed: the expected signal yields and efficiencies in the final signal region need to be calculated for each signal point in the signal grid; the background yield in the final SR needs to be estimated, and the background estimation method needs to be validated in the dedicated validation plane, both of which are to be performed with full data in the finalized ABCD plane and SR; the systematic uncertainties associated with the expected signal and background yields need to be calculated; and statistical tests on the final results need to be performed.

As this is the first iteration of the Emerging Jets search, a large amount of time was spent designing the analysis from scratch in order to eventually yield results for the first dedicated search of its kind performed at ATLAS for the novel signature at hand. Future iterations in Run 3 can then use this analysis as a benchmark to improve the signal efficiencies, background estimates, and resulting limits on the EJs signal model. The definitions of the DV and EJ object selection working points and the corresponding overall potential signal regions could be improved in the future, as the current selections are designed primarily by eye, by comparing the signal and background distributions and placing cuts where the dis-

crimination appears visually to be the best. This method could be improved to optimize the sensitivity of the search, i.e. with multivariate machine learning techniques. Additionally, track trimming could be applied to the displaced vertices, which could potentially improve the discrimination between signal and fake DVs by removing bad tracks, thus changing the overall DV kinematics and possibly rendering some of the tighter DV cuts, like the minimum track $|d_0|$, unnecessary, which could increase the signal efficiency without adding to the overall background yield. The DV matching to jets could also be improved, either by tightening the ΔR threshold or by implementing an alternative matching method altogether, i.e. based on the opening angle between the PV-DV pointing vector and the jet axis. The EJ cuts in particular could be improved to better target emerging-like signal jets, and ongoing studies are already underway to investigate further or alternative discriminating variables, though additional targeted EJ selections would ultimately decrease the overall model independence of the search.

Appendices

A

RDOAnalysis Digitization Validation Package

The `RDOAnalysis` package is a digitization validation tool, based on the `HitAnalysis` simulation validation package. Designed to test and validate the output of digitization jobs, `RDOAnalysis` is used to validate standard digitization against code changes, as well as to

validate fast digitization against standard digitization. The package consists of the following individual tools for each sub-detector where digitization signals are found:

- `BCM_RDOAnalysis` for the Beam Conditions Monitor;
- `PixelRDOAnalysis`, `SCT_RDOAnalysis`, and `TRT_RDOAnalysis` for the Pixel, SCT, and TRT of the Inner Detector;
- `TileRDOAnalysis` and `LArRDOAnalysis` for the tile and liquid argon calorimeters;
- `MDT_RDOAnalysis`, `CSC_RDOAnalysis`, `RPC_RDOAnalysis`, and `TGC_RDOAnalysis` for the MDT, CSC, RPC, and TGC of the muon spectrometer.

Each tool in the package reads an input Raw Data Object (RDO), or digitization output file, which contains detector and read-out response information in RDO containers and simulation information associated with the digitization in SDO containers for all of the above sub-detectors. Each tool then creates, fills, and outputs an ntuple containing the relevant information found in the corresponding sub-detector containers, as well as basic histograms of variables of interest, such as the offline identifier of the readout channel and region within the relevant sub-detector where the signal is found. The package also contains the following tools specific to testing fast-digitization in the inner detector:

- `PixelFastRDOAnalysis` ;
- `SCT_FastRDOAnalysis` ;
- `TRT_FastRDOAnalysis` .

These “fast” tools take Prep Raw Data (PRD), or fast-digitization output, files as input, rather than RDOs. Python job options are used to run the jobs, with one job options file per tool, as well as an inclusive file, `RDOAnalysis_topOptions`, that runs all tools in a single job. The `RDOAnalysis` code can be found on gitlab [136].

The beam conditions monitor and inner detector tools, `BCM_RDOAnalysis` , `Pixel-RDOAnalysis` , `SCT_RDOAnalysis` , and `TRT_RDOAnalysis` , test the digitization output found in the BCM, Pixel, SCT, and TRT sub-detectors, respectively. The RDOs contain two main container types corresponding to these detector components: `InDetRawDataContainer`, holding the RDO information, and `InDetSimDataCollection`, holding the SDO information. The RDO variables common to the BCM and all ID components are the offline identifier for the readout channel where the signal occurs, or the `rdoID`, and the raw data word associated with signal. The common SDO variables are the `sdoID` and `word`, the barcode and event index of the `HepMCParticleLink` of the associated truth particle that deposited the signal, and the charge, or the energy deposited by the charged particle. In the case of the inner detector tools, helper classes are also available to decode the identifiers associated with the data objects in order to identify the sub-detector regions where the signals are found. The `Pixel_ID`, `SCT_ID`, and `TRT_ID` helpers are used to decode the RDOs, and the `Pixel_SimHelper`, `SCT_SimHelper`, and `TRT_SimHelper` are used to decode the SDOs.

The main variables associated with the BCM digitization algorithm are `pulse1Pos`, `pulse1Width`, `pulse2Pos`, `pulse2Width`, representing the positions and widths of the first two digital pulses on each channel, and `channel`, representing the identifier of the channel itself, as seen in Figure [A.1](#).

In the Pixel, the important digitization variables are the time over threshold, or `ToT`, of the signal and the regions of the pixel detector, including the specific layer or disk (`layerDisk`), ϕ and η modules (`phiModule` and `etaModule`), and ϕ and η module indices (`phiIndex` and `etaIndex`) of the pixel barrel or end-cap (`barrelEndcap`) where the signal occurs. Example histograms output from the `PixelRDOAnalysis` tool are shown in Figure [A.2](#).

The main variables associated with SCT digitization are the size of the group of consecutive strips where the signal is measured (`groupSize`), measured from RDO information, and the strip number where the hit occurs (`strip`), pulled from SDO information, as well as the regions of the SCT, like the specific layer or wheel (`layerWheel`), ϕ and η modules (`phiModule` and `etaModule`), side (`side`), and strip (`strip`) in the SCT barrel or end-cap (`barrelEndcap`) where the signal is found. Some of these variables are displayed in the histograms shown in Figure [A.3](#).

The variables of interest in the TRT digitization algorithm are the time over (high-level) threshold (`ToT` and `ToT_HL`), the drift time bin (`driftTimeBin`), and the position of

the trailing edge (`TrailEdge`) of the digital signal, as well as the specific φ module (`phiModule`), layer or wheel (`layerWheel`), straw layer (`strawLayer`), and straw (`straw`) of the TRT barrel or end-cap (`barrelEndcap`) where the signal is found. The ToT ranges from 0 to 75 ns, corresponding to three 25-ns bunch crossings, and is recorded in 3.125-ns intervals, or eight time bins per bunch crossing. A value of $\text{ToT} = 0$ ns represents an invalid digit, and a value of $\text{ToT} = 76$ ns represents a digit with no trailing edge, where the signal never drops back below threshold. The drift time bin represents the position, in terms of the 25 signal time-bins, of the leading edge, where the first low threshold transition occurs. The trailing edge represents the last transition back below low threshold. Example `TRT_RDOAnalysis` tool output histograms of the ToT, high-level ToT, drift time bin, and trailing edge variables are shown in Figure [A.4](#).

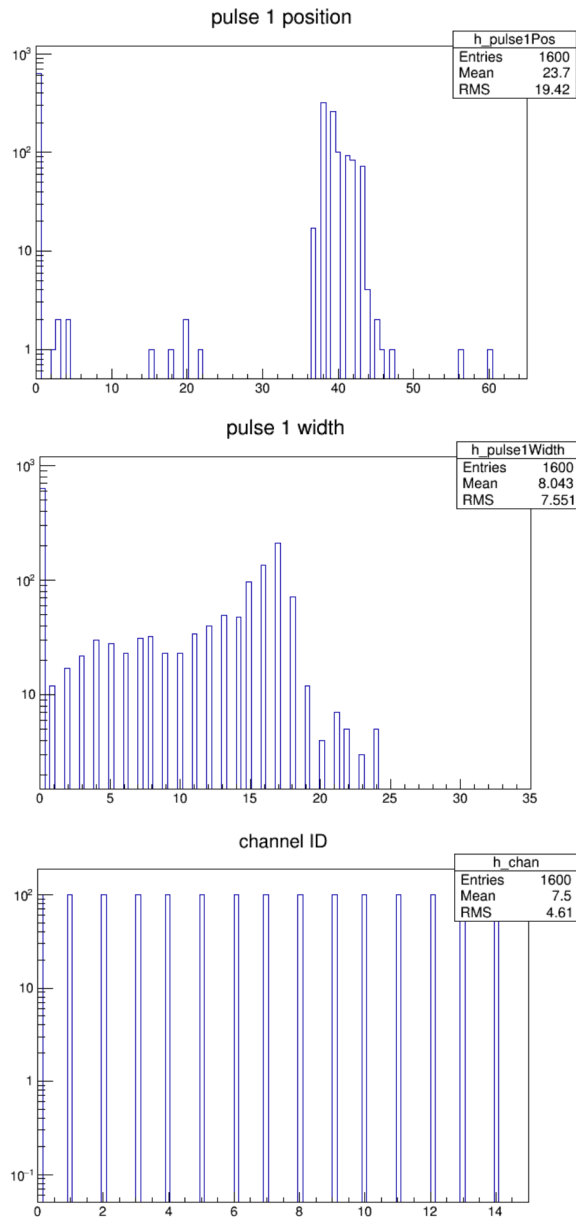


Figure A.1: Example histogram output from the `BCM_RDOAnalysis` tool, displaying the position (top) and width (middle) of pulse-one and the channel (bottom) where the digital pulses are measured.

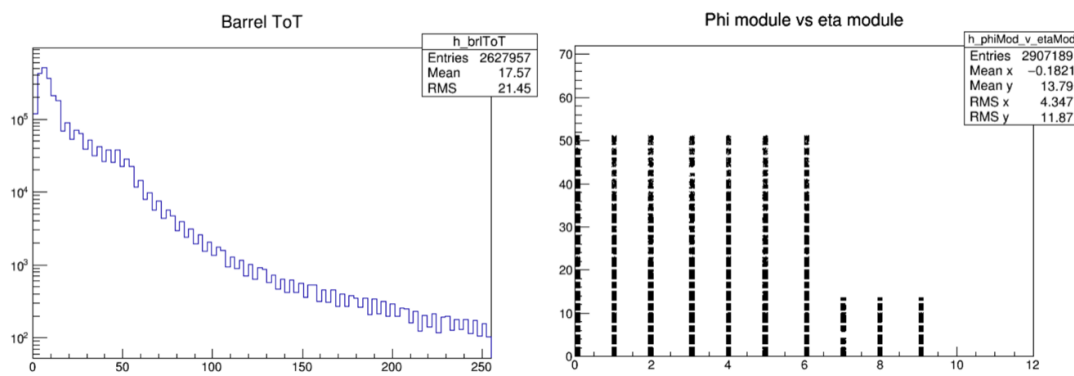


Figure A.2: Example histogram output from the `PixelRDOAnalysis` tool, showing the time over threshold in the barrel (left) and the $\phi - \eta$ modules where the signal is measured (right).

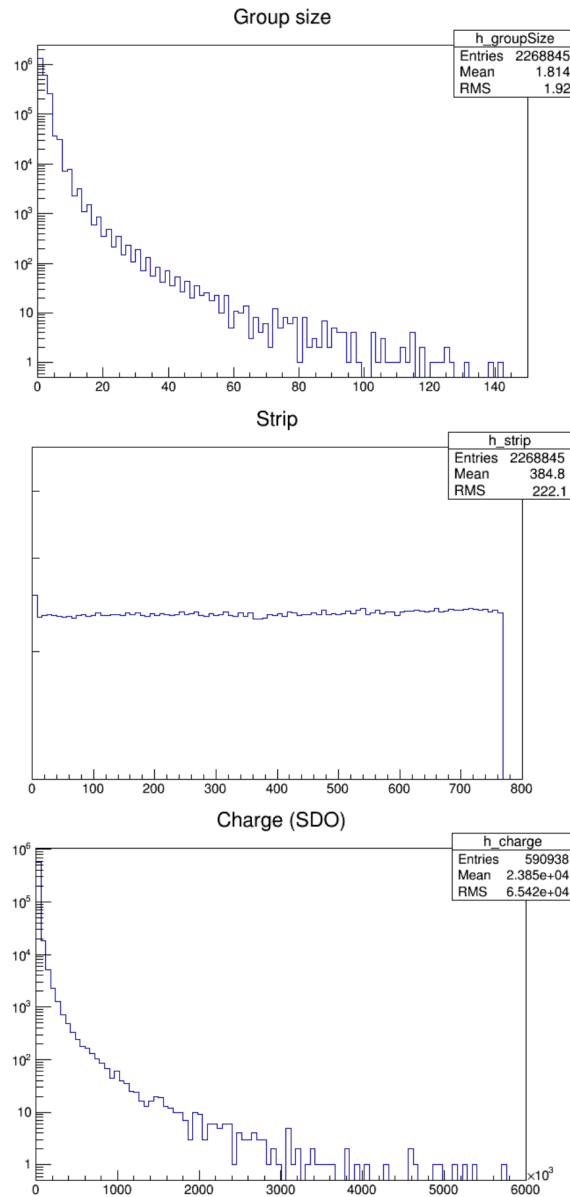


Figure A.3: Example histogram output from the `SCT_RDOAnalysis` tool, including the group-strip size (top) and individual strip (middle) where the signal is measured, and the charge (bottom) deposited by the hit.

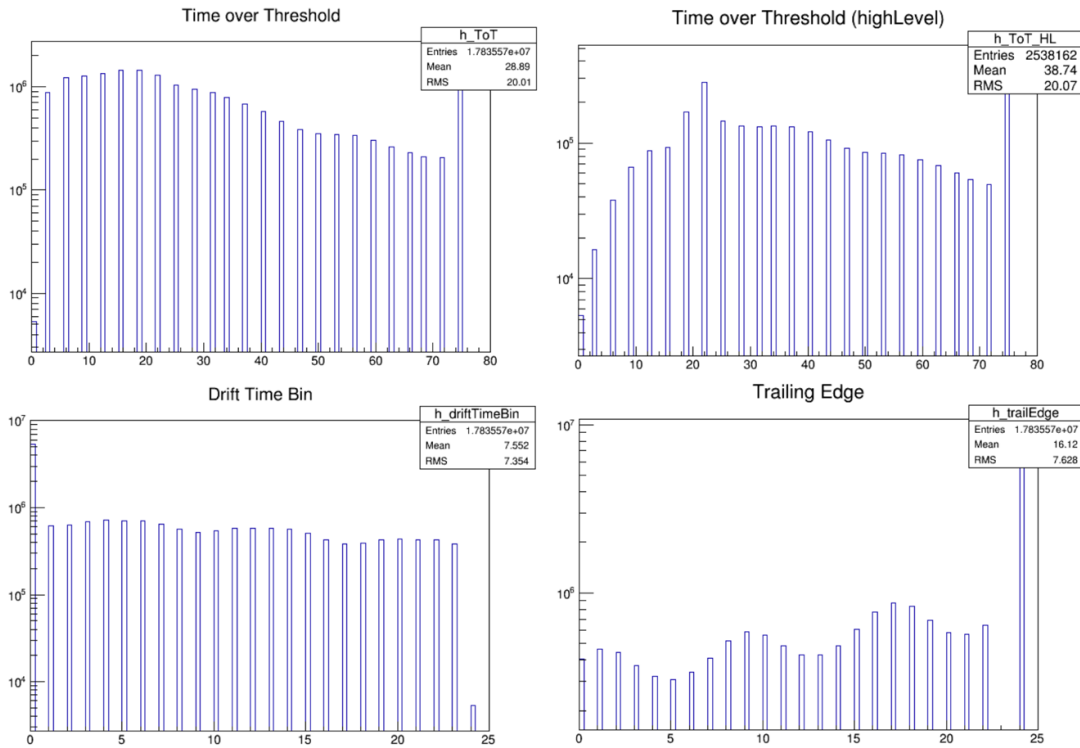


Figure A.4: Example histogram output from the `TRT_RDOAnalysis` tool, showing the time over threshold (top left), time over high-level threshold (top right), drift time bin (bottom left), and trailing edge (bottom right) of the digitized signal.

The calorimeter tools, `TileRDOAnalysis` and `LArRDOAnalysis`, test the digitization output found in the tile and liquid argon calorimeters, respectively. The raw information related to the tile and LAr calorimeters, including identifiers, raw qualities, and digital amplitudes from the Read Out Drivers (RODs), is held in the `TileRawChannel`, `TileDigits`, `LarRawChannel`, and `LarDigits` RDO containers, and the trigger information related to the tile and LAr calorimeters, including the information from the L1 trigger towers, is held in the `TileTTL1`, `TileMuonReceiver`, `TileL2`, and `LarTTL1` RDO containers.

The main variables processed by the tile calorimeter digitization algorithm are the amplitude, or pulse height (`rawAmp`), time (`rawTime`), and quality (`rawQual`) of the raw signal, the actual digits transmitted to the RODs (`digits`), the energy estimated in the muon receiver (`muRcv_energy`), as well as the decision (`muRcv_dec`) and threshold (`muRcv_thresh`) of the muon receiver, and the L1 calorimeter cells (`ttl1_digits` and `ttl1_ID`) used to form trigger towers, some of which are shown in Figure A.5.

The LAr calorimeter digitization tool processes the raw signal information, such as the raw energy (`energy`), time (`time`), quality (`qual`), and gain (`gain`), as well as the online and offline identifiers and sample values of the L1 hadronic and electromagnetic calorimeter cells (`hadOnID`, `hadOffID`, `hadSamples`, `emOnID`, `emOffID`, and `emSamples`) associated with the digitized signal. Some of these main variables are displayed in Figure A.6.

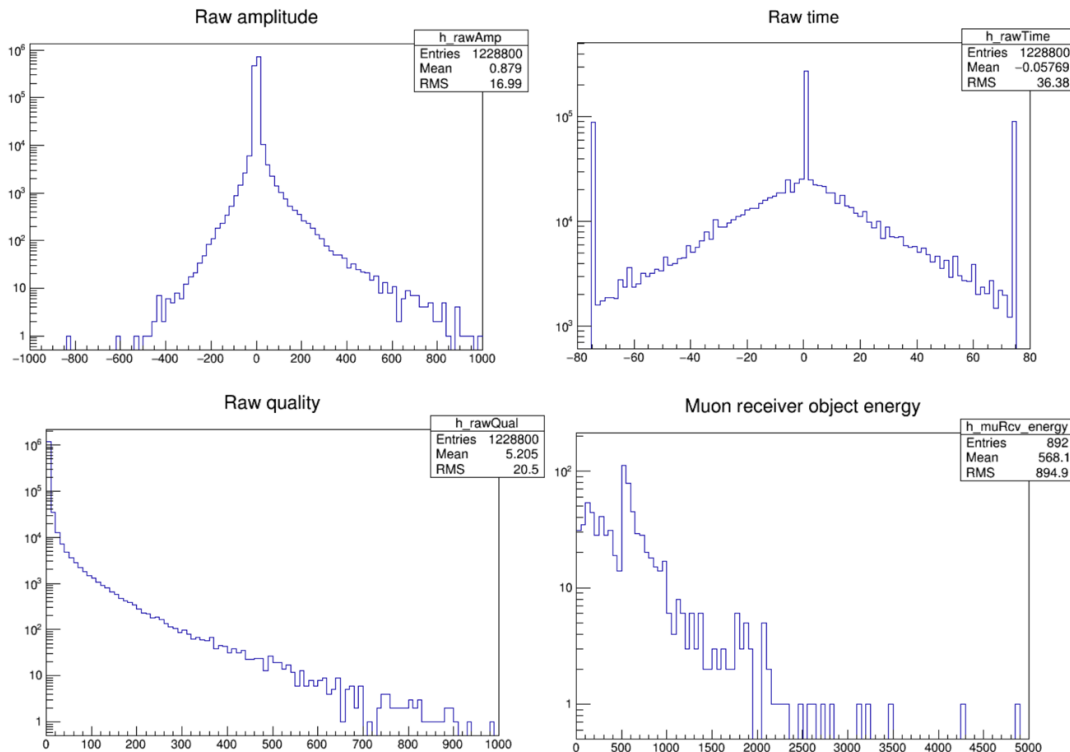


Figure A.5: Example histogram output from the `TileRDOAnalysis` tool, including the raw signal amplitude (top left), time (top right), and quality (bottom left), as well as the muon receiver energy (bottom right).

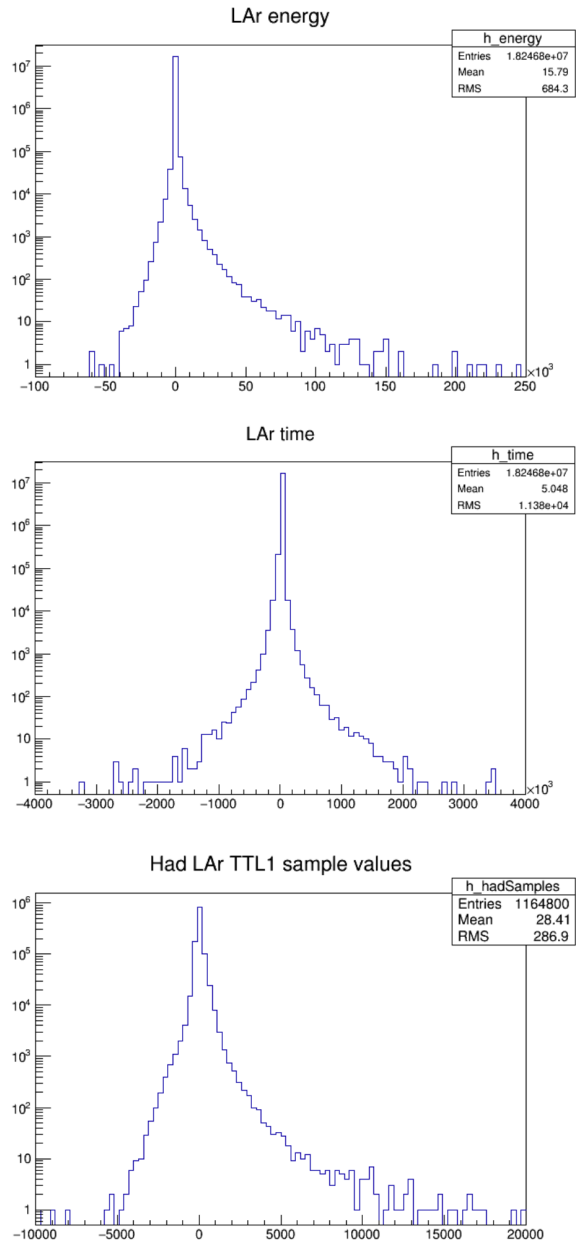


Figure A.6: Example histogram output from the `LArRDOAnalysis` tool, showing the raw signal energy (top) and time (middle), as well as the hadronic TTL1 sample values (bottom).

The muon spectrometer tools, `MDT_RDOAnalysis` , `CSC_RDOAnalysis` , `RPC_-RDOAnalysis` , and `TGC_RDOAnalysis` , test the digitization output found in the MDT, CSC, RPC, and TGC muon detectors, respectively. Each muon detector has a corresponding container type holding the relevant RDO information: `MdtCsmContainer`, holding the AMT (ATLAS Muon Time-to-Digital Converter) hits in a single MDT chamber; `CscRawDataContainer`, holding the CSC raw data; `RpcPadContainer`, holding the RPC readout pads, the coincidence matrices, and the channels where the triggers fired; and `TgcRdoContainer`, holding the TGC hit and coincidence raw information. The `MuonSimDataCollection` contains SDO information, including global position, radius, local z-position, and charge for the MDT, RPC, and TGC muon detectors, and `CscSimDataCollection` contains SDO information, including y-position, z-position, energy, and charge for the CSC muon detector.

The raw information variables of interest produced by the digitization algorithm for the monitored drift tube (MDT) chambers of the muon spectrometer are the identifiers for the specific MDT chamber (`mdtID`) and individual electronics piece where the signal occurs, as well as the coarse and fine drift time (`coarse` and `fine`) and the width (`width`) of the signal pulse. The MDT digitization algorithm also produces truth information associated with the digital signal, including the three-dimensional global position (`xPos`, `yPos`, and `zPos`), the radius (`radius`), and the local z-position (`localZ`) of the simulated hit. Exam-

ple histograms for some of these raw and truth variables are shown in Figure A.7.

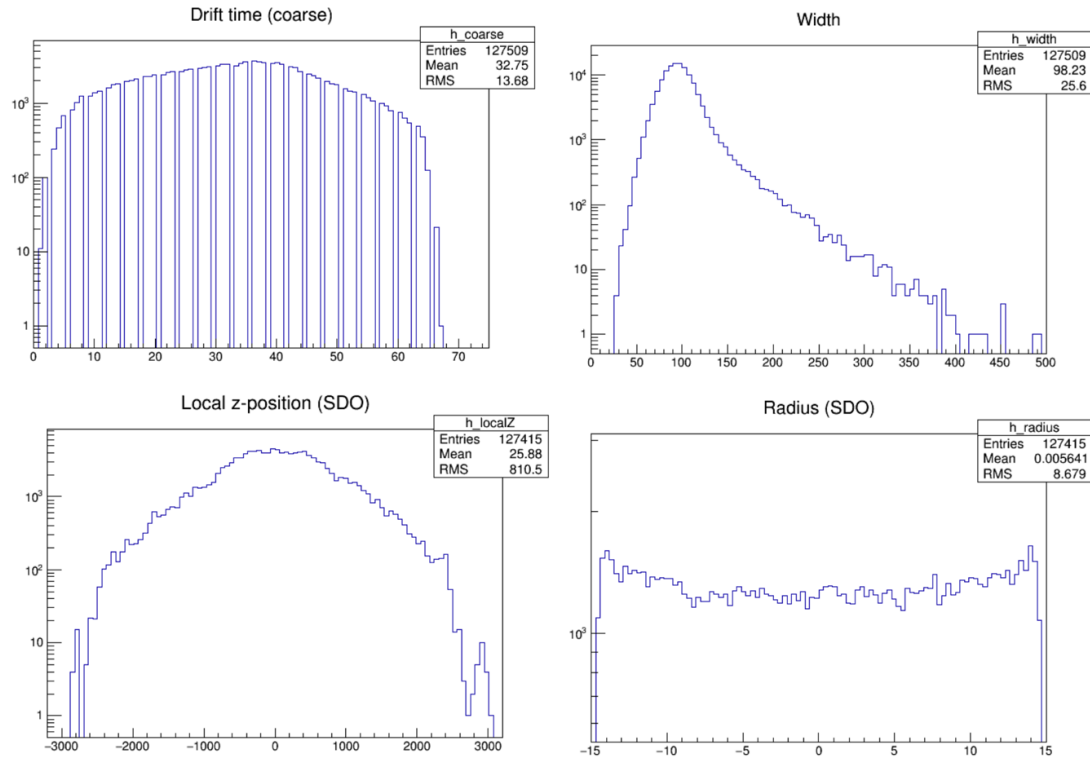


Figure A.7: Example histogram output from the MDT_RDOAnalysis tool, including the raw signal coarse drift time (top left) and pulse width (top right), as well as the local z-position (bottom left) and radius (bottom right) of the truth hit.

The cathode strip chambers (CSC) digitization output includes ADC time samplings (`cscSmp1`) used to describe the induced charge on a strip, the width of the strip cluster (`cscWidth`) and the time of the first strip in the cluster (`cscTime`), as well as identifiers for the first strip (`cscAdd`), the strip collection (`cscID`), and the specific individual electronics piece where the signal is found. Additionally, truth information is produced detailing the

energy (`energy`) and position (`ypos` and `zpos`) of the truth hit. Example outputs of the ADC samples and strip cluster widths are displayed in Figure [A.8](#).

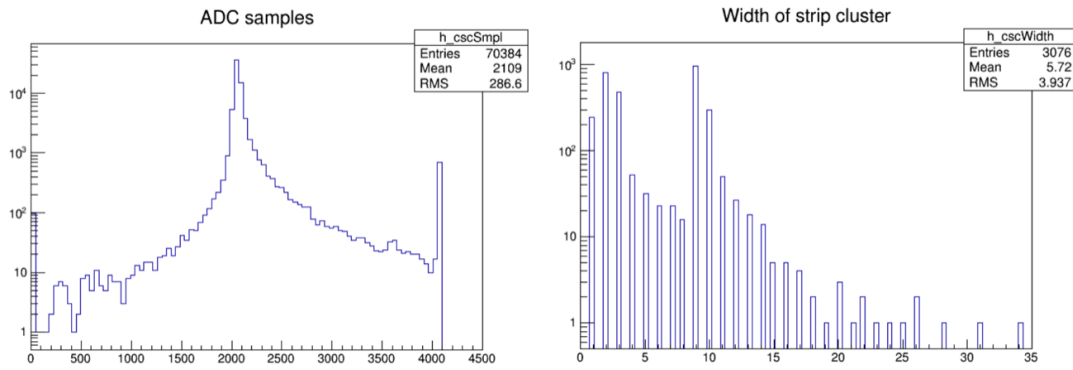


Figure A.8: Example histogram output from the `CSC_RDOAnalysis` tool, displaying the ADC samples (left) and strip collection width (right).

The RDO output for the resistive plate chambers (RPC) includes information about the fired channel in the coincidence matrix, including the channel number and time at which the channel is fired (`firedChan` and `firedTime`), as seen in Figure [A.9](#), about the coincidence matrix where the channel is fired, and about the RPC pad where the coincidence matrix resides, including the pad sector and identifier (`sector` and `rpcID`). Truth information is also produced, including the global position (`xPos`, `yPos`, and `zPos`), radius (`radius`), and local z-position (`localZ`) of the simulated hit. The thin gap chambers (TGC) digitization output consists mainly of identifiers for the various boards and electronics, along with the same truth information as for the RPC output.

The fast tools, `PixelFastRDOAnalysis`, `SCT_FastRDOAnalysis`, and `TRT_Fast-`

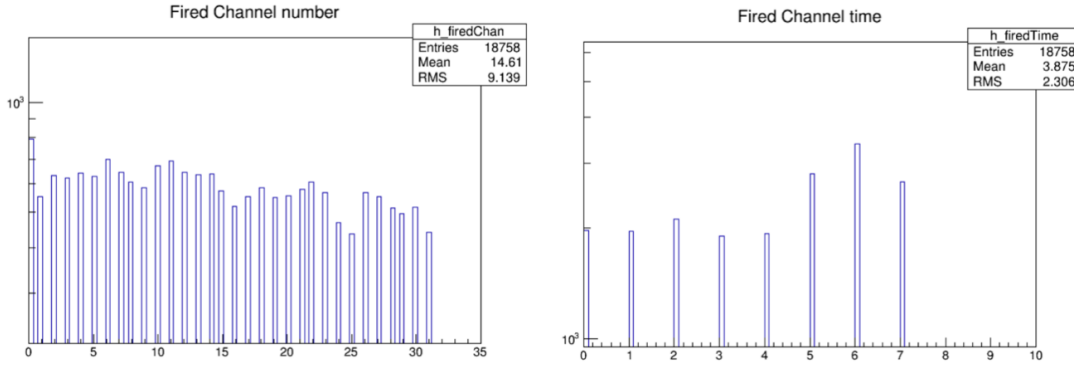


Figure A.9: Example histogram output from the `RPC_RDOAnalysis` tool, with the number (left) and time (right) of the fired channel.

`RDOAnalysis`, test the digitization output from the fast algorithms run in the Pixel, SCT, and TRT inner detector components, respectively. They read PRD information from the `InDetPrepRawData` container, which holds cluster information, including position and estimated charge, along with the detector element where the cluster is found, for the silicon Pixel and SCT detectors and holds drift circle information, including position and estimated raw drift time, along with the detector element where the drift circle is found, for the TRT.

The development of the `RDOAnalysis` package, along with an update of the `HitAnalysis` package for R21, was performed over the course of a year as an ATLAS authorship qualification task by the author.

B

DRAW_RPVLL Monitoring

Long-lived particle searches are hindered by significantly reduced reconstruction efficiencies at ATLAS due to the insensitivity of standard reconstruction algorithms to very displaced tracks and vertices. Several analyses within the R-Parity Violating and Long-Lived (RPVLL) SUSY and Unconventional signatures and Exotics Higgs (UEH) Exotics groups target LLP signatures that require specialized reconstruction methods to be run over RAW

hit information. A special reprocessing of the data from `RAW` to `AOD` format in specialized streams is performed once per major Tier-0 processing release, with reconstruction of the dedicated `DRAW_RPVLL` stream to `DAOD_RPVLL` output performed with the large-radius tracking and secondary vertexing algorithms designed for LLP searches.

The `DRAW_RPVLL` stream is a `RAW` data stream containing a subset of events filtered from the primary physics stream, `physics_Main`, by a set of individual analysis-specific filters. The stream stores full events in `RAW` format to be used for later reprocessing with nonstandard reconstruction by RPVLL physics analyses. Reconstruction is then run on the `DRAW_RPVLL` stream at a later time with large- d_0 tracking and secondary vertexing and output to the `DAOD_RPVLL` stream, where the `DAOD_RPVLL` format is not a derivation, as the name implies, but a modified `AOD`. MS hits are also saved in the `DAOD_RPVLL` events. An additional small `DESDM_EXOTHIP` format that stores ESDs instead of `RAW` hits is produced and stored during the `DRAW_RPVLL` filtering step for the highly ionized particle (HIP) search. This particular filter is not strictly a `DRAW_RPVLL` filter and is not discussed in detail any further.

The `DRAW_RPVLL` filtering code is contained in the `LongLivedParticleDPDMaker` package [137]. The filter skimming is based primarily on trigger selections, with additional offline requirements on the kinematics of standard physics objects used to regulate the event filter rate, or the rate of saving events to the stream, as needed. Each analysis uses its

own set of filters defining loose selection criteria tuned to optimally target signal-like events containing the associated final states while keeping the overall rate relatively low, that is, under some specified target rate limit as per the data preparation coordinators (DPC).

Initial DPC recommendations were to keep the overall rate of the `DRAW_RPVLL` stream below about 30 Hz on average. This limit, however, was consistently exceeded throughout Run 2, primarily due to the high luminosities and pileup rates, both of which the filter rates are dependent on, since they are primarily trigger-based. In reality, the hard limit under which the overall average rate was attempted to be maintained was closer to 50 to 100 Hz. The rates for each individual filter and for the overall stream are monitored throughout the LHC Run by the `DRAW_RPVLL` managers. The filter rate, also sometimes referred to as the average filter rate, is defined as

$$\text{filter rate} = \frac{\text{number of events selected by filter}}{\text{number of events in physics_Main}} \times \text{physics_Main average rate. (B.1)}$$

The rates are compiled by parsing the log files produced at Tier-0, which are only available in the few weeks following the run, so the filters must be monitored continuously, every week or, throughout the course of data-taking. From 2017 to 2020, this oversight was performed by the author, who acted as the stream manager during this time. The role of the stream manager includes the following tasks:

- monitoring the individual and overall filter rates during the LHC Run by tracking

the rate of the `DRAW_RPVLL` events recorded in each run, both per filter and globally, and watching for significant rate changes;

- analyzing the rate-breakdown of individual filters, informing the corresponding analyses of any spikes in individual rates, and aiding in making any necessary changes to reduce rates;
- acting as contact and coordinator for analyses using the `DRAW_RPVLL` stream and for those adding or updating filters; this includes aiding in developing filters and testing rates, advising on reducing large rates, and informing analyses of changes affecting filters, as needed;
- maintaining the filter package, including the rate compilation scripts.

B.i DRAW_RPVLL FILTER STREAM

The individual filters contained in the `LongLivedParticleDPDMaker` filtering package used to build the `DRAW_RPVLL` stream and the associated analyses and working groups to which they belong are summarized in Table B.i. The individual filters in their current state, as of 2018 data-taking and the latest Run 2 reprocessing, are overviewed in more detail below.

B.i.i RPPVLL SUSY FILTERS

The RPVLL SUSY analyses using the `DRAW_RPVLL` stream are the dilepton displaced vertices analysis, using the `DiLep` filters, the multi-track displaced vertices analysis, using the

Working Group	Analysis	Filter	
SUSY	Dilepton Displaced Vertices	DiLep_SiElectron DiLep_SiPhotonX DiLep_SiMuon DiLep_SiMuonBa DiLep_DiElectron DiLep_DiPhoton DiLep_DiElPh DiLep_DiLoElPh	
		DVMuon	
		DV_Photon	
		DV_PhotonPlusTLJet	
		DV_MultiJet	
		DV_MET	
		KinkedTrackJet KinkedTrackMultiJet KinkedTrackStublet KinkedTrackZee KinkedTrackZmumu	
	Heavy Neutral Lepton	Hn1	
	Disappearing Tracks	HV_Muvtx HV_CalRatio	
Exotics		Emerging	
		Highly Ionized Particles	
Heavily Ionized Particles	DESDM_EXOTHIP		

Table B.1: The `DRAW_RPVLL` filters contained in the `LongLivedParticleDDPMaker` filtering code package, listed by the analyses that use them and the working groups to which those analyses belong.

DV filters, and the disappearing tracks analysis, using the `KinkedTrack` filters. The filters belonging to each of these analysis teams are summarized below.

B.I.I.I DILEPTON DISPLACED VERTICES (DiLep) FILTERS

The dilepton displaced vertices analysis involves a search for a massive LLP decaying to a dilepton pair, with either a $\mu\mu$, ee , or $e\mu$ final state, in the context of an R-parity violating

Minimal Supersymmetric Standard Model (RPV MSSM) [138]. This analysis requires large- d_{o} tracking to reconstruct displaced vertices in the inner detector with at least two lepton tracks. A set of multiple `DiLep` filters are defined to target events containing displaced dileptons by selecting events with a single electron, single photon, single muon, dielectron, or diphoton in the final state, indicative of the final-state dilepton channels. The filter criteria includes a single photon, diphoton, or MS-only single muon trigger, plus additional offline cuts on the candidate objects.

Events are required to pass one of the following HLTs to be included in the `DiLep` filter selections:

- single photon triggers = one photon above p_{T} threshold:
 - `HLT_g140_loose`;
 - `HLT_g200_loose`;
 - `HLT_g200_loose_L1EM24VHIM`;
- diphoton triggers = two photons above p_{T} threshold:
 - `HLT_2g50_loose`;
 - `HLT_2g50_loose_L12EM20VH`;
 - `HLT_2g60_loose_L12EM20VH`;
- single muon trigger = one muon above p_{T} threshold using MS information only:
 - `HLT_mu80_msonly_3layersEC`;

- single muon barrel trigger = one muon above p_T threshold within $0 < |\eta| < 1.05$ using MS information only:
 - `HLT_mu60_0eta105_msonly.`

The photon triggers are used for both the photon and electron filters, since electron triggers suffer from lower efficiencies for largely displaced electrons due to the requirements on the associated ID tracks. The muon filters use MS-only muon triggers to avoid a dependence on ID tracks and thus increase sensitivity to displaced muons.

The individual `DiLep` filters and their full selection criteria are listed below:

- `DiLep_SiElectron` events are required to pass a single photon trigger and contain a single high- p_T electron with $p_T > 160 \text{ GeV}$, $|\eta| < 2.5$, and $|d_o| > 2.0 \text{ mm}$.
- `DiLep_SiPhotonX` events are required to pass a single photon trigger and contain a single loose high- p_T photon with $p_T > 160 \text{ GeV}$ and $|\eta| < 2.5$ in conjunction with another low- p_T candidate object, where the additional candidate is either another loose photon with $p_T > 10 \text{ GeV}$ and $|\eta| < 2.5$, or an electron or muon with $p_T > 10 \text{ GeV}$, $|\eta| < 2.5$, and $|d_o| > 2.0 \text{ mm}$. The additional low- p_T candidate object is required to limit the filter rate.
- `DiLep_SiMuon` events are required to pass a single full MS-only muon trigger and contain a single muon with $p_T > 80 \text{ GeV}$, $|\eta| < 2.5$, and $|d_o| > 2.0 \text{ mm}$.
- `DiLep_SiMuonBa` events are required to pass a single barrel-only MS-only muon trigger and contain a single muon with $p_T > 60 \text{ GeV}$, $|\eta| < 1.07$, and $|d_o| > 2.0 \text{ mm}$.
- `DiLep_DiElectron` events are required to pass a diphoton trigger and contain two electrons with $p_T > 60 \text{ GeV}$, $|\eta| < 2.5$, and $|d_o| > 2.0 \text{ mm}$.

- `DiLep_DiPhoton` events are required to pass a diphoton trigger and contain two loose photons with $p_T > 60 \text{ GeV}$ and $|\eta| < 2.5$.
- `DiLep_DiElPh` events are required to pass a diphoton trigger and contain a loose electron and a loose photon with $p_T > 60 \text{ GeV}$ and $|\eta| < 2.5$.
- `DiLep_DiLoElPh` events are required to pass a diphoton trigger and contain an electron and a loose photon with $p_T > 60 \text{ GeV}$ and $|\eta| < 2.5$, with the electron also required to have $|d_o| > 2.0 \text{ mm}$.

In the muon filters, the d_o cuts are only applied to good-quality muon tracks, where good-quality means the ID-to-MS match has a fit quality of $\chi^2/N_{\text{DoF}} < 5$, and the kinematic cuts are applied to the combined muon track if the match is good and to the MS track otherwise.

The rates for each individual `DiLep` filter as a function of the average `physics_Main` rate throughout 2017 and 2018 are shown in Figure [B.1](#). The `DiLep_SiMuonBa` filter only appears in the 2018 plot, as it was added between data-taking periods. The only other major update to the `DiLep` filters in Run 2 was the addition of the `HLT_mu80_msonly_3layersEC` trigger in 2018.

The single-photon filter dominates the rate but only increases approximately linearly with the luminosity, as shown in Figure [B.2](#), with the d_o cuts implemented in the filter keeping the rate to a manageable level.

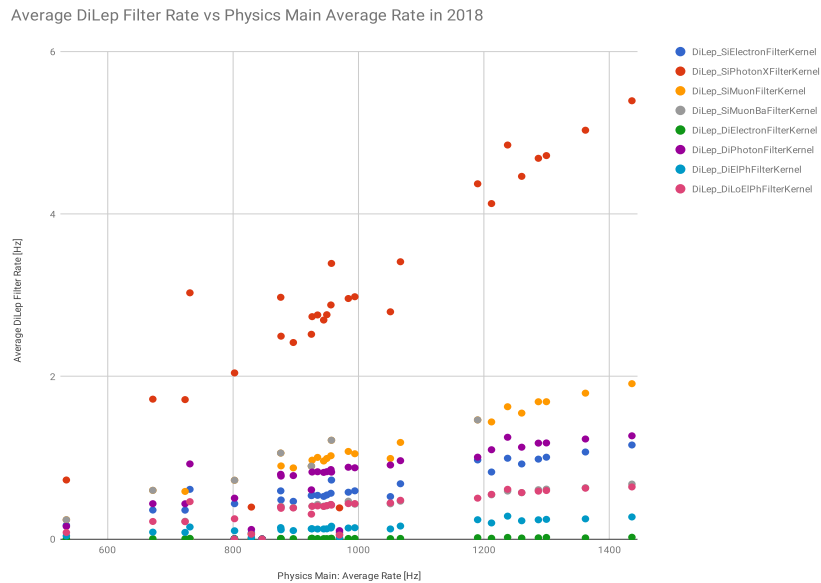
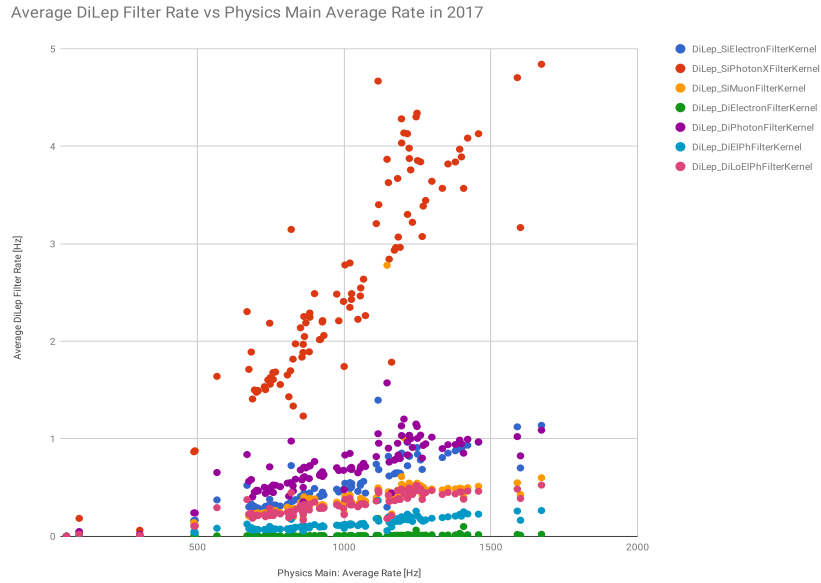


Figure B.1: Average DiLep DRAW_RPVLL filter rates as a function of average physics_Main rate throughout data-taking in 2017 (top) and 2018 (bottom). The DiLep_SiMuonBa filter was added between data-taking periods.

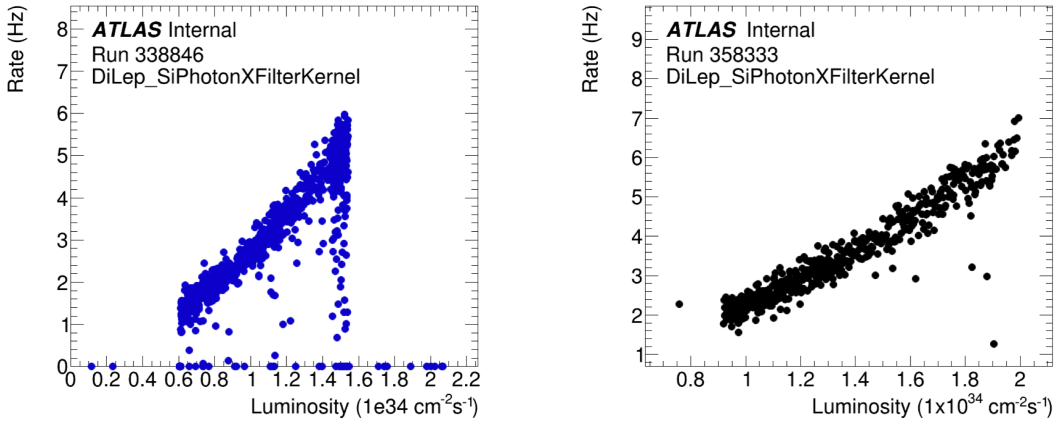


Figure B.2: The Di Lep_SiPhotonX DRAW_RPVLL filter rate as a function of instantaneous luminosity in individual representative runs in 2017 (left) and 2018 (right).

B.1.1.2 MULTI-TRACK DISPLACED VERTICES (DV) FILTERS

The multi-track displaced vertices analysis implements a search for a massive LLP with final states containing a displaced vertex in conjunction with either a high- p_T muon or jet or with high jet multiplicity or large missing transverse momentum (MET) in the context of R-parity violating SUSY [139]. This requires large- d_o track reconstruction to feed the secondary vertex reconstruction algorithm intended to reconstruct final-state displaced vertices. A collection of DV filters are defined to target events containing massive displaced vertices with high track multiplicities and a range of final-state displaced objects, with the filter criteria including MS-only single muon, single photon, MET, or multijet triggers plus additional offline cuts on the corresponding displaced objects. Each final-state displaced

object is associated to a different filter designed to target candidate multi-track DV events containing that displaced object.

The full selection criteria of the individual DV filters are as follows:

- **DVMuon** events are required to either pass a single barrel-only MS-only muon trigger and contain a muon with $p_T > 60$ GeV and $|\eta| < 1.1$ or to pass a single full MS-only muon trigger and contain a muon with $p_T > 80$ GeV and $|\eta| < 2.5$.
- **DV_Photon** events are required to pass a single photon trigger and contain a loose photon with $p_T > 150$ GeV and $|\eta| < 2.5$. This filter also implements a prescale of 20.
- **DV_PhotonPlusTLJet** events are required to pass a single photon trigger and contain a loose photon with $p_T > 150$ GeV and $|\eta| < 2.5$ and either one hard trackless jet with $p_T > 70$ GeV and $|\eta| < 2.5$ or two soft trackless jets with $p_T > 50$ GeV and $|\eta| < 2.5$, where a trackless jet is defined as having a sum- p_T of ghost-associated tracks of less than 5 GeV.
- **DV_MultiJet** events are required to pass any of the three-, four-, five-, six-, or seven-jet triggers and contain either three jets with $p_T > 120$ GeV with at least two jets above 220 GeV, four jets with $p_T > 100$ GeV, five jets with $p_T > 75$ GeV, six jets with $p_T > 50$ GeV, or seven jets with $p_T > 45$ GeV, plus one hard trackless jet or two soft trackless jets.
- **DV_MET** events are required to pass any of the MET triggers and contain LocHadTopo MET of at least 180 GeV, where LocHadTopo MET is calculated from topo-clusters calibrated at the hadronic scale.

The single muon and single photon triggers used in the DV filters are the same as those used in the DiLep filters, as listed above.

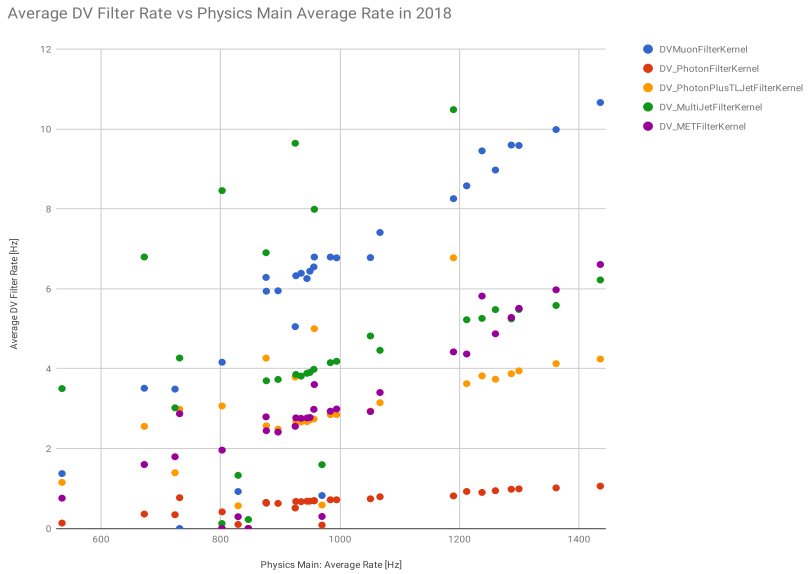
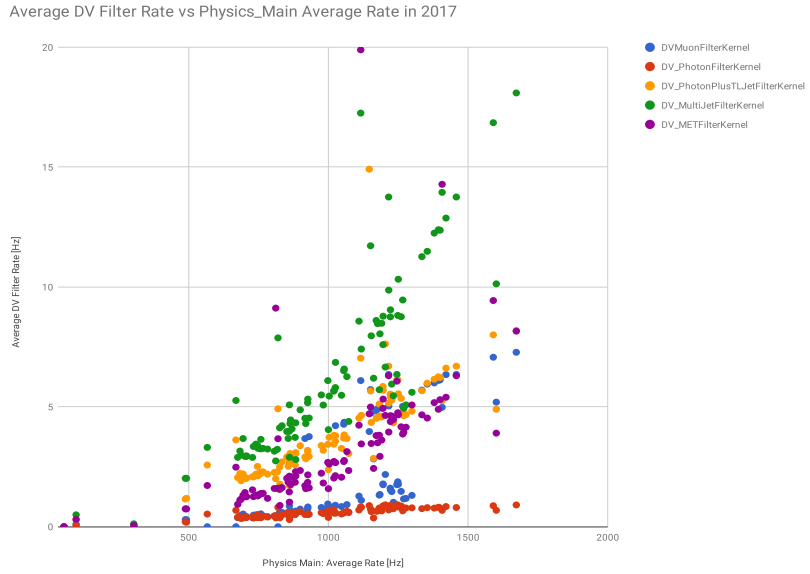


Figure B.3: Average DV DRAW_RPVLL filter rates as a function of average physics_Main rate throughout data-taking in 2017 (top) and 2018 (bottom).

Figure B.3 shows the rates for the individual DV filters versus the average `physics_Main` rate in 2017 and 2018. In 2017, the rate was dominated by the multijet filter, which showed a nearly exponential increase with luminosity and pileup; the filter was modified in 2018, increasing the p_T threshold of the two-trackless-jet requirement from 25 to 50 GeV, to mitigate this pileup dependence and decrease the rate, as seen in Figure B.4. The muon filter was also modified between 2017 and 2018, dropping an original d_o and MS-only requirement on the selected muon and adding the `HLT_mu80_msonly_3layersEC` trigger, hence the increase in muon filter rate in 2018 compared to 2017.

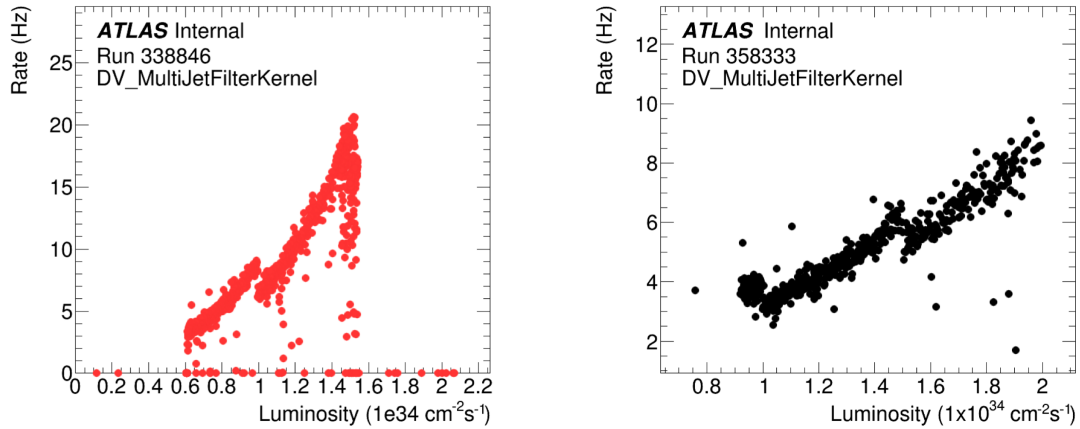


Figure B.4: The DV_MultiJet DRAW_RPVLL filter rate as a function of instantaneous luminosity in individual representative runs in 2017 (left) and 2018 (right).

B.I.I.3 DISAPPEARING TRACKS (`KinkedTrack`) FILTERS

The disappearing tracks analysis employs a search for long-lived charginos that are nearly mass-degenerate with the stable neutralino, which yields a final state involving a disappearing track, where track disappearance is defined by the non-existence of SCT hits on the trajectory of a tracklet, plus a single energetic jet or multiple jets, in the case of electroweak or strong production, respectively, and large MET [140]. This search requires specialized pixel tracklet reconstruction, which reconstructs artificial tracklets using only pixel hits from standard tracks in a second pass tracking step. Multiple `KinkedTrack` filters are defined to target candidate disappearing track signal events from electroweak production, with single jet final states, or from strong production, with multijet final states, or to target SM Z to $\mu\mu$ or Z to ee processes for studying potential backgrounds. The selection criteria for the signal filters include MET triggers plus offline cuts on the missing energy, jets, and isolated tracks, and the selection criteria for the background filters include single lepton triggers and Z -boson mass cuts.

The `KinkedTrack` filters selection criteria are detailed below:

- `KinkedTrackJet` events are required to pass any of the MET triggers and contain FinalTrk MET of at least 60 GeV, where FinalTrk MET is the total MET calculated from the sum of calibrated objects and track-based soft terms, one jet with $p_T > 80$ GeV and $|\eta| < 3.2$, and one isolated track or tracklet. Additionally, the filter implements a lepton veto and requires a minimum φ separation between the jet and MET of $\Delta\varphi_{\min}(\text{jet}, \text{MET}) > 1.0$.

- **KinkedTrackMultiJet** events are required to pass any of the MET triggers and contain FinalTrk MET of at least 170 GeV and two jets with $p_T > 60$ GeV and $|\eta| < 3.2$. Additionally, the filter implements a lepton veto and requires a minimum φ separation between the jet and MET of $\Delta\varphi_{\min}(\text{jet}, \text{MET}) > 2.0$.
- **KinkedTrackStublet** events are required to pass any of the MET triggers and contain FinalTrkMET of at least 90 GeV and one jet with $p_T > 90$ GeV and $|\eta| < 3.2$. Additionally, the filter implements a lepton veto and a prescale of 10 and requires a minimum φ separation between the jet and MET of $\Delta\varphi_{\min}(\text{jet}, \text{MET}) > 1.0$.
- **KinkedTrackZee** events are required to pass a single electron trigger and contain an electron-calorimeter-cluster pair that reconstructs the Z -boson mass within 40 GeV, where the electron is required to have $p_T > 40$ GeV and $|\eta| < 2.5$ and the calorimeter cluster is required to have $p_T > 15$ GeV and $|\eta| < 2.5$. Additionally, the filter implements a prescale of 5.
- **KinkedTrackZmumu** events are required to pass a single muon trigger and contain a muon-MS-track pair that reconstructs the Z -boson mass within 40 GeV, where the muon is required to have $p_T > 40$ GeV and $|\eta| < 2.5$ and the MS track is required to have $p_T > 15$ GeV and $|\eta| < 2.5$. Additionally, the filter implements a prescale of 5.

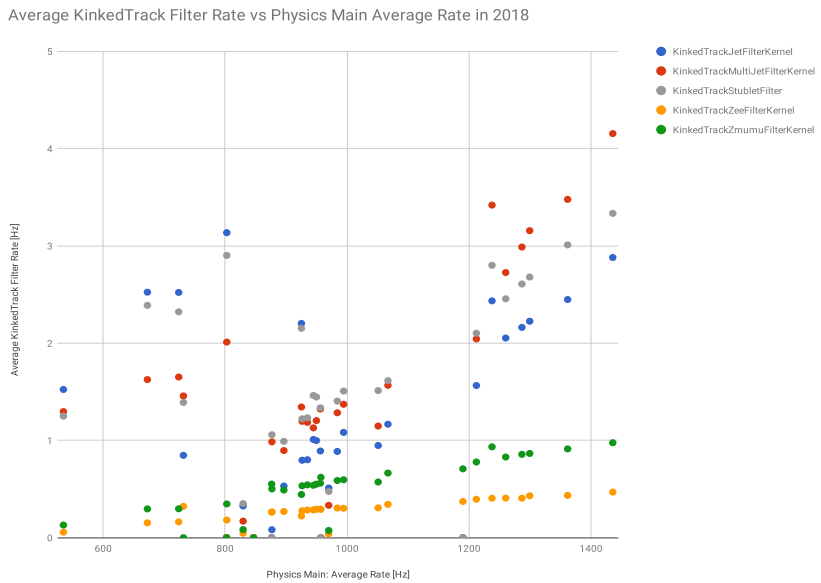
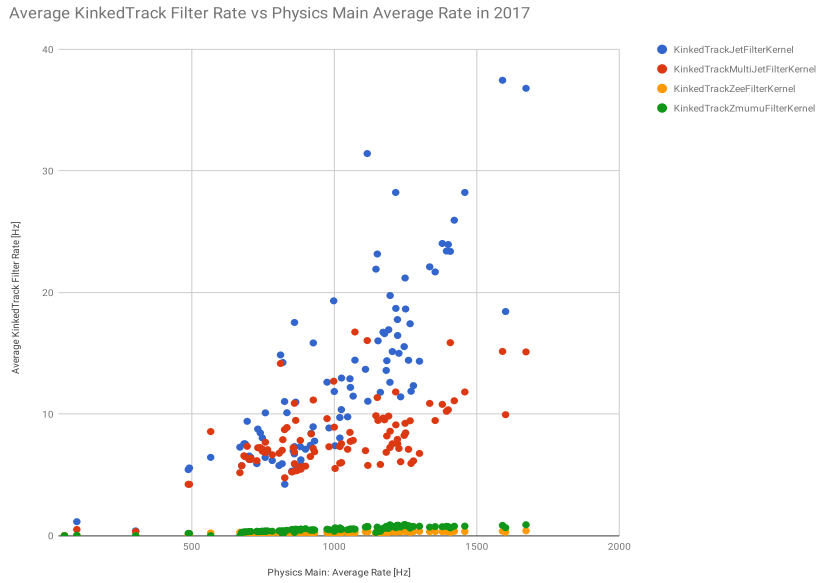


Figure B.5: Average KinkedTrack DRAW_RPVLL filter rates as a function of average physics_Main rate throughout data-taking in 2017 (top) and 2018 (bottom).

The filter rates for each individual `KinkedTrack` filter are shown as a function of the average `physics_Main` rate in 2017 and 2018 in Figure B.5. The `KinkedTrackStublet` filter was new in 2018. The single-jet and multijet filters were also modified mid-year in 2017 to drastically reduce their rates after they were both seen to dominate the `KinkedTrack` portion of the `DRAW_RPVLL` stream and grow exponentially with luminosity, as seen in Figure B.6. The single jet filter added new constraints to the selected isolated tracklet, requiring it pass a certain p_T threshold, be within a certain $|\eta|$, have a good quality-of-fit χ^2/N_{DoF} , and have a certain number of contributing pixel layer hits in its trajectory. The multijet filter reconfigured its original criteria, requiring two jets instead of the original three, but increasing the p_T threshold and adding an additional requirement on the total MET in the event. The single-jet and multijet filter changes significantly reduced the rates, by a factor of roughly five and ten, respectively, before the 2018 run and the full Run 2 reprocessing.

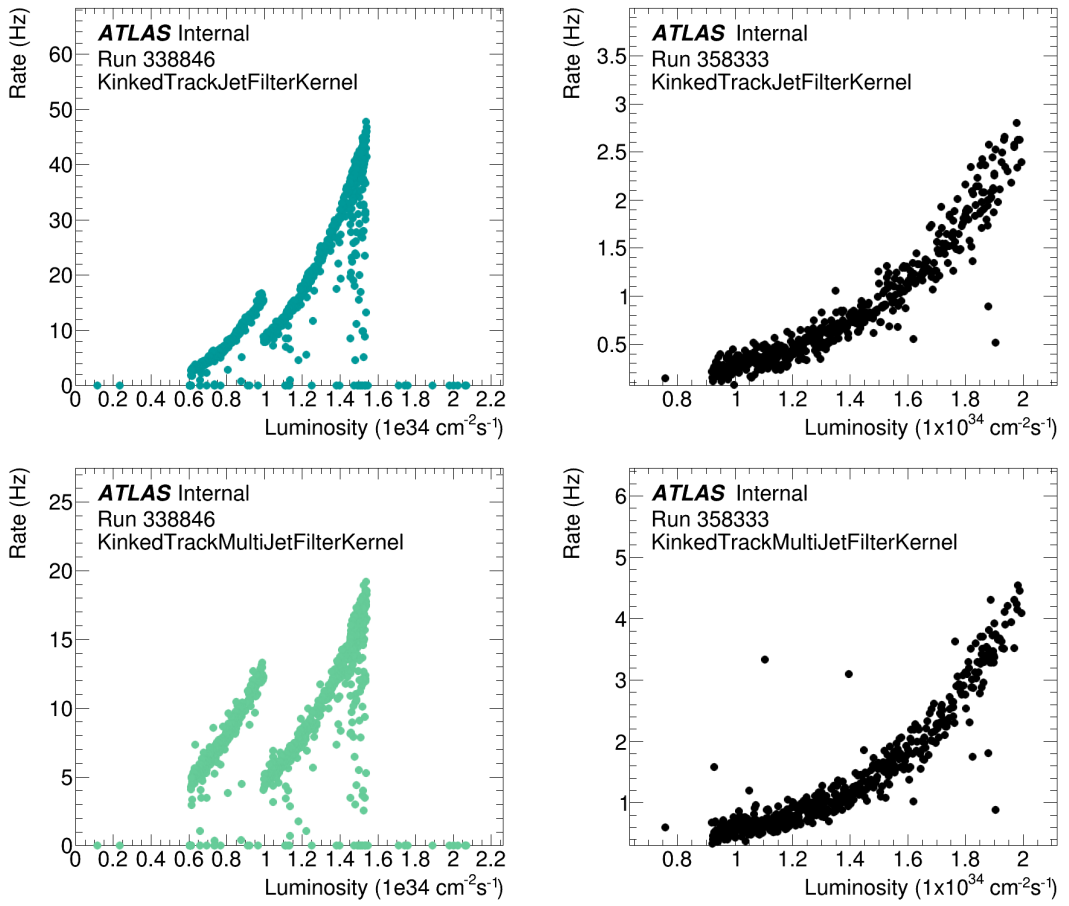


Figure B.6: The KinkedTrack DRAW_RPVLL single-jet and multijet filter rates as a function of instantaneous luminosity in individual representative runs in 2017 (left) and 2018 (right).

B.I.2 UEH EXOTICS FILTERS

The UEH Exotics analyses using the `DRAW_RPVLL` stream are the heavy neutral lepton (dHNL) analysis, using the `HnL` filter, the displaced jets / Hidden Valley (HV) analysis, using the `HV` filters, and the emerging jets (EJs) analysis, using the `Emerging` filter. The highly ionized particle (HIP) analysis using the `DESDM_EXOTHIP` filter is also included in this list, but is not described in this appendix.

B.I.2.1 HEAVY NEUTRAL LEPTON (`HnL`) FILTERS

The displaced heavy neutral lepton (dHNL) analysis searches for long-lived HNLs produced through mixing with muon or electron neutrinos from leptonic W -boson decays with a final state of a prompt lepton and a significantly displaced dilepton [141] and requires large-radius tracking and secondary vertexing algorithms to reconstruct the displaced dilepton vertex. The analysis uses a single `HnL` filter designed to select candidate dHNL signal events containing one prompt lepton and one displaced lepton, with the filter criteria including single lepton or multi-lepton triggers plus a single isolated prompt lepton and a single displaced lepton with offline p_T cuts.

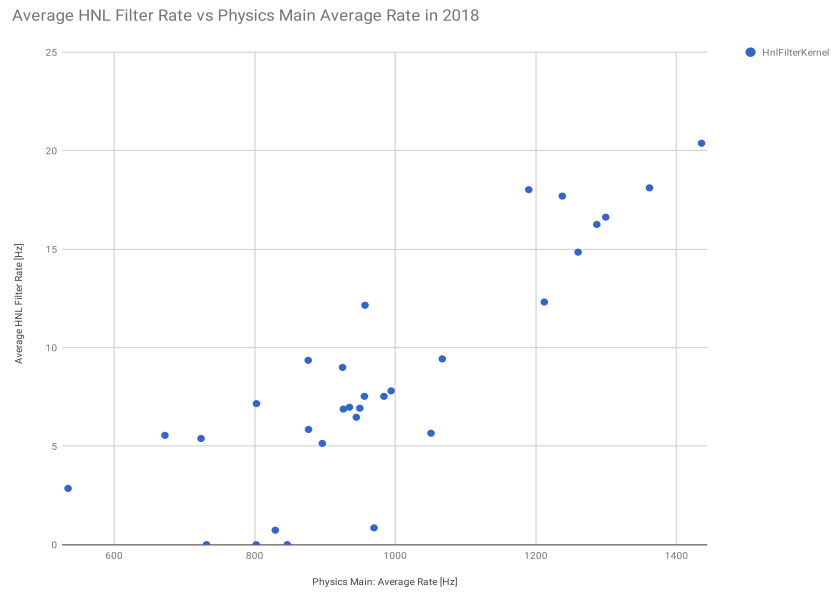
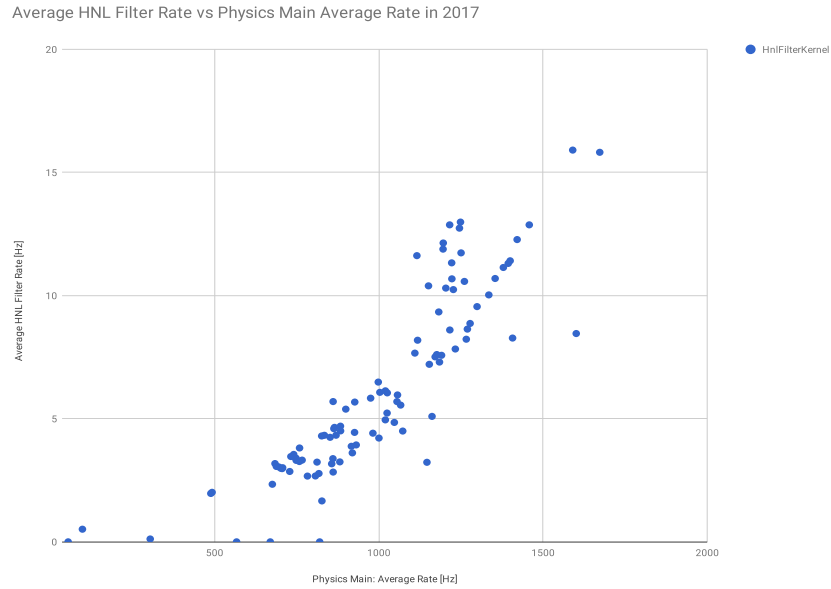


Figure B.7: Average Hnl DRAW_RPVLL filter rate as a function of average physics_Main rate throughout data-taking in 2017 (top) and 2018 (bottom).

Below is the full selection criteria for the $\text{Hn}\ell$ filter:

- $\text{Hn}\ell$ events are required to pass a single muon, single electron, multi-muon, or multi-electron trigger and contain one prompt lepton with $p_T > 28 \text{ GeV}$ and one displaced lepton with $p_T > 5 \text{ GeV}$, where the prompt and displaced leptons can be any combination of muons and electrons and are required to have $|\eta| < 2.5$. The prompt lepton must be isolated; the prompt muon, if any, must be of combined type; and the displaced muon, if any, must be either of standalone type or have $|d_0| > 0.1 \text{ mm}$ or have poor quality of fit $\chi^2/N_{\text{DoF}} > 5$.

The $\text{Hn}\ell$ filter rates in 2017 and 2018 are shown in Figure B.7. No major changes were made to the filter during Run 2.

B.1.2.2 DISPLACED JETS (HV) FILTERS

The displaced hadronic jets analysis implements searches for neutral long-lived particles decaying into displaced hadronic jets in the inner detector (ID), hadronic calorimeter (HCal), and muon spectrometer (MS) in the context of Hidden Valley (HV) models, with Run 2 analysis signatures of an ID vertex plus an MS vertex or an ID vertex plus an HCal jet [142, 143]. The analysis requires large- d_0 retracking to reconstruct the displaced ID vertices and MS hits for offline performance studies of the displaced MS vertices. A pair of HV filters are used to target candidate displaced jet signal events with MS vertex or HCal jet signatures based solely on dedicated LLP muon ROI or CalRatio triggers, designed to select events containing decays of neutral LLPs into jets in the muon spectrometer or hadronic calorimeter, respectively.

Events are required to pass one of the following LLP HLTs to be included in the HV filters:

- Muon ROI triggers:
 - `HLT_j30_muvtx`;
 - `HLT_j30_muvtx_noiso`;
- CalRatio triggers:
 - `HLT_j30_jes_cleanLLP_PS_llp_L1TAU60`;
 - `HLT_j30_jes_cleanLLP_PS_llp_noiso_L1TAU60`;
 - `HLT_j30_jes_cleanLLP_PS_llp_L1LLP-NOMATCH`;
 - `HLT_j30_jes_cleanLLP_PS_llp_noiso_L1LLP-NOMATCH`;
 - `HLT_j30_jes_cleanLLP_PS_llp_L1TAU100`;
 - `HLT_j30_jes_cleanLLP_PS_llp_noiso_L1TAU100`;
 - `HLT_j30_jes_cleanLLP_PS_llp_L1LLP-RO`;
 - `HLT_j30_jes_cleanLLP_PS_llp_noiso_L1LLP-RO`.

The Muon ROI and CalRatio `noiso` triggers are background triggers, while the rest of the Muon ROI and CalRatio triggers listed above are primary signal triggers.

The Muon ROI trigger is designed to target events with LLP hadronic decays producing jets in the muon spectrometer, which are characterized by clusters of L1 muon RoIs centered around the LLP line-of-flight. The trigger requires at least three (four) RoIs in

the barrel (end-caps) in a cone of radius $\Delta R = 0.4$ and additional isolation criteria for the signal (non-noiso) trigger.

The CalRatio trigger is designed specifically to select CalRatio jets, where the CalRatio is defined as the ratio of the jet's energy deposited in the HCal to that deposited in the ECal, $E_H/E_{EM} = 1/EMF - 1$, with EMF being the jet electromagnetic fraction. The CalRatio jet is characterized by a lack of reconstructed ID tracks and a relatively narrow width, and the CalRatio trigger thus selects jet events based on narrowness, tracklessness, and low EMF, triggering on an L1 τ -lepton item, which sums energy in a narrower window than an L1 jet item, and an HLT jet that lacks reconstructed ID tracks with $p_T > 2 \text{ GeV}$ in $\Delta R < 0.2$ of the HLT jet axis and has a log-ratio $\log(E_H/E_{EM}) > 1.2$ [144].

The CalRatio trigger names describe how the pieces of the trigger algorithm are applied as follows:

- `j30_jes` means a 30 GeV cut is applied at the jet energy scale;
- `cleanLLP` means that cleaning requirements are applied to reject bad jets from LAr noise bursts;
- `PS` means jets are only reconstructed in a “super RoI” around the L1 seed, rather than in the full HCal, to save resources;
- `llp` means the trigger includes the standard CalRatio trigger cuts described above;
- `noiso` refers to the nominal version of the trigger that includes an algorithm to reject non-collision background;
- `L1TAU60` and `L1TAU100` refer to the nominal L1 τ item with p_T threshold of 60 and 100 GeV, respectively, that seeds the HLT;

- L1LLP-NOMATCH refers to the L1 Topo item that selects events with a τ object not matched to any EM object with $p_T > 3 \text{ GeV}$; this is used to recover low- p_T jets rejected by L1_TAU60;
- L1LLP-RO refers to the L1 Topo item that selects events with a τ object matched to an EM object with $p_T > 3 \text{ GeV}$ and log-ratio greater than one.

The full selection criteria for the HV filters are simple:

- HV_Muvtx events are required to pass an LLP Muon ROI trigger.
- HV_CalRatio events are required to pass an LLP CalRatio trigger.

Figure B.8 shows the average HV filter rates versus the `physics_Main` average rate in 2017 and 2018. The only change to the HV filters during Run 2 was to update the CalRatio triggers to include the last four items in the trigger list above.

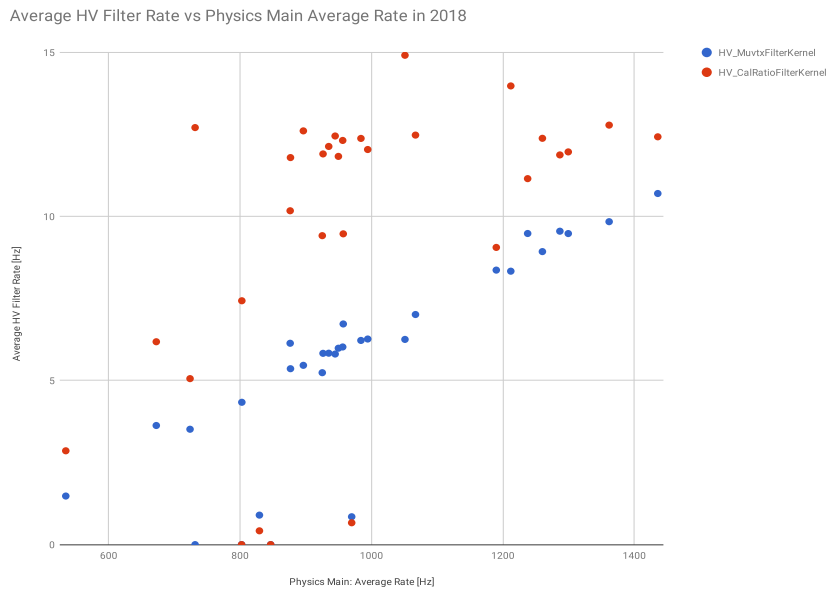
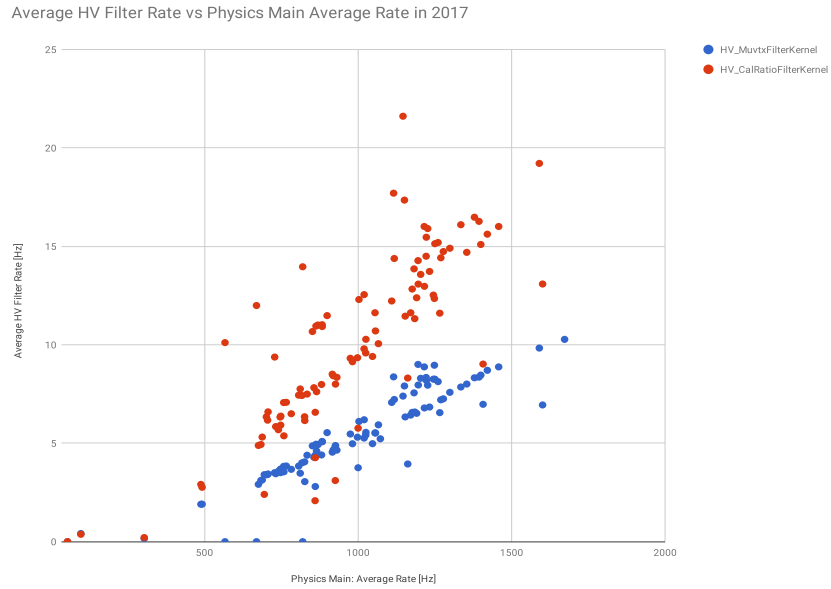


Figure B.8: Average HV DRAW_RPVLL filter rates as a function of average physics_Main rate throughout data-taking in 2017 (top) and 2018 (bottom).

B.I.2.3 EMERGING JETS (**Emerging**) FILTERS

The emerging jets (EJs) analysis involves a search for emerging jets, characterized by multiple displaced vertices of varying displacements within single jet objects from decays of long-lived dark pions, with a four-jet final state and a signature of two high- p_T QCD jets and two high- p_T EJs, in the context of dark QCD. The search requires large- d_o tracking and secondary vertexing to positively identify the multiple distinct displaced vertices characteristic of the emerging jet topology. A single filter is implemented to select four-jet signal events for the search and prescaled dijet background events for data-driven background estimates. The filter criteria includes a lowest unprescaled four-jet trigger plus a four-jet requirement for signal-like events or a heavily prescaled single jet trigger plus a two-jet requirement for background-like events.

Events selected by the **Emerging** filter are required to pass one of following HLTs:

- four-jet triggers = four jets above p_T threshold:
 - HLT_4j90;
 - HLT_4j100;
 - HLT_4j110;
 - HLT_4j120;
 - HLT_4j130;
 - HLT_4j140;
 - HLT_4j150;

- single-jet triggers = one jet above p_T threshold with heavy prescale:
 - `HLT_j110`.

The full `Emerging` filter selection criteria are listed below:

- `Emerging` events are required to either pass the lowest unprescaled four-jet trigger and contain four jets with $p_T > 120$ GeV and $|\eta| < 2.5$ or to pass a heavily prescaled single-jet trigger and contain two jets with $p_T > 120$ GeV and $|\eta| < 2.5$. The four-jet selection is intended to target candidate emerging jet signal events, while the dijet selection is intended to select background events.

The average `Emerging` filter rate as a function of the `physics_Main` average rate in 2017 and 2018 is shown in Figure [B.9](#). The filter was developed in 2017 with the initial criteria of the `HLT_4j100` trigger and four jets with $p_T > 100$ GeV, designed only to select four-jet signal events. Mid-year, the trigger menu changed at high-luminosity without notice, resulting in the filter excluding all four-jet high-luminosity events that should have been selected. The filter was designed to select events passing the lowest unprescaled four-jet trigger, but the trigger implemented in the filter was only correct at low-luminosity, since the lowest unprescaled trigger threshold increased from 100 to 120 GeV at high-luminosity. Therefore, the `Emerging` filter rate was often zero for part or all of a run, and much of the `Emerging` data was lost from the first half of 2017, as evidenced in Figure [B.10](#).

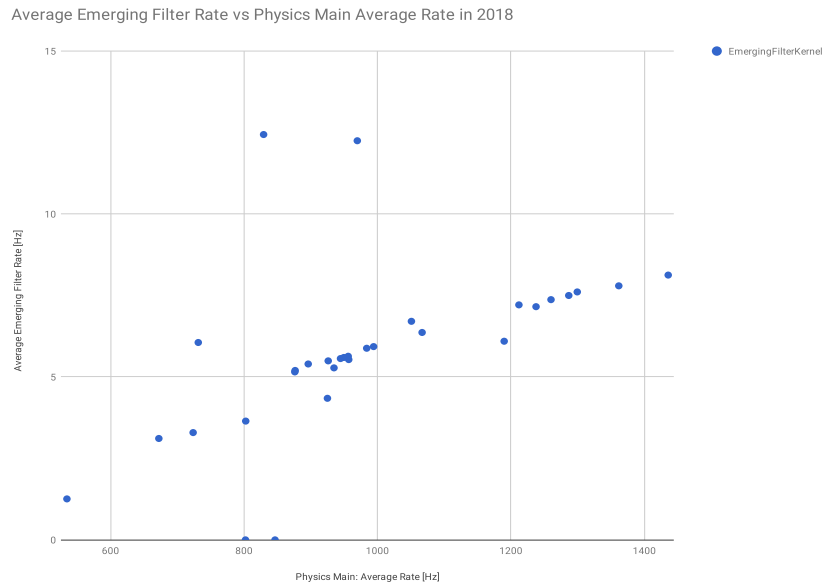
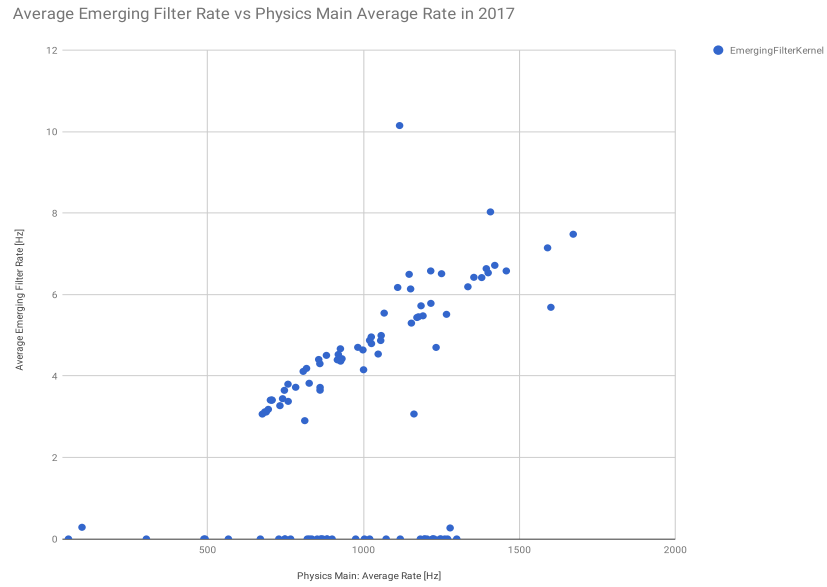


Figure B.9: Average Emerging DRAW_RPVLL filter rate as a function of average physics_Main rate throughout data-taking in 2017 (top) and 2018 (bottom).

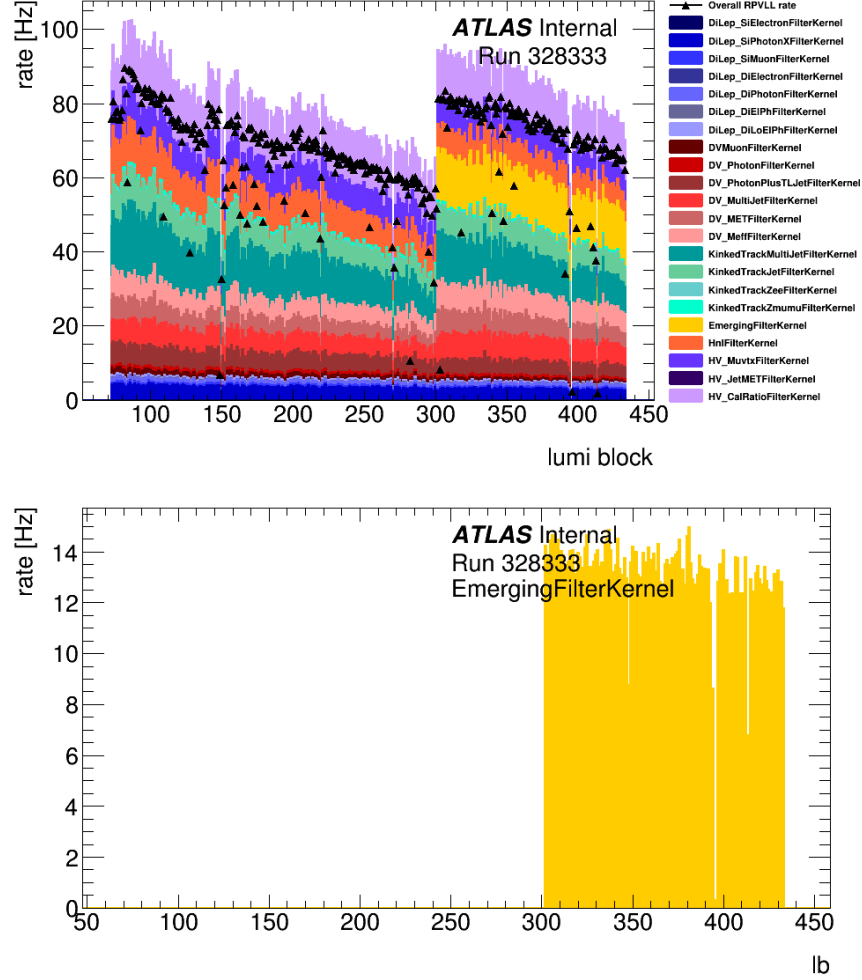


Figure B.10: Evidence of the multijet trigger issue plaguing the Emerging filter in the first half of 2017. The stacked rates for all individual DRAW_RPVLL filters (top) and for the Emerging filter alone (bottom) are shown as a function of the luminosity block for a representative run from early 2017. The low lumi-blocks correspond to the beginning of the run when the luminosity is at its peak. The lumi-block where the Emerging filter (yellow) turns on corresponds to the point where the luminosity drops below threshold and the trigger menu changes to the low-luminosity version, which uses the lower-threshold four-jet trigger implemented in the first iteration of the Emerging filter; hence, the filter begins to select events.

Upon discovering the issue, the `Emerging` trigger list was modified to include the lowest unprescaled four-jet triggers of the updated trigger menu, as well as any potential four-jet triggers that could hypothetically be used in any further trigger menu updates in order to avoid suffering the same problem in the future. At the same time, the offline jet p_T thresholds were raised from 100 to 120 GeV to reduce the rate increase from the trigger fix, and the dijet selection was added to save events for background studies. Extensive studies were performed to find the optimal prescaled single jet trigger and dijet p_T threshold to minimally increase the rate. The lost data were restored in the full Run 2 reprocessing.

B.I.3 OVERALL RATES IN RUN 2

Figure B.11 illustrates the stacked individual filter rates and the overall filter rate as a function of lumi-block for two representative runs, one in 2017 and one in 2018. The rate of the stream starts out high at the beginning of the run, where the luminosity is at its peak, and decreases throughout the run as the luminosity decreases.

The average overall `DRAW_RPVLL` filter rate throughout 2017 and 2018 is shown as a function of the average `physics_Main` rate and as a function of the average $\langle\mu\rangle$ in Figure B.12. The overall rate increases almost linearly with the luminosity and pileup throughout the year, but the overall rates are lower on average in 2018 than in 2017, as significant efforts were made between years to reduce the luminosity and pileup dependence of various filters and to lower the overall `DRAW_RPVLL` rate at Tier-0, as discussed above.

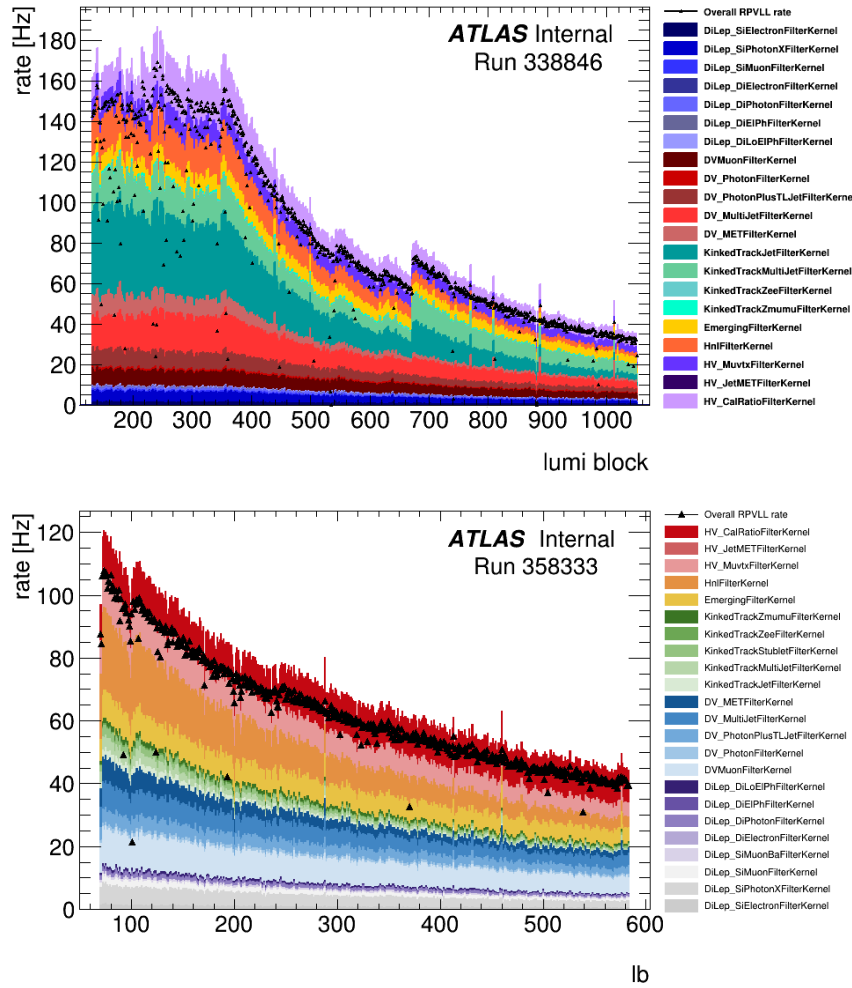


Figure B.11: Individual (colored) and overall (black) DRAW_RPVLL filter rates as a function of luminosity block for a representative run in 2017 (top) and 2018 (bottom).

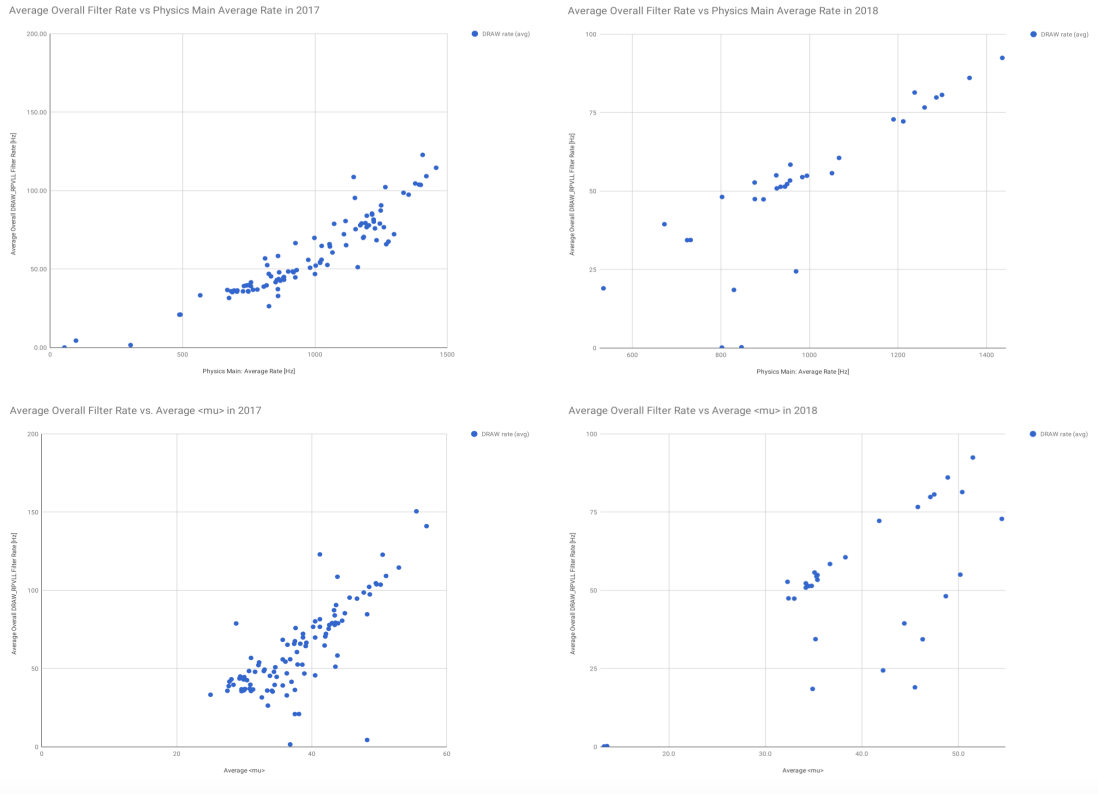


Figure B.12: The overall average DRAW_RPVLL rate as a function of physics_Main average rate (top) and average $\langle \mu \rangle$ (bottom) in 2017 (left) and 2018 (right).

The fraction of the total DRAW_RPVLL stream occupied by each individual filter and the stacked individual filter rate of each DRAW_RPVLL filter per run in 2017 and 2018 are shown in Figure B.13. The KinkedTrack filters occupied the most space in the stream in 2017 and drastically reduced their size in 2018.

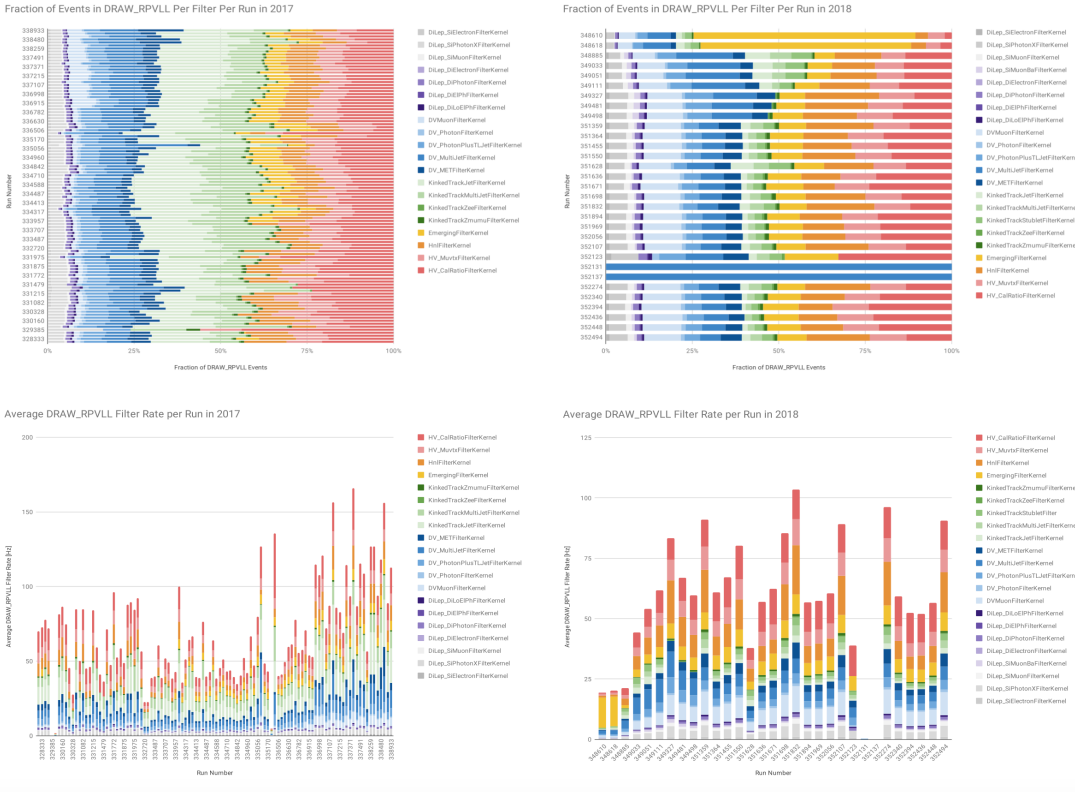


Figure B.13: DRAW_RPVLL filter fractions (top) and rates (bottom) for individual filters per run in 2017 (left) and 2018 (right).

B.2 TriggerAPI IMPLEMENTATION

The DRAW_RPVLL filters skim based on hard-coded trigger lists, which can be dangerous when the trigger menu changes unexpectedly or without notice and the filters are not updated accordingly, resulting in a loss of data for analyses, as was the case for the Emerging filter in 2017, as explained above. In an attempt to prevent such an issue from happening again, a solution was proposed to supplement the hard-coded lists with back-up trigger

lists pulled directly from the trigger menu so that filters are automatically updated to any changes. This is implemented with the `TriggerAPI` tool, a python interface designed to retrieve the trigger information for a given signature and period. The tool obtains specific trigger information, including lists of the always or sometimes unprescaled lowest- p_T -threshold HLT chains, for a given trigger period, type, and matching-pattern.

The `RPVLLTriggers` python class was developed to implement the `TriggerAPI` tool in the `LongLivedParticleDPDMaker DRAW_RPVLL` filtering package. The class defines filter-specific methods to generate the corresponding trigger lists by reading the relevant trigger menu through the `TriggerAPI` interface. Each method gets a list of all of the unprescaled triggers of a specified type and matching-pattern from the current or future trigger menu for the given filter and appends this list of `TriggerAPI`-generated triggers to the hard-coded list in the corresponding filter code. These generated trigger lists are thus intended to be used as backups to the hard-coded lists in the case of menu changes. The `RPVLLTriggers` class also contains a switch to turn the implementation on and off as needed.

Unfortunately, the initial `DRAW_RPVLL` implementation of the `TriggerAPI` tool in the `RPVLLTriggers` class had issues reading from the wrong trigger menu to generate the specified trigger lists. The `TriggerAPI` tool is programmed to grab the trigger menu stored in the current release, so calls to the current trigger period in `RPVLLTriggers` read from

the trigger menu stored in the 21.0.YY release where the filtering code is run, as opposed to the trigger menu stored in the 21.1.ZZ release used by the trigger at P₁ for the given run, as desired. The trigger menu in 21.0 is often many months behind the menu stored in 21.1. Meanwhile, calls to the future trigger period read from the latest available 21.1.ZZ release, which could be many iterations ahead of the trigger menu used in the run being processed.. Either way, the current implementation of the `TriggerAPI` tool in the `DRAW_RPVLL` filtering code is inaccurate and needs to be updated to read from the proper trigger menu of the P₁ release used in the corresponding run.

The correct workflow for the filtering job at Tier-0 with the `TriggerAPI` tool is as follows:

1. Process run XXXXXX in release 21.0.YY.
2. Identify the 21.1.ZZ release used at P₁ for run XXXXXX.
3. Retrieve the trigger menu stored in 21.1.ZZ.
4. Generate the trigger lists, and filter the events accordingly.

Steps 1 and 4 are already implemented, and step 3 is easily implementable with the “setRelease” `TriggerAPI` function, newly designed to set the release of the stored trigger menu to be read. The proper P₁ release simply needs to be identified and fed to the `TriggerAPI` tool at the top of the `RPVLLTriggers` class. Setting the release is easy, but getting the release within the filtering code (step 2) is non-trivial. One can manually find the P₁ release used for a given run with the ATLAS Run Query tool. The python-based command

line interface `AtlRunQuery.py`, which outputs a text file with the run query results, including the P1 release, can potentially be used within the `RAW -to-DRAW_RPVLL` filtering job to grab the release used in the process to pass along to the `TriggerAPI` tool. However, the exact method with which to run the `AtlRunQuery.py` interface and read the output within a reconstruction job has not yet been determined; thus, the `TriggerAPI` implementation in the `DRAW_RPVLL` filters is currently turned off.

C

Truth dark jets

In dark QCD theory, where a dark sector analogous to QCD exists, a dark jet is a narrow cascade or collimated spray of dark hadrons produced as a result of the fragmentation of an initial dark quark. Dark quarks are produced in dark sector showers and hadronize in the dark sector in the same manner as SM quarks in the visible sector, producing dark mesons that form jet-like structures of dark hadrons, most of which are dark pions, traveling in

roughly the same direction as the initial quarks they originate from. This all happens in the dark sector, so the dark jets are totally invisible at this point. The dark mesons within the dark jets then decay to SM quarks with lifetimes of order millimeters to centimeters, so dark jets gradually become visible over length scales of a few centimeters, producing emerging jets. This is the basis of the collider phenomenology being explored in the Emerging Jets search, where emerging jets are essentially the decay products or the visible-sector extensions of dark jets.

On the experimental level, a dark jet is a truth jet containing only dark particles, or a cluster of “stable” truth dark hadrons into a conical object of radius R with an energy and direction corresponding to the original dark parton that produced it. A “stable” or “final-state” dark hadron is one that either does not decay or decays to SM particles, but not to other dark particles. Truth dark jets are essentially truth-level reconstruction objects representing the dark quarks produced in the hard process and can thus be used to distinguish between truth jets produced from dark quarks, corresponding to truth-level emerging jets, and truth jets produced from SM quarks, corresponding to truth-level QCD jets. This provides a method to identify emerging jets at the generator level, which aids in defining emerging jet objects at the reconstruction level.

As a consequence of the way showering is performed in Pythia, all dark hadrons in the event trace back to both dark quarks. The event contains two distinct dark quarks, but

both dark quarks have identical decay products, with both being co-parents to the same children, so it is impossible to determine which dark quark the final-state particles and jets originate from. Therefore, there is no way to confidently identify truth-level emerging jets based on dark quark matching alone. Originally, an attempt was made to ΔR -match truth jets to the initial dark quarks as a means of identifying emerging jets at the generator-level, but jets cannot be traced back to the individual quarks they are matched to, since it is impossible to distinguish one quark decay chain from the other. As such, there is no way to cross-check this identification method or be fully convinced of its accuracy. Instead, a better method to identify emerging jets at the generator level is employed, where the ΔR -matching is performed to the truth dark jets initiated by the dark quarks, rather than to the dark quarks themselves. In the ΔR -matching procedure, two objects are considered a match if their angular separation $\Delta R \equiv \sqrt{(\varphi_1 - \varphi_2)^2 + (\eta_1 - \eta_2)^2}$ is less than some small specified threshold.

Truth dark jets are not available at ATLAS by default and therefore need to be custom-built by clustering together “stable” truth dark hadrons with modified standard jet reconstruction algorithms. Algorithms to cluster jets from dark particles were developed specifically for this purpose, as dark jets had never been officially implemented in ATLAS prior to this analysis, so no such dark clustering methods were yet in place. The current method to build truth dark jet containers to be included in the final analysis output format was devel-

oped in stages.

For initial testing purposes, truth dark jets were first built inside truth derivations, during the `EVNT` to `TRUTH_DAOD` step, with local modifications applied to the necessary packages in order to add dark hadron clustering capabilities to the jet reconstruction algorithms and to schedule the dark jet algorithm in the truth derivation job. Truth dark jet building was then moved to run inside reconstruction, during the `ESD` to `AOD` step, in order to have access to the container in the fully-simulated and -reconstructed samples, with the necessary package modifications implemented in the central ATLAS software to enable the creation of truth dark jet containers privately and officially on the grid.

The `ParticleJetTools` package was modified to include options for dark hadron clustering in particle-level jets, with new selections added to include dark hadrons in the collection of truth particles to be used as inputs to the pseudojet-getter tool. If the option to include dark hadrons is enabled, then any truth dark hadron that does not decay to another dark particle is collected to be used in the truth jet clustering algorithm. A custom job options file can then be used to configure the truth dark jet clustering algorithm and build the output container during reconstruction. This is done by configuring the truth dark jet reconstruction with the jet tool manager and then adding the configured truth dark jet reconstruction to the algorithm sequence. First, the truth dark hadron selection is performed, and the output collection is input to the truth dark jet pseudojet builder, which

is added to the list of pseudojet-getter tools input to the jet tool manager. The pseudojet builder converts the input objects, in this case truth dark particles, into fastjet pseudojets, to be used as inputs to the jet finding algorithm. Then, the jet finder is created to configure the jet finding algorithm, with the corresponding output container name, jet algorithm, size parameter, and input pseudojet builder list specified. Lastly, the truth dark jet reconstruction algorithm is added to the algorithm sequence.

Finally, the truth dark jet container was moved to be built inside the dedicated derivation, during the DAOD_RPVLL to DAOD_EXOT23 step. Building custom jet containers within derivations is conventional practice, since reconstruction is performed centrally for multiple analyses and must therefore remain uniform. The truth dark jet building is implemented in the derivation step in much the same way as in reconstruction, but the creation of the jet finder and the addition of the algorithm to the algorithm sequence is instead handled by the “addStandardJets” function common to the jet derivation framework. The function had to be modified slightly to accept custom pseudojet-getters, not explicitly listed in the pseudojet-getter map, for use in the jet finder algorithm.

D

PYTHIA HV running coupling validation

Simulating the dark sector with a running gauge coupling is necessary to generate events with narrow, QCD-like dark jets and subsequent emerging jets analogous in shape to standard QCD jets. The coupling in the hidden sector directly affects the width of the dark jets, with wider jets produced from fixed couplings, which in turn directly impacts the signal. To generate QCD-like behavior in the dark sector and produce the expected signal with

narrow emerging jets, the dark gauge coupling must be allowed to run.

Initially, a local patch was applied to the PYTHIA Hidden Valley model in release 8.183 to include the option to enable a running coupling in the hidden sector. The HV model implemented in PYTHIA contains two species of HV mesons: flavor-diagonal and off-diagonal, which are neutral and charged under the hidden sector, respectively. In this model, the mediator is implicitly assumed to be a vector (Z'), which results in unstable diagonal (dark-neutral) dark pions, analogous to the neutral SM pion, and stable off-diagonal (dark-charged) dark pions, analogous to the charged SM pions, which are stable by default in PYTHIA. In the dark QCD model under consideration, however, the mediator is a heavy scalar, in which case dark charge is not a conserved quantum number and all dark mesons are theoretically allowed to decay. Hence, dark-charged off-diagonal dark mesons can theoretically decay to SM particles that do not carry dark charge. Additionally, it is a sensible assumption that the couplings governing the off-diagonal dark mesons and the flavor-diagonal dark mesons are roughly the same size and that the lifetimes of the two dark mesons species are therefore the same.

In the initial local PYTHIA patch, the stable off-diagonal dark mesons are avoided by keeping the number of Hidden Valley flavors to one, which results in a single quark species and thus a single dark meson species, with only flavor-diagonal unstable dark mesons being produced. The running coupling was then controlled by a separate independent param-

eter. In the official implementation of the running HV coupling in PYTHIA release 8.223 and onward, the number of HV flavors instead controls both the evolution of the coupling and the number of dark meson species. Setting the number of HV flavors to seven, as required to reproduce a QCD-like running coupling, thus yields a large number of stable off-diagonal dark mesons and only a small fraction of the unstable diagonal dark mesons produced in the original implementation, resulting in a significant decrease in the number of displaced vertices, the jet p_T , and the overall signal. To recover the expected signal distributions, all dark mesons, both diagonal and off-diagonal, are forced to decay, and both species of dark pions are explicitly given the same long lifetime.

Validation plots comparing signal sample production with running dark coupling in the locally hacked and official PYTHIA releases for two signal points are presented below. The two signal points being compared are Model A (with $m_{X_d} = 1000$ GeV and $c\tau_{\pi_d} = 150$ mm) and ModelB (with $m_{X_d} = 1000$ GeV - $c\tau_{\pi_d} = 5$ mm). In all but Figure D.3, the following PYTHIA versions are compared for both signal points:

1. locally hacked PYTHIA 8.183 with running dark coupling;
2. official PYTHIA 8.224 with running dark coupling, number of HV flavors $n_f = 7$, and stable off-diagonal dark mesons;
3. official PYTHIA 8.224 with running dark coupling, $n_f = 1$, and stable off-diagonal dark mesons;
4. locally hacked PYTHIA 8.224 with running dark coupling, $n_f = 1$, overridden number of dark meson species $nfl = 7$, and stable off-diagonal dark mesons;

5. official PYTHIA 8.224 with running dark coupling, $n_f = 7$, and (unsuccessful) off-diagonal dark meson decays;
6. official PYTHIA 8.224 with running dark coupling, $n_f = 7$, and forced off-diagonal dark meson decays with explicit off-diagonal dark meson masses.

Samples (1) and (6) are shown in solid red and green and represent the initial private samples produced with the locally modified PYTHIA version to which all others are being compared and the final successfully validated samples produced with the running coupling implementation in an official release, respectively. The rest are intermediate test samples produced throughout the validation studies in an attempt to reproduce sample (1). The final validated sample was produced by forcing the off-diagonal dark mesons to decay and explicitly setting their mass so the decays are possible.

The number of dark quark decay products and off-diagonal mesons produced from dark quark decays are shown in Figure D.1. The dark quarks produce the same number of decay products in both samples (1) and (6), but far more “extra” dark particles are produced in the official PYTHIA implementation, where “extra” refers to dark particles that are not flavor-diagonal dark mesons, i.e. dark gluons or off-diagonal dark mesons. This is due to the increased number of dark meson species, as described above.

Figure D.2 displays the number of flavor-diagonal dark pions and dark rhos produced in the event, with significantly fewer diagonal dark mesons being produced in the official PYTHIA samples. This is because the dark quark decay products are now split between

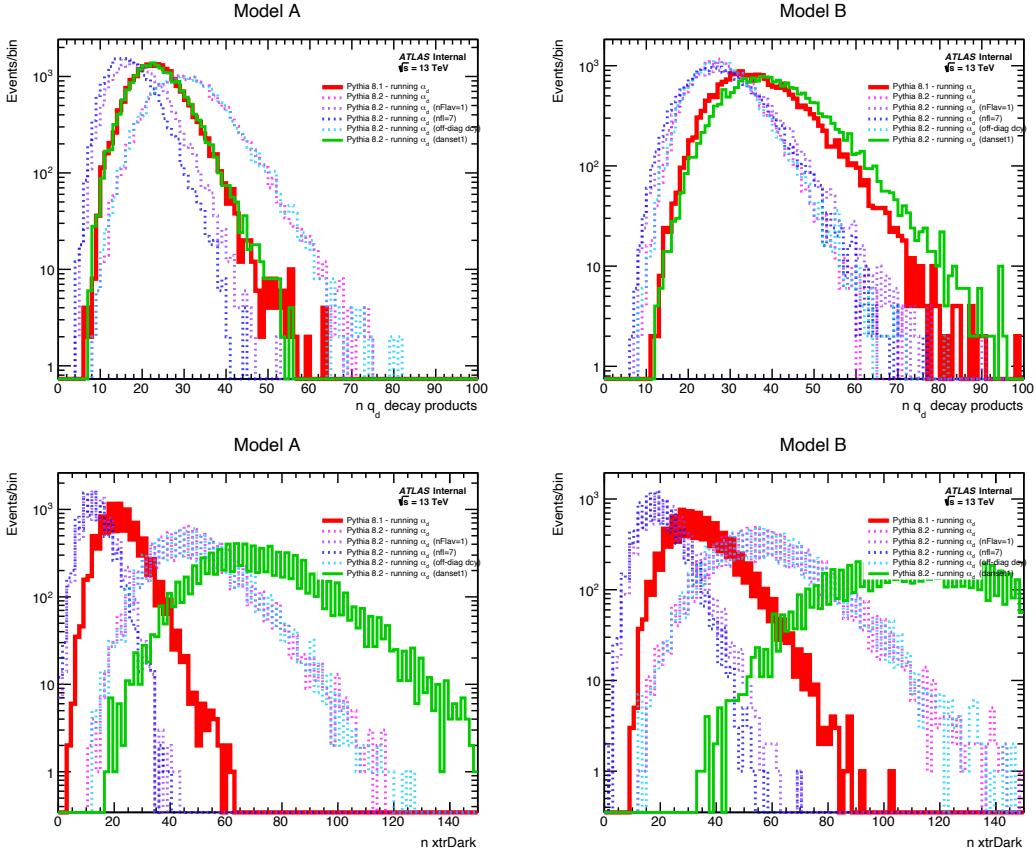


Figure D.1: The number of dark quark decay products (top) and “extra” dark particles (bottom) produced in the event for Model A (left) and Model B (right) in various test implementations of the Pythia model. Here, “extra” dark particles are all those other than the scalar mediator, dark quarks, and flavor-diagonal mesons, with the difference in extra dark particles produced between samples providing a measure of the number of off-diagonal dark mesons produced.

the two dark meson species, as opposed to always going to the single diagonal dark meson species allowed in the locally hacked samples.

The number of “inclusive” dark pions are shown in Figure D.3 (top), where “inclusive” refers to both the diagonal and off-diagonal dark pions in the event. While the numbers of diagonal and off-diagonal dark pions differ between the samples produced with the lo-

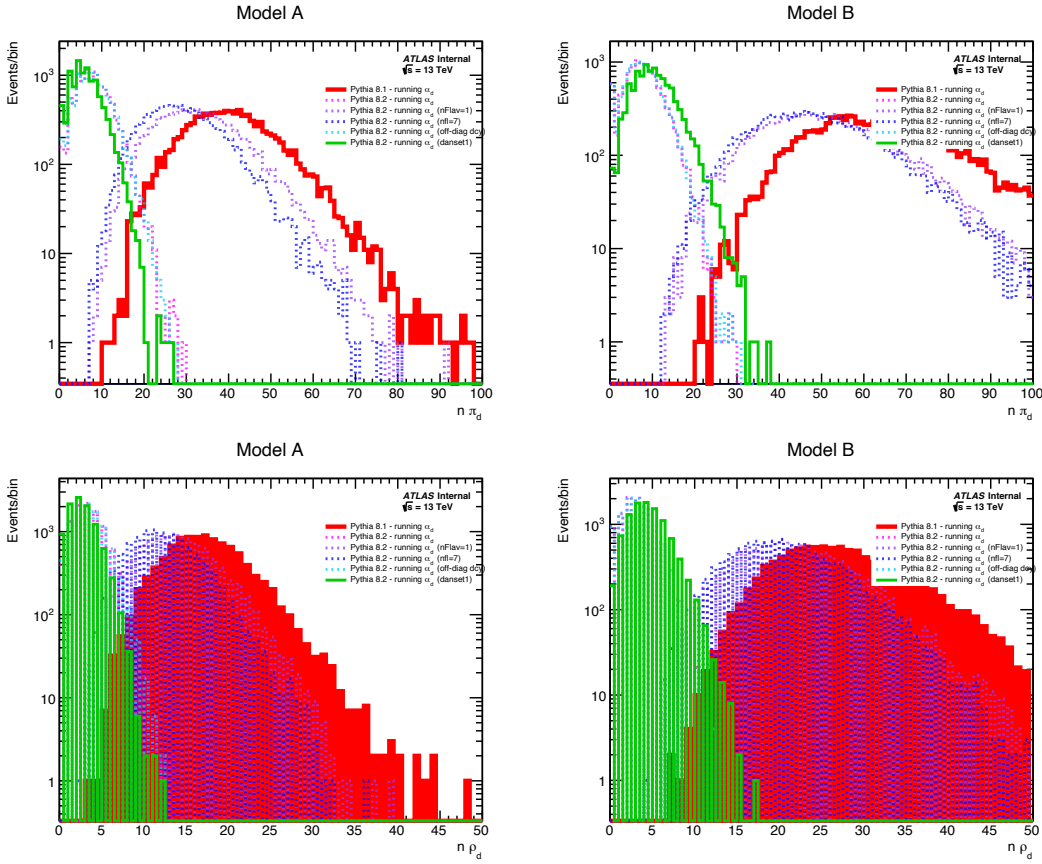


Figure D.2: The number of flavor-diagonal dark pions (top) and dark rhos (bottom) in Model A (left) and Model B (right).

cally modified and official PYTHIA versions, the number of inclusive dark pions remains constant. In this plot, three samples are compared across two models:

- locally hacked PYTHIA 8.183 with running dark coupling;
- official PYTHIA 8.230 with running dark coupling;
- official PYTHIA 8.230 with running dark coupling and explicit off-diagonal dark meson lifetimes.

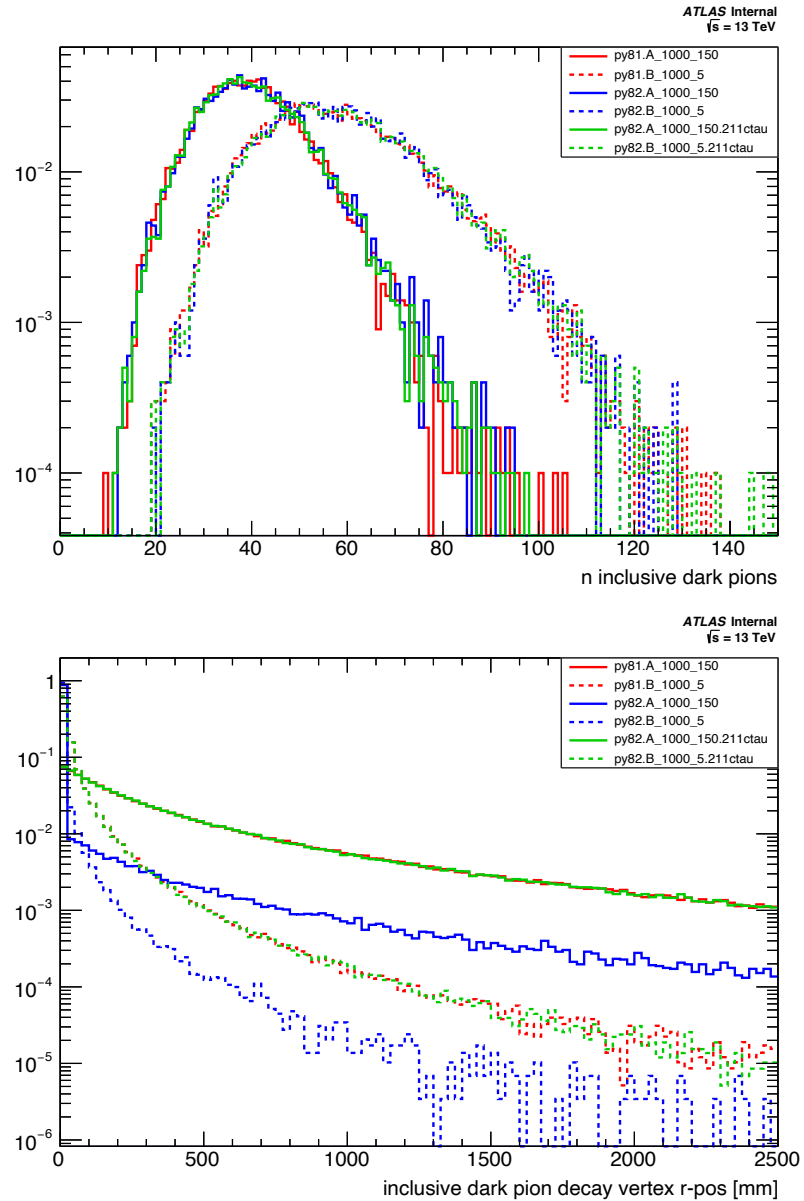
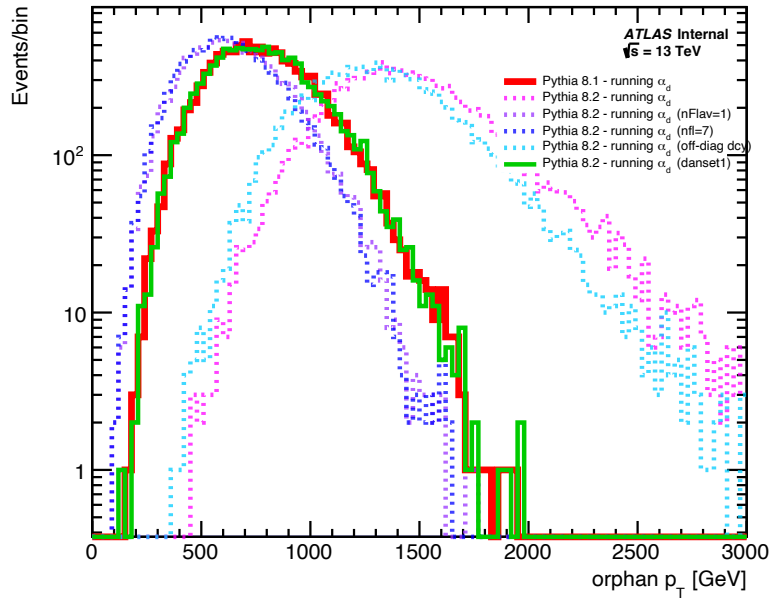


Figure D.3: The number (top) and radial decay position (bottom) of “inclusive” dark pions in the event. Here, “inclusive” dark pions are both flavor-diagonal and off-diagonal dark pions. The solid-line distributions represent Model A, and the dashed-line distributions represent Model B.

Model A samples are represented by solid lines and Model B samples are represented by dashed lines. Samples (a) and (b) correspond to samples (1) and (6) above, with an update in release between samples (6) and (b) that have no significant impact on the output. Sample (c) corresponds to the final version of the PYTHIA HV implementation used for official MC signal sample production, with the only change from sample (b) being the explicit introduction of off-diagonal dark meson lifetimes. The off-diagonal dark pion lifetimes are set to be the same as the diagonal dark pion lifetimes, as defined by the $c\tau_{\pi_d}$ parameter of the signal grid. Without the explicit off-diagonal dark pion lifetimes, such particles will decay promptly, reducing the overall signal, as described above. This effect is illustrated in Figure D.3 (bottom plot), where the distribution of dark pion decay radial positions is significantly lower in the PYTHIA 8.230 samples without explicit off-diagonal lifetimes.

The orphan p_T , defined as the sum- p_T of particles not clustered into truth jets of $p_T > 200$ GeV, is shown in Figure D.4. The number, p_T , and width of the truth dark and truth jets are shown in Figures D.5, D.6, and D.7, respectively. Here, the truth (dark) jet width is calculated from the girth, as defined in Section 4.2.2.1.1. All distributions are consistent between samples (1) and (6), as expected.

Model A



Model B

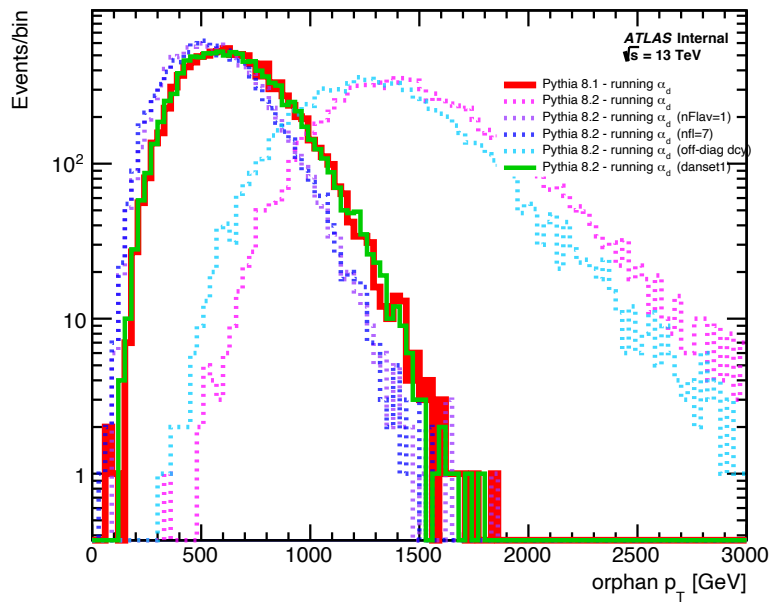


Figure D.4: The orphan p_T , or leftover p_T in the event not clustered into hard jets, in Model A (top) and Model B (bottom).

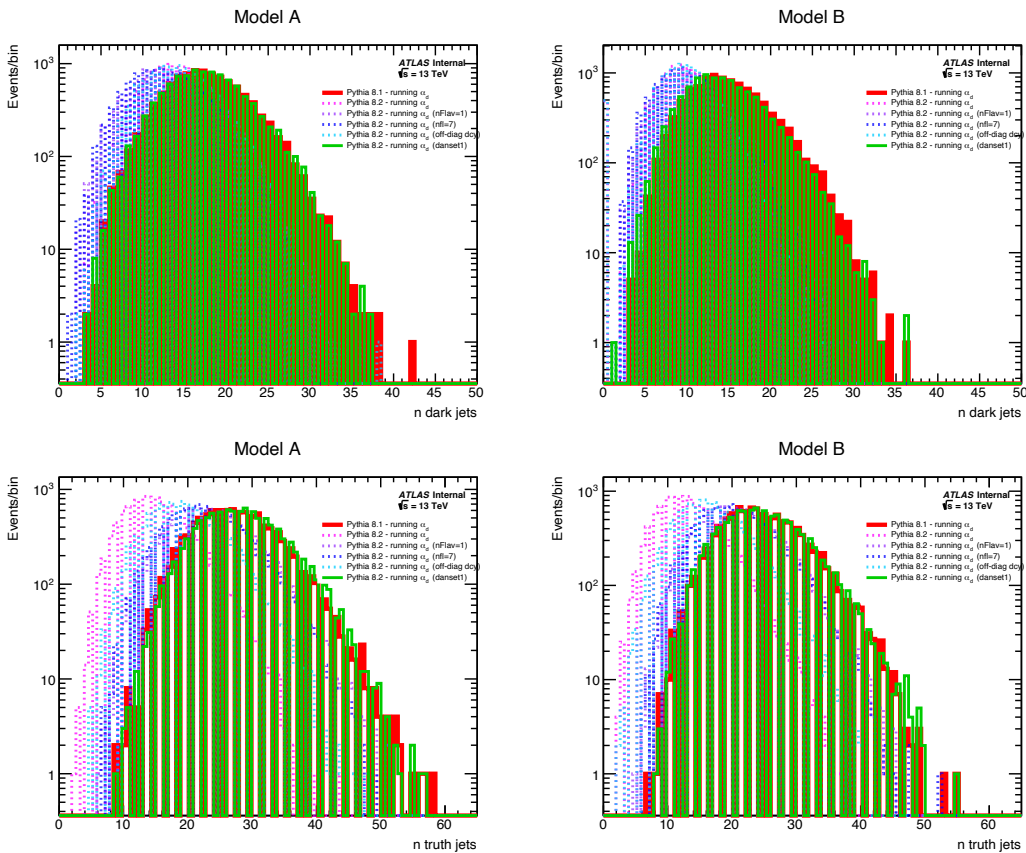


Figure D.5: The number of truth dark (top) and truth (bottom) jets per event in Model A (left) and Model B (right).

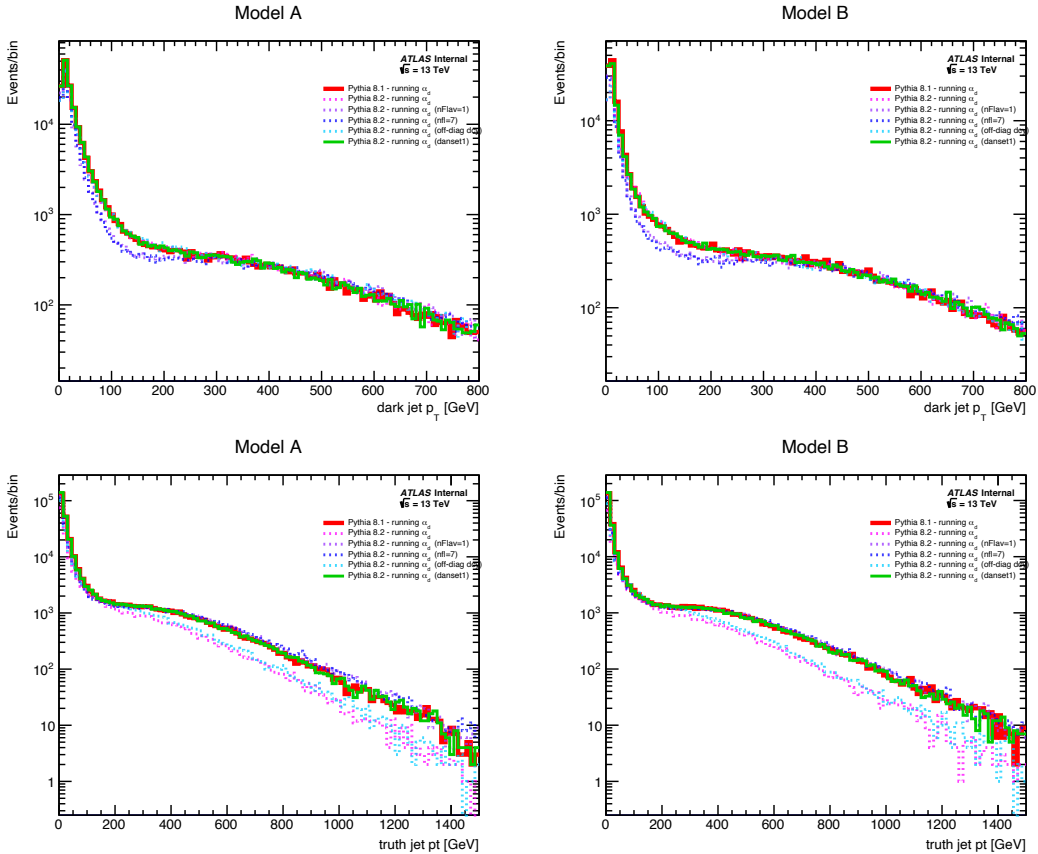


Figure D.6: The p_T of truth dark (top) and truth (bottom) jets per event in Model A (left) and Model B (right).

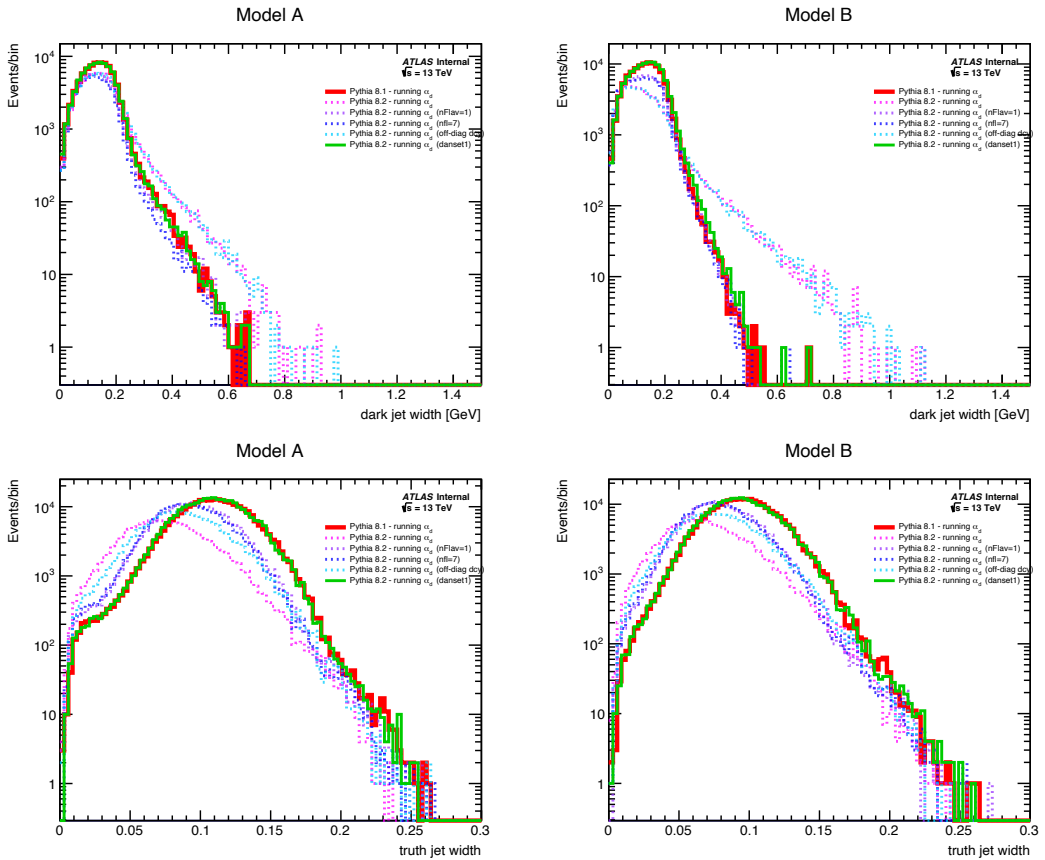


Figure D.7: The width, or girth, of truth dark (top) and truth (bottom) jets per event in Model A (left) and Model B (right).

References

- [1] S. Weinberg. The making of the standard model. *The European Physical Journal C*, 34(1):5–13, May 2004.
- [2] G. Aad, T. Abajyan, B. Abbott, J. Abdallah, S. Abdel Khalek, A.A. Abdelalim, O. Abdinov, R. Aben, B. Abi, M. Abolins, and et al. Observation of a new particle in the search for the standard model higgs boson with the atlas detector at the lhc. *Physics Letters B*, 716(1):1–29, Sep 2012.
- [3] S. Chatrchyan, V. Khachatryan, A.M. Sirunyan, A. Tumasyan, W. Adam, E. Aguilo, T. Bergauer, M. Dragicevic, J. Erö, C. Fabjan, and et al. Observation of a new boson at a mass of 125 gev with the cms experiment at the lhc. *Physics Letters B*, 716(1):30–61, Sep 2012.
- [4] Lyndon Evans and Philip Bryant. LHC machine. *Journal of Instrumentation*, 3(08):S08001–S08001, aug 2008.

- [5] ATLAS Collaboration. The ATLAS experiment at the CERN large hadron collider. *Journal of Instrumentation*, 3(08):S08003–S08003, aug 2008.
- [6] The CMS Collaboration. The CMS experiment at the CERN LHC. *Journal of Instrumentation*, 3(08):S08004–S08004, aug 2008.
- [7] S.L. Glashow. Partial Symmetries of Weak Interactions. *Nucl. Phys.*, 22:579–588, 1961.
- [8] Steven Weinberg. A model of leptons. *Phys. Rev. Lett.*, 19:1264–1266, Nov 1967.
- [9] Abdus Salam. Weak and Electromagnetic Interactions. *Conf. Proc. C*, 680519:367–377, 1968.
- [10] H. Fritzsch, Murray Gell-Mann, and H. Leutwyler. Advantages of the Color Octet Gluon Picture. *Phys. Lett. B*, 47:365–368, 1973.
- [11] Harald Fritzsch and Murray Gell-Mann. Current Algebra: Quarks and What Else? *eConf*, C720906V2(hep-ph/0208010):135–165. 21 p, Aug 2002.
- [12] Peter W. Higgs. Broken symmetries and the masses of gauge bosons. *Phys. Rev. Lett.*, 13:508–509, Oct 1964.
- [13] Katherine Garrett and Gintaras Duda. Dark matter: A primer. *Advances in Astronomy*, 2011:1–22, 2011.

- [14] Stefano Giagu. WIMP Dark Matter Searches With the ATLAS Detector at the LHC. *Front. in Phys.*, 7:75, 2019.
- [15] Kalliopi Petraki and Raymond R. Volkas. Review of asymmetric dark matter. *International Journal of Modern Physics A*, 28(19):1330028, Jul 2013.
- [16] Yang Bai and Pedro Schwaller. Scale of dark qcd. *Phys. Rev. D*, 89:063522, Mar 2014.
- [17] Pedro Schwaller, Daniel Stolarski, and Andreas Weiler. Emerging jets. *Journal of High Energy Physics*, 2015(5), May 2015.
- [18] Michael E. Peskin and Daniel V. Schroeder. *An Introduction to Quantum Field Theory*. Westview Press, 1995.
- [19] Mark Thomson. *Modern Particle Physics*. Cambridge University Press, 2013.
- [20] David Griffiths. *Introduction to Elementary Particles*. Wiley-VCH, 2nd edition, 2008.
- [21] Vernon D. Barger and Roger J.N. Phillips. *Collider Physics*. Addison-Wesley Publishing Company, updated edition, 1997.
- [22] W. Hollik. Quantum field theory and the standard model, 2010.
- [23] Particle Data Group. Review of particle physics. *Phys. Rev. D*, 98:030001, Aug 2018.

- [24] David J. Gross and Frank Wilczek. Ultraviolet behavior of non-abelian gauge theories. *Phys. Rev. Lett.*, 30:1343–1346, Jun 1973.
- [25] H. David Politzer. Reliable perturbative results for strong interactions? *Phys. Rev. Lett.*, 30:1346–1349, Jun 1973.
- [26] Kenneth G. Wilson. Confinement of quarks. *Phys. Rev. D*, 10:2445–2459, Oct 1974.
- [27] Makoto Kobayashi and Toshihide Maskawa. CP-Violation in the Renormalizable Theory of Weak Interaction. *Progress of Theoretical Physics*, 49(2):652–657, 02 1973.
- [28] Valerii A Rubakov and M E Shaposhnikov. Electroweak baryon number non-conservation in the early universe and in high-energy collisions. *Physics-Uspekhi*, 39(5):461–502, May 1996.
- [29] Csaba Balazs. Baryogenesis: A small review of the big picture, 2014.
- [30] Andrei D Sakharov. Violation of CP in variance, casymmetry, and baryon asymmetry of the universe. *Soviet Physics Uspekhi*, 34(5):392–393, may 1991.
- [31] Planck Collaboration. *Planck 2018 results. VI. Cosmological parameters*. 7 2018.
- [32] Rolf Kappl and Martin Wolfgang Winkler. The cosmic ray antiproton background for ams-02. *Journal of Cosmology and Astroparticle Physics*, 2014(09):051–051, Sep 2014.

- [33] V.A. Kuzmin, V.A. Rubakov, and M.E. Shaposhnikov. On anomalous electroweak baryon-number non-conservation in the early universe. *Physics Letters B*, 155(1):36 – 42, 1985.
- [34] Edward W. Kolb and Michael S. Turner. *The Early Universe*. Addison-Wesley Publishing Company, 1990.
- [35] J H Oort. The force exerted by the stellar system in the direction perpendicular to the galactic plane and some related problems. *Bull. Astron. Inst. Netherlands*, 6:249–287, 1932.
- [36] F. Zwicky. On the Masses of Nebulae and of Clusters of Nebulae. *Astrophys. J.*, 86:217–246, 1937.
- [37] V. C. Rubin. Dark matter in spiral galaxies. *Scientific American*, 248:96–106, June 1983.
- [38] Douglas Clowe, Maruša Bradač, Anthony H. Gonzalez, Maxim Markevitch, Scott W. Randall, Christine Jones, and Dennis Zaritsky. A direct empirical proof of the existence of dark matter. *The Astrophysical Journal*, 648(2):L109–L113, Aug 2006.
- [39] Robert Wagoner, William Fowler, and F. Hoyle. On the synthesis of elements at very high temperatures. *The Astrophysical Journal*, 148:3, 03 1967.

- [40] Arno A. Penzias and Robert Woodrow Wilson. A Measurement of excess antenna temperature at 4080-Mc/s. *Astrophys. J.*, 142:419–421, 1965.
- [41] George Smoot, C. Bennett, A. Kogut, E. Wright, J. Aymon, N. Boggess, E. Cheng, Giovanni de Amici, Samuel Gulkis, M. Hauser, G. Hinshaw, P. Jackson, M. Janssen, E. Kaita, T. Kelsall, Phil Keegstra, Charley Lineweaver, Karen Loewenstein, Philip Lubin, and D. Wilkinson. Structure in the cobe differential microwave radiometer first-year maps. *The Astrophysical Journal*, 396:L1–L5, 09 1992.
- [42] et.al. Hinshaw, G. F.
- [43] STEPHEN P. MARTIN. A supersymmetry primer. *Advanced Series on Directions in High Energy Physics*, page 1–98, Jul 1998.
- [44] Edward Witten. Baryons in the $1/n$ expansion. *Nucl. Phys.*, B160:57–115, 1979.
- [45] Oliver Sim Brüning, Paul Collier, P Lebrun, Stephen Myers, Ranko Ostojic, John Poole, and Paul Proudlock. *LHC Design Report*. CERN Yellow Reports: Monographs. CERN, Geneva, 2004.
- [46] ATLAS Collaboration. *ATLAS detector and physics performance: Technical Design Report, 1.* Technical Design Report ATLAS. CERN, Geneva, 1999.

- [47] ATLAS Collaboration. *ATLAS detector and physics performance: Technical Design Report, 2.* Technical Design Report ATLAS. CERN, Geneva, 1999.
- [48] The ALICE Collaboration. The ALICE experiment at the CERN LHC. *Journal of Instrumentation*, 3(08):S08002–S08002, aug 2008.
- [49] The LHCb Collaboration. The LHCb detector at the LHC. *Journal of Instrumentation*, 3(08):S08005–S08005, aug 2008.
- [50] Radiofrequency cavities. Sep 2012.
- [51] Werner Herr and B Muratori. Concept of luminosity. 2006.
- [52] Esma Mobs. The CERN accelerator complex. ComPLEXe des accélérateurs du CERN. Jul 2016. General Photo.
- [53] ATLAS Collaboration. Luminosity determination in $p\bar{p}$ collisions at $\sqrt{s} = 13$ TeV using the ATLAS detector at the LHC. Technical Report ATLAS-CONF-2019-021, CERN, Geneva, Jun 2019.
- [54] ATLAS Collaboration. Luminosity public results run2. <https://twiki.cern.ch/twiki/bin/view/AtlasPublic/LuminosityPublicResultsRun2>, 2019.

- [55] H. Pernegger on behalf of the ATLAS Collaboration. The pixel detector of the ATLAS experiment for LHC run-2. *Journal of Instrumentation*, 10(06):Co6012–Co6012, jun 2015.
- [56] ATLAS Collaboration. ATLAS pixel detector electronics and sensors. *Journal of Instrumentation*, 3(07):Po7007–Po7007, jul 2008.
- [57] M Capeans, G Darbo, K Einsweiller, M Elsing, T Flick, M Garcia-Sciveres, C Gemme, H Pernegger, O Rohne, and R Vuillermet. ATLAS Insertable B-Layer Technical Design Report. Technical Report CERN-LHCC-2010-013. ATLAS-TDR-19, Sep 2010.
- [58] The ATLAS collaboration. Operation and performance of the atlas semiconductor tracker. *Journal of Instrumentation*, 9(08):Po8009–Po8009, Aug 2014.
- [59] E. Hines. Performance of Particle Identification with the ATLAS Transition Radiation Tracker. Technical Report arXiv:1109.5925, CERN, Geneva, Sep 2011. Comments: 8 pages, 7 figures. Conference proceedings for the Meeting of the Division of Particles and Fields of the American Physical Society (DPF), 2011.
- [60] M. Aaboud, G. Aad, B. Abbott, J. Abdallah, O. Abdinov, B. Abelos, R. Aben, O. S. AbouZeid, N. L. Abraham, and et al. Performance of the atlas trigger system in 2015. *The European Physical Journal C*, 77(5), May 2017.

- [61] Arantxa Ruiz, Martínez. The atlas run-2 trigger menu for higher luminosities: Design, performance and operational aspects. *EPJ Web Conf.*, 182:02083, 2018.
- [62] R Achenbach, P Adragna, V Andrei, P Apostologlou, B Åsman, C Ay, B M Barnett, B Bauss, M Bendel, C Bohm, J R A Booth, I P Brawn, P Bright-Thomas, D G Charlton, N J Collins, C J Curtis, A Dahlhoff, A O Davis, S Eckweiler, J P Edwards, E F Eisenhandler, P J W Faulkner, J Fleckner, F Föhlisch, J Garvey, C N P Gee, A R Gillman, P Hanke, R P Hatley, S Hellman, A Hidvegi, S J Hillier, K Jakobs, M Johansen, E E Kluge, M Landon, V Lendermann, J N Lilley, K Mahboubi, G Mahout, A Mass, K Meier, T Moa, E Moyse, F Müller, A Neusiedl, C Nöding, B Oltmann, J M Pentney, V J O Perera, U Pfeiffer, D P F Prieur, W Qian, D L Rees, S Rieke, F Rühr, D P C Sankey, U Schäfer, K Schmitt, H C Schultz-Coulon, C Schumacher, S Silverstein, R J Staley, R Stamen, M C Stockton, S Tapprogge, J P Thomas, T Trezger, P M Watkins, A Watson, P Weber, and E E Woehrli. The ATLAS Level-1 Calorimeter Trigger. Technical Report ATL-DAQ-PUB-2008-001. ATL-COM-DAQ-2008-002, CERN, Geneva, Jan 2008.
- [63] A. Nairz. ATLAS distributed computing: experience and evolution. *J. Phys. Conf. Ser.*, 523:012020, 2014.
- [64] G. Aad, B. Abbott, J. Abdallah, A. A. Abdelalim, A. Abdesselam, O. Abdinov,

B. Abi, M. Abolins, H. Abramowicz, and et al. The atlas simulation infrastructure.

The European Physical Journal C, 70(3):823–874, Sep 2010.

[65] Athena core software. <http://atlas-computing.web.cern.ch/>

atlas-computing/packages/athenaCore/athenaCore.php, 2006.

[66] S Agostinelli, J Allison, K Amako, John Apostolakis, H M Araújo, P Arce, M Asai, D A Axen, S Banerjee, G Barrand, F Behner, L Bellagamba, J Boudreau, L Broglia, A Brunengo, S Chauvie, J Chuma, R Chytracek, G Cooperman, G Cosmo, P V Degt-yarenko, A Dell’Acqua, G O De Paola, D D Dietrich, R Enami, A Feliciello, C Ferguson, H S Fesefeldt, G Folger, F Foppiano, A C Forti, S Garelli, S Giani, R Giannitrapani, D Gibin, JJ Gómez-Cadenas, I González, G Gracía-Abril, L G Greeniaus, W Greiner, V M Grichine, A Grossheim, P Gumplinger, R Hamatsu, K Hashimoto, H Hasui, A M Heikkinen, A Howard, A M Hutton, V N Ivanchenko, A Johnson, F W Jones, Jeff Kallenbach, N Kanaya, M Kawabata, Y Kawabata, M Kawaguti, S Kelner, P Kent, T Kodama, R P Kokoulin, M Kossov, H Kurashige, E Lamanna, T Lampen, V Lara, V Lefébure, F Lei, M Liendl, W Lockman, F Longo, S Magni, M Maire, B A Mecking, E Medernach, K Minamimoto, P Mora de Freitas, Y Morita, K Murakami, M Nagamatu, R Nartallo, P Nieminen, T Nishimura, K Ohtsubo, M Okamura, S W O’Neale, Y O’Ohata, J Perl, A Pfeiffer, M G Pia, F Ranjard, A Rybin, S Sadilov, E Di Salvo, G Santin, T Sasaki, N Savvas, Y Sawada, S Scherer, S Sei,

V I Sirotenko, D Smith, N Starkov, H Stöcker, J Sulkimo, M Takahata, S Tanaka, E Chernyaev, F Safai-Tehrani, M Tropeano, P R Truscott, H Uno, L Urbà, P Urban, M Verderi, A Walkden, W Wander, H Weber, J P Wellisch, T Wenaus, D C Williams, D Wright, T Yamada, H Yoshida, and D Zschiesche. GEANT4: A Simulation toolkit. *Nucl. Instrum. Methods Phys. Res., A*, 506(CERN-IT-2002-003. SLAC-PUB-9350. 3):250–303. 86 p, Jul 2002.

- [67] J Allison. Geant4 developments and applications. *IEEE Trans. Nucl. Sci.*, 53:270, 2006.
- [68] Nicholas Metropolis and S. Ulam. The monte carlo method. *Journal of the American Statistical Association*, 44(247):335–341, 1949. PMID: 18139350.
- [69] Michael H. Seymour and Marilyn Marx. Monte carlo event generators, 2013.
- [70] Andy Buckley, Jonathan Butterworth, Stefan Gieseke, David Grellscheid, Stefan Höche, Hendrik Hoeth, Frank Krauss, Leif Lönnblad, Emily Nurse, Peter Richardson, and et al. General-purpose event generators for lhc physics. *Physics Reports*, 504(5):145–233, Jul 2011.
- [71] B. Webber. Parton shower Monte Carlo event generators. *Scholarpedia*, 6(12):10662, 2011. revision #128236.

- [72] M Dobbs and J B Hansen. The HepMC C++ Monte Carlo Event Record for High Energy Physics. Technical Report ATL-SOFT-2000-001, CERN, Geneva, Jun 2000.
revised version number 1 submitted on 2001-02-27 09:54:32.
- [73] ATLAS Pythia 8 tunes to 7 TeV datas. Technical Report ATL-PHYS-PUB-2014-021, CERN, Geneva, Nov 2014.
- [74] G. Altarelli. QCD evolution equations for parton densities. *Scholarpedia*, 4(1):7124, 2009. revision #91681.
- [75] J. Feltesse. Introduction to Parton Distribution Functions. *Scholarpedia*, 5(11):10160, 2010. revision #186761.
- [76] D Bourilkov, R C Group, and M R Whalley. Lhapdf: Pdf use from the tevatron to the lhc, 2006.
- [77] M R Whalley and D Bourilkov. The Les Houches Accord PDFs (LHAPDF) and Lhaglue. (hep-ph/0508110):8 p, Aug 2005.
- [78] B. Andersson, G. Gustafson, G. Ingelman, and T. Sjöstrand. Parton fragmentation and string dynamics. *Physics Reports*, 97(2):31 – 145, 1983.
- [79] Bo Andersson. *The Lund Model*. Cambridge Monographs on Particle Physics, Nuclear Physics and Cosmology. Cambridge University Press, 1998.

- [80] Torbjörn Sjöstrand, Stefan Ask, Jesper R. Christiansen, Richard Corke, Nishita Desai, Philip Ilten, Stephen Mrenna, Stefan Prestel, Christine O. Rasmussen, and Peter Z. Skands. An introduction to pythia 8.2. *Computer Physics Communications*, 191:159–177, Jun 2015.
- [81] Christian Bierlich, Nishita Desai, Ilkka Helenius, Philip Ilten, Leif Lönnblad, Stephen Mrenna, Stefan Prestel, Christine Rasmussen, Torbjörn Sjöstrand, and Peter Skands. PYTHIA 8.2 Homepage. <http://home.thep.lu.se/Pythia/>.
- [82] Zachary Marshall. Simulation of pile-up in the ATLAS experiment. *Journal of Physics: Conference Series*, 513(2):022024, jun 2014.
- [83] A Basalaev and Z Marshall and. The fast simulation chain for ATLAS. *Journal of Physics: Conference Series*, 898:042016, oct 2017.
- [84] Wolfgang Lukas. Fast simulation for ATLAS: Atlfast-II and ISF. *Journal of Physics: Conference Series*, 396(2):022031, dec 2012.
- [85] Roland Jansky. The ATLAS fast monte carlo production chain project. *Journal of Physics: Conference Series*, 664(7):072024, dec 2015.
- [86] Takashi Yamanaka and. The ATLAS calorimeter simulation FastCaloSim. *Journal of Physics: Conference Series*, 331(3):032053, dec 2011.

- [87] Z Hubacek and. Upgrading the ATLAS fast calorimeter simulation. *Journal of Physics: Conference Series*, 762:012054, oct 2016.
- [88] K Edmonds, S Fleischmann, T Lenz, C Magass, J Mechnich, and A Salzburger. The Fast ATLAS Track Simulation (FATRAS). Technical Report ATL-SOFT-PUB-2008-001. ATL-COM-SOFT-2008-002, CERN, Geneva, Mar 2008.
- [89] Jörg Mechnich and. FATRAS - the ATLAS fast track simulation project. *Journal of Physics: Conference Series*, 331(3):032046, dec 2011.
- [90] Joao Pequenao and Paul Schaffner. How ATLAS detects particles: diagram of particle paths in the detector. Jan 2013.
- [91] Rebecca Carney, Sam Silverstein, Sara Strandberg, and Maurice Garcia-Sciveres. Silicon Tracking and a Search for Long-lived Particles, Apr 2019. Presented on 13 Jun 2019.
- [92] A Salzburger. The ATLAS Track Extrapolation Package. Technical Report ATL-SOFT-PUB-2007-005. ATL-COM-SOFT-2007-010, CERN, Geneva, Jun 2007.
- [93] Performance of the reconstruction of large impact parameter tracks in the ATLAS inner detector. Technical Report ATL-PHYS-PUB-2017-014, CERN, Geneva, Jul 2017.

- [94] T Cornelissen, M Elsing, S Fleischmann, W Liebig, E Moyse, and A Salzburger. Concepts, Design and Implementation of the ATLAS New Tracking (NEWT). Technical Report ATL-SOFT-PUB-2007-007. ATL-COM-SOFT-2007-002, CERN, Geneva, Mar 2007.
- [95] Performance of the ATLAS Silicon Pattern Recognition Algorithm in Data and Simulation at $\sqrt{s} = 7$ TeV. Technical Report ATLAS-CONF-2010-072, CERN, Geneva, Jul 2010.
- [96] R. Frühwirth. Application of kalman filtering to track and vertex fitting. *Nuclear Instruments and Methods in Physics Research Section A: Accelerators, Spectrometers, Detectors and Associated Equipment*, 262(2):444 – 450, 1987.
- [97] The Optimization of ATLAS Track Reconstruction in Dense Environments. Technical Report ATL-PHYS-PUB-2015-006, CERN, Geneva, Mar 2015.
- [98] M. Aaboud, G. Aad, B. Abbott, J. Abdallah, O. Abdinov, B. Abelos, S. H. Abidi, O. S. AbouZeid, N. L. Abraham, and et al. Performance of the atlas track reconstruction algorithms in dense environments in lhc run 2. *The European Physical Journal C*, 77(10), Oct 2017.
- [99] Richard O. Duda and Peter E. Hart. Use of the hough transformation to detect lines and curves in pictures. *Commun. ACM*, 15(1):11–15, January 1972.

- [100] Track Reconstruction Performance of the ATLAS Inner Detector at $\sqrt{s} = 13$ TeV. Technical Report ATL-PHYS-PUB-2015-018, CERN, Geneva, Jul 2015.
- [101] Early Inner Detector Tracking Performance in the 2015 data at $\sqrt{s} = 13$ TeV. Technical Report ATL-PHYS-PUB-2015-051, CERN, Geneva, Dec 2015.
- [102] M. Aaboud, G. Aad, B. Abbott, J. Abdallah, O. Abdinov, B. Abelos, R. Aben, O. S. AbouZeid, N. L. Abraham, and et al. Reconstruction of primary vertices at the atlas experiment in run 1 proton–proton collisions at the lhc. *The European Physical Journal C*, 77(5), May 2017.
- [103] Vertex Reconstruction Performance of the ATLAS Detector at $\sqrt{s} = 13$ TeV. Technical Report ATL-PHYS-PUB-2015-026, CERN, Geneva, Jul 2015.
- [104] Wolfgang Waltenberger, Rudolf Frühwirth, and Pascal Vanlaer. Adaptive vertex fitting. *Journal of Physics G: Nuclear and Particle Physics*, 34(12):N343–N356, nov 2007.
- [105] Hideyuki Oide. VrtSecInclusive: an inclusive displaced vertex reconstruction package in release 21. Technical Report ATL-COM-INDET-2018-006, CERN, Geneva, Feb 2018.
- [106] VrtSecInclusive Package. <https://gitlab.cern.ch/atlas/athena/-/tree/21.0/Reconstruction%2FVKalVrt%2FvrtSecInclusive>.

- [107] Performance of vertex reconstruction algorithms for detection of new long-lived particle decays within the ATLAS inner detector. Technical Report ATL-PHYS-PUB-2019-013, CERN, Geneva, Mar 2019.
- [108] Karri Folan Di Petrillo, Lawrence Lee JR, Melissa Franklin, Rebecca Carney, Laura Jeanty, Christian Ohm, Hideyuki Oide, Hidetoshi Otono, Simone Pagan Griso, Jennifer Kathryn Roloff, Abner Soffer, and Filip Backman. Search for long-lived, massive particles in events with a displaced vertex and muon in $p\bar{p}$ collisions at $\sqrt{s} = 13$ TeV with the ATLAS detector. Technical Report ATL-COM-PHYS-2018-1138, CERN, Geneva, Aug 2018.
- [109] Treatment of mc truth and calculation of reconstruction efficiency for vrtsecinclusive algorithm. <https://gitlab.cern.ch/Atlas-Inner-Tracking/SecVtxPUBNote/-/wikis/home>.
- [110] John E. Huth et al. Toward a standardization of jet definitions. In *1990 DPF Summer Study on High-energy Physics: Research Directions for the Decade (Snowmass 90)*, pages 0134–136, 12 1990.
- [111] Gavin P. Salam. Towards jetography. *The European Physical Journal C*, 67(3–4):637–686, May 2010.

- [112] Matteo Cacciari, Gavin P Salam, and Gregory Soyez. The anti-ktjet clustering algorithm. *Journal of High Energy Physics*, 2008(04):063–063, Apr 2008.
- [113] G. Aad, B. Abbott, J. Abdallah, O. Abdinov, R. Aben, M. Abolins, O. S. AbouZeid, H. Abramowicz, H. Abreu, and et al. Topological cell clustering in the atlas calorimeters and its performance in lhc run i. *The European Physical Journal C*, 77(7), Jul 2017.
- [114] Peter Loch and. Jet measurements in ATLAS. *Journal of Physics: Conference Series*, 323:012002, nov 2011.
- [115] Gerald C. Blazey, Jay R. Dittmann, Stephen D. Ellis, V. Daniel Elvira, K. Frame, S. Grinstein, Robert Hirosky, R. Piegaia, H. Schellman, R. Snihur, V. Sorin, and Dieter Zeppenfeld. Run ii jet physics: Proceedings of the run ii qcd and weak boson physics workshop, 2000.
- [116] G. Aad, B. Abbott, J. Abdallah, A. A. Abdelalim, A. Abdesselam, O. Abdinov, B. Abi, M. Abolins, H. Abramowicz, and et al. Jet energy measurement with the ATLAS detector in proton-proton collisions at $\sqrt{s} = 7$ TeV. *The European Physical Journal C*, 73(3), Mar 2013.
- [117] G. Aad, T. Abajyan, B. Abbott, J. Abdallah, S. Abdel Khalek, O. Abdinov, R. Aben, B. Abi, M. Abolins, and et al. Jet energy measurement and its systematic uncertainty

in proton–proton collisions at $\sqrt{s} = 7$ tev with the atlas detector. *The European Physical Journal C*, 75(1), Jan 2015.

- [118] M. Aaboud, G. Aad, B. Abbott, J. Abdallah, O. Abdinov, B. Abelos, S. H. Abidi, O. S. AbouZeid, N. L. Abraham, H. Abramowicz, and et al. Jet energy scale measurements and their systematic uncertainties in proton-proton collisions at $s=13$ tev with the atlas detector. *Physical Review D*, 96(7), Oct 2017.
- [119] Matteo Cacciari, Gavin P Salam, and Gregory Soyez. The catchment area of jets. *Journal of High Energy Physics*, 2008(04):005–005, apr 2008.
- [120] Tagging and suppression of pileup jets with the ATLAS detector. Technical Report ATLAS-CONF-2014-018, CERN, Geneva, May 2014.
- [121] Selection of jets produced in 13TeV proton-proton collisions with the ATLAS detector. Technical Report ATLAS-CONF-2015-029, CERN, Geneva, Jul 2015.
- [122] Matthew J. Strassler and Kathryn M. Zurek. Echoes of a hidden valley at hadron colliders. *Physics Letters B*, 651(5-6):374–379, Aug 2007.
- [123] James Catmore. The ATLAS data processing chain: from collisions to papers.
https://indico.cern.ch/event/472469/contributions/1982677/attachments/1220934/1785823/intro_slides.pdf, February 2016. Join Oslo/Bergen/NBI ATLAS Software Tutorial.

- [124] DAOD_EXOT₂₃ code. <https://gitlab.cern.ch/atlas/athena/-/blob/21.2/PhysicsAnalysis/DerivationFramework/DerivationFrameworkExotics/share/EXOT23.py>.
- [125] EmergingJetsAnalysis framework. <https://gitlab.cern.ch/EmergingJets/EmergingJetsAnalysis>.
- [126] Lisa Carloni and Torbjörn Sjöstrand. Visible effects of invisible hidden valley radiation. *Journal of High Energy Physics*, 2010(9), Sep 2010.
- [127] Lisa Carloni, Johan Rathsman, and Torbjörn Sjöstrand. Discerning secluded sector gauge structures. *Journal of High Energy Physics*, 2011(4), Apr 2011.
- [128] Richard D. Ball, Valerio Bertone, Stefano Carrazza, Christopher S. Deans, Luigi Del Debbio, Stefano Forte, Alberto Guffanti, Nathan P. Hartland, José I. Latorre, Juan Rojo, and et al. Parton distributions with lhc data. *Nuclear Physics B*, 867(2):244–289, Feb 2013.
- [129] Stefano Carrazza, Stefano Forte, and Juan Rojo. Parton distributions and event generators, 2013.
- [130] Modified pythia 8.183 with running dark coupling. <https://github.com/pedroschwaller/EmergingJets>.

- [131] ATLAS Collaboration. Beamspot public results. <https://twiki.cern.ch/twiki/bin/view/AtlasPublic/BeamSpotPublicResults>, 2017.
- [132] Julia Gonski. Jet Cleaning in 2016 and the Event Level Cleaning Tool. Technical Report ATL-COM-PHYS-2017-982, CERN, Geneva, Jun 2017.
- [133] ATLAS Collaboration. Public jet trigger plots for collision data. <https://twiki.cern.ch/twiki/bin/view/AtlasPublic/JetTriggerPublicResults>, 2018.
- [134] M. Aaboud, G. Aad, B. Abbott, J. Abdallah, O. Abdinov, B. Abeloos, S.H. Abidi, O.S. AbouZeid, N.L. Abraham, H. Abramowicz, and et al. Study of the material of the atlas inner detector for run 2 of the lhc. *Journal of Instrumentation*, 12(12):P12009–P12009, Dec 2017.
- [135] ATLAS Collaboration. Search for long-lived, massive particles in events with a displaced vertex and a muon with large impact parameter in $p\bar{p}$ collisions at $\sqrt{s} = 13$ tev with the atlas detector, 2020.
- [136] RDOAnalysis package. <https://gitlab.cern.ch/atlas/athena/-/tree/master/Simulation/Tools/RDOAnalysis>.

- [137] LongLivedParticleDPDMaker code. <https://gitlab.cern.ch/atlas/athena/-/tree/21.0/PhysicsAnalysis/SUSYPhys/LongLivedParticleDPDMaker>.
- [138] Dominik Krauss, Siinn Che, Christopher Blake Martin, and K.K. Gan. Search for long-lived, massive particles decaying into leptons in pp collisions at 13 TeV centre-of-mass energy, with the ATLAS detector at the LHC. Technical Report ATL-COM-PHYS-2017-1060, CERN, Geneva, Jul 2017.
- [139] N Barlow, K Bentdz, J Bouffard, G Cottin, J Ernst, A Fischer, V Jain, H J Kim, D Milstead, H Otono, N Pettersson, A Soffer, N Soni, N Taiblum, and Teng Jian Khoo. Search for long-lived, heavy particles using a multi-track displaced vertex, in pp collisions at 8 TeV centre-of-mass energy, with the ATLAS detector at the LHC. Technical Report ATL-COM-PHYS-2014-370, CERN, Geneva, Apr 2014.
- [140] M. Aaboud, G. Aad, B. Abbott, O. Abdinov, B. Abeloos, S. H. Abidi, O. S. AbouZeid, N. L. Abraham, H. Abramowicz, and et al. Search for long-lived charginos based on a disappearing-track signature in pp collisions at $\sqrt{s} = 13$ TeV with the ATLAS detector. *Journal of High Energy Physics*, 2018(6), Jun 2018.
- [141] G. Aad, B. Abbott, D. C. Abbott, O. Abdinov, A. Abed Abud, K. Abeling, D. K. Abhayasinghe, S. H. Abidi, O. S. AbouZeid, and et al. Search for heavy neutral

leptons in decays of w bosons produced in 13 tev pp collisions using prompt and displaced signatures with the atlas detector. *Journal of High Energy Physics*, 2019(10), Oct 2019.

- [142] G. Aad, B. Abbott, J. Abdallah, A. A. Abdelalim, A. Abdesselam, O. Abdinov, B. Abi, M. Abolins, O. S. AbouZeid, H. Abramowicz, and et al. Search for a light higgs boson decaying to long-lived weakly interacting particles in proton-proton collisions at $s=7$ tevwith the atlas detector. *Physical Review Letters*, 108(25), Jun 2012.

- [143] G. Aad, B. Abbott, J. Abdallah, S. Abdel Khalek, O. Abdinov, R. Aben, B. Abi, M. Abolins, O.S. AbouZeid, H. Abramowicz, and et al. Search for pair-produced long-lived neutral particles decaying to jets in the atlas hadronic calorimeter in pp collisions at $s=8$ tev. *Physics Letters B*, 743:15–34, Apr 2015.

- [144] *Journal of Instrumentation*, (07):Po7015–Po7015, Jul 2013.